A MONTE CARLO ANALYSIS OF COMPUTERIZED TOMOGRAPHY

THESIS

Karyl J. Davis, Captain, USAF

AFIT/ENP/GAP/95D-3

DEPARTMENT OF THE AIR FORCE
AIR UNIVERSITY
AIR FORCE INSTITUTE OF TECHNOLOGY

Wright-Patterson Air Force Base, Ohio

AFIT/ENP/GAP/95D-3

A MONTE CARLO ANALYSIS OF COMPUTERIZED TOMOGRAPHY

THESIS

Karyl J. Davis, Captain, USAF

AFIT/ENP/GAP/95D-3

The views expressed in this thesis are those of the author
and do not reflect the official policy or position
of the Department of Defense or the U.S. Government.

AFIT/ENP/GAP/95D-3

A MONTE CARLO ANALYSIS OF COMPUTERIZED TOMOGRAPHY

THESIS

Presented to the Faculty of the School of Engineering
Air Education Training Command
In Partial Fulfillment of the Requirements for the
Degree of Master of Science

Karyl J. Davis, B.S.,
Captain, USAF

December 1995

AFIT/ENP/GAP/95D-3

A MONTE CARLO ANALYSIS OF COMPUTERIZED TOMOGRAPHY

Karyl J. Davis, B.S.,
Captain, USAF

Approved:

Jeffrey B. Martin — 22 Nov 95
Jeffrey Martin
Chairman, Advisory Committee

George John — 27 Nov 95
George John
Member, Advisory Committee

Kirk Mathews — 22 Nov 95
Kirk Mathews
Member, Advisory Committee

William H. Ruck II — 22 NOV 95
William Ruck
Member, Advisory Committee

Acknowledgments

I would like to thank my thesis advisor, Captain Jeffrey Martin, for his patience, direction, and bravery in taking on a non-nuclear type attempting a medical thesis. His persistence and dedication to the "hard-science" approach contributed immeasurably to the education I received during the thesis process.

Next, I would like to thank my committee members: Dr. George John, for the reality checks his experimentalist background provided and Dr. Mathews for the Monte Carlo tutorial that gave a real understanding of the MCNP model. Their input kept the process going in the right direction. Captain Ruck was always available to answer my many questions about the CT unit and its operation as were his colleague, Susan Poteat, and the CT medical technicians at WPMC.

I would also like to thank Captain Charles Brennan, AFIT doctoral candidate, for his interest, invaluable assistance, but, above that, his tolerance as I repeatedly interrupted *his* work with questions about mine.

Completion would not have been possible without Tony Schooler and Joe Hamlin, AFIT/SC, who loaded the unloadable software and buffered me from the numerous inquiries about "that kdavis running that MCNP code on all the SUNs".

Finally, I would like to thank my family: my brother, who worked on his wedding day to give me the computational gusto I needed and my husband, Steve, and son, Josh, for their unconditional support and sanity checks when I needed them most.

Karyl J. Davis

TABLE OF CONTENTS

Table of Figures

Table of Tables

Abstract

The purpose of this thesis was to model a computerized tomography device (CT) using Monte Carlo methods to determine the scattered radiation spectrum inside and the dose outside the suite at Wright-Patterson Medical Center and at a generic suite to non-occupational personnel. This was driven by the recent inclusion of the most recent NCRP recommended dose limits into 10CFR20 of 50 mSv, occupational; 1 mSv, non-occupational continuous exposure; and 5 mSv, infrequent exposure. The rotating fan beam of the CT was modeled for MCNP, a general-purpose Monte Carlo n-particle transport model. The CT target was a standard human phantom defined in MIRD Pamphlet 5. The source and phantom were rotated 27° with respect to the walls. A head scan and an abdomen scan were simulated. CT usage factors were set equal to average WPMC values. The suite walls were modeled alternately with 1/16" and 1/8" lead shielding between gypsum drywall for the occupational and non-occupational dose, respectively. With CT isocenter as problem origin, test detectors were placed 30 cm outside the walls on two sets of axes defined by (a) the walls and (b) the source-body axes. Film badges placed in the CT suite at WPMC agreed with MCNP modeling results by a factor of two, validating the method. The analysis showed that outside both the WPMC CT suite and the generic room the continuous-exposure non-occupational dose limit was exceeded below the floor and above the ceiling; the infrequent exposure non-occupational dose limit was exceeded below the floor. Modeled results exceeded the occupational and non-occupational dose limits outside two walls of the generic suite. Modeled dose was below the occupational limit at all test locations. The scattered radiation spectrum is a softened source spectrum minus the 60 and 68 keV X-ray tube bremsstrahlung peaks.

A MONTE CARLO ANALYSIS OF COMPUTERIZED TOMOGRAPHY

1. Introduction

Tomography, or sectional radiography, is defined as "making radiographs of plane sections of a body or an object, its purpose is to show detail in a predetermined plane of the body." (Parker, 1989) Computerized tomography (CT) uses computers to process the many image projections. One means of obtaining a CT image is by passing X-rays through the object (usually a human body) to be imaged. The by-product, however, of this type of imagery is scattered radiation. Because of the potentially harmful effects of radiation on the human body, it is absolutely necessary to know the dose received by hospital occupants from scattered radiation produced by X-ray imagery. Recent changes to U.S. Federal Law, Title 10 Code of Federal Regulations Part 20 or 10CFR20 (NRC, 1995), have required additional efforts to characterize radiation-producing systems. Direct measurement of the scattered radiation can be difficult and only tests the radiation field at a few, selected points. Computer modeling, however, is a non-destructive, safe method of interpolating/extrapolating the dose from scattered radiation from a variety of radiation producing systems to other locations.

1.1 Background

The International Commission on Radiation Units and Measurements (ICRU), since its inception in 1925, and the National Council on Radiation Protection and Measurements (NCRP), chartered in 1964 by Congress, are responsible for promulgating information and recommendations based on leading scientific judgment in matters of radiation protection and measurement. NCRP Report 49 contains the most recent comprehensive shielding guidance for diagnostic X-ray facilities (NCRP, 1976). The shielding guidance was based on NCRP's then-recommended annual dose limits of 50 mSv[1] and 5 mSv for occupational and non-occupational personnel, respectively[2]. As early as 1984, NCRP reduced the non-occupational dose limit recommendation to 1 mSv for continuous exposure (retaining the non-occupational dose limit of 5 mSv for infrequent exposure). In January 1994 the most recent NCRP dose limits were included in Title 10 Code of Federal Regulations Part 20. With the recommendations now law, there is obvious concern whether facilities built according to NCRP Report 49 guidelines and the older, greater dose limits will meet the new limits.

Robert Metzger, et. al. used the Monte Carlo: N-Particle transport program

---

[1] Gray (Gy) and sievert (Sv) are the special units of dose and dose equivalent, respectively, adopted by the ICRU in 1979 to conform to the SI unit standard. They replace rad and rem: 1 Gy = 1 J/kg = 100 rad and 1 Sv = 100 J/kg = 100 rem thus 50 mSv = 5 rem, etc.

[2] *Occupational personnel* are assumed to spend their entire work period in *controlled areas* defined as areas in which the exposure of persons to radiation is under the supervision of a Radiation Protection Supervisor (implying control of access, occupancy and working conditions for radiation protection purposes). Non-occupational personal are assumed to be restricted to *uncontrolled areas* defined as any area not meeting the definition of a controlled area (hallways, offices, waiting rooms, etc.). Patients are not included in either of these definitions with the assumption that the dose received is acceptable given the benefits of the treatment or imagery.

(MCNP) to analyze the effectiveness of NCRP Report 49 shielding recommendations in standard diagnostic X-ray rooms (Metzger, 1993). They note that typical shielding calculations ignore absorption by the patient, film cassettes, table, and frequently, the gypsum wallboard because of the overall complex geometry involved and lack of material attenuation data in NCRP Report 49. Using MCNP for shielding calculations eliminated these difficulties.

MCNP (1993) is a general-purpose Monte Carlo N-particle code (N: many) for calculating the time-dependent energy transport of neutrons, photons, and/or electrons in user-defined three-dimensional geometry. The code uses the Monte Carlo methods derived from research done during the Manhattan Project in the early 1940's. Its strength, and thus, suitability for shielding analysis, comes from four key features: (1) the ability to model complex geometry, (2) the wide selection of variance-reduction techniques, (3) the inclusion of extensive cross-section libraries (allowing the use of materials of any composition), and (4) the ability to model sources of complicated shape or spectra. (Briesmeister, 1993).

Metzger's analysis revealed that, in general, a standard diagnostic X-ray suite configuration[3] shielded according to NCRP Report 49 guidelines would meet the new standards assuming modern X-ray equipment, usage and films. They clearly, however, stated that the final result could not be extrapolated to CT units (Metzger, 1993). Modern CT units use a fan shaped beam that rotates around the patient with the imaging material

---

[3]A standard diagnostic X-ray suite configuration would consist of a supine patient on a table or an upright patient with a wall mounted film cassette both with simple conic or pyramid shaped beams.

(detector) rotating opposite the source. Given this radically different source, patient and detector configuration, Metzger's assertion is understandable. Their method of analysis, however, could be applied to any type of diagnostic or therapeutic radiation units.

1.2 Problem Statement

Dose outside the CT suite at Wright-Patterson Medical Center (WPMC) needs to be estimated and compared to dose limit requirements in 10CFR20. Captain William Ruck, WPMC's radiation protection officer (Wright-Patterson Air Force Base, OH) suggested this analysis for the General Electric Hi-Speed Advantage Computerized Tomography unit installed in the medical center's CT suite. He recommended, however, that the analysis be generalized to a standard suite configuration. This could be accomplished using the manufacturer's recommended room dimensions and performing the analysis for a variety of shielding conditions, i.e., varying thickness' of lead shielding in the walls or concrete in the floors and ceiling. Additionally, research indicated that information about the scattered spectrum within a CT suite was not available (Simpkin, 1995) which limits analysis of CT dose by methods other than those used here. MCNP was able to provide an estimate of the spectrum.

1.3 Approach

First, the results of Metzger, et al. were duplicated to ensure their work and method were correctly understood and to confirm their calculations. Next, a CT unit (source, detectors, and shielding) was placed in Metzger's X-ray room with its primary axes parallel to the walls. This configuration was used for test runs. The analysis runs included

modeling Wright-Patterson's CT suite, containing the CT unit rotated with respect to the walls, with various degrees of shielding. In addition, the manufacturer's recommended room size was modeled with the rotated CT unit. As a test of modeling accuracy, radiation film badges were placed in Wright-Patterson's CT suite and their reported exposure compared to MCNP's predictions.

Since no modeled scenario can ever perfectly mimic reality without unmanageable overhead (input detail and/or computer resources), approximations are necessary. Two factors affect the validity of the approximations: how well the model duplicates actual events and the level of significance a particular input (and its operating range) has on the desired output. These factors were weighed against available computer resources (memory, computation time, etc.). The approximations and limitations and their affect on the results were thoroughly investigated.

1.4 Contents

Chapter 2 discusses X-ray interactions. Chapter 3 presents the Monte Carlo method and its application to particle transport. Chapter 4 contains a description of MCNP (the code used for the analysis). Chapter 5 describes a standard CT unit, how it was modeled for MCNP and the assumptions/limitations used in the modeling process. Chapter 6 contains the calculations and methods used and analysis of preliminary test runs. Chapter 7 presents the results and analysis of the MCNP runs for inside and outside the CT suite at WPMC and outside the GE recommended room. Last, Chapter 8 contains conclusions, recommendations and possible follow-on analysis.

2. X-Ray Interactions

2.1 Introduction

Diagnostic X-ray and computerized tomography produce their images by using interactions of X-ray photons with matter. In both imaging techniques, the target to be imaged is positioned between a beam (or source) of X-rays and a recording material, film or detector. The image is produced from the measured or recorded X-ray transmissions. X-ray energy used for diagnostic purposes is confined to 25 to 1000 keV to maintain reasonable resolution with acceptable attenuation levels (Macovski, 1983).

There are three primary types of X-ray interactions which must be considered in radiological physics: Compton effect, photoelectric effect and Rayleigh (coherent) scattering. The first two are important since they result in the transfer of energy to electrons which, in turn, impart that energy to matter (targets). Rayleigh scattering, although prevalent in the diagnostic range, only removes the X-rays from the beam with no other implied interactions. In addition, photonuclear interactions and pair production are possible X-ray interactions but they are not significant in the diagnostic energy range. The consequences of these interactions depend on both the photon quantum energy ($E = h\nu$) and the atomic number, Z, of the absorbing media. (Attix, 1986; Chilton, 1984; and Profio, 1979).

2.2 Compton Effect

The Compton effect can be split into two aspects: kinematics, relating the energies and angles of the particles, and cross-sections, which predict the probability of an interaction occurring. An incoming photon collides with an electron that is assumed to be initially unbound and stationary. This is an accurate approximation for two reasons: the energy the electron receives is much greater than its binding or kinetic energy and, in the diagnostic range, any errors that result from the approximation will be much less than the competing photoelectric effect. (Attix, 1986; Chilton, 1984; and Profio, 1979).

2.2.1 Kinematics.

Figure 2.1 shows a typical photon-electron collision. The photon has an initial

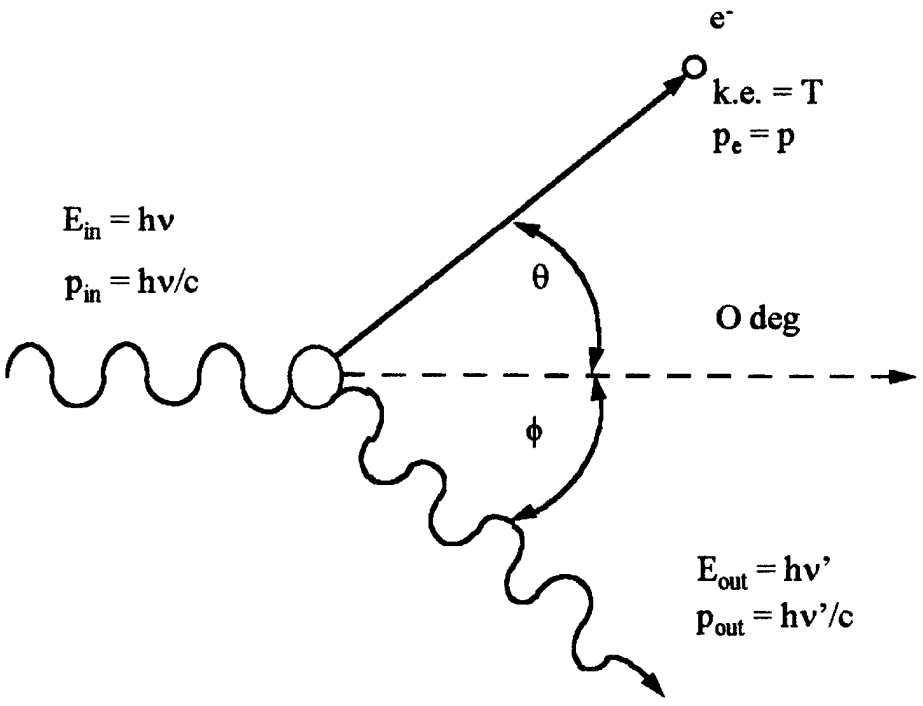

Figure 2. 1 Kinematics of the Compton effect.

energy, E = hν and momentum, P = hν/c. The electron is stationary. After the collision, the electron departs at an angle θ, with kinetic energy T and momentum p. The photon scatters at an angle ϕ with a new, lower energy, hν', and momentum, hν'/c. The collision kinetics solution is based upon conservation of both energy and momentum. Energy conservation requires

$$T = h\nu - h\nu'. \tag{2.1}$$

Conservation of momentum in the original photon direction, 0°, requires

$$\frac{h\nu}{c} = \frac{h\nu'}{c}\cos\phi + p\cos\theta \tag{2.2}$$

and perpendicular to the direction of incidence requires

$$h\nu'\sin\phi = pc\cos\theta. \tag{2.3}$$

Using relativistic relationships, pc can be expressed in terms of T and m_0 (electron rest mass)

$$pc = \left[T\left(T + 2m_0 c^2 \right) \right]^{1/2}. \tag{2.4}$$

Eqs. (2.1), (2.2), and (2.3) (with the (2.4) substitution) are a set of three simultaneous equations in hν, hν', T, θ and ϕ. A complete solution to the kinematics of Compton interactions can thus be derived given any two of the five parameters

$$h\nu' = \frac{h\nu}{1 + (h\nu / m_0 c^2)(1 - \cos\phi)}; \tag{2.5}$$

$$T = h\nu - h\nu'; \tag{2.6}$$

$$\cot\theta = \left(1 + \frac{h\nu}{m_0 c^2}\right)\tan\left(\frac{\phi}{2}\right), \tag{2.7}$$

where the rest mass energy of the electron, m_0c^2, is 0.511 MeV and hν, hν' and T are also expressed in MeV.

Eq. (2.5) shows that hν, hν' and angle ϕ of the scattered photon are uniquely correlated. Eq. (2.6) then provides the electron's kinetic energy while Eq. (2.7) gives its scattering angle, θ. Figure 2.2 shows the relationship between hν, hν' and T for a selection of photon scattering angles, ϕ, at energies in the diagnostic range. Figure 2.3 shows the relationship between the scattering angles, ϕ and θ, for a selection of photon energies, hν. (Attix, 1986; Chilton, 1984; and Profio, 1979).

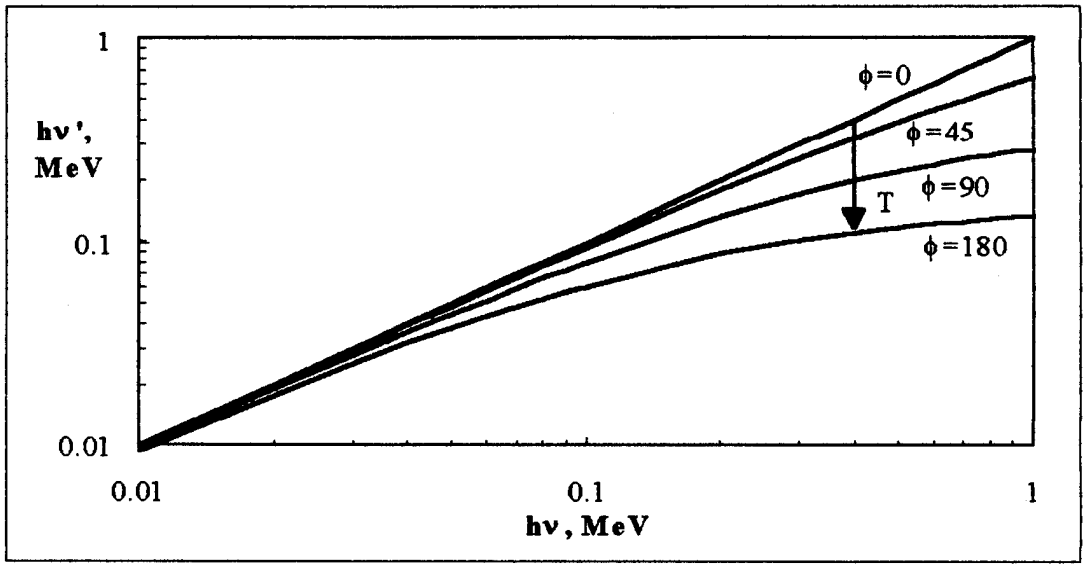

Figure 2. 2 Kinematic relationship of hν, hν' and T. T can be interpreted as the vertical separation of the ϕ curve from the ϕ = 0 diagonal.

2.2.2 Cross Section

J.J. Thompson derived the earliest theoretical description of photon-electron scattering. He assumed the electron to be freely oscillating under the influence of an

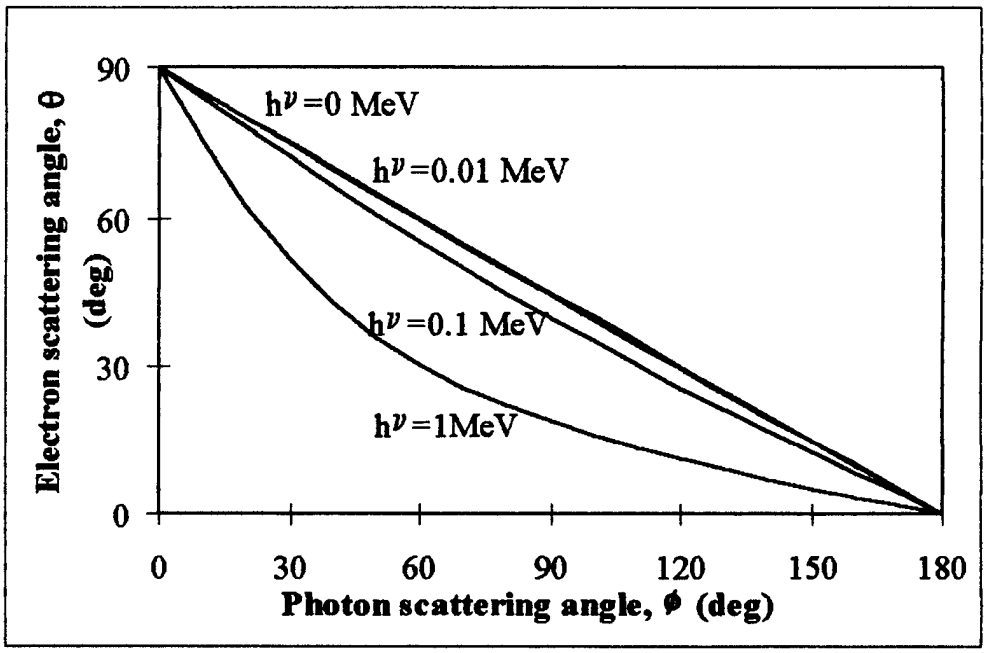

Figure 2. 3 Scattering angle relationships in Compton scattering.

electric field and re-emitting photons of the same energy as the incident photon. The electron will thus retain no kinetic energy from the photon. By 1928 it was known that Thompson's value was too large for hν > 10 keV, thus, Klein and Nishina applied Dirac's relativistic theory of the electron to the Compton effect. They also assumed unbound electrons initially at rest. Eq. (2.8) could then be re-written as

$$\frac{d_e\sigma}{d\Omega_\phi} = \frac{r_0^{\,2}}{2}\left(\frac{h\nu'}{h\nu}\right)^2\left(\frac{h\nu}{h\nu'}+\frac{h\nu'}{h\nu}-\sin^2\phi\right), \qquad (2.8)$$

where hν' is given by Eq. (2.5). Figure 2.4 shows this relationship for a selection of incident photon energies, hν. The total Klein-Nishina cross section per electron ($_E\sigma$,

typically called the Compton scattering or incoherent scattering cross section) can be obtained by integrating Eq. (2.10) over all photon scattering angles

$$ {}_E\sigma = 2\pi r_0^2 \left\{ \frac{1+\alpha}{\alpha^2} \left[\frac{2(1+\alpha)}{1+2\alpha} - \frac{\ln(1+2\alpha)}{\alpha} \right] + \frac{\ln(1+2\alpha)}{2\alpha} - \frac{1+3\alpha}{(1+2\alpha)^2} \right\}, \qquad (2.9) $$

where $\alpha = h\nu / m_0 c^2$. The Klein-Nishina cross section per electron, ${}_E\sigma$, in Eq. (2.11) is independent of Z. The Klein-Nishina cross section per atom, ${}_A\sigma$, is

$$ {}_A\sigma = Z \times {}_E\sigma \quad (\text{cm}^2/\text{atom}) \qquad (2.10) $$

Equivalently, the Klein-Nishina cross section per mass is obtained from

$$ \frac{\sigma}{\rho} = \frac{N_A Z}{A} {}_E\sigma \quad (\text{cm}^2/\text{g}) \qquad (2.11) $$

where N_A is Avogadro's number, A is atomic weight and ρ is the density in g/cm^3 ($N_A Z / A$ is the number of electrons per gram of material). σ/ρ is called the partial mass attenuation coefficient, or less frequently, the Compton mass attenuation coefficient.

The cross section (which can be thought of as an effective target area for the photon) is numerically equal to the probability of a Thompson scattering event occurring when a single photon passes through a layer containing one electron per cm^2. It is also the fraction of photons that will scatter in passing through that same layer, e.g., approximately 665 events for 10^{27} photons. (Attix, 1986; Chilton, 1984; and Profio, 1979).

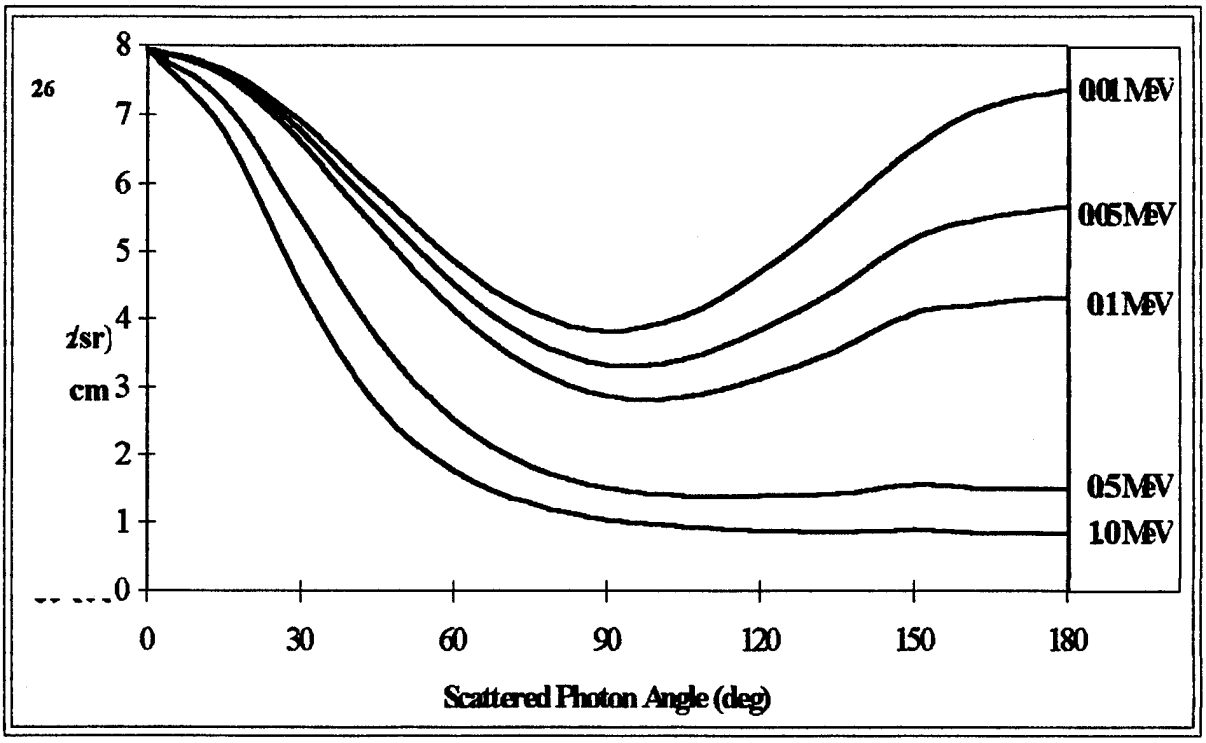

Figure 2. 4 Differential Klein-Nishina cross section vs. scattered photon angle, ϕ, for $h\nu$ = 0.01, 0.05, 0.1, 0.5, and 1.0 MeV.

2.3 Photoelectric Effect

The photoelectric effect is the most important interaction of low-energy photons with matter because the photoelectric cross sections increase strongly as photon energy decreases, particularly for high Z media. Again, there are kinematic considerations relating energies and angles of the participating particles to the cross section predicting the interaction probability. (Attix, 1986; Chilton, 1984; Profio, 1979).

2.3.1 Kinematics.

The photoelectric effect (for X-ray interactions) differs from the Compton effect in that the photon always gives up all of its energy to the electron it collides with because, unlike the Compton effect, the encounter is with a tightly bound electron, such as those in

the atom's inner shell, especially of high atomic number. Figure 2.5 shows a typical photoelectric interaction. An incident photon of quantum energy hν is shown interacting with an atomic-shell electron with a binding energy, E_b. The photon will be totally absorbed by the electron, giving it enough energy to overcome its binding energy. The electron will depart at angle θ with kinetic energy, T , and momentum, p. The atom will depart at angle ϕ with its kinetic energy, T_a, very nearly 0. The photon energy, hν, must be greater than the electron's binding, E_b, but, the closer the two energies are, the greater the probability of a photoelectric interaction. The kinetic energy, independent of its scattering angle θ, is

$$T = h\nu - E_b - T_a \cong h\nu - E_b. \qquad (2.12)$$

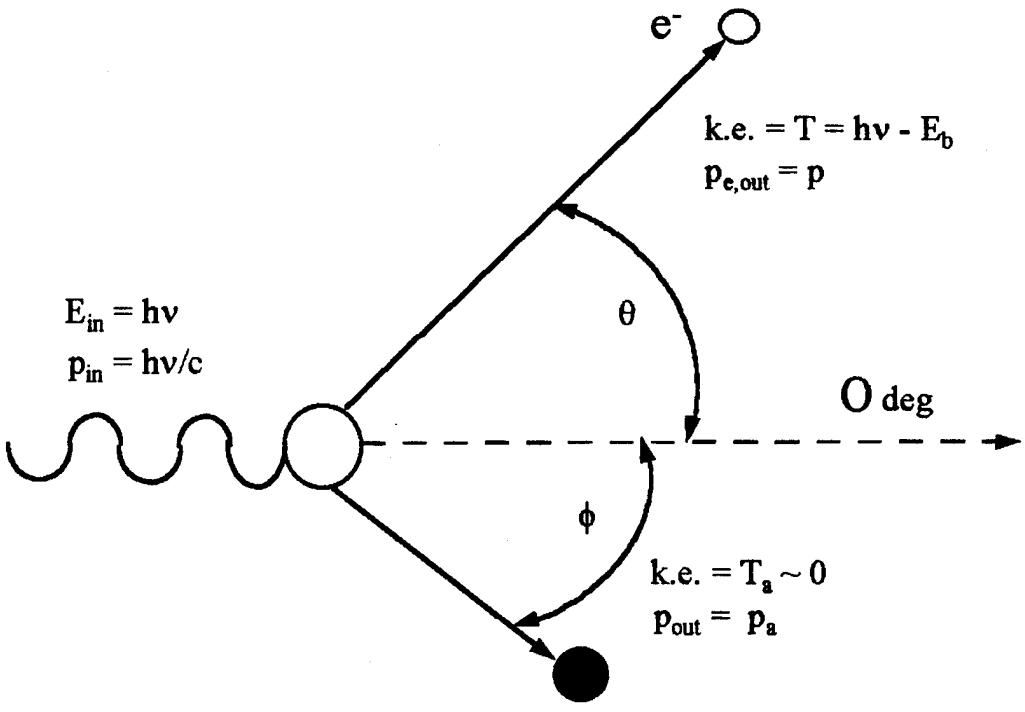

Figure 2. 5 Kinematics of the photoelectric effect.

2.3.2 Cross Section.

Derivation of the interaction cross section for the photoelectric effect is difficult because of the complications arising from the binding of the electron (Attix, 1986). There is no equation analogous to the Klein-Nishina formula. Published tables are based on experimental results supplemented by interpolations for other energies and absorbing media.

Photoelectrons are ejected predominately sideways for low photon energies. With increasing energy the distribution is pushed more toward smaller, but still non-zero, angles. A convenient representation uses the "bipartisan" angle, i.e., the median ejection angle.

Integrated over all angles of emission, the cross section can be written

$$\tau \cong \begin{cases} k\dfrac{Z^n}{(h\nu)^m} & h\nu \geq E_b \\ 0 & \text{otherwise} \end{cases} \qquad (cm^2/atom), \qquad (2.13)$$

where k is a constant, n is $\cong 4$ at $h\nu = 100$ keV, gradually rising to about 4.6 at 3000 keV, and $m \cong 3$ below $h\nu = 100$ keV, gradually decreasing to about 1 at 5000 keV. Using the same conversions as in Eqs. (2.12) and (2.13) for $h\nu < 100$ keV, the photoelectric cross section per unit mass is

$$\frac{\tau}{\rho} \propto \left(\frac{Z}{h\nu}\right)^3 \quad (cm^2/g) \qquad (2.14)$$

This is called the photoelectric mass attenuation coefficient.

When an electron is removed from an inner atomic shell, the resulting vacancy is promptly filled by another electron from a less tightly bound shell. This may be

accompanied by the emission of a fluorescence X-ray of quantum energy equal to the difference between the two energy levels. Binding energy, Eb, not completely removed by a fluorescence X-ray may be given to one or more ejected electrons. This alternative excess binding energy disposal mechanism is called the Auger effect (Attix, 1986). An atom may emit a number of Auger electrons more or less simultaneously in a kind of chain reaction, resulting eventually in more than one vacancies in the outermost shell.

2.4 Rayleigh (Coherent) Scattering

Rayleigh scattering is an elastic collision between a photon and particle. The photon loses essentially none of its energy, it is, however, redirected through some small angle. Rayleigh scattering removes photons from a collimated beam, but does not contribute significantly to total dose since no energy is given to charged particles, and no ionization or excitation is produced. The scattering angle dependents on both Z and photon energy giving a Rayleigh cross section per atom of

$$ {}_a\sigma_R \propto \frac{Z^2}{(h\nu)^2} \quad (cm^2/atom), \tag{2.15} $$

or, in mass units

$$ \frac{\sigma_R}{\rho} \propto \frac{Z}{(h\nu)^2} \quad (cm^2/g) \tag{2.16} $$

Rayleigh scattering is nearly insignificant when compared to the Compton or photoelectric effects for high Z, high energy interactions. It increases, however, for low Z, low energy events such as diagnostic X rays in tissue, composed primarily of water, H_20. (Attix, 1986; Chilton, 1984; Profio, 1979).

2.5 Other Interactions

There are two other photonic interactions: photonuclear and pair production. In a photonuclear interaction an energetic photon (exceeding a few MeV) enters and excites a nucleus. Required photon energies are well above the diagnostic range. Pair production is an absorption process in which a photon disappears and gives rise to an electron and a positron. A minimum photon energy of $2m_0c^2 = 1.022$ MeV is obviously required, again, out of the diagnostic range. (Attix, 1986; Chilton, 1984; Profio, 1979).

2.6 Attenuation Coefficients

All of these effects are present in different magnitudes depending on X ray energy and target material. Mass attenuation coefficients can be combined (neglecting photonuclear and pair production) to obtain a total mass attenuation coefficient

$$\frac{\mu}{\rho} = \frac{\tau}{\rho} + \frac{\sigma}{\rho} + \frac{\sigma_R}{\rho} \quad (\text{cm}^2/\text{g}), \tag{2.17}$$

where τ/ρ is the contribution of the photoelectric effect, σ/ρ is the Compton effect and σ_R/ρ is for Rayleigh scattering.

Since all target media are not simple elements, the Bragg rule can be applied to mass attenuation for compounds or intimate mixtures of elements

$$\left(\frac{\mu}{\rho}\right)_{mix} = \left(\frac{\mu}{\rho}\right)_A f_A + \left(\frac{\mu}{\rho}\right)_B f_B + \cdots, \tag{2.18}$$

where f_A, f_B, . . ., are the weight fractions for the separate elements (A, B, . . .) present. (Attix, 1986; Chilton, 1984; Profio, 1979).

2.6.1 Examples of Mass Attenuation Coefficients.

Figure 2.6 shows the Compton, photoelectric and Rayleigh mass attenuation coefficients for two common elements, carbon, low Z, and lead, high Z, as a function of photon energy. The three interaction cross sections and their total are shown. Figure 2.7 shows the mass coefficients for a mixture, gypsum, present in drywall.

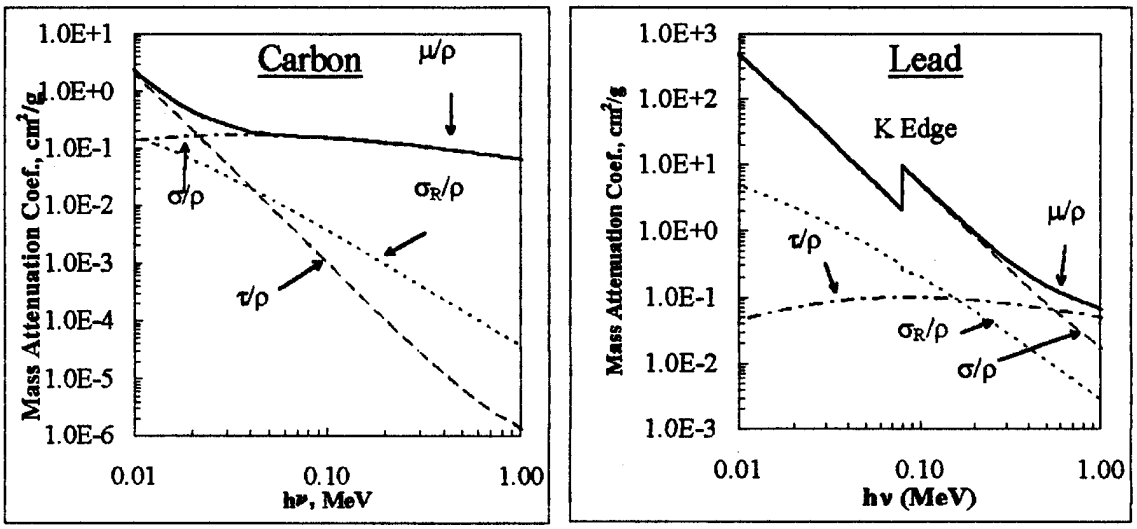

Figure 2. 6 Mass attenuation coefficients for carbon and lead.

2.6.2 Beam Attenuation.

Once the total cross section is identified for a material, the attenuation of the beam through that material can be determined. Recall that the cross section identifies the probability of interaction in a unit thickness of material traversed. The probability that it will interact in an infinitesimal thickness *dl* is μdl. If N particles are incident upon *dl*, the change *d*N in the number N due to absorption is given by

$$dN = -N\left(\frac{\mu}{\rho}\right)(\rho\, dl). \tag{2.19}$$

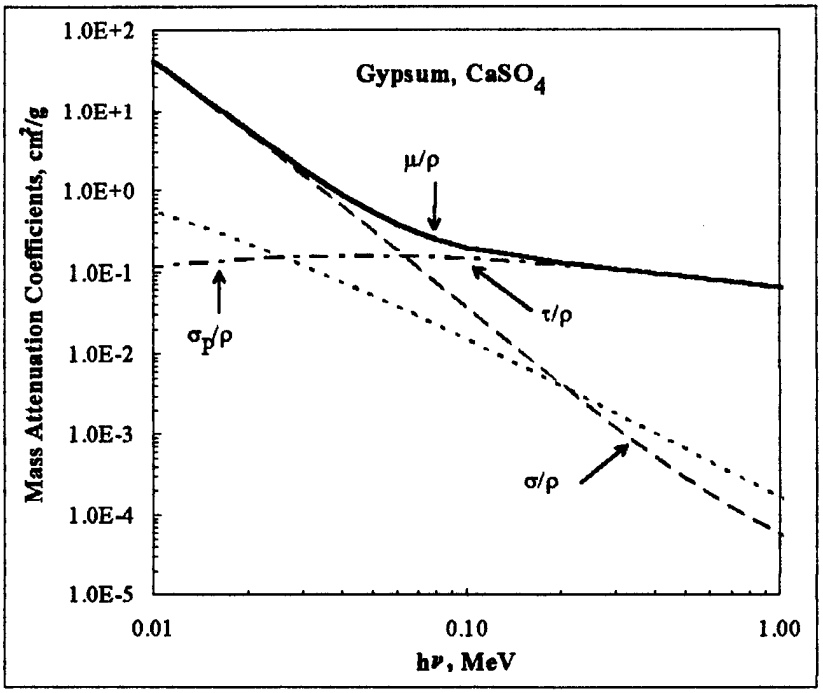

Figure 2. 7 Mass attenuation coefficients for gypsum (drywall).

where μ is the mass attenuation coefficient. Integrating over the thickness, l, from 0 to L, and corresponding particle populations from N_0 to N_L gives the law of exponential attenuation

$$N_L = N_0 e^{(-\mu L)}. \tag{2.20}$$

If μ is a total attenuation coefficient it is simply replaced by the sum of individual coefficients, $\sigma + \tau + \sigma_R$. If the attenuation coefficient is energy dependent, the integration must be accomplished for each energy interval. The effect of the energy dependent attenuation coefficient for lead (see Fig. 2.6) on an exponential spectrum is shown in Figure 2.8.

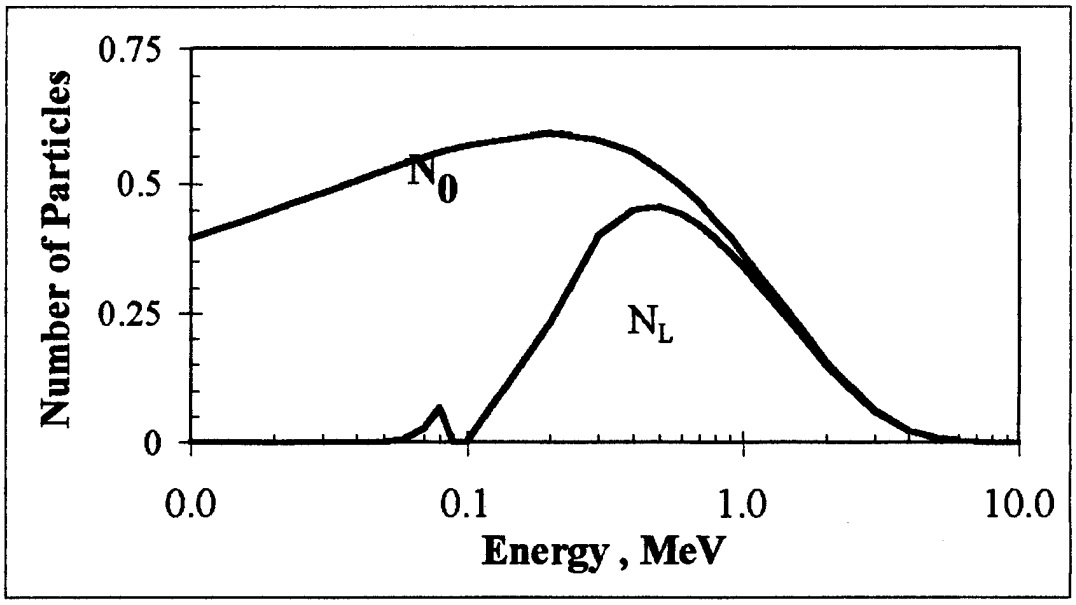

Figure 2. 8 Attenuation of an exponential energy function passing through 1 cm lead.

2.7 Ionizing Radiation Quantities

To fully understand ionizing radiation a description and definition of the quantities and units typically used is necessary. For example, flux can be used to describe the progress of the photons throughout the problem. Quantities such as kerma and dose relate photon flux to the effect of radiation on humans. (Attix, 1986; Profio, 1979).

2.7.1 Fluence.

Fluence is the mean number of rays striking a finite sphere surrounding a point, P, during an arbitrary time interval. Fluence, therefore, is

$$\Phi = \frac{dN_e}{da}, \tag{2.21}$$

where N_e is the number of particles and a the great circle area of the sphere. It is expressed in units of m^{-2} or cm^{-2}. Fluence expresses the sum of rays incident from all directions, irrespective of individual quantum or kinetic energies. Chilton's alternate definition of fluence quoted by Attix is: "fluence at a point P is numerically equal to the expectation value of the sum of the particle track lengths that occur in an infinitesimal volume dV at P divided by dV." This definition eliminates the need for the spherical volume, lending itself to dosimetry calculations by the Monte Carlo method. (Attix, 1986). Chilton's definition of fluence, when multiplied by cross-section, μ (effectively, collision probability per path length), gives collision density:

$$\left(\frac{\text{path length travelled by x-rays}}{\text{Volume}}\right)\left[\frac{\text{cm}}{\text{cm}^3}\right] \times \left(\frac{\text{collisions}}{\text{cm of path length}}\right)\left[\frac{\text{collisions}}{\text{cm}}\right] = \text{collision density}\left[\frac{\text{collisions}}{\text{cm}^3}\right]. \tag{2.22}$$

2.7.2 Flux.

At any point during the above arbitrary time, a flux, or fluence rate, is the change in fluence as a function of time

$$\varphi = \frac{d\Phi}{dt}, \tag{2.23}$$

usually expressed in units or $m^{-2}\ s^{-1}$ or $cm^{-2}\ s^{-1}$. Flux expresses the sum of rays incident from all directions, irrespective of individual quantum or kinetic energies.

2.7.3 Energy Fluence.

The energies of the individual rays are accounted for in the quantity energy fluence

$$\Psi = \frac{dR}{da}, \tag{2.24}$$

where R is the mean total energy emitted, transferred or received (excluding rest-mass energy) within the volume. Energy fluence is usually expressed in units of J/m^2 or erg/cm^2. For the case of a single energy, R is simply expressed $R = EN_e$ and energy fluence can be related to particle fluence, $\Psi = E\Phi$. The energy fluence rate would be the time differential of the energy fluence

$$\psi = \frac{d\Psi}{dt} \tag{2.25}$$

expressed in units of $J\ m^{-2}\ s^{-1}$ or $erg\ cm^{-2}\ s^{-1}$.

2.7.4 Kerma.

Kerma, the kinetic energy released in material, is mean energy transferred to charged particles for unit mass at a point of interest, including radiative-loss energy but excluding energy passed from one charged particle to another. It can be defined in terms of energy transferred, ε_{tr}, and radiant energy, R,

$$\varepsilon_{tr} = (R_{in})_u - (R_{out})_u^{nonr} + \Sigma Q, \tag{2.26}$$

where $(R_{in})_u$ is the radiant energy of the uncharged particles entering V, $(R_{out})_u^{nonr}$ is the radiant energy of uncharged particles leaving V, except that originating from radiative losses of kinetic energy by charged particles while in V, and ΣQ, the rest mass conversion term, is the net energy derived from rest mass in V. Radiative losses are the conversion of

charged-particle kinetic energy to photon energy. Energy transferred is simply the kinetic energy received by charged particles in the specified finite volume, V. Kerma, therefore, is

$$K \equiv \frac{d\varepsilon_{tr}}{dm}. \tag{2.27}$$

Average kerma is the mean energy divided by the mass

$$K_A = \frac{\varepsilon_{tr}}{m}. \tag{2.28}$$

Kerma and average kerma can be expressed in units of erg/g, rad, J/kg or gray (Gy) simply related by

$$1\,\text{Gy} = 1\frac{\text{J}}{\text{kg}} = 10^2\ \text{rad} = 10^4\ \frac{\text{erg}}{\text{g}}. \tag{2.29}$$

The kerma from monoenergetic photons is related to the energy fluence by the mass energy-transfer coefficient, $(\mu_{tr}/\rho)_{E,Z}$

$$K = \Psi \times \left(\frac{\mu_{tr}}{\rho}\right)_{E,Z}. \tag{2.30}$$

2.7.5 Absorbed Dose.

The *absorbed dose*, D, the mean energy imparted to matter per unit mass at a point, can also be defined in terms of the total energy imparted by ionizing radiation to matter of mass, m, in finite volume, V,

$$\varepsilon = (R_{in})_u - (R_{out})_u^{nonr} + (R_{in})_c - (R_{out})_c^{nonr} + \Sigma Q, \tag{2.31}$$

where the sum now includes the uncharged and charged radiant energies (see Eq. 2.28) . The absorbed dose is therefore

$$D = \frac{d\varepsilon}{dm}. \tag{2.32}$$

Dose has the same units as kerma, J/kg, erg/g, rads or gray and, like the average kerma, the average absorbed dose is the energy imparted divided by the mass within the volume

$$D_A = \frac{\varepsilon}{m}. \tag{2.33}$$

2.7.6 Exposure.

Exposure, X, is

$$X = \frac{dQ}{dm}, \tag{2.34}$$

where dQ is "the absolute value of the total charge of the ions of one sign produced in air when all the electrons liberated by photons in air of mass dm are completely stopped in air" (ICRU, 1980). Exposure has units of C/kg, esu/g, or more commonly, roentgen (R) where 1 R = 2.58×10^{-4} C/kg. With the conversion (in air, independent of photon energy) of 33.97 J/C for the mean energy expended in a gas per ion pair formed, 1 R = 8.78×10^{-3} Gy = 0.878 rad (Attix, 1986; Cember, 1983). Exposure rate is the change in exposure over time. The conversion from exposure in air to exposure in a material is the ratio of the mass energy-absorption coefficient $(\mu_{en}/\rho)_{mat}$ for the material to that of air, $(\mu_{en}/\rho)_{air}$ which, for muscle tissue, is nearly constant over the diagnostic energy range, i.e. $1.07 \pm 3\%$.

2.7.7 Dose Equivalent.

Dose equivalent, H, (now called equivalent dose by ICRP) allows the average absorbed dose to be associated with a risk factor which is an estimate of the relative human hazard from different ionizing radiation energies. *Effective dose equivalent*, E, (now called effective dose by ICRP) weights the dose equivalent by tissue factors to associate a risk by body part susceptibility:

$$\begin{aligned} H &= W_R \times D_A; \\ E &= W_T \times H, \end{aligned} \tag{2.35}$$

where D_A is the average absorbed dose (section 2.8.5), W_R is the radiation weighting factor (also denoted by Q) and W_T is the tissue weighting factor. The units of dose equivalent and effective dose equivalent are J kg^{-1} and are given the special name of sievert, Sv (previously rem, where 1 Sv = 100 rem). Tissue and radiation weighting factors differ from source to source. 10CFR20 and NCRP use the ICRP recommendations. Table 2.1 contains the recommended the tissue weighting factors found in ICRP Publication 60. The NRC's recommended tissue weighting factors are in Table 2.2. All source agree on a radiation weighting factor, W_R = 1 for X rays of all energies. (Scleien, 1993).

Table 2.1 ICRP Tissue Weighting Factors (Scleien, 1993)

W_T	0.01	0.05	0.12	0.20
Organs	Bone surfaces	Bladder	Colon	Gonad
	Skin	Breast	Lung	
		Liver	Red bone marrow	
		Oesphagas	Stomach	
		Thyroid		
		Remainder[a]		
Totals	0.02	0.30	0.48	0.20

[a]Remainder: 13 organs, including muscle, sharing equally 0.05, i.e. $\simeq$0.004.

Table 2.2 NRC Tissue Weighting Factors (Scleien, 1993)

Organ or Tissue	W_T
Gonads	0.25
Breast	0.15
Red bone marrow	0.12
Lung	0.12
Thyroid	0.03
Bone surfaces	0.03
Remainder[a]	0.30
Whole body[b]	1.00

[a] For weighting the external whole body dose to add to the internal dose.
[b] 0.30 results from 0.06 from each of 5 remainder organs (excluding skin and lens of the eye) that receive the highest dose.

3. Monte Carlo Method

3.1 Introduction

As discussed in Chapter 2, the particle cross sections can be considered a probability of particle interaction. Given this, production and transport of ionizing radiation can be treated as a statistical process controlled by the energy of the impinging photons and the atomic number(s) of the target material. Statistical treatment, and thus, statistical results, is well suited to larger scale nuclear analysis when average (statistical) behavior is the goal. The Monte Carlo method of simulating individual particles and recording some aspects of their average behavior is one such statistical tool.

In the Monte Carlo method, average behavior of the particles in the physical system is inferred from the average behavior of the simulated particles. The simulations are performed on a digital computer because the number of trials necessary to adequately describe the phenomenon is usually quite large. The statistical sampling process is based on the selection of random numbers - analogous to throwing dice in a gambling casino - hence the name "Monte Carlo". The Monte Carlo method, in short, duplicates a process by drawing random numbers which sample a probability distribution that reflects known behavior, such as scattering angle or track length distance between collisions. In particle transport applications, for each of many particle histories, a particle is followed from a source throughout its life in a series of individual events to its death in some terminal category (absorption, escape, etc.). Only the outcome of each individual step is determined by the random draw.

3.2 Probability Distribution Functions

Two functions essential to Monte Carlo calculations are the probability density function and the cumulative probability density function. The probability density function, f(x) is the probability that some value (in this case, the random draw, x') will fall between x and Δx. It is necessary that $f(x) \geq 0$ and normalized over its restricted interval, [a, b]

$$\int_a^b f(x)dx = 1. \tag{3.1}$$

The cumulative probability distribution function, F(x), is the probability that the random variable, x', is less than or equal to x, thus

$$F(x) = \int_{-\infty}^{x} f(x')dx'. \tag{3.2}$$

It is often convenient to write Eq. (3.2) in the form

$$\frac{dF(x)}{dx} = f(x). \tag{3.3}$$

Figure 3.1 shows the relationship between f(x) and F(x).

The Monte Carlo method relies on known probability functions. To use these relationships, rules of transformation must be applied to the randomly drawn variables. For y = y(x), let g(y)dy be the probability that y is between y and y + dy, and f(x)dx be the probability that x is between x and x + dx. It is important to note that y' (in y to y + dy) and x' (in x to x + dx) both describe the same event such that one happens if and only if the other happens. The probability density functions g(y) and f(*x*) must satisfy

$$\left| g(y)dy \right| = \left| f(x)dx \right|, \tag{3.4}$$

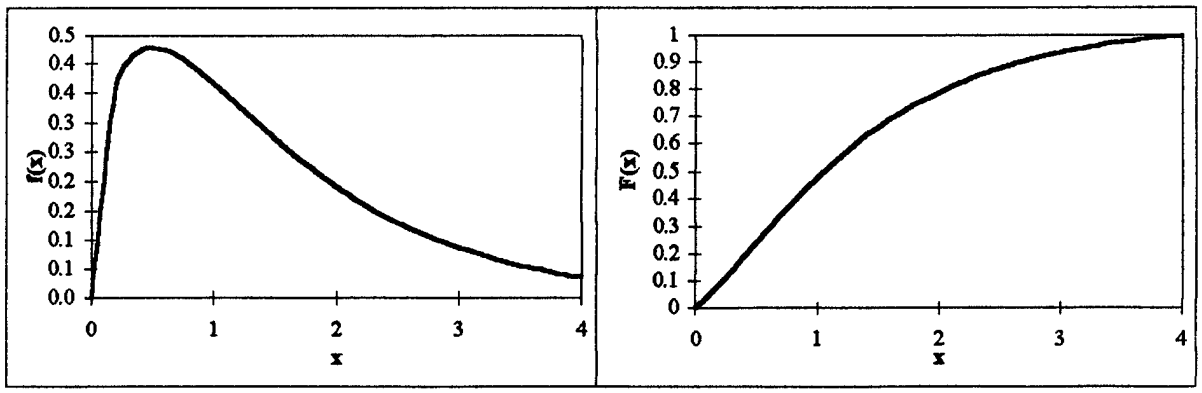

Figure 3. 1 Example of (a) probability density function, f(x), and (b) cumulative probability distribution function, F(x), for normalized f(x).

or, since $g(y) > 0$ and $f(x) > 0$

$$g(y) = f(x)\left|\frac{dx}{dy}\right|. \tag{3.5}$$

Now, if $y = F(x)$ of the random variable x, Eq. (3.5) becomes

$$g(F) = f(x)\left|\frac{dx}{dF}\right|. \tag{3.6}$$

Eq. (3.3) can now be used for this particular transformation to obtain

$$g(F) = 1, \quad 0 \leq F \leq 1. \tag{3.7}$$

Since g(F) is the probability density function of the random variable F, the probability of F taking on a value between F and F + dF is just equal to dF and thus is uniformly distributed between zero and one. The random numbers, ξ, available on most computers via library routines or built-in language functions are also sampled between zero and one, thus F(x) may be sampled uniformly

$$F(x) = \xi. \tag{3.8}$$

However, we need to sample the distribution of x and not F(x), thus, after each call, we must perform the inversion

$$x = F^{-1}(\xi). \tag{3.9}$$

(Lewis, 1984).

3.3 Random Numbers

Random numbers are generated by a computer system with complicated numerical algorithms. The use of the algorithm means that the numbers are not truly random, but, in fact, pseudo random, i.e., their sequence can be duplicated and there is only a finite number of unique "random" numbers. Processes such as the Monte Carlo method can use an extraordinary number of random numbers - as many as tens of thousands per particle history. A sample Monte Carlo run performed for this analysis used 300 million random numbers to process two million particles, with a maximum of 28,000 for a single history. It is important, therefore, to make efficient use of the limited number of random numbers available. This is accomplished through selection or rejection schemes. The choice of the scheme is driven by the nature of the probability density function. A simple, intuitive method of sampling randomly from a given distribution function uses prepared look-up tables. Analytically integrable functions can use the more mathematically attractive and efficient inverse cumulative function method (also called the selection method). Those that are not analytically integrable must use the rejection method (with possible enhancements to improve efficiency).

3.3.1 Selection.

To illustrate selection methods of random numbers, consider the case of choosing a random distribution over a circle as shown in Figure 3.2. We could choose random x's and

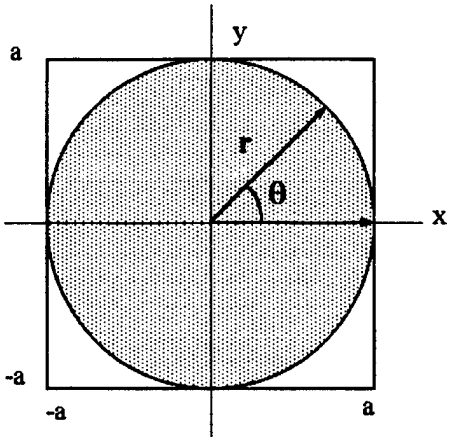

Figure 3. 2 Choosing a uniformly distributed random point within a circle.

y's over the interval [-a, a]. This, however would fill the entire square and thus waste those random numbers falling outside the circle. On the other hand, we could choose random r's over the interval [0,r] and θ's over the interval [0,2π]. This, however, would cause "clumping" of points in the center of the circle, i.e. a non-uniform distribution. Instead, let dA, the differential area of the circle, be equally likely where $dA = r\,dr\,d\theta$ Using the method starting with Eq. (3.6)

$$g(\theta) = f(x)\left|\frac{dx}{d\theta}\right| = r\,dr\left|\frac{d\theta}{d\theta}\right| = C_\theta \ (\text{constant}). \tag{3.10}$$

Since we know θ must be distributed around the entire circle, we let $C = 1/(2\pi)$ to normalize g(θ) to one. Then

$$g(\theta) = \frac{1}{2\pi} = \frac{d\Theta}{d\theta}, \tag{3.11}$$

where Θ is the cumulative probability function over θ.

Using Eq. (3.8):

$$\Theta = \int \frac{d\theta}{2\pi} = \frac{\theta}{2\pi} \tag{3.12}$$

and performing the inversion

$$\Theta^{-1}(\xi) = \theta = 2\pi\xi_\theta . \tag{3.13}$$

Following the same steps for r:

$$g(r) = f(x)\left|\frac{dx}{dr}\right| = d\theta\left|\frac{r\,dr}{dr}\right| = r C_r . \tag{3.14}$$

To normalize

$$\int g(r)\,dr = \int_0^a r C_r dr = 1 \quad \text{such that} \quad C_r = \frac{2}{a^2}. \tag{3.15}$$

then

$$R = \int g(r)dr = \int_0^r \frac{2r'}{a^2}dr' = \frac{r^2}{a^2} = \xi_r ,$$

(3.16) and

$$R^{-1}(\xi) = r = \sqrt{\xi_r a^2} . \tag{3.17}$$

Thus, for every point within the circle, two random numbers will be drawn, ξ_r and ξ_θ, which, via Eqs. (3.13) and (3.17), will become the (r, θ) pair describing the location of the point. The selection method will efficiently produce uniformly distributed points throughout the circle without the need to reject any numbers. This method, however, only works for analytically integrable functions. Non-integrable functions may be numerically integrated to get F(x) followed by table interpolation to evaluate $F^{-1}(\xi)$. (Mathews, 1995).

3.3.2 Rejection.

The rejection method is used for non-intgrable functions and is not as efficient as the selection method described in section 3.3.2. In implementing the rejection method, the function is not integrated (relating explicitly a given x to some y via the function), so two random numbers must be drawn to define a single point. The position of the point relative to the function determines acceptance/rejection. The first random draw determines x_i on the interval $[x_1, x_4]$ (see upper section of Figure 3.3). The next draw will choose a point, y_i, on the x_i line. If $y_i > f(x_i)$, it will be rejected; if $y_i \geq f(x_i)$, it is accepted. (Note: the ratio of accepted to rejected numbers is the volume under the curve, i.e. integration..)

The lower portion of Figure 3.3 illustrates an enhancement to the rejection method that may be used to improve efficiency. The function is broken into a number piece-wise integrable functions. They are expanded to fill y. Appropriate weights are assigned to each interval

$$\begin{aligned} w_1 &= \int_{x_1}^{x_2} f_1(x)dx \\ w_2 &= \int_{x_2}^{x_3} f_2(x)dx \\ w_3 &= \int_{x_3}^{x_4} f_3(x)dx \end{aligned} \qquad (3.18)$$

If, for example, in Figure 3. 3, $x_i \leq w_1$, selection/rejection is determined with $f_1(x)$; if $x_i \leq w_2$, with $f_2(x)$; etc. In this example, the ratio of the rejection areas to the acceptance areas are seen to be smaller than before, thus, fewer numbers will be discarded.

3.3.3 Discrete Sampling.

When, instead of assigning a value such as distance to collision, the random number is used to answer a question, discrete sampling is used. For example, we may need to know if the next event will be a capture, elastic scatter, etc. Recalling the cross-sections of Chapter 2, the total cross-section is

$$\sigma_T = \sigma_1 + \sigma_2 + \sigma_3 + \sigma_4 + \cdots \tag{3. 19}$$

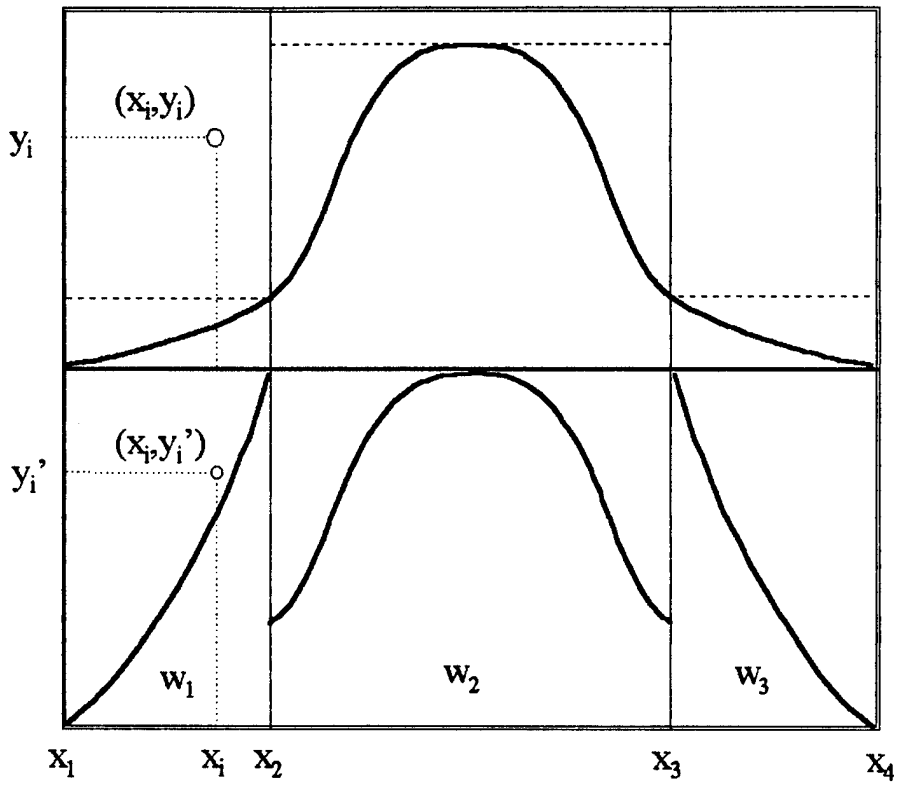

Figure 3. 3 Rejection method shown in upper portion. Lower portion illustrates an enhancement to the rejection method.

The unit line representing the range of random numbers (0-1) is subdivided into intervals proportional to (σ_1 / σ_T), (σ_2 / σ_T), etc. The random number falls into one of the intervals which correspond to the "answer" sought. (Lewis, 1984)

3.4 Errors

The final answer obtained in Monte Carlo analysis is the average of the contributions from many histories. Equally important to the answer is the statistical error or uncertainty associated with the answer. Not only the absolute error, but its behavior as you increment particle histories, must be analyzed to ensure confidence in the results.

3.4.1 Means, Variances and Standard Deviations.

The random nature of a Monte Carlo analysis typically produces a range of scores depending on the area of interest and the variance reduction methods (see section 3.5 Variance Reduction) chosen. As seen above, the expectation value of x subject to f(x), the score probability density function is

$$E(x) = \langle x \rangle = \int x\, f(x)dx = \text{true mean}. \tag{3.20}$$

Since f(x) is seldom explicitly known, it is implicitly sampled by the Monte Carlo random walk process. The sample mean is then an estimate of the true mean, $\bar{x}$

$$\bar{x} = \frac{1}{N}\sum_{i=1}^{N} x_i, \tag{3.21}$$

where x_i is the value of x selected from f(x) for the i^{th} history and N is the number of histories calculated in the problem. The Strong Law of Large Numbers states that if E(x) is finite, $\bar{x}$ tends to the limit E(x) as N approaches infinity thus providing a relationship

between E(x) and $\bar{x}$. The variance of the population of x values is a measure of the difference in the two values and is given by

$$\sigma^2 = \int (x - E(x))^2 f(x)dx = E(x^2) - (E(x))^2 . \tag{3.22}$$

The square root of the variance, σ, is called the standard deviation of the population. As with E(x), σ is seldom known but can be estimated by Monte Carlo as S, which for large numbers is

$$S^2 = \frac{\sum_{i-1}^{N} (x_i - \bar{x})^2}{N-1} \cong \overline{x^2} - \bar{x}^2 . \tag{3.23}$$

The quantity S is the estimated standard deviation of the population of x based on the values of x_i that were actually sampled. The estimated variance of $\bar{x}$ is

$$S_{\bar{x}}^2 = \frac{S^2}{N} \tag{3.24}$$

It is important to note that $S_{\bar{x}}$ is proportional to $1/N^{1/2}$. This is a drawback because four times the number of histories must be run to halve $S_{\bar{x}}$ which can be computationally expensive. Another way to reduce estimated variance is by reducing S, the estimated standard deviation, using variance reduction techniques (see Section 3.5).

3.4.2 Estimated Relative Errors.

A convenient representation of error is the estimated relative error, R

$$R \equiv \frac{S_{\bar{x}}}{\bar{x}} = \left[\frac{1}{N} \left(\frac{\overline{x^2}}{\bar{x}^2} - 1 \right) \right]^{1/2} = \left[\frac{\sum_{i=1}^{N} x_i^2}{\left(\sum_{i=1}^{N} x_i \right)^2} - \frac{1}{N} \right]^{1/2} \tag{3.25}$$

It represents statistical precision as a fractional result with respect to the estimated mean. Based on the experience of Monte Carlo practitioners and years of experience using MCNP on wide variety of problems, Table 3.1 presents the recommended interpretation of the estimated 1σ confidence intervals (Briesmeister, 1993).

Table 3. 1 Guidelines for Interpreting the Relative Error, R

Range of R	Quality of the Tally
0.5 to 1	Useless
0.2 to 0.5	Limited usefulness
0.1 to 0.2	Questionable
< 0.10	Generally reliable

3.4.3 Figure of Merit.

By definition R^2 should be proportional to 1/N and the computer time, T, proportional to N, thus, $1/(R^2T)$, the Monte Carlo figure of merit (FOM), should be approximately constant within any one run (with the exception of statistical fluctuations early in the problem.) It is advantageous to have a large FOM since that would indicate an efficient run yielding a small relative error from short computer run times.

3.5 Variance Reduction

Variance reduction, as discussed above, is a method to reduce errors efficiently. There are three basic types: splitting, Russian roulette and sampling from nonanalog probability density functions. Critical to all three techniques is the process of weighting, which refers to the relative contribution of a particle to the final results. Each particle is multiplied by a weight, *w*, so that the full results of the *w* physical particles represented by each particle modeled are exhibited in the final results. Specific variance reduction

techniques will be discussed in Chapter 4 with the MCNP description. (Briesmeister, 1993).

3.5.1 Splitting.

Splitting refers to dividing the particle's weight among two or more daughter particles and following them independently. Usually, the weight is divided evenly among k identical daughter particles whose characteristics are identical to the parent except for the factor $1/k$ in weight. The weight, however, may be unevenly divided to represent the expected number of physical particles that would select outcome j from a set of k mutually exclusive outcomes.

3.5.2 Russian Roulette.

Russian roulette takes a particle of weight w_0, turns it into a particle of weight $w_1 > w_0$ with probability w_0/w_1 and kills it (weight = 0) with probability (1 - w_0/w_1). The expected weight is $w_1 * w_0/w_1 + (1 - w_0/w_1) * 0 = w_0$ so the method doesn't bias the results as will also be seen in the analog game.

3.5.3 Sampling From Nonanalog Probability Density Functions.

An analog Monte Carlo calculation samples the events according to their natural physical probabilities, thus estimating the number of particles executing any given random walk. Nonanalog techniques are free to do anything that will preserve the correct particle density while, hopefully, reducing the variance. This is accomplished by adjusting the weights so the outcome matches that of the analog game.

4. Monte Carlo N-Particle Transport Code System (MCNP)

4.1 Introduction

The Monte Carlo N-Particle Transport Code System (MCNP, formerly Monte Carlo Neutron-Photon) is a general-purpose, continuous-energy, generalized-geometry, time-dependent, coupled neutron/photon Monte Carlo transport code. It was first developed by Los Alamos National Laboratory (LANL) using the Monte Carlo methods that emerged from work done there during World War II by Fermi, von Neumann, Ulam, Metropolis and Richtmeyer. Version I, a compilation of early work with neutron and photon transport, appeared in 1973. It's present version, 4a, has over 350 man-years invested in code production, testing and optimization by the Monte Carlo section of the radiation transport group (X-6) of the applied theoretical physics division (Xdivision) of the LANL. Its single source code complies with the FORTRAN 77 standard and thus can be run on many different types of computers: Cray, CDC, IBM, VAX, PRIME, SIEMENS, RIDGE, APOLLO, PC's and SUN. MCNP is able to analyze neutron-only, photon-only or combined neutron/photon transport. A user created input file is subsequently read by MCNP. This file contains information about the problem to be modeled: the evaluations to use, the location and characteristics of the neutron or photon source, the geometry of the problem, the type of answers or tallies desired and any variance-reduction techniques used to make the problem run more efficiently. (Briesmeister, 1993).

4.2 Method

The Monte Carlo method solves a transport problem by simulating particle histories that are transported between events (for example, collisions) that are separated in space and time. The individual probabilistic events that comprise a process are simulated sequentially and the probability distributions governing these events are statistically sampled to describe the total phenomenon. The sampling process is based on the selection of random numbers. Each particle is followed from a source, through events, to its death in some terminal category (absorption, escape, etc.).

MCNP uses continuous-energy nuclear data libraries. There are over 500 data tables for neutron interaction, photon interaction, and neutron dosimetry or activation for approximately 100 different isotopes or elements. The data tables are sufficiently dense on the energy grid that linear-linear interpolation induces less than 1% deviation from the evaluated cross sections. Cross sections are available for nearly 2000 dosimetry or activation reactions involving over 400 target nuclei in ground and excited states. The best available evaluation is clearly marked on the tables of nuclides included with the model. (Briesmeister, 1993)

4.2.1 Source.

MCNP's generalized user-input source capability allows the user to specify a wide variety of source conditions without requiring code modifications. Independent probability distributions may be specified for the source variables (energy, time, position, and directions) and other parameters (such as starting cell or surface). Built-in distribution

functions are available for various energy spectra such as Watt, Maxwellian and Gaussian; Gaussian for time; and isotropic, cosine and mono-directional for direction.

4.2.2 Tallies.

MCNP provides a measured quantity called a tally. A variety of particle flux and particle current tallies are obtainable: (1) current as a function of direction across any set of surfaces, surface segments or sum of surfaces and (2) flux across any set of surfaces, surface segments, sum of surfaces and within cells, cell segments or sum of cells. All tallies are normalized per starting particle.

4.2.2.1 Flux Tallies.

Standard flux tallies (where the term "flux" is used throughout the model documentation and output files regardless of the actual measured quantity) are obtained with point or ring detectors (used exclusively in this analysis). They are estimates of

$$F_5 = \int_t \int_E \phi(\vec{r}, E, t)\, dE\, dt, \qquad (4.1)$$

where ϕ, particle flux density, is the number of particles at distance r and time t with energies between E and $E + \Delta E$. The units of the flux tally are the units of the source. If the source has units of particles per unit time, the tally is also particles per unit time. When the source has units of particles, this tally represents a fluence tally. Flux can be obtained from the fluence tally for a time-dependent source by dividing the tally by the time interval assuming the source is constant over time.

The flux tally is obtained at user defined point detector locations. A point detector is a stochastic estimate (from each event location) of the flux at a point in space. It is known as a "next event estimator" because it is a tally of the flux at a point if the next event is a trajectory without further collision directly to the point detector. Contributions to the point detector tally are made at every event throughout the random walk. Each contribution to the flux tally can, therefore, be thought of as the transport of a pseudo-particle to the detector. The final quantity reported in MCNP (before the final normalization per starting particle) for the flux tallies is the sum of the scores from each of N individual events. Each score is a function of the particle weight, w, its distance, R, to the detector, the cosine of the angle between surface normal and particle trajectory, μ, and the total mean free path to the detector, λ:

$$\text{tally} = \sum_{i=1}^{N} w_i \times p(\mu_i) \times \frac{\exp(-\lambda_i)}{2\pi R_i^{\,2}}. \qquad (4.2)$$

The $\exp(-\lambda)$ term accounts for the attenuation between the present event and the detector point. The $p(\mu)$ term accounts for the probability of scattering toward the detector (instead of the direction selected by the random walk). The $1/(2\pi R^2)$ term accounts for the solid angle, $d\Omega$, the particle must scatter into to arrive at the detector. The R^2 term in the denominator can cause a singularity and thus infinite flux if a source or collision event occurs near the detector point. For that reason, a fictitious sphere is placed around the detector becoming an average flux region, i.e. individual contributions within the sphere are not counted, rather, the average flux is assumed within the sphere.

A ring detector tally is, in essence, a point detector tally with the point detector location not fixed but, instead, sampled from some location on a ring. It can be thought of as a floating point detector that moves to the location on the ring nearest an event. The tally is averaged over the circumference of the ring. Ring detectors can be much more efficient than point detectors but their use is only valid when the problem geometry is axially symmetric.

Point and ring detectors are subject to dramatic jumps in the tally from high weight particles. It is therefore vital that a sufficient number of particles be made to enter a region or volume of interest so it may be thoroughly sampled using, for example, a combination of importance biasing and geometry splitting, typical variance reduction techniques. Tally fluctuation charts contain a cumulative history of the tally as the run progresses and must be examined to confirm convergence.

4.2.2.2 Errors.

Associated with each tally in the output file is the estimated relative error, R, corresponding to one standard deviation of the mean $S_{\bar{x}}$ divided by the mean, $\bar{x}$, which, for a well-behaved tally, will be proportional to $N^{1/2}$ where N is the number of histories. *This variance refers only to the precision of the Monte Carlo calculation itself and not to the accuracy of the result compared to the true physical value.* MCNP also reports a figure of merit, FOM, for one tally bin of each tally as a function of the number of histories where $FOM = 1/(R^2T)$ (T, computer time in minutes). The more efficient the Monte Carlo run, the larger the FOM.

4.2.3 Variance Reduction.

The error in a Monte Carlo result is directly related to the number of particles simulated. One could, of course, run a large number of particles until acceptable error is obtained. There is value, however, in reducing the errors by less costly means, i.e. variance reduction techniques. The strength of MCNP lies in the large variety of variance reduction techniques available.

In the simplest Monte Carlo model, particles are followed from event to event with the next event sampled from a number of possibilities according to natural event probabilities. This analog model works well when a significant fraction of the particles contribute to each estimate. However, many cases arise where the fraction of particles detected is very small: the Monte Carlo model then fails with unaccepable statistical uncertainties.

Although the analog model is simple, there are other probability models for transport that will estimate the same average value with a much smaller variance. A non-analog model attempts to follow interesting particles more than uninteresting ones, where the interesting particle is one that contributes a large amount to the quantities that need to be estimated. To ensure the average score remains the same, the score is modified to remove the effect of biasing the natural odds. Thus, if a particle is artificially made q times as likely to execute a given random walk, its score is weighted by $1/q$, preserving the average score.

Any scheme that increases the number of particles available for scoring will decrease the error. Related to an increase in particles is use of the particles in an efficient

manner. An efficient scheme would remove particles not likely to contribute significantly to the tally, allowing more total particles to be run within the same time. A problem with some variance reduction techniques is that they often are tailored to aid one tally at the expense of all others. This forces separate runs for each optimized tally. The following non-analog variance reduction schemes operate to increase the number of particles, increase the efficiency with which they are used or both:

1. *Importance Sampling*: Regions in the problem geometry are assigned relative importances so particles transported from a region of higher importance to a region of lower importance can be Russian rouletted, that is, killed a fraction of the time according to the ratio of the regions' importances. The survivors will be counted more by increasing their weight. Particles transported into a region of higher importance will be split into two or more particles with lower weight.
2. *Time and Energy Cutoff*: Particles with a time or energy out of the range of interest are killed.
3. *Implicit Capture vs. Analog capture*: A particle has a probability of capture when it collides with a nucleus. Analog capture kills the particle with that probability. In implicit capture (survival biasing), the particle's weight is reduced by the capture probability, thus allowing important particles to survive the collisional capture.
4. *Exponential Transformation*: To transport particles long distances, the distance between collisions in the preferred direction is artificially increased and the weight is decreased. (Used with weight windows because of the large weight fluctuations.)
5. *Forced Collisions:* When a particle enters an almost transparent cell (low cross-section), it may be forced to undergo a collision by splitting it and its weight into collided and uncollided parts.
6. *Energy Splitting/Russian Roulette:* Particles entering important and less important energy ranges can be split or Russian rouletted, respectively.
7. *Correlated Sampling:* The i^{th} history will always start at the same point in the random number sequence regardless of the $(i-1)^{th}$ particle's history so statistical fluctuations in the solution will not mask small variations caused by the problem specification. In particular, it allows two possible slightly differing calculations to be compared independent of differences caused by random number generation.
8. *Source Biasing:* Source particles of higher importance are emitted with a higher frequency but with a compensating lower weight than less important source particles.
9. *Point Detectors:* The probability of transporting a particle precisely to a point detector is vanishingly small. Therefore, pseudo-particles are directed to the point instead. With every new particle from the source and at each event or collision, the pseudo-particle's probability of reaching the detector's location is used as its weight

with the weighted pseudo-particles summed to obtain the flux at the point detector. Ring detectors are essentially circular point detectors over which the flux is averaged. They are only available for problems with axial symmetry.

10. *DXTRAN:* When the problem contains a small region of interest that otherwise would be difficult to sample, a user-specified "DXTRAN sphere" can be used that will sum particles weighted by their probability of entering the sphere with no other collisions. Any particle that tries to enter the sphere will be killed since it has already been accounted for deterministically.
11. *Weight Window:* To keep the particle weight distribution within reasonable bounds, low-weighted particles are eliminated by Russian roulette and high weighted particles are split as a function of energy, geometric location or both. MCNP can provide nearly appropriate weight windows (determined for only one detector at a time) through its weight window generator function.

4.2.4 Geometry.

The geometry utility of MCNP treats an arbitrary three-dimensional configuration of user-defined materials in geometric cells bounded by first- and second- degree surfaces and some special fourth-degree surfaces (elliptical tori). Cells are defined by intersections, unions and complements of the surfaces bounding the desired regions. Surfaces are defined by supplying coefficients to the Cartesian coordinate analytic surface equations or for certain types of surfaces, by supplying known points on the surfaces. The code does extensive internal checking to find input errors. In addition, an elaborate geometry-plotting capability allows the user to view, and thus, define and check the geometry.

4.2.5 Cross Sections.

As discussed in Chapter 2, transport problems require particle interaction cross sections for each material. The producers of MCNP have taken the responsibility to ensure that the most current and accurate nuclear data tables are available. Tables are provided that cover all the different interactions modeled by MCNP.

Each nuclide library contains an energy grid including the photoelectric edges and pair production thresholds. These are followed by tables of coherent and incoherent form factors tabulated as a function of momentum transfer. Next are incoherent scattering, coherent scattering, photoelectric and pair production cross sections. The total cross section is a summation of the other cross sections.

Angular distributions of secondary photons are isotropic for photoelectric effect, fluorescence and pair production and are obtained by sampling the well-known Thomson and Klein-Nishina formulas for coherent and incoherent scattering, respectively. The energy of incoherently scattered photons is calculated from the sampled scattering angles, using the Compton relation.

4.3 Physics

MCNP treats photon interactions the same as neutrons for sampling of a collision nuclide, analog capture, implicit capture and variance reduction. The collision physics, however, are completely different. (Briesmeister, 1993).

4.3.1 Sampling of a Collision Nuclide.

When a photon interacts within a material composed of more than one element (compound, mixture, etc.) the particle type it collides with is determined by the relative proportions of the individual cross sections within the total (see Eqs. 2-19 and 3-19)

4.3.2 Capture: Analog and Implicit.

Analog capture kills particles with probability σ_a / σ_T where σ_a and σ_T are the absorption and total cross sections of the collision nuclide at the incoming photon energy. All particles killed by analog capture have their entire particle energy and weight deposited in the collision cell.

Implicit capture reduces the photon's weight, w_0, to w_0'

$$w_0' = (1 - \frac{\sigma_a}{\sigma_T}) \times w_0 \qquad (4.2)$$

If the new weight, w_0', is below the problem weight cutoff, the photon is rouletted, resulting in fewer particles with larger weights. A fraction, σ_a / σ_T, of the incident particle's weight and energy are deposited in the collision cell corresponding to the portion of the particle captured. Implicit capture is the default method of capture in MCNP.

4.3.3 Collisions.

MCNP has two interaction modes for modeling collisions, simple and detailed. The simple treatment is characterized by its neglect of coherent scattering and fluorescent photons from photoelectric absorption and is intended for high energy photons (model default: 100MeV). The detailed treatment includes coherent scattering and accounts for fluorescent photons after photoelectric absorption. The detailed treatment is described in the following sections.

4.3.3.1 Incoherent (Compton) Scattering.

MCNP determines the angle θ (scattering angle relative to the incident line of flight), hν', the new energy of the photon and hν - hν', the recoil kinetic energy of the electron. MCNP uses the Klein-Nishina cross section modified by an appropriate scattering factor to determine θ. This scattering factor acts to decrease the Klein-Nishina cross section (per electron) in the forward directions for low hν and high Z, independently.

4.3.3.2 Coherent (Thomson or Rayleigh) Scattering.

For coherent scatter events, only the scattering angle θ is computed after which transport of the photon continues. MCNP modifies the energy independent Thomson cross section with a form factor that acts to decrease the cross section for backward scattering of high hν, low Z interactions. This strongly peaks the cross section in the forward direction to the extent that at high energies, coherent scattering can be ignored.

4.3.3.3 Photoelectric Effect.

The phototelectric effect consists of the absorption of the incident photon (with energy E) and the subsequent emission of fluorescent photons and the ejection or excitation of an orbital electron (binding energy, $e < E$). Three cases of the photoelectric effect are treated: the emission of zero, one and two fluorescent photons with energy greater than 1 keV after the ejection or excitation of an orbital electron. In the *first* case, since no photons are emitted, the photon track is terminated and scored like an analog capture in the summary table of the output file. The cascade of electrons that fills up the

orbital vacancy left by the ejection (Auger effect) produces electrons and low-energy photons within the model. In the *second* case, one photon is emitted with an energy equal to the incident photon energy less the ejected electron kinetic energy less a residual excitation energy. The Auger effect and creation of electrons and low energy photons is again seen. In the *last* case, two photons can be emitted if the residual excitation of the second case is greater than 1 keV. As before, the residual excitation is dissipated by further Auger events and electron production. In all cases, the photons are assumed to be emitted isotropically. A photoelectric event is terminal for elements $Z < 12$ because the possible fluorescence energy is below 1 keV. A single event is possible for $12 \leq Z < 31$ with double fluorescence possible for $Z \geq 31$.

4.4 Inputs/Outputs

Input to MCNP consists of a file containing the entire problem description: geometry, source, tallies, etc. Appendix A contains a sample input file for this analysis. The specific entries will be discussed in Chapter 5 with the description of the modeled CT source and configuration. MCNP produces an output data file containing an entire problem summary. It includes a copy of the input file (fixed data), explicit source definitions, sampling values (expected vs sampled), and a thorough analysis of each tally including the results of ten statistical checks for each tally history. Appendix B contains the output file that resulted from running the input file in Appendix A. This example does not contain the fixed data since that is contained in the input file. It also eliminates the sampling results since, with such a complicated source, the amount of information is

overwhelming and with 2,000,000 particles per source point run, quite uniform and well sampled. Figure 4.1 shows the virtually indistinguishable normalized input CT spectrum and the sampled spectrum (for only 66,000 particles) which supports the decision not to present sampling results.

In addition to the regular output file, an optional MCTAL file can be requested. It contains strictly formated tally and spectal data. The file can be can be reformatted with a relatively simple FORTRAN program. The reformatted data is better suited to data processing. That option was utilized in this work. MCNP produces the RUNTPE file that is used to continue runs that were interrupted or unexpectedly killed. Frequent and periodic dumps to the RUNTPE file ensure minimal loss of data in case a continuation is necessary. The number of saved dumps can be controlled, thus limiting the size of the RUNTPE file.

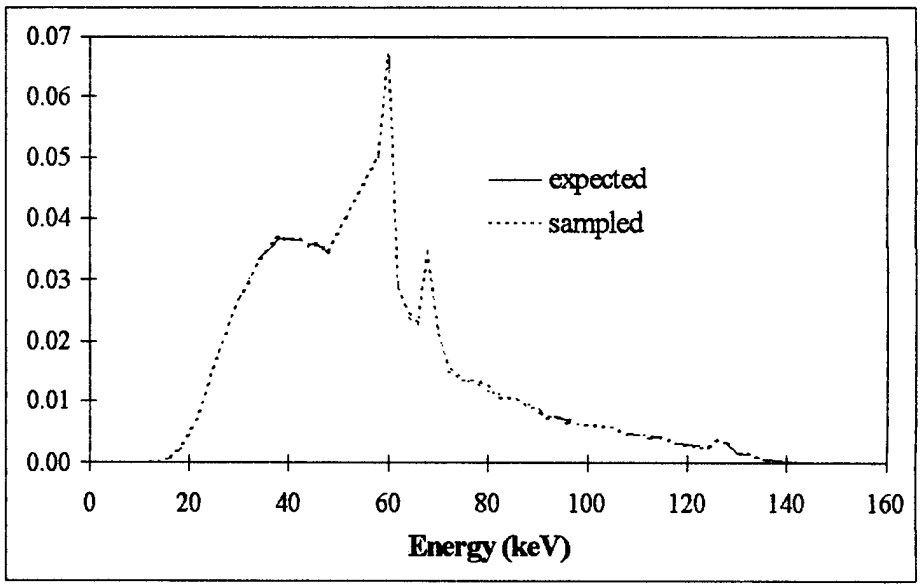

Figure 4. 1 Normalized sampled vs expected source spectra.

5. Computerized Tomography

5.1 Introduction

Tomography refers to the cross-sectional imaging of an object from either transmission or reflection data collected by illuminating the object from many different directions (Kak, 1987). Although tomography is primarily an imaging technique, that particular aspect will not explicitly be covered since this thesis is concerned with the source and system configuration and their impact on the non-occupational dose outside the suite. With that focus, the following sections will cover a description of the source, the detector, the suite configuration, and how all of these were modeled within MCNP.

5.2 Source

A CT source is uniquely defined by its method of scanning, its spectrum and its fan-shaped beam. Detector choice is determined by source since, with CT, unlike other radiographic imaging processes, the characteristics of the source force a definition of the detector. (Kak, 191987; Mackovski, 1983).

5.2.1 Scan Modalities.

In 1973 a revolutionary concept in tomography, known *as computerized axial tomography*, was introduced that provided an isolated image of a plane within a volume completely eliminating all other planes. Figure 5.1 (a) shows the operation of the first generation of scanners. They consisted of a single source and single detector that were

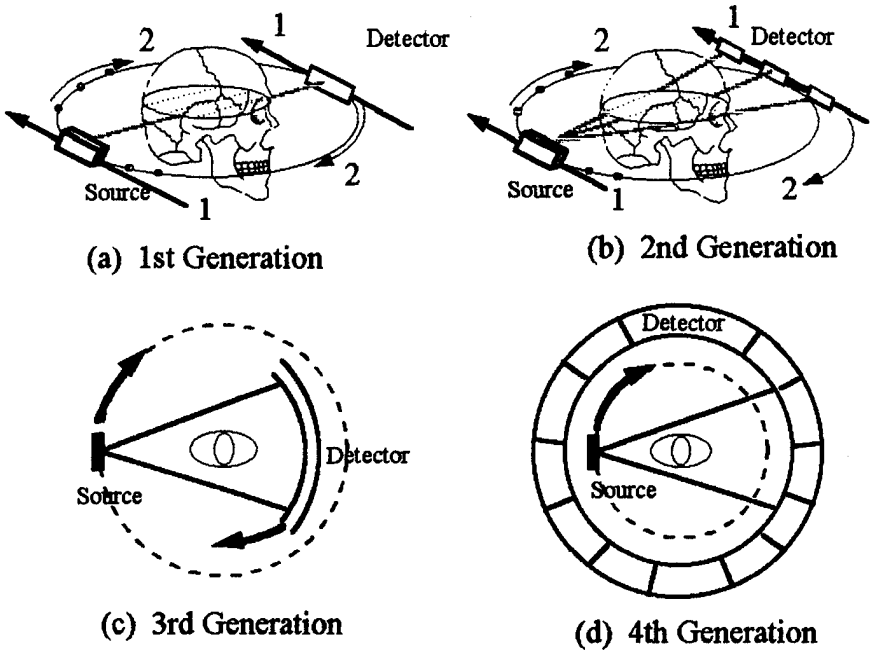

Figure 5. 1 Four scanner modalities.

translated simultaneously along straight parallel paths (1) with the target between them thus producing a single projection. The source-detector set were then rotated about the object (2) and the translation repeated. The problem with this method was the relatively long total scan periods, on the order of several minutes. This was acceptable for relatively stationary targets, but insufficient for restless patients (like children) or abdomenal images, where it was difficult for patients to hold their breath for the necessary length of time.

The second generation of scanners consisted of a thin fan-shaped source beam with multiple detectors that were again moved simultaneously along parallel axes, Figure 5.1 (b). The multiple projections (to each of the multiple detectors) for each lateral scan reduced the number of rotations required, and thus the scan times, to a fraction of a minute.

The scanner in WPMC's CT suite is a third generation scanner with a single fan-beam source and multiple detectors simultaneously rotating around the target, Figure 5.1 (c). This geometry eliminates the need for the translation motion. Scan times for third generation scanners are as low as one second with more than 1000 projections taken in a given 360 degree rotation. Five to seven hundred elements are contained in the detector array, allowing a very high resolution image. Some rotational smearing may be present (from the continuous rotation), but is minimal in the final image (Kak, 1987).

The newest scanners, fourth generation, have a single fan-beam source and a stationary detector ring completely surrounding the target. The source is rotated around the target, within the detector ring, Figure 5.1 (d).

The CT unit at WPMC is a GE Hi-Speed Advantage. Its fan beam has an angular extent adjustable from 25 to 48 degrees (25 to 48 cm at isocenter). A 35 degree beam was used in the analysis as a typical choice (Poteat, 1995). The beam's thickness is adjustable from one to ten mm. A ten mm beam thickness was used for the analysis. The source rotates 63 cm from isocenter. Scan times for WPMC's GE CT are adjustable from one to four seconds, with the time determined by the type of slice and operating current. During March, April and May of 1995 all scans were one second long with the exception of head scans which are done for two seconds at half the current. (GE, 1991).

5.2.2 Detectors.

The scan modalities of later generation CT's presented unique detector requirements. The fast scan times required rapid-response detector materials. Since the X

rays impinge on the detector perpendicularly, relatively deep, and thus highly collimating, detectors can be used. Thus, this allows the use of a gaseous ionization detector material like xenon. Solid scintillation detector materials are also common. The crystal traps most of the X-ray photons (absorption is dependent on photon energy and crystal size). The photons most likely undergo photoelectric absorption which results in the production of secondary electrons. Within the crystal, the kinetic energy of the secondary electrons transforms into flashes of light which are detected by a photomultiplier tube or solid state photodiode. (Kak, 1987)

The CT at WPMC uses a solid scintillation material, possibly cadmium tungstate ($CdWO_4$). The exact material composition, although confirmed as solid state, is proprietary to GE. The detector was modeled as $CdWO_4$ with a density of 7 g/cm^3. The material was required to absorb 99% of the photons impinging on it to match the machine specifications. As defined by third generation scanning, the detector is an arc with a radius defined by the source-to-detector distance, 110 cm. The detector array of 852 elements is one meter long. (GE, 1991).

5.2.3 Spectrum.

Fewell and Shuping published CT spectra for a variety of manufacturer's X-ray tubes (Fewell, 1981). Their spectrum for the GE tube was used for preliminary runs, but the tube spectrum for the GE HiSpeed Advantage was obtained from GE and used for the final runs. Figure 5.2 shows normalized spectra from Fewell and Shuping and from GE. The GE tube consists of a source of electrons impinging on a tungsten target which

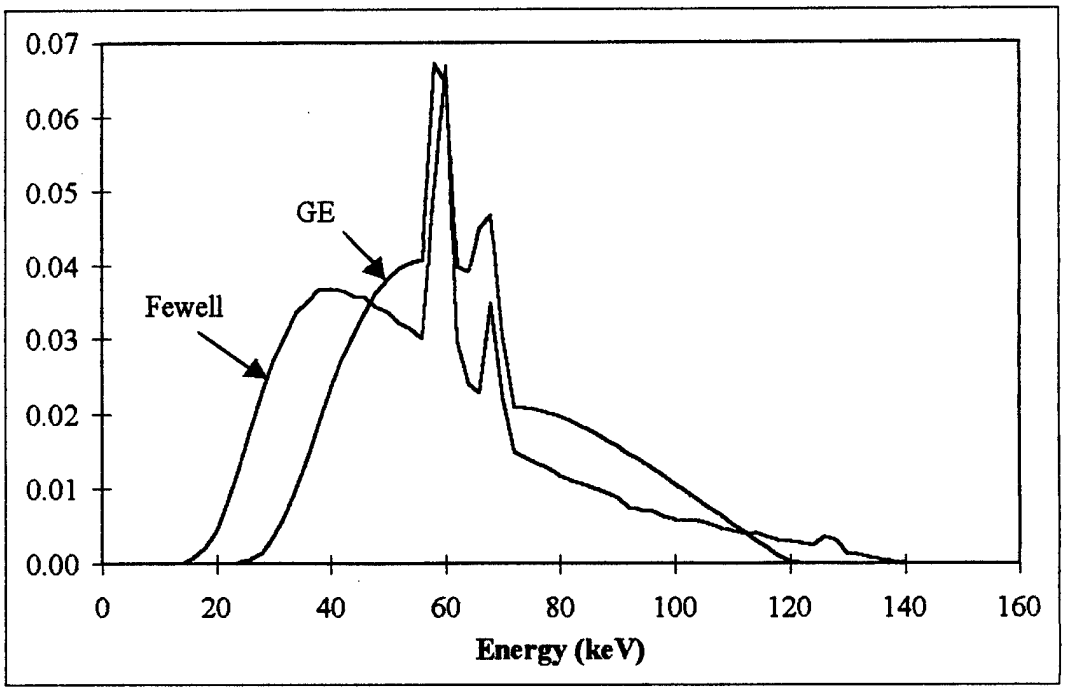

Figure 5. 2 Normalized CT spectra from Fewell and Shuping (Fewell, 1981) and GE (Fox, 1995a).

produces a Bremsstrahlung radiation spectrum from the collisional interactions between the electrons and the tungsten. The photon beam is collimated, narrowing it to one to ten mm thickness as describedabove. This beam is passed through a Teflon bowtie-shaped filter: flat on one side with an 18^{th} order polynomial surface on the other side (see Figure 5.3). The purpose of the bowtie filter is to reduce the total energy of the fan beam at the wider angles. This is desirable since the thickness of the human body is less at the higher fan beam angles. The filter reduces unnecessary radiation in the patient (Fox, 1995a). The exact filter shape and energy dependent attenuation coeffients (propriety: available for the analysis but not release) were used to modify the 35° fan beam at one degree intervals.

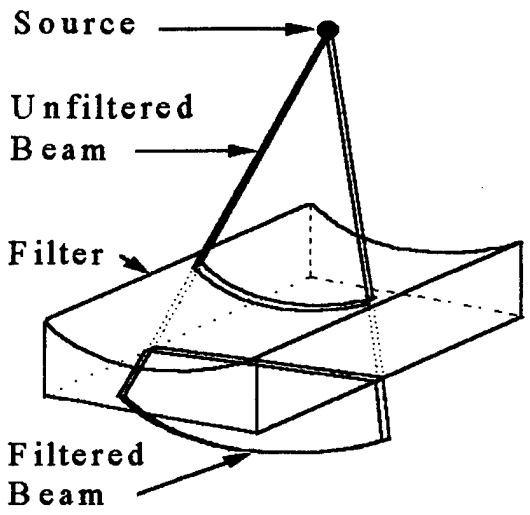

Figure 5. 3 GE's CT X-ray tube bowtie filter shown with a representative fan beam.

5.3 Configuration

CT units may be placed parallel to the walls or rotated. The rotated configuration is often desirable since it gives the patient easier access to the table and also allows the technician to observe the patient during the scan. The rotated configuration is found in approximately 70 - 80% of CT installations (Livingston,1995). The predominance of the rotated configuration dictated its use for the majority of the runs (see Figure 5.4). As described in the introduction, runs were accomplished with the CT unit in the X-ray room described by Metzger. Those results can be generalized to the non-rotated configuration. The Hi-Speed Advantage's product data booklet supplied by GE contained a

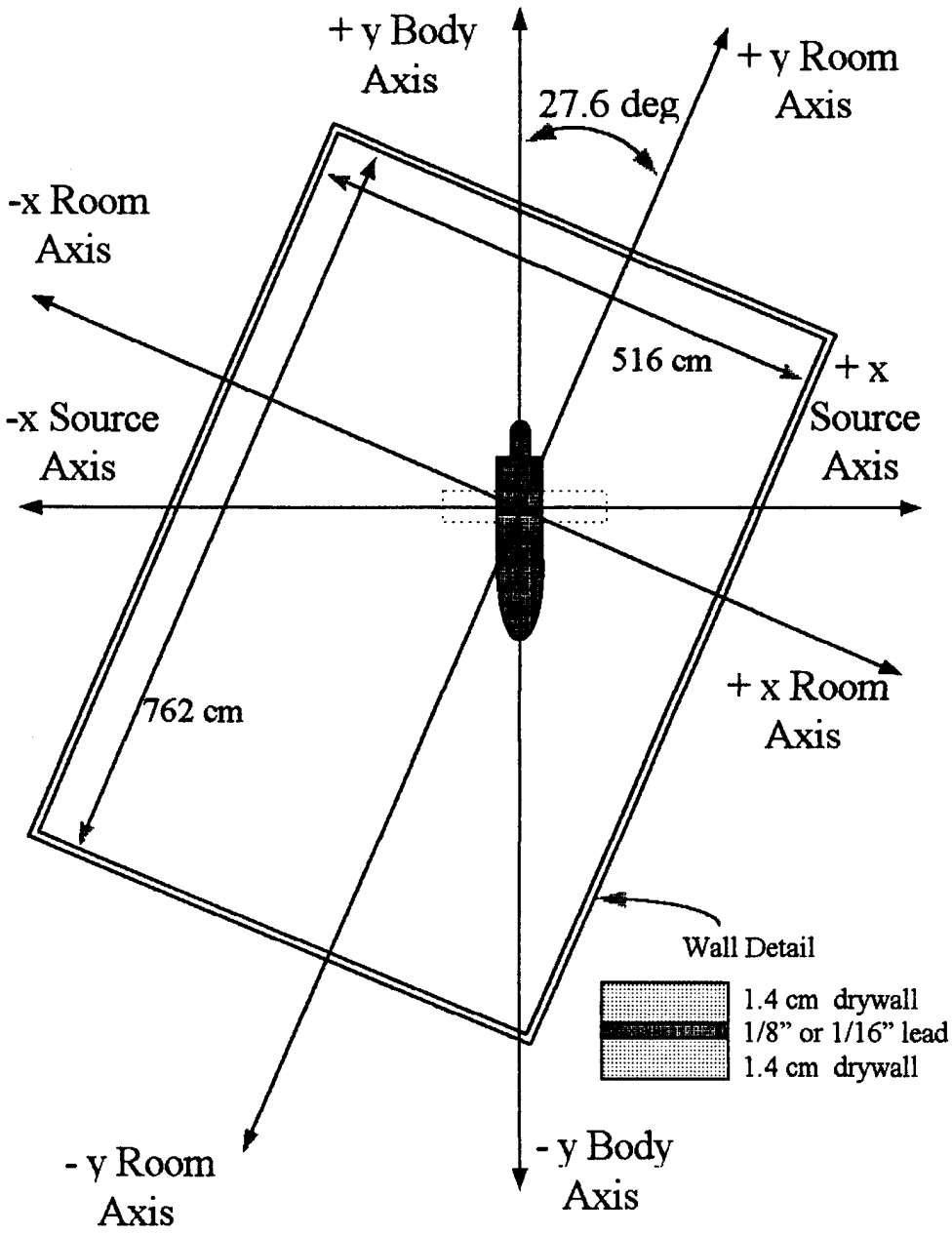

Figure 5. 4 Room, patient and source configuration for sample input file. This is the configuration that was used for the analyses.

recommended minimum suite size which was used for the general case. The exact dimensions and shielding in the CT suite at WPMC were used for WPMC analysis.

The patient lies on a translatable table that is positioned within the source-detector ring. The table was assumed to be effectively transparent to X rays since it supports the entire patient during scans and a non-tansparent table would interfere with imaging.

5.4 CT Model for MCNP

Appendix A contains a sample MCNP input file. It is for one source point (beam position) in the analysis of a CT head slice in the WPMC's CT suite. It contains a stylized human phantom consisting of a homogenous flesh material (Snyder, 1978) in a supine position rotated about the vertical axis. The walls are sheets of gypsum drywall on either side of a 1/8" layer of lead. The ceiling and floor are each 15 cm of concrete. The CT detector and aluminum structural supports are modeled. The typical CT fan beam (modeled as 35 lateral pencil beams) emanating from a single point source is used.

5.4.1 Cell Geometry.

Section I of Appendix A shows a list of cell *cards*: a line in the input file defining some specific aspect of the problem. *Cells* are volumes of interest containing a single material. They are built from surfaces (defined later). The first number on a card is its unique numerical identifier. The next two numbers refer to the material contained in the cell and its density. A cell can be defined as a "void" meaning all particles that enter it are killed (see cell 20). The next list of positive and negative numbers on the card are the surfaces defining the cell. The sign of the surface indicates its *sense*, i.e. up from, down

from, to the left of, to the right of, etc. Associating a sign with a surface actually, then, defines the volume in some direction relative to the surface. A space between two surface numbers indicates the intersection of the two volumes. A spherical shell could be described as the intersection of the region inside a larger sphere with the region outside a smaller, concentric sphere. A colon between two numbers indicates the union of two (or more) volumes. A cell entry shown with a pound sign (#4), where the number is another cell number, indicates that the cell contains everything but that cell. In the previous spherical shell example, the cell could have been described as everything inside the larger sphere but not in the smaller sphere (defined elsewhere as a cell). The last number is the cell's importance used for the variance reduction techniques.

Note cell 105, the torso, in the appendix. It is the intersection of the interior of an elliptical cylinder parallel to the y axis (surface 10) bound top and bottom by two x-z planes (surfaces 6 and 8). The torso cell does not include the lungs, hence, #101 and #103. It is composed of the homogenous flesh material, m2, with a density of 0.9869 g/cm^3. It has a photon importance of 1.

5.4.2 Surface Geometry

Section II of Appendix A shows a list of *surface* cards. The first number in a surface card is again the unique numerical identifier. This is followed by a letter(s) describing the type of surface and a list of numbers that satisfy the description of the surface. For example, planar surfaces are indicated by a p, and are described by their coefficients in the equation of a plane: $Ax + By + Cz + D = 0$ (see surface 70 or 71).

Volumetric surfaces (sphere, ellipsoid, cone) are described by their size and the location of their center. Surface 2 is an ellipsoid whose upper half defines the top of the head. The coefficients (A, B, C, D, E, F, G, x', y', z') satisfy the equation: $A(x - x')^2 + B(y - y')^2 + C(z - z')^2 + 2D(x - x') + 2E(y - y') + 2F(z - z') + G = 0$.

5.4.3 Materials.

Section III of Appendix A contains descriptions of the materials used in the problem. Each material is uniquely numbered and described as a list of the elements and their atomic or weight fraction. (For other than photon analyses, the desired cross section library would also be specified.) Material 11 (m11), cadmium tungstate, an example of a material specified by atomic fractions, has the chemical formula $CdWO_4$. Material 1 (m1), lung tissue, an example of a material specified by weight fractions, is composed of 10.21% hydrogen, 10.01% carbon, 2.8% nitrogen, etc.

5.4.4 Source.

MCNP's general source utility was used to describe the CT source. It requires the energy spectrum and the beam positions, directions and shape. Since MCNP does not have the capability to directly model the continuous, rotating, fan-shaped beam, the CT source was modeled as 32 discrete point sources, each consisting of 35 individual pencil beams which simulated the fan shaped beam (see Figure 5.5). Each source point was run individually because of the detector configuration. Recall that the detector rotates opposite to, but syncronous with the source. MCNP could not model a detector that moved as the source was sampled from different beam positions. The source is on a radius larger than

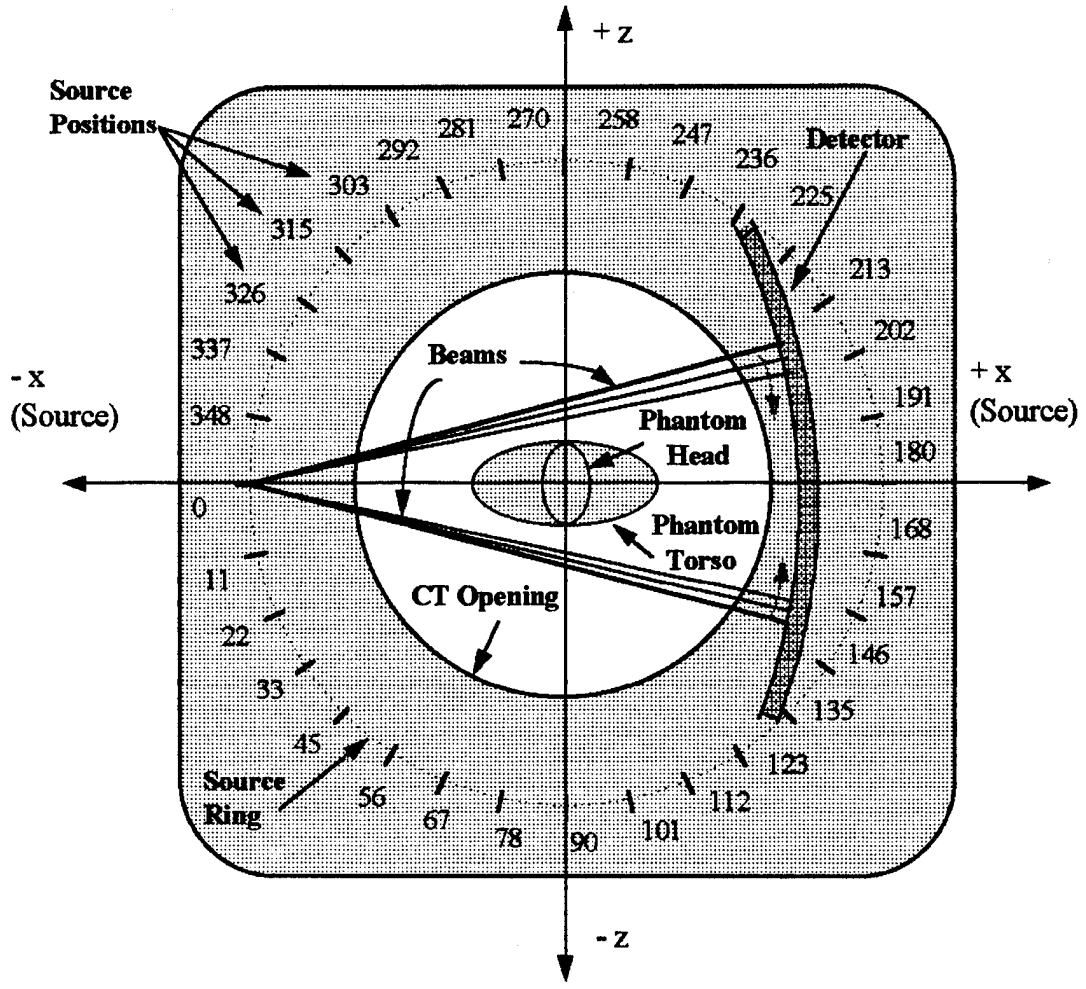

Figure 5. 5 View of the modeled CT source in the x-z plane. Note the labels at the source positions.

the detector radius. Attempting to place a continuous detector in the configuration would block the source, thus the 32 individual runs necessary to model a single source rotation. Section IV of Appendix A contains the complete modeled source.

The first uncommented card is the general description of the source. Each variable (erg, pos, etc.) points to an associated distribution, dxxx. The position (pos = d1) is

described as a distribution of positions, each with equal probability (sp1). Since the appendix is an input file for only one of the discrete beam positions, the position, that is, the point of origin for the source point, for each of the 35 pencil beams is the same. The beam shape (dir = d2), for each of the 35 individual beams is a very narrow cone, or pencil, beam. The si2 card is the cosine of the angular extent of the beam, one degree. It represents the distribution values of the particles for any selected pencil beam. Its probability, on the sp2 card, is always one.

The beam direction (vec = fpos = d3) is defined by a vector passing through the source point with a direction determined by its position within the fan beam. Envision a line from the source point to isocenter. The fan extends 17.5 degrees to either side of this line. The beam vector is determined by the beam's position in the fan beam but, defined relative to the problem geometry axes. Each of the pencil beams (initially produced with the pos variable) is associated with one vector in the list of distribution labels, ds3. The labels point to the individual vector descriptors: si201, si202, etc. All of the vectors, again, have equal probability (sp201 = sp202 = . . . = sp235 = 1).

The energy, or distribution of energy, is input with the erg variable, erg = fpos = d4. As described above, the primary source passes through the bowtie filter (uniform about its center) to reduce its energy at the outer fan beam angles. The spectral differences produced in each pencil beam by the filter are seen in the 18 different spectra pointed to with ds4, the distribution labels, which then point to the individual sets of spectal values (si117, si116, etc.).

The last two cards in the source description, df0 and de0, are the flux-to-exposure conversion factors. These cards are used to scale the tally as a function of particle energy. They are typically used to convert the tally to an energy-dependent dose equivalent rate in rem per hour. The conversion factors shown here (used by Metzger in his diagnostic X-ray system analysis) are the ICRP-2 standard (MCNP, 1993) provided with MCNP, scaled by rem-to-Roentgen factors and converted from hours to seconds. This results in a tally reported as an exposure rate in Roentgen per sec which was converted to gray per sec (see Section 2.8.6).

5.4.5 Tallies.

Section V contains the tallies (see section 4.2.2.1) that were computed for this example. Flux tallies are identified by a numerical designator ending in "5". The "p" indicates a photon (X-ray) tally. In this example, with the phantom rotated about the vertical axis, tallies were computed along two different axes sets, the first set defined by the body axis and source plane and the second set by the room walls (see Figures 5.4 and 5.5) 30 cm outside the walls. In addition, floor and ceiling tallies were done, again, 30 cm outside the enclosure. Not shown in the example file is a ring detector that was placed 30 cm within the source ring. This tally was used a baseline for kerma rate computation (section 6.1.2).

The "dd" card describes the Russian roulette game: the first number is the fraction of the average weight below which particles will be rouletted. Example: a value of .01 would kill all particles with weights below 1% of the average. The "0" entry here indicates

that low weight particles will not be killed. The "1e25" entry is used only to discriminate which score histories to write to the output file. A very large value, as seen here, will prevent all entries from being written to the output file. This was done solely to minimize output file size. Since obtaining the spectrum of the escaped dose was a goal in this analysis, the "e0" card was used which lists the energy bins desired. The "prdmp" card indicates the frequency the continuation file and tally dumps are written. As with the "dd" card, the high value limits the number of dumps, again, to minimize file size. This card also specifies that a MCTAL file (see section 4.4) be written. The last card, "nps", specifies the number of particles to run.

5.5 MCNP Output

Appendix B contains the output file produced by a run using the input file in Appendix A. As stated previously, it does not contain the fixed data or the sampled values. The fixed data and sampled values would be located before the output seen in the appendix.

5.5.1 Photon Creation.

Section I of Appendix B is a summary of photon creation information. Note that many of the listed values are those produced by the different variance-reduction techniques (weight cutoff, DXTRAN, etc.). This section also contains run-time figures: computer time, source particles per minute and random number generation figures. This particular run used almost 300 million random numbers for the 2 million particles.

5.5.2 Cell Activity.

The information contained in Section II is useful for improving cell importances. Ideally, the number of particle tracks entering a cell (tracks column) would be equal for all cells to equalize error contributions per cell. Large differences could indicate a need for further geometric splitting of either of two adjacent cells. The above guidelines, however, must be tempered with the knowledge of the problem geometry. For example, cell 9 shows a much larger number of entering tracks than cell 8. Cell 9, however, is the cell containing all of the space within the room that is not explicitly another object (torso, detector, etc.). It would naturally have a greater number of tracks. The tracks column increments every time a particle enters a cell, even if it is re-entering the cell. The population column lists a track only the first time it enters a cell. Comparison of the population column with the tracks column can provide a rough estimate of the amount of backscatter into a cell.

5.5.3 Tally

All of the information on a given tally is grouped together. Section III shows one example of a tally summary. It starts with a description of the tally - name, location, and type. If the tally has been modified by a dose function (de0 and df0, section 5.4.4) a comment to indicate that will appear. Recall that the energy spectrum of the tally was desired. This information is listed (with its error) for the collided and uncollided photon flux. The total tally and error are provided at the bottom of the spectrum. The *score* contributions by cell can also assist importance function determination. Cells that

contribute little to the score do not require large importances. The score misses information summarizes the zero score tallies and their importance to the tally value. The next table shows the impact the largest scoring particle history in the run would have on tally and error if it were to occur in the next history.

MCNP performs ten statistical checks of each tally to help the user test for reliability. The desired and observed behavior of the tally, error, variance of the variance, figure of merit and probability density function tail are compared and given a pass/fail score.

The last information provided for the individual tallies is the tally density chart. It is a graphic representation of the unnormed probability density. It should be relatively smooth with no holes (which could indicate undersampled regions of the probability density function). The probability density chart is not provided if the tally passes all ten statistical checks.

Everything described above is repeated for each tally. The last entry in Section III is a summary of the statistical checks of all tallies.

5.5.4 Tally Fluctuation Charts.

The tally fluctuation chart in Section IV is a cumulative history of the tally at regular intervals in the run. The mean, error, variance of the variance and figure of merit should be examined for convergence. Erratic results could indicate a poorly defined problem, the need for additional particle histories or inappropriate variance reduction parameters.

5.5.5 Final.

This last section contains run termination information. This run ended when two million particle histories had been completed. It could also show that a run had been terminated because of geometry problems, missing inputs, etc. Section V again summarizes computer run-time information. This last section is particularly useful during a run. The UNIX "tail" command prints the last lines of a file, i.e. run status, to the screen eliminating the need to open a file and scroll to the bottom, preventing possible file corruption.

6. Calculations and Method

Metzger provided a method to determine dose outside a diagnostic X-ray facility using Monte Carlo analysis techniques (Metzger, 1993). His method is the basis for the method used in this study to determine dose outside a computerized tomography (CT) suite. The first section below describes the calculations necessary for both an X-ray room and a CT suite. The following sections describe how Metzger's results were reproduced for a standard X-ray room. The last section describes the CT modeled within the standard X-ray room with the body and source axes parallel to the walls. Within that configuration, the importance of variations in the phantom and CT detector were investigated. With those investigations completed, the set of 32 beam positions (representing discrete points around a full scan rotation) for the CT in the X-ray room was run.

6.1 Calculations

The following sections present the calculations and data manipulation done to obtain the dose outside the CT suite. In general, the dose calculation is determined from the MCNP tallies, X-ray tube spatial beam width and potential usage factors, CT tube current protocols, and average air kerma. The specific calculations are described below.

6.1.1 Work Load.

Both X-ray and CT units can be operated in different tube potential, current and beam size modes determined by the image required (Michael, 1995; GE, 1995a). *Work load* refers to the degree of use of a particular source mode or the proportion of time it is

operated in each mode (NCRP, 1976). It is important to include the workload in the analyses because it directly impacts the total dose. The area to be imaged determines the beam width, operating tube potential, number of rotations per scan and beam current. The total workload for a given time interval is, therefore, a summation over the beam width and tube potential usage factors (U_{BW} and U_{TP}) and the the area to be imaged:

$$\text{Work Load}\left(\frac{\text{mA}\cdot\text{min}}{\text{time interval}}\right) = \sum_i U_{BW,i} \sum_j U_{TP,j} \sum_k \left(\frac{\text{ScanSets}}{\text{time interval}}\right)_k \times \left(\frac{\text{Rotations}}{\text{ScanSet}}\right)_k \times \text{Current}_k(\text{mA}) \times \text{RotationTime}_k(\text{sec}) \times \frac{1(\text{min})}{60(\text{sec})} \qquad (6.1)$$

Unique workloads were determined for the head and abdomen scans.

6.1.1.1 Tube Potential Usage Factor.

Typically, X-ray tube potential is be varied from 45 kVp to 140 kVp, determined by the size or area of the body to be imaged. Tube potential usage factors are determined by the length of time each potential is used. The times are normalized to one and applied to the workload and kerma (air kerma varies with tube potential; NCRP,1989). The tube potential usage factors are different for the chest (standing patient with wall-mounted recording film) and radiographic (supine patient on table) rooms which Metzger obtained from published reports. The radiographic room usage factors used by Metzger are seen in Figure 6.1. Since tube potential usage factors were not available for CT units, those used for this analysis were based on typical usage protocols at WPMC (Michael,

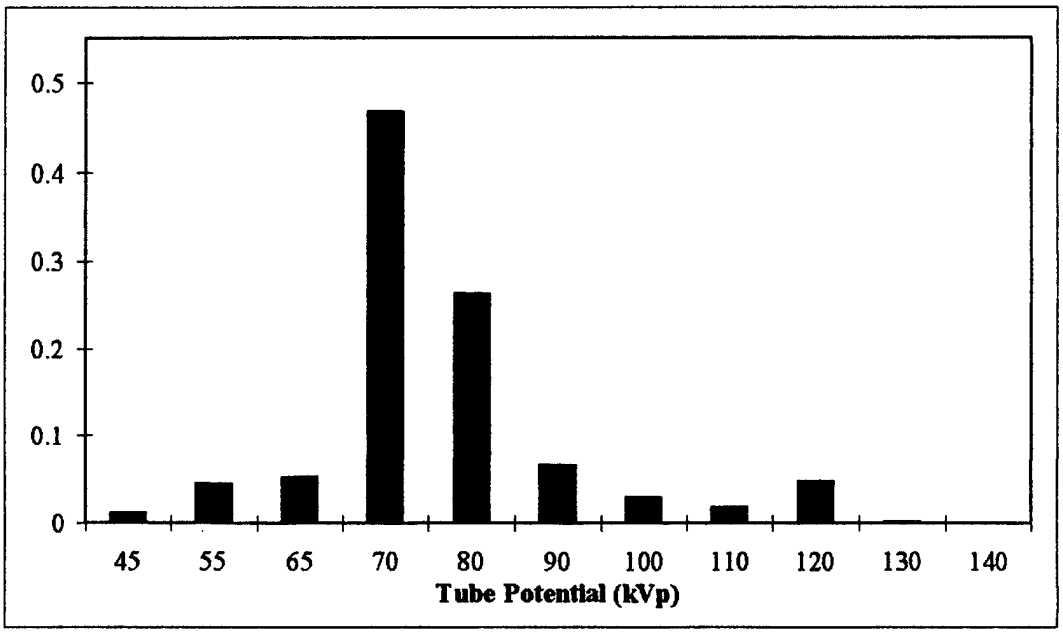

Figure 6. 1 Normalized radiographic room tube potential workload used by Metzger.

1995). As can be seen in Table 6.1, their CT tube was operated exclusively at 120 kVp corresponding to a usage factor, U_{TP}, of one.

Table 6. 1 GE HiSpeed Advantage CT Protocols

Scan Type	Potential (kVp)	Current (mA)	Time (sec)	# Rotations
Head	120	140	2	25
Sinus	120	280	1	35
Body	-	-	-	-
Chest	120	280	1	35
Abdomen	120	280	1	40
Pelvis	120	280	1	20
Chest/Abd/Pel	120	280	1	80
Abd/Pel	120	280	1	50
Liver	120	280	1	40
Renal	120	280	1	30
Pan	120	280	1	30

6.1.1.2 Current Workload.

X-ray tube current is again determined by the patient area to be imaged. NCRP 49 contains average current work loads for diagnostic X-ray rooms which Metzger modified from the suggested 1000 mA-min per week down to 400-500 mA-min per week based on the use of modern, faster exposure films. These figures, however cannot be applied to CT units. The CT usage summary from WPMC, averaged over March, April and May 1994 and the CT protocols (Tables 6.2 and 6.1, respectively), was used for this analysis. (The number of individual body scans are a percentage of the total number of reported body scans.) Current workload was determined separately for the head and abdomen scans and applied to the head and abdomen MCNP results. The total current workload for the CT unit, about 16,000 mA-min per week, is much larger than the X-ray current workload of 400 to 500 mA-min per week.

6.1.1.3 Beam Size.

Metzger used a conic X-ray beam collimated to 1536 cm^2 at the patient. The GE HiSpeed Advantage's fan-shaped beams angle is adjustable from 25 to 48 degrees and beam width from one to ten mm. The beam angle is reduced by blocking the source which thus reduces the total energy out. Since data was not available to quantify the reduction, the original source strength was used with a 35° fan angle (approximately 39 cm at isocenter), 10 mm wide as a worst-case assumption. Since the source utility in MCNP is only able to model point sources uniform about a central axis, the narrow beam width required modeling the fan beam as 35 individual beams.

Table 6. 2 Summary of WPMC's CT Usage

Scan Type	Number of Scan Sets			Total	S.S./ week	Work Load mA-min wk^{-1}
	March	April	May			
Head	108	101	110	319	24.5	2863
Sinus	51	44	38	133	10.2	1671
				Head Total		**4534**
Body	*243*	*204*	*266*	*713*	-	-
Chest (3%)	7.3	6.1	8.0	21.4	1.6	269
Abd (40%)	97.2	81.6	106.4	285.2	21.9	4095
Pelvis (3%)	7.3	6.1	8.0	21.4	1.6	154
Chest/Abd/Pel (4%)	9.7	8.2	10.6	28.5	2.2	819
Abd/Pel (40%)	97.2	81.6	106.4	285.2	21.9	5119
Liver	11	18	7	36	2.8	517
Renal	15	7	12	34	2.6	366
Pancreas	5	6	1	12	0.9	129
				Abdomen Total		**11468**

6.1.2 Air Kerma.

Average air kerma is a function of tube potential and distance from the source. NCRP Report 102 provides a list of average air kerma rates by X-ray tubes potential and distance from the source. Given the MCNP tallies for a known source for two locations, A and B, air kerma can be determined at detector location B if the air kerma at detector location A is known simply by scaling the average air kerma from location A by a ratio of the detector tallies

$$\text{Air Kerma}_B = \text{Air Kerma}_A \times \frac{\text{Tally}_B}{\text{Tally}_A} \qquad (6.2)$$

This method of relating kermas via a detector tally ratio eliminates constants produced from converting from degrees to radians, etc. It is only valid for exposure tallies: flux and fluence tallies cannot be related to kermas because the particles in the flux/fluence have different energies. This method was applied to the analysis by placing a 33 cm ring detector on the same plane as and concentric within the 63 cm CT source ring (see Figure 5.5). The exposure tally at that ring detector could be associated with average air kerma 30 cm from a 120 kVp source (17.8 centi-Gray per 100 mA sec = 0.1068 Gy per mA-min; NCRP, 1989), and thus could produce a conversion from the exposure tallies to air kermas at those locations.

Air kerma is related to a material kerma by a ratio of mass energy-absorption coefficients. For example, consider the conversion from air to muscle tissue kerma:

$$\frac{(\mu_{en}\,\rho)_{tissue}}{(\mu_{en}\,\rho)_{air}} \cong 1.07 \pm 3\% \qquad (6.3)$$

(valid from 4 keV to 10 MeV, Attix, 1986). This is can be used to convert dose (grey) to equivalent dose (sievert). To convert the exposure tallies to effective dose for the film badge comparison, the method described in Eq. (6.2) was used. The resulting dose in air was multiplied by the radiation and tissue weighting factors (see section 2.8.7) used in 10CFR20 (those advocated by ICRP) to obtain an effective dose in skin.

6.1.3 Final Calculation.

Using the above work loads and kerma conversions, an annual dose can be obtained at each detector location from their respective exposure tallies

$$\text{Dose}_{\text{annual}}\left(\frac{\text{mSv}}{\text{year}}\right) = \frac{\text{Tally}_{\text{source}}}{\text{Tally}_{\text{det\_i}}} \times \text{Air Kerma}_{120\text{kVp @30cm}}\left(\frac{\text{Gy}}{\text{mA min}}\right) \times 1.07\left(\frac{\text{Sv}}{\text{Gy}}\right) \times \text{Current WorkLoad}\left(\frac{\text{mA min}}{\text{week}}\right) \times 52.1428\left(\frac{\text{weeks}}{\text{year}}\right) \times 1000\left(\frac{\text{mGy}}{\text{Gy}}\right) \tag{6.4}$$

A complete CT scan is modeled with 32 equally spaced beam positions around the source ring. Taking the average of the 32 tallies at each detector gives the equivalent tally of a single scan. Initial results indicated that some areas of the scan required additional beam positions and others could be eliminated (see Chapter 7 for a list). These were incorporated by appropriately weighting the new points and the original points surrounding them. For example, a weight of 1/32 is assigned to each of the 32 equally spaced beam positions. If an additional point was placed between beam positions 11.25 and 22.5, Figure 6.3 shows the adjusted weights, assuming each beam position contains the area from halfway between itself and its neighbor on each side. The errors are given the same weights as the exposure tallies. The composite error is thus

$$S_{\bar{x}tot} = \frac{S_{tot}}{\sqrt{N}} = \frac{\sqrt{\sum w_i S_i^2}}{\sqrt{N}} = \frac{\sqrt{\sum w_i S_{\bar{x}_i}^2 N}}{\sqrt{N}} = \sqrt{\sum w_i S_{\bar{x}}^2} = \sqrt{w} \times \sqrt{\sum S_{\bar{x}}^2} \text{ (equal weights)} \tag{6.5}$$

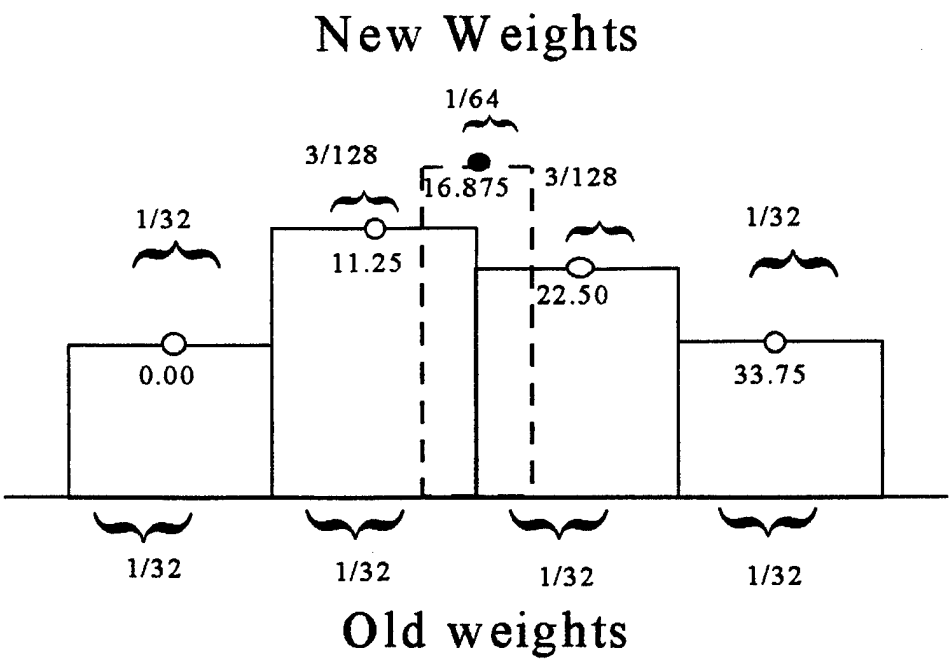

Figure 6. 2 Adjusted weights with the addition of points.

where S_i is the total error for a given tally, S_{xi} is the is the error reported for a single tally per particle, w_i is the tally weight and S_{xtot} is the composite weighted exposure tally error from all beam positions at a single detector location.

6.2 X-Ray Source in X-Ray Room

6.2.1 Reproduction of Metzger's Results.

Metzger's Monte Carlo analysis of a diagnostic X-ray room was duplicated primarily as a training exercise, but also however, to ensure the his method was properly interpreted. Metzger performed the dose calculations for the chest and the radiographic

rooms each with 1/16" and 1/32" lead, but it was sufficient here to duplicate only the 1/16" lead thickness. These MCNP runs were accomplished using input files provided by Metzger. Any differences noted would be a result only of the computer used and its random number generator. Tables 6.3.A and 6.3.B present a comparison of the results.

Table 6. 3 Comparison with Metzger's Results

A: Chest Room, 1/16" Lead							
	Pos	Air Kerma, Gy		Diff	Error, %		Within
		Davis	Metzger	%	Davis	Metzger	Error?[a]
Point Det	Pos x	1.46E-09	1.5E-09	2.7	5.2	8	Y
	Neg x	1.68E-09	1.5E-09	12.2	9.6	8	Y
	Neg y	1.37E-07	1.4E-07	2.1	1.7	2	Y
	Pos y	3.62E-10	3.6E-10	0.6	13.1	10	Y
	Ceiling	1.76E-09	1.9E-09	7.2	35.9	18	Y
	Floor	3.12E-09	3.1E-09	0.8	15.0	15	Y
Ring Det	Neg y	1.45E-07	1.4E-07	3.8	1.6	2	Y
	Pos y	3.49E-10	3.6E-10	3.2	10.1	10	Y
	Source	0.0085	0.0085	0.0	0.1	0.9	Y
B: Radiographic Room, 1/16" Lead (Using adjusted source tally: source tally/4)							
	Pos	Air Kerma, Gy		Diff	Error, %		Within
		Davis	Metzger	%	Davis	Metzger	Error?[a]
Point Det	Pos x	5.98E-11	5.5E-11	8.6	15.7	9	Y
	Neg x	5.17E-11	5.5E-11	6.0	13.4	9	Y
	Ceiling	2.07E-10	1.8E-09	88.5	16.7	11	N
	Floor	6.96E-09	6.8E-09	2.3	9.8	8	Y
	Source	4.69E-03	4.7E-03	0.0	0.1	0.1	Y
Ring Det	Pos y	3.86E-12	3.7E-12	4.4	12.6	23	Y
	Neg y	1.11E-10	1.6E-11	596.2	91.0	22	N[b]

a Error Criteria: Can error bars overlap? [b]Negative and positive y had different ring detector radii.

The chest room's source detector (see section 6.1.2) was placed one meter from the source in the center of the beam. This presented a problem with the supine phantom in the radiographic room, however, since it would placed the detector in the middle of the

torso. Metzger placed it, instead, 50 cm away and modified the results using the inverse sqared law, i.e. the distance was halved, therefore, to correct to a one meter position, the exposure is divided by four. Most agreed within statistical error. There are some notable exceptions, however. The negative-y tally ring detector for the radiographic room was discovered to have its radius much smaller than the positive-y tally ring detector, producing an tally with high error that differed significantly from Metzger's result. The ceiling results for the radiographic room, for an unknown reason, exhibited high error and very different results.

6.2.2 MCNP Versions.

The above runs were completed with Version 3a of MCNP. When Version 4a came available, the runs were repeated. The exposure and errors for all detectors were identical to all reported decimal places. Some of the tests that follow were accomplished with Version 3a and some with Version 4a. Given the exact agreement of results, those runs done with Version 3a were not repeated with Version 4a.

6.3 CT Source in X-Ray Room

The following sections describe the tests that were done to define and improve the inputs. Unless otherwise noted, they were all done using the CT source and configuration modeled within the X-ray room described by Metzger.

6.3.1 Phantom Considerations.

The phantom used for this analysis is the one defined in the Medical Internal Radiation Dosimetry (MIRD) Pamphlet No. 5 (Snyder, 1978). The pamphlet includes mathematical descriptions of the entire human body, including a stylized total body, organs, and bones. The pamphlet also contains the elemental composition of flesh, bone and lung tissue used in the analysis. With such complete phantom information, the questions were: "How much detail is necessary? Model the entire body or is the head sufficient? How much of the skeleton, if any, is necessary? Include the organs?" To satisfactorily answer these questions, test runs were done.

The elemental composition and density of internal organs reported in the pamphlet are nearly the same as the flesh tissue, with the exception of the lungs which have a much lower density. Therefore, the only internal organs retained were the lungs. The MIRD head consists of an elliptical cylinder topped by half an ellipsoid. The remainder of the body consists of another elliptical cylinder for the torso and two truncated cones for the legs. Problems with MCNP geometry were encountered when the leg cones were used. They were changed to a single half ellipsoid of the same total length, width and thickness (80 cm x 40 cm x 20 cm) resulting in a volume 2.7% greater that the cones.

6.3.1.1 Head Only vs Whole Body.

To determine if using only the head would produce significantly different results from using the entire body, an MCNP run using (a) only the top of the head and face and (b) the entire body were compared. Table 6.4 lists those results. The floor and

positive and negative-y exposures showed a significant difference indicating that inclusion of the entire body was necessary. In addition to the above comparison, exposure from detectors positioned off of the head (positive-y) and off of the feet (negative-y) within the

Table 6. 4 Head-Only to Whole Body Comparison

Position	Head Only		Whole Body		Diff, %	Within Error?
	Detector Tally, R s^{-1} $particle^{-1}$	Error, %	Detector Tally, R s^{-1} $particle^{-1}$	Error, %		
Pos x	3.06E-18	7.6	3.11E-18	7.5	1.6	Y
Neg x	4.66E-18	8.4	4.82E-18	8.7	3.4	Y
Ceiling	4.59E-20	15.7	5.48E-20	22.7	19.4	Y
Floor	5.48E-19	9.8	4.25E-19	7.2	22.4	N
Source	1.00E-12	8.2	9.98E-13	8.3	0.2	Y
Pos y	3.40E-20	10.1	5.96E-20	38.0	75.3	N
Neg y	1.46E-20	18.0	1.04E-20	27.78	28.8	Y

room were compared. Both exhibited the same behavior as the source was rotated, i.e. relatively uniform about a mean. The ratio of positive-y exposure to negative-y exposure, however, changed from about two, head-only, to about six, entire body. This reinforced the decision to include the entire body, particularly for the analysis inside the CT suite.

6.3.1.2 Skeleton.

The importance of including the skeleton in the phantom was analyzed using only the head phantom since it had the largest proportion of bone to tissue (by volume) and thus would be most affected by neglecting the bone. The skull was defined

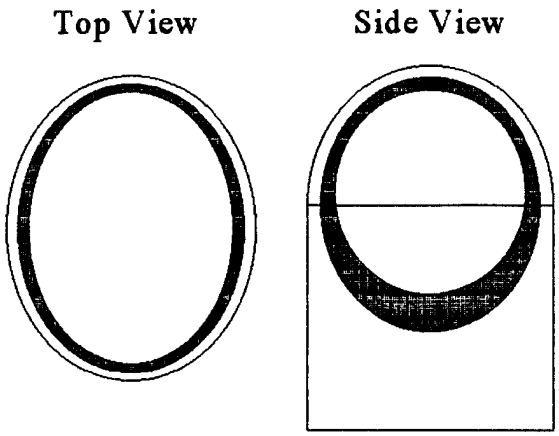

Figure 6. 3 Top and side view of head phantom showing location and size of skull.

as two slightly non-concentric ellipsoids (Figure 6.3). The homogeneous flesh tissue was used inside and outside the skull. Ring detectors were placed outside the walls, ceiling and floor and inside the room, 20 cm on either side of isocenter on the body axis (gantry detectors)

Table 6.5 shows the differences in exposure. Note, in particular, the positive and negative-y results: their difference is much smaller than the error. Appendix C, Figures C.1 through C.8 show the normalized spectra (without the roentgen conversion) obtained

Table 6. 5 Comparison of Bone-In to No-Bone Detector Tallies

Position	Bone		No Bone		Diff, %	Within Error?*
	Detector Tally, Rs^{-1} particle^{-1}	Error, %	Detector Tally, Rs^{-1} particle^{-1}	Error, %		
Pos x	8.171E-18	10.3	1.028E-17	11.1	20.54	N
Neg x	6.090E-18	12.1	7.390E-18	12.9	17.58	Y
Ceiling	5.215E-18	10.3	5.373E-18	8.1	2.95	Y
Floor	3.180E-17	7.0	3.596E-17	7.9	11.58	Y
Pos y	5.146E-20	25.3	4.836E-20	18.6	6.41	Y
Neg y	2.109E-20	23.9	2.140E-20	17.7	1.43	Y
Neg gantry	8.705E-16	0.8	1.388E-15	0.7	37.28	N
Pos gantry	1.230E-15	0.5	1.822E-15	0.6	32.50	N

* Within error criteria: Do the error bars overlap?

for each of the detectors comparing the results for bone-in and no-bone. The error bars in Figure C.1 shows that the difference falls within error. The only spectra that show noticeable differences are the gantry detector tallies, Figures C.7 and C.8, but they are *inside* the room and the interest in this thesis is the dose *outside* the walls. Since the difference in the area of interest (inside the room) is insignificant the skeleton was not included in the phantom.

6.3.2 CT Detector.

Proper modeling of the CT detector was critical. Any direct X rays penetrating through or not impinging on the phantom had to hit the detector. According to manufacturers specifications, the detector is a 99% absorber (GE, 1991). As described earlier, third and fourth generation scanners use either ionizing gas (xenon) or solid

scintillation detectors. Dr. Stanley Fox, CT Marketing, General Electric, verified that the Hi-Speed Advantage CT scanner at WPMC uses a solid state detector, but he could not reveal its exact composition since the information is proprietary (Fox, 1995). Susan Poteat, in WPMC's radiation safety office, confirmed that cadmium tungstate ($CdWO_4$) was a possible candidate. The CRC Handbook of Material Science (Lynch, 1975), however, did not list a density for this material. Based on the densities of carbon tungstate and several cadmium compounds, an approximate density of 7 g/cm^3 was tested. Measurement of the detector array unit in WPMC's CT indicated the array was no thicker than five cm. An MCNP run was prepared, therefore, with a five cm thick, one meter long, 110 cm radius detector composed of cadmium tunstate with a density of 7 g/cm^3. An air filled cell was placed immediately behind the detector cell conforming to its shape. The number of tracks entering the detector cell and the adjacent cell were compared (see Appendix B, Section II, "photon activity in each cell"). With the exception of some minimal backscatter, the tracks entering the air filled cell could only come from the detector cell, thus, the absorption percent could be determined for the composite source. The absorption of the detector was 99.7%.

6.3.3 Exposure Tallies and Spectra.

With the information from the above tests, a complete set, consisting of 32 beam positions, was run with MCNP for the CT unit in the X-ray room (with 1/16" lead shielding) as described by Metzger (Metzger, 1993). Appendix D, contains the exposure tallies by beam position and normalized average spectal plots (with the roentgen conversion

removed). The beam positions are labeled "Pt XX" where XX is the truncated beam position angle, i.e. 11.25 degree beam angle = Pt 11, 33.75 degree beam angle = Pt 33. The exposure tally at each detector from each beam position (with error bars) and the mean (with its error) are shown in Figures D.1 through D.7, Figures D.8 through D.10 show average spectral plots for each detector location. The source detector specta shows that the source spectrum was maintained at 30 cm. These exposure and spectral results for the X-ray room could be generalized to a CT positioned parallel to the walls assuming the results were appropriately weighted to account for room size and variations in shielding. From these results, some general trends were observed showing the combined effects of detector and beam position.

6.3.3.1 Tally Detector Location.

Figure 6.4 shows a representative scatter survey for the GE HiSpeed Advantage CT scanner (GE, 1995). As expected, the dose is not isotropically distributed. The same general behavior was expected in the MCNP runs. The MCNP results show similar behavior about the on-axis direct beam position or all positive and negative sets of results. Next, although the negative-x and positive-x axis detector mean exposures are approximately equal (Appendix D, Figures D.1 and D.2), the mean exposure of the positive-y axis detector is greater than the negative-y axis detector (Figures D.3 and D.4). This is due to the positive-y detector being located closer to the source than the negative-y detector. The positive and negative-y axis results display, however, the same behavior, i.e. no real dependence on source position. The floor mean exposure is greater than the ceiling

mean exposure, again, because it is much closer to the source. The floor and ceiling results, like the x-axis results, display a very marked dependence on source position, but again, they are similar about the on-axis direct beam position (Figures D.5 and D.6). Figure D.7 shows the uniformity in the source detector exposure as a function of beam position.

Although an attempt was made to make the geometry identical for all beam positions, problems were encountered with the 90° and 270° source beam positions. The geometry utility within MCNP for these two beam positions was detecting a surface within the CT detector that caused it to consider a portion of the detector to be undefined, and thus "lose" particles in this undefined area. To clear this fault, the detector for only these two points was split into two adjacent cells with the same total volume, position and shape. This, in turn, produced another undefined region where the gantry shielding and detector met. To solve this problem, the gantry shield for both beam positions was changed from a 65 cm inner-radius cylindrical shell to a 68 cm inner-radius cylindrical shell. It appears that increasing the radius of the gantry shielding allowed an opening through which particles leaked. Since MCNP forced these changes, they could not be immediately corrected. In addition, note that the ceiling and floor exibit very high central peaks. It was suspected that a problem in MCNP caused only these irregular peaks. Source positions were analyzed 0.5° and 0.01° from the 90° and 270° beam positions. The results from these additional runs more closed matched the beam position dependance seen for the positive-x and negative-x tally results. It is likely, therefore, that the exposure results for 90°

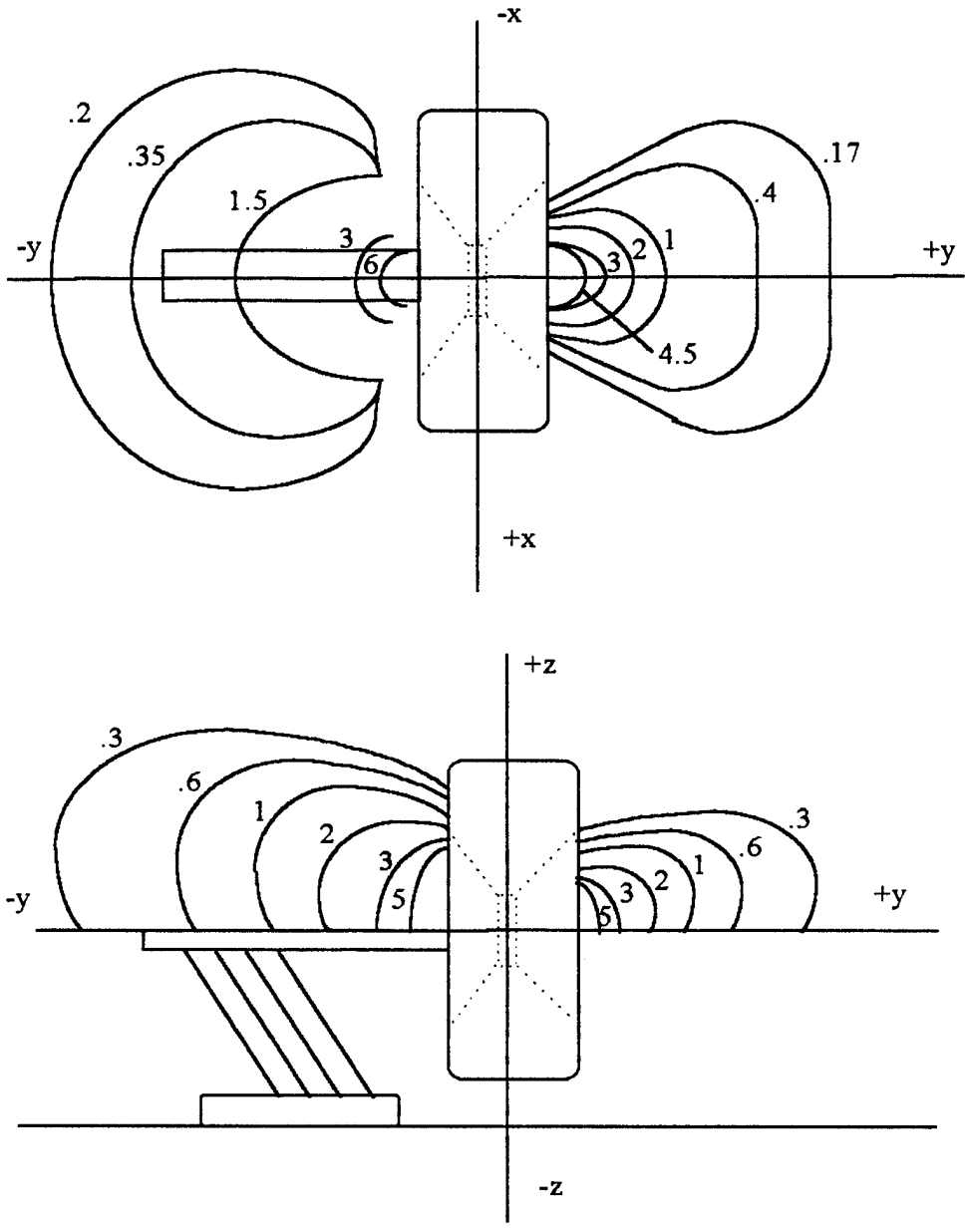

Figure 6. 4 Typical scatter survey of the GE HiSpeed Advantage scanning a body phantom, units are mrem/scan, but should be used for comparison as relative. The values would change as the phantom is changed, but characteristic contours remain the same.

and 270° beam positions for the floor and ceiling tally detectors are unreliable, thus, they were removed where suspect. Where possible, the 0.5 and 0.01 results were inserted.

6.3.3.2 Summary.

In general, the x-axis, floor and ceiling exposure tallies in the remaining analysis configurations are expected to be strongly dependent on beam position, particularly those on and near the on-axis direct beams. The y-axis exposure tallies will be much more uniform. Since anomalous results appear at exactly the 90° and 270° beam positions, they were deleted where suspect. More in-depth analysis of exposure and spectral behavior follows in Chapter 7 with the discussions of the other configurations.

7. Results

Three different room configurations were modeled: inside and outside the CT suite at WPMC, and outside the GE minimum recommended CT suite. Both a head and abdomen scan were modeled inside the suite at WPMC. The results from inside were compared to the results from film badges that were placed in the suite for a two week period. Head and abdomen scans were modeled for the dose outside the CT suite at WPMC with 1/16" and 1/8" lead wall shielding. Only a head scan in the GE minimum recommended room with 1/16" lead wall shielding was model, with the WPMC results for abdomen and 1/8" shielding extended to the GE results.

7.1 Validation: Film Badges Inside WPMC CT Suite

To validate the modeling effort and MCNP's results, radiation film badges were exposed during normal operation within WPMC's CT suite from 14 to 28 August 1995. The reported dose equivalent (in mrem, for deep, eye and shallow tissue) was compared to the results of an MCNP run modeling the location of the film badges for both a head and abdomen slice. Twelve film badges were placed on the source, body and x and y-room axes (one at each location, 8 total) and on the ceiling and floor (two at each location, 4 total), see Figure 5.4. The duplicate badges on the floor and ceiling were used to verify the precision of the reported badge measurements. To speed computation, the suite was modeled with no walls. This was valid since test runs had shown that backscatter from the walls into the room was less than 1%. The results from inside the suite were used as a standard for later analyses.

7.1.1 Comparison.

Before comparing the film badge results to the MCNP results, note some general behavior that relies solely on distance from isocenter. The floor badges were about one meter below isocenter and the ceiling badges about two meters above. The floor dose, therefore is expected to be about four times larger than the ceiling dose (using the inverse squared law for distance). Since the positive and negative sides of the rooms were about equidistant from isocenter, the badge results for the positive and negative source should be about equal. The same should be seen for the x-room axis badges. The y-room and y-body axes results cannot be compared simply by distance since the presence of the patient affects the results. With the exception of the negative x-room axis badge and the higher floor badge results, these relationships were, in general, as expected.

Table 7.1 shows the results from the MCNP runs for the head and abdomen scans using Eq. (6.4) to determine effective dose. The average weekly current workloads were 3980 mA-min per week and 10913 mA-min per week for the head and abdomen scans, respectively, which differed from the 4534 mA-min per week and 11468 mA-min averages seen in Table 6.2. Table 7.2 presents a comparison of the badge to MCNP results. Note, first, that although the two measured ceiling doses were equal, the floor doses differed significantly. This difference was used to assign a 15% uncertainty in the precision of the badge results. The wall badges were located about four feet above the floor with, unfortunately, the potential of being blocked sometime during the 15 day exposure period, by the carts, tables and miscellaneous accessories located around the room. It was reported by the medical technician that the badges on the negative and positive x walls were likely

Table 7. 1 MCNP Results from Inside the CT Suite at WPMC

	Exposure by Scan Type, $R s^{-1}$ particle^{-1}				Effective dose, mrem*		
	Head	Fractional Error	Abdomen	Fractional Error	Head	Abdomen	Total
Source, +x	4.77E-18	0.0223	3.64E-18	0.0105	16.7	34.9	51.5
Source, -x	5.95E-18	0.0264	4.73E-18	0.0111	20.8	45.3	66.1
Body, +y	2.24E-17	0.0076	7.54E-18	0.0128	78.3	72.2	150.5
Body, -y	2.76E-18	0.0545	2.08E-18	0.0072	9.6	20.0	29.6
Room, +x	3.85E-17	0.0102	3.63E-17	0.0049	134.6	347.5	482.1
Room, -x	2.74E-17	0.0096	1.18E-17	0.0058	95.6	112.8	208.4
Room, +y	2.58E-17	0.0091	1.33E-17	0.0103	90.1	127.7	217.8
Room, -y	3.37E-18	0.0455	4.83E-18	0.0153	11.8	46.3	58.1
Ceiling	2.59E-18	0.0618	2.34E-18	0.0319	9.0	22.4	31.4
Floor	2.13E-17	0.0360	1.25E-17	0.0266	74.3	119.3	193.6

*Effec dose = Relative x 0.1068(Gy/mA-min)/0.00868(R/Gy) x Current(mA-min/wk) x 2(wk) x 1000(mrem/rem) x 0.01(rem/R)

Table 7. 2 Comparison of Film Badge and MCNP Results Inside WPMC CT Suite

Badge Number	Location	Badge Effective Dose, mrem	MCNP Effective Dose, mrem	Badge / MCNP
11	Source, +x	30	51.5	0.58
8	Source, -x	30	66.1	0.45
5	Body, +y	150	150.5	1.00
4	Body, -y	20	29.6	0.68
1	Room, +x	90	482.1	0.19
2	Room, -x	0	208.4	-
6	Room, +y	230	217.8	1.06
3	Room, -y	60	58.1	1.03
9	Ceiling	60	31.4	1.91
12	Ceiling	60	31.4	1.91
7	Floor	320	193.6	1.65
10	Floor	250	193.6	1.29

Effective Dose=Relative x Aver Air Kerma(0.1068 Gy/mA min)/0.00868(R/Gy) x Current(3980 or 10920 mA min) x 2 wks x 1000(mrem/rem) x 0.01(rem/R)

blocked for some or all of the 15 days. Note that the negative x-room axis badge dose was zero and that the positive x-room axis badge and MCNP doses differ significantly. With these exceptions, the reported badge doses were within a factor of two of the MCNP results, some greater, some lesser.

7.1.2 Baseline Results.

The MCNP results from inside the CT suite in WPMC suite were used as a standard against which the remaining analyses were compared because they show the scattered spectrum and dose as a function of only the CT unit. Appendices E and F contain the exposure (by beam position) and spectral plots obtained for the head and abdomen scans, respectively. The head scan results are used to describe the exposure and spectral differences. They are then compared to the abdomen exposure and spectral results.

7.1.2.1 Exposure.

The exposure tallies as a function of beam position for each tally detector location illustrate two effects on the exposure behavior as the source is rotated: (a) the position/direction of the beam relative to the tally detector, i.e. the beam pointing directly at or away from the tally detector and (b) the cross sectional area of the target (head) being scanned. Figure 7.1 shows a sample exposure plot with error bars, mean and mean error.

The x-z plane exposures (+/- x-source axes, Figs. E.1 and E.2, ceiling, Fig. E.9, and floor, Fig. E.10) illustrate effect (a). They show a dramatic increase in contribution from beam positions directed at the tally detector. The twin-peaked response seen in the source axes and floor exposure are caused by photons scattering around the CT detector

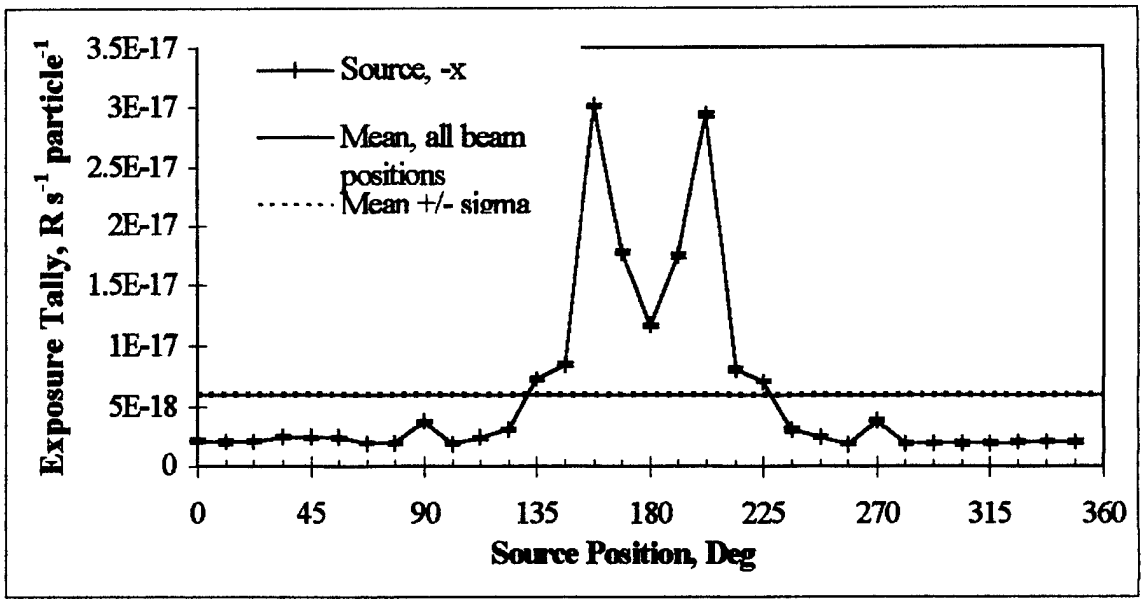

Figure 7. 1 Example of exposure tally (by beam position) plot. Direct beam from 180° beam position.

with minimal absorption by the gantry shielding (see Figure 7.2). The ceiling exposure behavior differs from the source axis and floor exposures with a central peak. Since the ceiling is much farther away from the source than the floor, the scattered photons have a greater opportunity to scatter back toward the tally detector (see Figure 7.3).

The effect of target size is seen in the positive and negative y exposures (Figures D.5 and D.6). The Pt 90 and 270 beam positions, directly below and above the head, respectively, strike the narrowest target cross-section, thus less head scatter and a lower exposure (see Figure 5.5). Recall that 99.7% of the beam missing the head is absorbed by the CT detector. The negative y-body axis exposure does not have as large of a variation as the beam rotates since the majority of the body is along that axis which is an additional source of absorption.

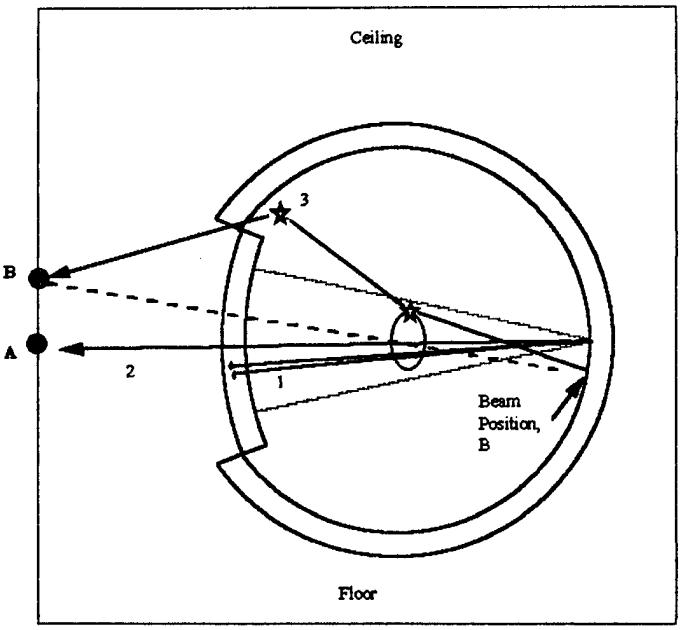

Figure 7. 2 Possible scattering mechanisms producing peaks from off axis beam positions : (1) shows photons stopped by the CT detector. (2) shows a direct contribution to tally detector A from the axis beam. (3) shows a possible scattering path that would result in a greater exposure at tally detector location B (its position shown relative to the source location) from off-axis beam positions.

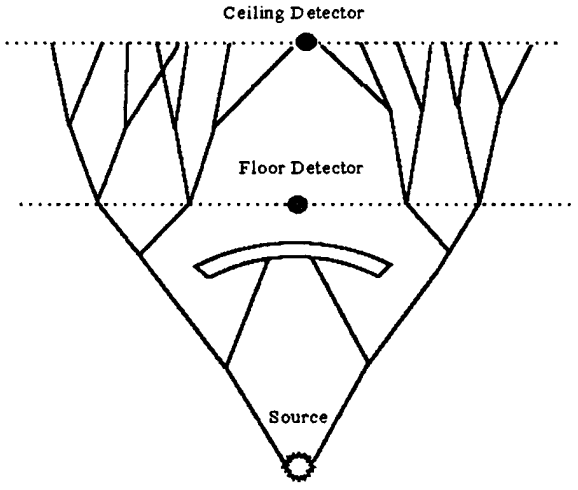

Figure 7. 3 As photons travel away from the source, they are scattered across a wider area with the CT detector blocking some of the scattered photons. Since the ceiling is a greater distance from the source, the photons are more able to scatter back towards a tally detector located opposite the source.

The exposure at tally detectors located on the room axes (Figs. E.3, E.4, E.7 and E.8) inside the CT suite, like the y-room and y-source axis results, shows only target size effects. They show means and variations in amplitude similar to the y-room and y-source axis results. The relative mean exposures compare well with the typical scatter survey (Figure 6.4).

7.1.2.2 Spectral Results.

D. Simpkin (Simpkin, 1995), identified the lack of patient scatter spectra from CT units since available test equipment was unable to measure the high flux inside the room (Simpkin, 1995). MCNP bins the tally by user specified energy intervals thus providing the scattered spectrum. The conversion to Roentgens was removed from the average spectra in Appendix E and the resulting spectra normalized to one. First, observe that although the individual tally detector locations' exposure tally means and behavior are quite different inside the CT suite, they all have very similar spectra (Figs. E.12 through E.17) from 10 to 70 keV. Above 70 keV, however, the x-z plane tally detectors spectra exhibit a larger value at the higher energies. In addition to the mean spectrum, Figs. E.11, E.12, E.16 and E.17 contain additional spectra from beam positions directed at or nearly at the tally detector. They exhibit a noticeable increase in the higher energy ranges, particularly those adjacent to, but not on, the axis. (All of the other beam positions mimicked the average.) Recalling the scattering mechanisms described above (Figures 7.1 and 7.2), the higher energy humps are clearly from photons passing through the CT detector and gantry with little attenuation.

Next, observe the sharp spikes at 24 and 28 keV in the average and individual specta as seen in Fig. E.11 or E.12. These are fluorescent peaks from the cadmium tungstate CT detector. The 24 keV spike is from the L_1 to K shell transition of cadmium and the 28 keV spike is probably from summed X rays resulting from the de-excitation cascade. Sharp spikes are also seen in the lowest energy bin containing 0-10 keV. They are the fluorescent peaks from the intermediate shell transitions and from low Z elements in the problem, primarily aluminum (used for the gantry shields). Remnants of the source spectrum's peaks at 60 and 68 keV are also seen.

Last, a spectral shift is referred to as either *hardened* or *softened.* Removing the lower energy components results in a hardened spectrum , that is, one with a greater average energy, and removing the higher energy components results in a softer spectrum, one with a lower average energy. Figure 7.4 shows that the source spectrum, upon scattering off the phantom was softened slightly, with the maximum shifted approximately 10 keV.

7.1.2.3 Head vs Abdomen.

Appendix F contains the exposure and spectral plots from the MCNP run inside the CT suite at WPMC for an abdomen scan. Different exposure behaviors were expected from the abdomen because the target is considerably different.

First, although the MIRD phantom's abdomen and head x-z plane cross sections are both elliptical, the major and minor axes are opposite. The variation with source angle seen with the head slice from relative target thickness should be opposite that of the head scan. This, however was not seen (see Figs. G.3 and H.3). *Second*, the abdomen is much

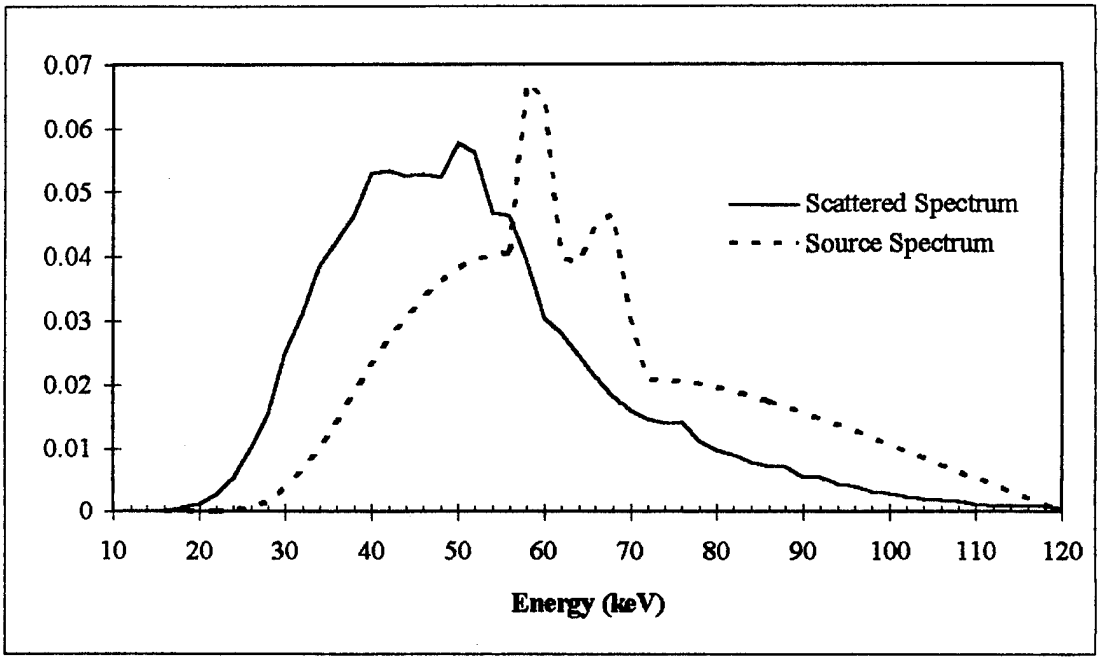

Figure 7. 4 Scattered spectrum vs source spectrum.

thicker than the head in the x direction (14 cm vs 40 cm). The contribution to the x-axis tally detectors opposite the 0° and 180° beam positions should, therefore, be reduced. Figure 7.5 shows a representation of the x-source axis tally detectors for the abdomen scan. The reduction can be seen in Figs. F.1, F.2, F.9, and F.10 when compared to the analogous head scan figures in Appendix E. Tissue, however, a primarily low-Z material, is not as strong absorber as, say, lead or cadmium tungstate, so there is not a large reduction.

Third, the surface of the target being irradiated is considerably closer to the 0° and 180° beams and thus closer to the tally detectors *behind* these beams. Recalling that a fluence tally computed in MCNP is a function of distance and weight, this surface radiation may contribute more to the exposure tally when the beam is directed *away* from the tally

detector (see Figure 7.5). Associated with this is a possible increased effect from the rotation of the phantom and CT unit about the z axis. The position where the phantom receives maximum radiation will be closer to the negative y tally detector when the beam position is 0° and conversely, closer to the positive y tally detector when the beam position is 180°. The results illustrated in Figure 7.5 for the positive x- and y-room axes exposures are seen in Figs. F.3 and F.7: the maximum occurred when the beam was directed *away* from the tally detector. The second part of this expectation is seen in Figs. F.7 and F.8. The maximum is seen at 0° for the negative-y tally detector and at 180° for the positive-y tally detector.

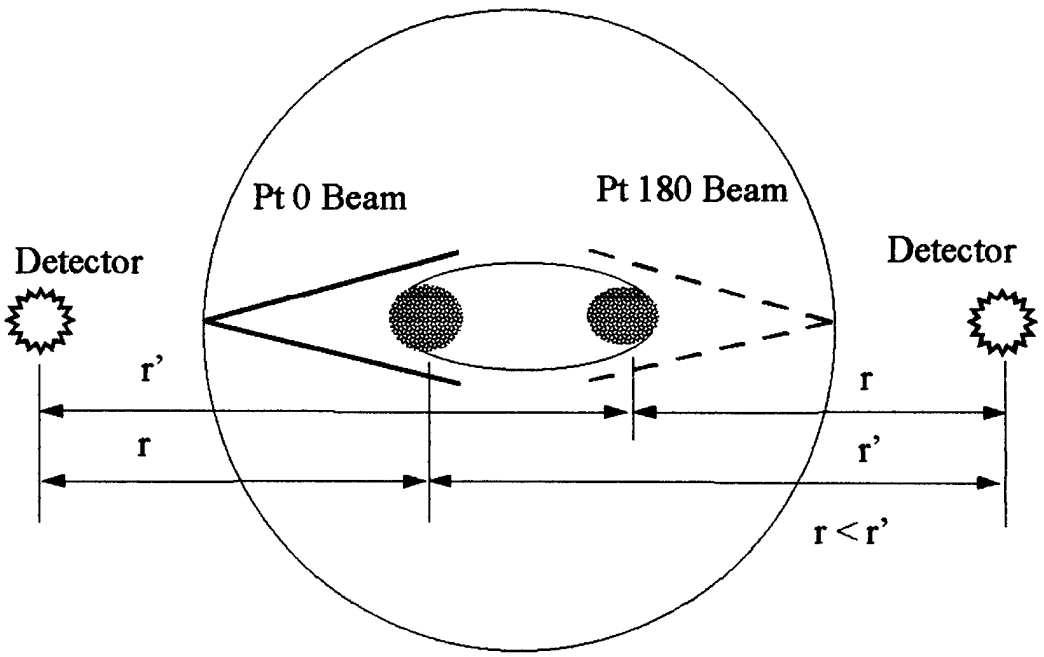

Figure 7. 5 Effect on exposure as a function of distance to radiated area.

Fourth, the beam positions adjacent to the on-axis positions (i.e. Pts 11 and 22 adjacent to Pt 0) should still exhibit the sharp rise in exposure. The maximum, however, may come from a position further from the on-axis position than noted with the head scan because, referencing Figure 7.2, to maintain the nearly straight line sequence of interactions from source to tally detector, the source would need to be further from the on-axis position to get around the wider abdomen. Figs. F.1, F.2, F.9 and F. 10 show this change. The exposure from the off-axis beam positions closest to the on-axis positions (Pts 11, 168, 78 and 258, respectively) are reduced.

Fifth, the phantom is approximately centered longitudinally on isocenter during an abdomen scan. Differences noted before between the positive- and negative-y axes (room and body) should be reduced. The negative-y tally detectors, however, are still about twice as far from isocenter as the positive tally detectors, so, greater average exposures from the positive direction are still expected. The positive and negative mean exposures are closer than seen with the head scan. In addition, the change in exposure as the beam rotates is more obvious in the negative-y-body and room tally detector tallies (Figs. F.6 and F.8).

All of the above differences were present simultaneously for all tally detectors. Some dominated leaving the others virtually unnoticeable.

A problem in the CT model was found as the data was being analyzed. A fixed fan-beam angle of 35° was used throughout the analysis. However, along its major axis, the abdomen subtends a slightly wider angle (37°) than the fan-beam angle. This means that at the 90° and 270° beam positions, no portion of the beam will go past the phantom directly to the CT detector. The most noticeable effect expected is a reduction in the contribution to exposure from the beam positions adjacent to the on-axis beam positions

(Pts 11 and 348 for the Pt 0 on-axis beam position). Another effect may be a flattening near the 90° and 270° points in exposure variation for the ceiling and floor tally detectors. This mistake is not expected to contribute significant error to the results.

The differences in the spectra between the head and abdomen scans for all tally detector locations was insignificant as can be seen by comparing Figs. F.11 through F.15 to their counterparts in Figs. E.11 through E.15. Therefore, the spectra outside the walls should also be comparable for the head and abdomen scans. The similarity in the spectra leads to the supposition that, when the shielded walls are added to the scenario, similar changes to the head and abdomen scans should be noted. For example, the difference between doses at a given tally detector from a head scan to an abdomen scan will decrease by the same factor for the 1/16" lead shielded room and the 1/8" lead shielded room at the same tally detector. That is, the head-to-abdomen dose ratio will be the same outside either room.

7.1.3 Modifications.

The results from inside the CT suite at WPMC drove modifications in subsequent runs. The most significant change was eliminating the analysis of some tally detector locations for certain beam positions. The exposure was expected to decrease across the board as the shielded walls were added because of the similarity of their spectra. Note, for example, the exposure by beam position plot for the positive x-source axis tally detector (Fig. E.1). The only significant contributions to the total exposure were from the beam positions from Pt 0 to Pt 101 and from Pt 258 to Pt 348. Thus, the positive x-source axis exposure was not computed for the beam positions from Pt 112 to Pt 247. When the

exposure displayed uniform behavior at all beam positions, like the negative y-body axis exposure (Fig. E.6), only a few beam positions were analyzed. Conservation of computer resources was the primary motivation for this reduction in exposure computations. Table 7.3 lists the exposures that were computed for each beam position. Comparison with the exposure plots in Appendix E explain the choices that were made. Prior to completion of the runs inside the suite, runs were started for the analysis outside the suite, thus, extra exposure data points are included in some plots. As described in Section 6.1.3, the exposure tallies and errors that remained were weighted appropriately.

In addition, a need was determined for additional beam positions near the exposure maximums to better define exposure behavior and thus exposure mean. However, time constraints caused by limited computer resources prevented their analysis concurrent with the results presented here.

The results also raised questions about exposure behavior between and around the selected tally detector locations. The concern whether the true maximums were indeed at the source and room axes locations was investigated by placing tally detectors at 50 cm intervals in the positive- and negative y direction in line with the existing tally detectors. This was accomplished for the analysis of the CT suite in WPMC for the positive and negative x walls. Those results, shown in Figure 7.6, indicate that there is indeed a "hot spot" not sampled exactly at the source or room axis tally detectors. The negative x wall displayed a maximum 20 cm from the source axis tally detector and the positive x wall displayed a maximum 10 cm from the source axis tally detector. The existence of these hot spots may indicated the existence of others that were not sought out.

Table 7. 3 Modified Exposure Tallies by Beam Position

Beam Position	0	11	22	33	45	56	67	78	90	101	112	123	135	146	157	168
Source, -x											X	X	X	X	X	X
Source, +x	X	X	X	X	X	X	X	X	X	X	X					
Body, +y	X		X		X	X	X	X	X	X		X		X		X
Body, -y								X	X	X						
Room, -x	X	X	X	X	X	X	X	X	X	X	X	X	X	X	X	X
Room, +x	X	X	X	X	X	X	X	X	X	X	X	X	X	X	X	X
Ceiling						X	X	X	X	X	X	X				
Floor																
Room, +y			X		X		X	X	X	X	X		X		X	
Room, -y	X								X							
Beam Position	**180**	**191**	**202**	**213**	**225**	**236**	**247**	**258**	**270**	**281**	**292**	**303**	**315**	**326**	**337**	**348**
Source, -x	X	X	X	X	X	X	X	X	X	X	X					
Source, +x							X	X	X	X	X	X	X	X	X	X
Body, +y		X		X		X	X	X	X	X	X	X	X	X	X	X
Body, -y								X	X	X						
Room, -x	X	X	X	X	X	X	X	X	X	X	X	X	X	X	X	X
Room, +x	X	X	X	X	X	X	X	X	X	X	X	X	X	X	X	X
Ceiling																
Floor			X	X	X	X	X	X	X	X	X	X	X	X	X	
Room, +y	X		X		X	X	X	X	X	X		X		X		X
Room, -y	X								X							X

7.2 WPMC CT Suite

The main objective of this thesis was to determine the dose outside the walls of the CT suite at WPMC to determine if its shielding met the recently revised requirements for non-occupational dose in 10CFR20. The following results deal directly with that issue. The suite was modeled alternately with 1/8" lead shielding and 1/16" lead shielding in the walls. The Monte Carlo simulation was conducted for both a head scan and an abdomen

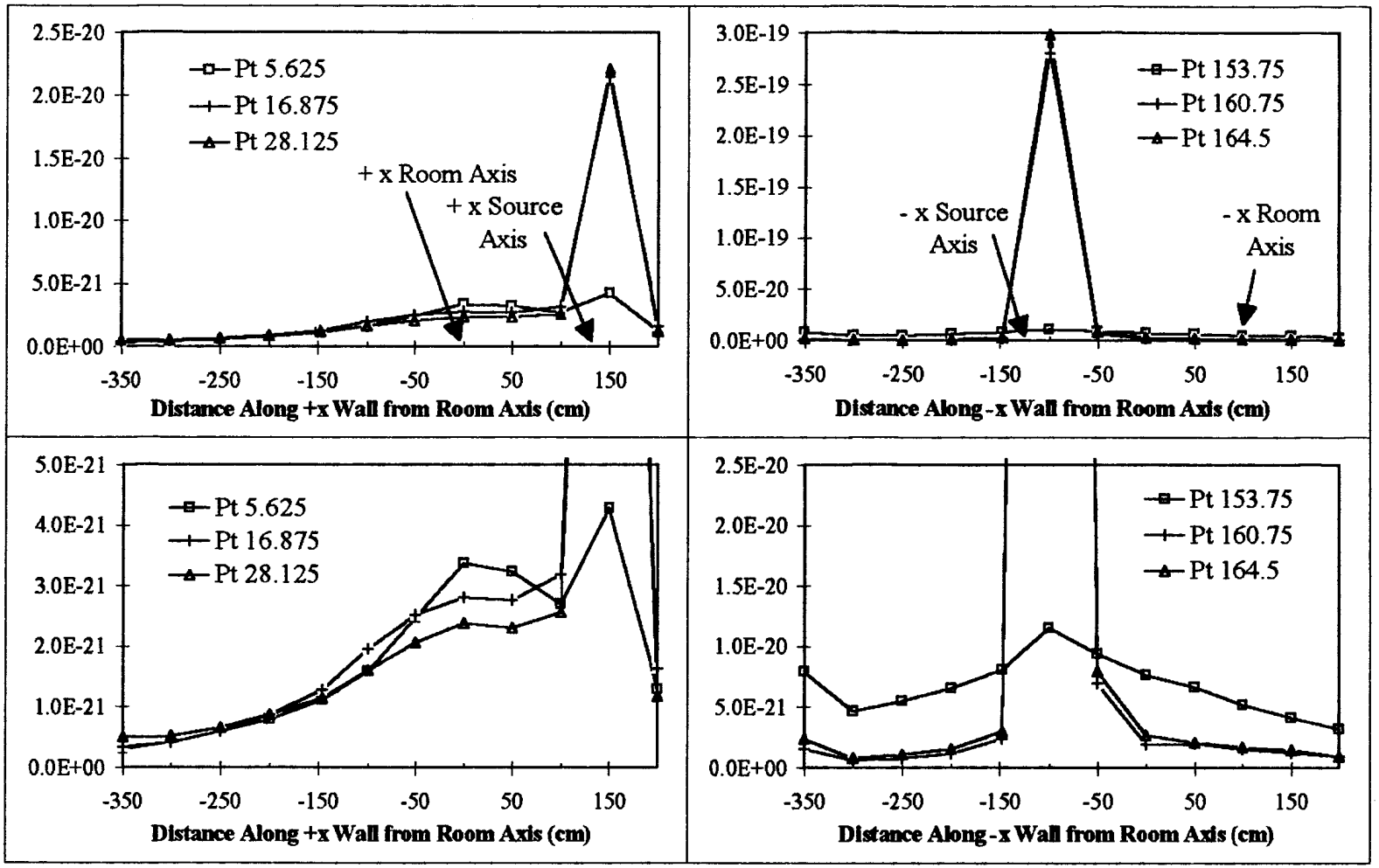

(a) (b)

Figure 7. 6 Exposure outside of and along the (a) positive x wall and (b) negative x wall. They show maxima at (a) +150 cm from the wall axis and (b) -100 cm from the wall axis. The lower plot is an expanded view of the upper plot.

scan at 10 locations outside the walls for selected beam positions. The weighted average exposure for the head and abdomen scans were totaled to obtain the dose at each tally detector location.

7.2.1 1/16" Lead Shielding.

The CT suite at WPMC was modeled with 1/16" lead shielding for both head and abdomen scans. The exposure plots (by beam position) and normalized spectral results (with Roentgen conversion removed) are in Appendices G and H. The exposure behavior of the head and abdomen scans are as expected: diminished considerably in magnitude and starting to lose some structure as a function of source positions when compared to the exposure tallies from inside the suite. Recall that the largest exposures (on- and near-axis beam positions directed at the tally detector) had a high energy component in their spectrum. The lead shielding absorbed most of that, and, since the total exposure tally is effectively an integration of the spectrum, the peaks with the high energy component were reduced relatively more than the other beam positions in the scan. In particular, compare Pt 22 for the positive x-source axis in Fig. E.1 with the same beam position in Fig. G.1. More than half of its spectrum was above 80 keV for this particular point (Fig. E.11), which has all been removed by the room shielding. A similar comparison of Pt 157 in Figs. E.2 and G.2 reveal the same effect as do Pts 78 and 258 for the ceiling and floor exposures, respectively, in Figs. E.9, E.10, G.9, and G.10. The same effects are noted with the abdomen exposure plots. The smooth variation seen in the y-axes tally detector exposure plots is starting to disappear with the addition of the lead shielding (compare Fig.

E.3 to Fig G.3 and E.5 to G.5). The exposure plots showing a uniformity for all beam positions have maintained their uniformity (compare Fig. E.8 to Fig G.8). In addition, note that as the mean went down, so did the spread in the individual exposure values. Compare Fig. E.5 with a mean of 2.3×10^{-17} and spread of about 1×10^{-17} to Fig. G.5 with a mean of 1.5×10^{-20} and a spread of about 1×10^{-20}.

Dramatic spectral differences are noted between the spectra outside and inside the CT suite. This was expected since lead shielding is chosen to reduce the higher energy photons, i.e. modify the spectrum. First, note that the spectra for the head and abdomen scans were indistinguishable (Figs. G.11 through G.15 and H.11 through H.15). Next, observe that the wall spectra (G.11 thorough G.14) are abruptly cut off near 90 keV. Comparison with the attenuation cross-section for lead (Figure 2.7) shows the K-edge at 88 keV which effectively attenuates the entire CT spectrum above that point.

7.2.2 1/8" Lead Shielding.

The CT suite at WPMC was next modeled with 1/8" lead shielding for head and abdomen scans. The exposure and spectral results are in Appendices I and J. The exposure plots for the head and abdomen are as expected: further diminished in magnitude and structure. Once again, the largest individual exposures (from beam positions directed at or nearly at the tally detector) which had a high energy component in their spectrum inside the room are reduced relatively more than the other beam positions in the scan. Compare now Pt 11 for the positive x-source axis in Fig. G.1 with the same beam position in Fig. I.1. A similar comparison of Pt 168 in Figs. G.2 and I.2 reveal the same effect.

The slight variation left in the 1/8" lead shielded room seen in the y-axes tally detector exposures has almost completely disappeared (compare Fig. G.3 to Fig I.3 and G.5 to I.5). The exposures that were uniform for all beam positions have again maintained their uniformity (compare Fig. E.8 to Fig G.8).

The spectral differences between the 1/16" and 1/8" shielded rooms are not as pronounced as those noted between the spectra outside with 1/8" lead shielding and inside the CT suite, however, there are some differences. First, however, note that the spectra for the head and abdomen scans were again indistinguishable (Figs. I.11 through I.15 and J.11 through J.15). Each spectrum now displays a softer spectrum compared to the 1/16" lead shielding spectra. The energies near 88 keV have been reduced more extremely, allowing the energies between 40 keV and 70 keV to appear larger by comparison.

7.2.3 Dose.

Table 7.4 contains the calculated dose outside the CT suite at WPMC for 1/16" and 1/8" lead shielding for the head and abdomen scans and their total. The dose was calculated using Eqs. (6.1), (6.2) and (6.4). Recall that the annual dose limits required by 10CFR20 were 1 mSv (non-occupational, continuous exposure), 5 mSv (non-occupational, infrequent exposure) and 50 mSv (occupational). The ratio of tissue to air mass energy absorption coefficients was used to convert of these results in units of Gray to units of Sieverts as discussed in section 2.8.6. Both the 1/8" lead shielded and 1/16" lead shielded rooms were modeled: first, for completeness and second, because the CT suite at WPMC has 1/8" lead shielding in the walls adjacent to public areas (negative x and positive

y walls) and 1/16" lead shielding in the walls adjacent to the occupational areas (positive x and negative y walls). Therefore, non-occupational dose is indicated in the positive y and negative x-room and x-source tally detector locations. The occupational dose is indicated in the negative y and positive x-room and x-source tally detector locations.

With these guidelines, the only tally detector locations that exceed the non-occupational dose limits are the ceiling and floor. Since the badge results showed an underestimation by the Monte Carlo simulation inside the room, one of two conclusions must be drawn: (a) the dose above the ceiling and below the floor is unacceptable by 10CFR20 standards or (b) the concrete shielding was insufficiently modeled. Recall that six inch slabs of concrete were placed in the ceiling and floor. The floor and ceiling of WPMC, however, have, in addition, two-inch thick waffle-weave concrete above and below the slab. As a worst case scenario (and to conserve computer resources) this additional concrete was not modeled. It would have contributed to the floor and ceiling attenuation, but, the exact amount is not presently known.

Table 7.4 shows that the occupational dose limit of 50 mSv is met at all tally detector locations. The floor and ceiling exposures are significantly higher than the rest, but still, well below the 10CFR20 dose limits.

7.3 General Electric Minimum Recommended Room Size

The product data sheet accompanying the GE HiSpeed Advantage Scanner System recommended a 13' x 19.5' (397 cm x 596 cm) exam room with a 9' (274 cm) ceiling. A drawing of the configuration showed isocenter 183 cm from the negative x wall and 213

Table 7. 4 Results for the CT Suite in WPMC for 1/16" and 1/8" Lead Shielding

WPMC, 1/16" Lead Shielding						
Detector Location	Head		Abdomen		Total	
	Annual Tissue Equivalent Dose, mSv	Fractional Error	Annual Tissue Equivalent Dose, mSv	Fractional Error	Annual Tissue Equivalent Dose, mSv	Fractional Error[C]
Source, -x	0.453	0.079	0.797	0.098	1.251	0.063
Source, +x[A]	0.391	0.078	0.731	0.086	1.122	0.071
Body, +y	1.481	0.071	1.324	0.091	2.804	0.066
Body, -y[A]	0.125	0.176	0.142	0.102	0.267	0.152
Room, -x	2.787	0.059	4.281	0.075	7.069	0.054
Room, +x[A]	2.571	0.053	5.250	0.052	7.821	0.047
Ceiling[A]	0.787	0.057	1.043	0.046	1.830	0.050
Floor[A]	10.817	0.035	7.671	0.032	18.488	0.031
Room, +y	2.872	0.059	3.969	0.071	6.841	0.054
Room, -y[A]	0.429	0.117	1.200	0.086	1.630	0.102
WPMC, 1/8" Lead Shielding						
Detector Location	Head		Abdomen		Total	
	Annual Tissue Equivalent Dose, mSv	Fractional Error	Annual Tissue Equivalent Dose, mSv	Fractional Error	Annual Tissue Equivalent Dose, mSv	Fractional Error
Source, -x[B]	0.062	0.125	0.123	0.123	0.185	0.096
Source, +x	0.060	0.142	0.122	0.146	0.182	0.110
Body, +y[B]	0.108	0.109	0.212	0.121	0.321	0.085
Body, -y	0.018	0.124	0.046	0.128	0.064	0.096
Room, -x[B]	0.160	0.098	0.317	0.120	0.477	0.078
Room, +x	0.171	0.105	0.369	0.100	0.541	0.080
Ceiling[B]	0.740	0.077	1.285	0.068	2.024	0.059
Floor[B]	4.292	0.033	7.753	0.029	12.045	0.025
Room, +y[B]	0.178	0.095	0.355	0.111	0.533	0.075
Room, -y	0.033	0.199	0.085	0.182	0.118	0.151

[A]Detector locations applicable to occupational dose.
[B]Detector locations applicable to non-occupational dose.
[C]Error is weighted by usage factors.

cm from the positive y wall and with the unit rotated 21.86 degrees from the positive y-room axis towards the negative x-room axis. Except for the dimensions and angle of

rotation, the room is identical to the CT suite at WPMC with 1.4 cm drywall sheets on either side of the 1/16" and 1/8" lead and six inch concrete slabs at the floor and ceiling.

7.3.1 1/16" Lead Shielding with Head Scan.

Appendices J and K contain the exposure and spectral plots for the minimum room size recommended by GE for the HiSpeed Advantage CT. Since the exposure behaviors and spectra are very similar to those seen in the CT suite with 1/16" lead shielding, a detailed analysis will not be presented here.

7.3.2 Extension of WPMC Results.

The differences in average dose from the head to the abdomen scan and from 1/16" to 1/8" lead shielding for the CT suite at WPMC were extended to the results from the GE room with 1/16" lead shielding for the head scan. Figure 7.5 shows two paths for obtaining the GE room results for 1/16" abdomen, 1/8" head scan and 1/8" abdomen scan. Since the conversion factors are constants, both paths produce the same results. Table 7.5 shows the ratios seen for the WPMC suite exposures that were applied by source location and conversion type to the GE room results. Table 7.6 contains the derived tissue exposure results for the GE room. Table 7.7 contains the annual tissue dose equivalents for the GE room using the usage factors described earlier.

Again, the positive x and negative y tally detector locations are pertinent to the *occupational* dose and the negative x and positive y tally detector locations for the *non-occupational* dose. The results from the GE room show unexpectedly large doses at the

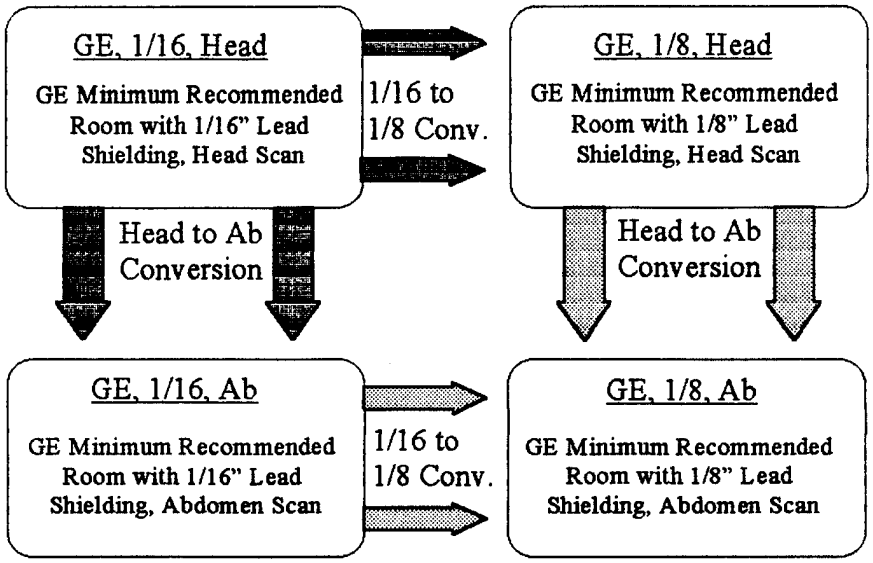

Figure 7. 7 Method of applying conversion factors to single Monte Carlo analysis of the GE room with 1/16" shielding to obtain the remaining results.

Table 7. 5 Ratios Between Exposures Outside the CT Suite at WPMC

Detector Location	Head to Abdomen Comparison				1/16" to 1/8" Comparison			
	1/16" Head: 1/16" Abdomen	Fractional Error	1/8" Head: 1/8" Abdomen	Fractional Error	1/16" Head: 1/8" Head	Fractional Error	1/16" Abdomen: 1/8" Abdomen	Fractio Erro
Source, -x	1.438	0.1128	1.269	0.1759	7.335	0.1458	6.473	0.149
Source, +x	1.352	0.1138	1.237	0.2039	6.549	0.1631	5.993	0.167
Body, +y	2.829	0.1156	1.289	0.1628	13.674	0.1300	6.231	0.151
Body, -y	2.236	0.1972	1.002	0.1783	6.892	0.2155	3.089	0.155
Room, -x	1.647	0.0954	1.273	0.1555	17.456	0.1147	13.493	0.141
Room, +x	1.238	0.0743	1.174	0.1448	15.007	0.1174	14.220	0.112
Ceiling	1.910	0.0612	1.457	0.1080	1.064	0.0961	0.812	0.071
Floor	3.567	0.0494	1.400	0.0442	2.520	0.0537	0.989	0.038
Room, +y	1.830	0.0921	1.268	0.1452	16.119	0.1118	11.173	0.130
Room, -y	0.905	0.1449	0.969	0.2683	13.156	0.2305	14.086	0.199

positive and negative wall-axes tally detectors. They are well above the limits set in 10CFR20 for the occupational dose and, even with the additional shielding, above the non-occupational dose limits. The floor, again, is above the non-occupational limit. It is, however, below the occupational dose limit. The positive and negative x-room and x-source exposures, particularly in the room with 1/16" shielding, were much greater, relatively, than the WPMC CT suite exposures. Recall that the differences between the rooms were size and angle of rotation of the CT unit. As seen before, room size, i.e. distance from isocenter, can have a significant impact on dose. It is also possible that the change in rotation picked up a "hot spot" not sampled in the WPMC scenario. Refer, for example, to Figure 7.6 showing the exposure variation at 50 cm intervals along the wall. The tally detector located -100 cm from the negative x wall axis shows one such hot spot. Similarly, the tally detector located +150 cm from the positive x-room axis has the same abnormally large exposure. These could indeed be points of excess radiation or they could show a weakness in how the CT unit (CT detector, shields, etc.) was modeled. That could only be determined by sampling additional tally detector locations and/or increasing the fidelity of the model.

Table 7. 6 Converted GE Room Exposure (R s^{-1} $particle^{-1}$)

GE Room, 1/16" Lead Shielding, Exposure				
Detector Location	Head	Fractional Error	Abdomen	Fractional Error
Source, -x	1.870E-19	0.032	1.300E-19	0.117
Source, +x	1.396E-19	0.034	1.033E-19	0.119
Body, +y	2.785E-20	0.077	9.845E-21	0.139
Body, -y	4.349E-21	0.112	1.945E-21	0.227
Room, -x	6.666E-19	0.022	4.048E-19	0.098
Room, +x	9.131E-19	0.019	7.373E-19	0.077
Ceiling	7.762E-21	0.062	4.065E-21	0.087
Floor	1.178E-19	0.029	3.301E-20	0.057
Room, +y	3.854E-20	0.079	2.106E-20	0.122
Room, -y	7.815E-21	0.153	8.634E-21	0.210
GE Room, 1/8" Lead Shielding, Exposure				
Detector Location	Head	Fractional Error	Abdomen	Fractional Error
Source, -x	2.549E-20	0.149	2.008E-20	0.190
Source, +x	2.132E-20	0.167	1.723E-20	0.205
Body, +y	2.037E-21	0.151	1.580E-21	0.205
Body, -y	6.311E-22	0.243	6.297E-22	0.275
Room, -x	3.819E-20	0.117	3.001E-20	0.172
Room, +x	6.085E-20	0.119	5.185E-20	0.136
Ceiling	7.294E-21	0.114	5.197E-21	0.113
Floor	4.674E-20	0.061	3.348E-20	0.069
Room, +y	2.391E-21	0.137	1.885E-21	0.179
Room, -y	5.941E-22	0.276	6.130E-22	0.290

Table 7. 7 Annual Tissue Dose Equivalent, GE Room

GE Room, 1/16" Lead Shielding			
Detector Location	Annual Tissue Dose Eqivalant, mSv		
	Head	Ab	Total
Source, -x	18.233	32.067	50.299
Source, +x[A]	13.616	25.472	39.088
Body, +y	2.716	2.428	5.145
Body, -y[A]	0.424	0.480	0.904
Room, -x	65.013	99.867	164.880
Room, +x[A]	89.051	181.868	270.918
Ceiling[A]	0.757	1.003	1.760
Floor[A]	11.489	8.136	19.363
Room, +y	3.759	5.195	8.954
Room, -y[A]	0.762	2.130	2.892
GE Room, 1/8" Lead Shielding			
Detector Location	Annual Tissue Dose Eqivalant, mSv		
	Head	Ab	Total
Source, -x[B]	2.486	4.954	7.439
Source, +x	2.079	4.250	6.779
Body, +y[B]	0.199	0.390	0.593
Body, -y	0.062	0.155	0.275
Room, -x[B]	3.724	7.402	11.620
Room, +x	5.934	12.790	18.761
Ceiling[B]	0.711	1.282	1.993
Floor[B]	4.559	8.260	12.818
Room, +y[B]	0.233	0.465	0.692
Room, -y	0.058	0.151	0.266

[A]Detector locations applicable to occupational dose.

[B]Detector locations applicable to non-occupational dose.

8. Summary and Discussion

The purpose of this thesis was to model a computerized tomography (CT) unit and suite using Monte Carlo methods to determine the non-occupational dose outside the suite. This was driven by the recent inclusion of the most recent NCRP dose limit recommendations into 10CFR20, which contain the national standards for protection against radiation. The dose limits above background are 1 mSv, non-occupational continuous exposure, 5 mSv, non-occupational infrequent exposure, and 50 mSv, occupational. The occupational limit would be applied to the medical technicians in the suite, the non-occupational continuous exposure limit to allied medical personnel with, for instance, offices adjacent to the suite, and the non-occupational infrequent exposure limits to other medical center patients traversing the corridors adjacent to the suite. Prior to this analysis, CT dose was difficult to determine because the scattered radiation spectrum from a CT was not available. MCNP, however, bins its result by particle energy, thus, providing the scattered spectra.

These goals were accomplished using a method outlined by Robert Metzger (Metzger, 1993) using MCNP, a general-purpose Monte Carlo n-particle transport model developed by Los Alamos National Laboratory (MCNP, 1993). The CT, a continuously rotating source, was modeled as 32 discrete beam positions, each comprised of 35 narrow conic beams to form the characteristic CT fan beam. The target was the standard human phantom composed entirely of a homogeneous tissue defined in MIRD Pamphlet 5 (with some minor changes; Snyder, 1978). Separate runs were done simulating a head scan and

an abdomen scan. Average usage of the CT at WPMC was used to establish usage factors and workload (Michael, 1995). The suite walls were modeled alternately with 1/16" and 1/8" lead shielding sandwiched between 1.4 cm thick gypsum drywall. The ceiling and floor were modeled as six inch slabs of concrete.

Validation of the modeling effort was accomplished by comparing the exposure of film badges placed within the CT suite to the results obtained from modeling the badge locations with MCNP. The badge/MCNP results agreed by approximately a factor of two (some more, some less) with the exception of badge locations that were likely blocked during the exposure period. In general, the MCNP results compared favorably with typical scatter surveys of the GE HiSpeed Advantage CT scanner unit. The results obtained in the analysis are presented below. They are followed by recommended improvements to the methodology and possible follow-on research.

8.1 Analysis Results

In addition to the primary goal of obtaining the *non-occupational* dose outside the CT suite, the analysis for 1/16" lead shielding (typically used in walls adjacent to occupational areas) *and* 1/8" lead shielding (typically used in walls adjacent non-occupational areas) provided the *occupational* dose as a by-product. MCNP, the model used for this analysis, can bin the total number of particles at a detector location by particle energy. Thus, a scattered energy spectrum was obtained at each location. The scattered spectra from a CT unit, previously unavailable (Simpkin, 1995), was also determined.

8.1.1 Non-Occupational Dose.

The dose from a CT unit at a given location is a function of many variables: source strength, spectrum and shape; target size, location and composition; CT shielding, frequency of use and mode of use; and wall/floor shielding between the source and detector location. All of these factors were included in the dose analysis. 10CFR20 contains the maximum non-occupational annual dose limits for continuous and infrequent exposure. These would correspond to allied medical personnel and non-related medical center patients, respectively. The negative x-room axis, negative x source axis , positive y-room axis, positive y-body axis, floor and ceiling results for 1/8" lead shielding (corresponding to the shielding and layout at WPMC) were used to determine the non-occupational dose. The analysis (Table 7.4, 1/8" shielding) determined that the dose limit for continuous exposure (allied medical personnel) of 1 mSv required by 10CFR20 was exceeded below the floor and above the ceiling of the CT suite. The dose limit of 5 mSv for infrequent exposure (non-related patients) was exceed only below the floor. The calculated dose values above the ceiling and below the floor, however, may be more a function of modeling than actual dose since the floor and ceiling concrete was modeled as six inch slabs instead of the six inch slab plus two inches of waffled concrete on each side that are in the CT suite.

8.1.2 Occupational Dose.

The positive x-room axis, positive x source axis, negative y-room axis, negative y-body axis, floor and ceiling results for 1/16" lead shielding were used to determine the

occupational dose. The analysis (Table 7.4, 1/16" shielding) determined that at all locations, dose to occupational workers was below the dose limit of 50 mSv required by 10CFR20.

8.1.3 Scattered Spectrum.

In general, the spectrum of scattered radiation is a slightly softened source spectra and is best represented by the bone-in test results seen in Figs. C.7 and C.8. The spectra obtained inside the WPMC CT suite show a spectral contribution from the cadmium tungstate CT detector which may not be relevant to all CT units. In addition, the phantom used in the analyses inside the suite did not include the skeleton, which was shown to affect the spectra.

8.1.4 Application of WPMC Results to a Generic CT Suite.

The tally behavior and spectral results for the WPMC CT suite with 1/16" lead shielding for a head scan were very similar to the analogous GE minimum recommended room results. The agreement suggested that the differences noted for the WPMC suite from 1/16" to 1/8" lead shielding, and, from a head to an abdomen scan could be applied to the single run done for the GE room with 1/16" lead shielding for the head scan via conversion factors. The conversion factors were determined by comparing 1/16" to 1/8" lead shielded room results at each detector location for the head and abdomen scans and by comparing the head to abdomen scan results for the 1/16" and 1/8" shielded rooms. The 1/16"-to-1/8" conversion factors (for each detector location) were applied to the results for GE 1/16" shielded room (head scan) to obtain GE 1/8" shielded room (head scan) values.

Similarly, the head-to-abdomen conversion factors were applied to the 1/16" and 1/8" shielded room results for the head scan to obtain results for an abdomen scan in those rooms.

In general, comparing the total annual dose equivalents by location for the WPMC suite in Tables 7.4 and for the GE room in Table 7.8, similar results are seen. The dose equivalents outside the GE room are slightly higher than outside the suite at WPMC. This was expected because the GE room is smaller than the WPMC room. The detectors located, however, on the positive and negative x walls outside the GE room were unexpectedly high. Thorough review of the input files revealed no cause for this, i.e. no mistakes were found in the files. Recalling that the CT unit is rotated at slightly different angles for the two rooms, a possible explanation is that the GE room x-wall detectors were placed directly on or much closer to a "hot spot" than the detectors outside the WPMC room.

With the notable exception of the positive x-room axis detector location, the same conclusions concerning conformity to the 10CFR20 dose limits are reached. That is, the annual dose limit for continuous exposure (allied medical personnel) of 1 mSv required by 10CFR20 was exceeded below the floor, above the ceiling, and outside the negative x wall of the GE room. The annual dose limit of 5 mSv for infrequent exposure (non-related patients) was exceeded only below the floor and outside the negative-x wall. At all the locations but the positive x-room axis, dose to occupational workers was below the annual dose limit of 50 mSv required by 10CFR20.

8.2 Recommended Improvements

As with any analysis, there is room for improvement in this thesis. The following sections describe problem areas and suggested fixes.

8.2.1 Geometry.

Two needed improvements to problem geometry were made obvious in the analysis: (1) better definition of the concrete floor and ceiling, and (2) defining a phantom that fits within the CT fan beam. The first could be investigated via test runs using much simpler scatter radiation sources than the CT unit with phantom. The test would determine primarily if the addition of the waffled concrete impacted the external dose. The second problem could be corrected either by widening the fan beam (via additional conic beams and) or, more simply, by reducing the dimensions of the phantom's abdomen.

8.2.2 Source.

The source spectra described in the input files was unwieldy since every pencil beam in the fan had a different spectrum resulting from passing beam through the Teflon bowtie filter. Examination of the different spectra (not included in this thesis because they were proprietary to GE) revealed that their magnitude across the spectrum differed from one another by a nearly constant factor. Streamlining the source definition could be done by replacing the different spectra with probabilities determined by a normalization of the integrated individual spectra. For example, if the spectra at 17.5^{o} had one half the integrated source strength of the central spectra, the beam at 17.5^{o} (with the same spectra

as the central beam) would be assigned a relative probability of one half that of the central beam. Although it would not reduce run time per number of particles, it would certainly reduce input file size.

8.2.3 Air Kerma.

Since the air kerma value for the particular tube used in this analysis was not available, the air kerma value used was obtained from a chart of average air kerma for diagnostic X-ray tubes of varying potentials (NCRP, 1989). This average air kerma, however, did not account for the changing spectrum as a function of fan beam angle as described above. An improvement to the air kerma figure would require the source strength for each energy bin in particles per some time interval, which, when given the values for energy deposited in air as a function of particle energy (the definition of kerma, section 2.8.4), could be used to determine the actual air kerma of this particular X-ray tube.

8.2.4 Sampling Interval.

Recall that some of the tally plots displayed large peaks. The beam positions around these peaks show a need for sampling additional beam positions to better define their shape and thus the average. For example, Fig. G.1, the positive source axis detector tally from the WPMC room with 1/16" shielding, shows a twin-peaked behavior on either side of the Pt 0 beam position. Clearly, these peaks contribute heavily to the mean exposure. If the peaks were, in fact, wider, the tally was underestimated; if the peaks are very narrow, the tally

was overestimated. All detector locations would not need the additional sampling points, it could be done on as as-needed basis.

8.2.5 Computer Resources.

This analysis, despite all efforts to conserve computer resources by reducing file size, run time and number of points sampled, still required imposing computer resources. Each individual beam position run was done on a separate Sun Sparc20 (AFIT computer lab, accessible to all AFIT students and faculty). Run times of one to two weeks were logged for two million particles (sharing resources with other users) for ten detector locations plus the source detector. Elimination of detector locations resulted in linear reductions in run times. Each of the 32 beam positions produced a set of computer files containing the input file, output file, continuation file (RUNTPE) and tally file (MCTAL) with a total approximately three megabytes. The eight runs (CT in X-ray room; CT inside WPMC, head and abdomen; CT at WPMC with 1/16" and 1/8" shielding for head and abdomen; and CT in GE room, head and abdomen) thus used almost 800 megabytes of disk space. It is safe to say that the average radiation safety officer would not have computer resources of this magnitude readily available.

A possible answer to this problem requires viewing the problem a different way. If, instead of performing this analysis for a given room, it focused instead on the CT unit and phantom, a data set could be produced that would have greater usefulness. Imagine a spherical surface surrounding the CT unit and phantom. If the dose were determined on

this surface, it could be extrapolated out to and through whatever surfaces confined it. This, in effect, would be equivalent to defining a non-isotropically radiating point source representative of the scattered radiation. The initial effort would require comparable computer resources described above, but they would not need to be repeated for every diagnostic facility.

8.3 Follow-On Research.

At the conclusion of any research defining or using a new method of analysis, follow-on studies immediately come to mind. This thesis is no exception. The results raised new questions about methods, materials or improved sources. In particular, two areas of further investigation present themselves: complete definition of the scattered spectrum and dose at all points surrounding the source and target.

8.3.1 Scattered Spectrum.

Early in thesis research, D. Simpkin (Simpkin, 1995) questioned the ability to complete this thesis because of the lack of a scattered spectrum from a CT unit. Previous methods of determining dose would have required it. The use of MCNP, however, precluded this. MCNP could produce a scattered spectrum given a well-defined source and problem geometry. Thus, one product of this research was the elusive scattered spectrum. It, however, was only defined at the particular detector locations. To be truly useful, the spectrum should be defined at all points surrounding the source and target for a variety of targets, sources, geometries and compositions. MCNP has a surface current

capability that would provide this type of information. This is an area ripe for further investigation.

8.3.2 Angle and Position Dependent Dose.

Another area for further investigation was presented in section 8.2.4, that is, determining the dose on a spherical surface surrounding the CT unit and target. Similar techniques used to define the spectrum at all points could be used. In fact, the use of MCNP would naturally tie these two together since the reported exposure tally is a function of the calculated spectrum. As discussed above, such a product would be very useful to radiation protection professionals to determine the most efficient and effective shielding needed around a CT suite.

8.4 Conclusions

The primary goal of determining the equivalent dose outside a computerized tomography (CT) suite was accomplished. The dose was compared to the recently revised dose limits required by 10CFR20 for occupational and non-occupational areas. At most test locations, the non-occupational and occupational dose limits were not exceeded. The limits are exceeded below floor and above ceiling of the WPMC CT suite and the GE room, subject, however, to further analysis. The GE room also exceeded the non-occupational limits outside the negative-x wall. In addition, a scattered radiation spectrum from a CT unit, previously unavailable, was produced. The method of using a Monte Carlo model described by Metzger, et. al. (Metzger, 1993) is considered valid to determine dose outside diagnostic X-ray facilities.

Appendix A Sample Input File

Section I: Cells

```
WP CT room w/MIRD phantom on
c    table in center of room.
c    Uses geometry splitting; floor, ceiling
c    and lead lining are divided
c
c    Lungs:
101     1 -.2958 7 -12 13                          imp:p=4
103     1 -.2958 7 -14 15                          imp:p=4
c    Torso
105     2 -.9869  8 -6 -10  #101 #103              imp:p=1
c    Legs
106     2 -.9869  -8 -16                           imp:p=1
c    Face
7     2 -.9869 -5 6 -1                             imp:p=1
c    Top of head:
8     2   -.9869 5 -2                              imp:p=1
c    Interior of room
9     3 -.0012  (-8:6:10) #8 #7 #30 #106 #40 #50
           401 -411  -201 211 301 -311              imp:p=1
c    Inner gypsum layer:
111   4 -.73   (201:-301:-211:311) -202 302 212 -312
           -411 401                                 imp:p=4
-------------------------
lines skipped
-------------------------
c    Sphere surrounding room
19    3 -.0012 (207:-307:-217:317:416:-406) -43     imp:p=4096
20    0 43                                         imp:p=0
c    Detector
30    10 -7.00   60   -61  71 -70  72  -73  74     imp:p=4
c    Psuedo Gantry
40    11 -2.69   -81 80 83 -82 (-71:70)            imp:p=4
c    Shield
50    11 -2.69    -91 90 -92 73                    imp:p=4
```

Section II: Surfaces

```
c    MIRD Phantom head in center of beam:
c
1    sq 100 0 49 0 0 0 -4900 0 1 0        $face
2    sq 7225 4900 3540.25 0 0 0 -354025 0  1 0  $top o' head
5    py 1       $top of face and side of detector
6    py -14.5   $top of torso
7    py -41     $bottom of lungs
8    py -84.5   $top of legs
10   sq 100 0 400 0 0 0 -40000 0  1 0   $torso
12   sq 32400 1406.25 14400 0 0 0 -810000  8.5 -41 0  $ lungs
13   sq 32400 1406.25 14400 0 0 0 -810000  2.5 -41 0
14   sq 32400 1406.25 14400 0 0 0 -810000 -8.5 -41 0
15   sq 32400 1406.25 14400 0 0 0 -810000 -2.5 -41 0
16   sq 16 1 64 0 0 0 -6400 0  -84.5 0 $legs
c    50' Sphere of air surrounding room:
43   so 1500
c    Wall to -x of patient
201  p -1.901 1 0 526.599
202  p -1.901 1 0 529.6068
-------------------------
lines skipped
-------------------------
406  pz  -123.6
c    Ceiling
411  pz  287.02
412  pz  290.02
413  pz  293.02
414  pz  296.02
415  pz  299.02
416  pz  302.02
c    detector
60   c/y -63 0 110
61   c/y -63 0 115
70   p -0.50953 0 1 32.1001
71   p 0.50953 0 1 -32.1001
72   py -2
73   py 2
74   px  0
c    Aluminum block to represent power supply, support, etc of gantry
80   cy          65
81   cy          68
82   py          15
83   py         -15
```

Section III: Materials

```
mode  p
c     Definition for lung tissue:
m1    1000 -.1021
      6000 -.1001
      7000 -.0280
      8000 -.7596
      11000 -.0019
      15000 -.00081
      16000 -.0023
      17000 -.0027
      19000 -.0020
      26000 -.00037
c     Standard tissue (non-lung):
m2    1000 -.1047
      6000 -.2302
      7000 -.0234
      8000 -.6321
      11000 -.0013
      12000 -.00015
      15000 -.0024
      16000 -.0022
      17000 -.0014
      19000 -.0021
-------------------------
lines skipped
-------------------------
c     Cadmium Tungstite, density=~7.00 g/cc
m11   74000 1 48000 1 8000 4
```

Section IV: Source

```
c     CT source with head in center
c     spectrum from GE
c     120 kVp with bowtie filter
sdef  pos=d1 dir=d2 vec=fpos=d3  erg=fpos=d4
si1   l     -63    0      0
            -63    0      0
            -63    0      0
-------------------------
lines skipped
-------------------------
            -63    0      0
```

```
          -63   0     0
          -63   0     0
sp1  0.01 0.01 0.01 0.01 0.01
     0.01 0.01 0.01 0.01 0.01
     0.01 0.01 0.01 0.01 0.01
     0.01 0.01 0.01 0.01 0.01
     0.01 0.01 0.01 0.01 0.01
     0.01 0.01 0.01 0.01 0.01
     0.01 0.01 0.01 0.01 0.01
si2       a   0.99984   1
sp2           1       1
ds3  s    201    202    203    204    205
          206    207    208    209    210
          211    212    213    214    215
          216    217    218    219    220
          221    222    223    224    225
          226    227    228    229    230
          231    232    233    234    235
si201     1    60.247    0     18.419
sp201          1
si202     1    60.559    0     17.365
sp202          1
-------------------------
lines skipped
-------------------------
si234     1    60.559    0     -17.365
sp234          1
si235     1    60.247    0     -18.419
sp235          1
c
ds4  s   117    116    115    114    113
         112    111    110    109    108
         107    106    105    104    103
         102    101    100    101    102
         103    104    105    106    107
         108    109    110    111    112
         113    114    115    116    117
c
#        si117   sp117   si116   sp116   si115   sp115
         0.016    0.00   0.016    0.00   0.016    0.00
         0.018    0.00   0.018    0.02   0.018    0.00
         0.02     0.00    0.02    0.76    0.02    0.01
         0.022    0.12   0.022    7.05   0.022    0.25
         0.024    1.25   0.024   37.42   0.024    2.36
         0.026    7.86   0.026  137.40   0.026   13.44
```

```
        0.028    36.22    0.028   415.14    0.028    57.23
        0.03    121.30    0.03   1002.43    0.03    180.27
-------------------------
lines skipped
-------------------------
        0.116   702.29    0.116   707.83    0.116   709.83
        0.118   370.37    0.118   373.27    0.118   374.32
        0.12     74.35    0.12     74.81    0.12     74.98
c     Tallies w/Roentgen conversion:
de0   .01 .015 .02 .03 .04 .05 .06 .08 .1 .15 .2 .3 .4 .5 .6
      .8 1.0 1.5 2.0 3.0 4.0 5.0 6.0 8.0 10.0 15.0 20.0
df0   .000000000854
      .000000000359
      .000000000193
-------------------------
lines skipped
-------------------------
      .00000000266
      .000000003726
      .00000000482
```

Section V: Tallies

```
c     Point Detector Tallies
c
fc5 (Src axis) Outside -x direction
f5:p  -316.48 0 0 7
fc105 Outside -x
f105:p  -247.92 130.38 0 7
c
f135:p 0 0 -153.6 7
c
-------------------------
lines skipped
-------------------------
fc165 outside, feet
f165:p -254.77 -484.44 0 7
dd   0 1e25
e0      .010 .012 .014 .016 .018 .020 .022 .024 .026 .028
-------------------------
lines skipped
-------------------------
       .150 .152 .154 .156 .158 .160
prdmp J 100000 2 2 100000
nps  2000000
```

Appendix B Sample Output File

Section I: Summary

1problem summary

run terminated when 2000000 particle histories were done.

\+ 09/02/95 10:34:27

Generic CT room w/MIRD head w/bone phantom on probid = 08/28/95 23:44:10

photon creation	tracks	weight (per source particle)	energy	photon loss	tracks	weight (per source particle)	energy
source	2000000	1.0000E+00	6.5010E-02	escape	1363631	1.6646E-04	1.1139E-05
				energy cutoff	0	0.	0.
				time cutoff	0	0.	0.
weight window	0	0.	0.	weight window	0	0.	0.
cell importance	10862319	1.0383E-01	5.9386E-03	cell importance	1055995	1.0404E-01	5.9479E-03
weight cutoff	0	0.	0.	weight cutoff	0	0.	0.
energy importance	0	0.	0.	energy importance	0	0.	0.
dxtran	0	0.	0.	dxtran	0	0.	0.
forced collisions	0	0.	0.	forced collisions	0	0.	0.
exp. transform	0	0.	0.	exp. transform	0	0.	0.
from neutrons	0	0.	0.	compton scatter	0	0.	1.1993E-02
bremsstrahlung	119464	8.6286E-03	4.9979E-05	capture	12891432	1.1765E+00	5.6053E-02
p-annihilation	0	0.	0.	pair production	0	0.	0.
electron x-rays	0	0.	0.				
1st fluorescence	2229016	1.5954E-01	2.9484E-03				
2nd fluorescence	100259	8.6970E-03	5.8255E-05				
total	15311058	1.2807E+00	7.4005E-02	total	15311058	1.2807E+00	7.4005E-02

number of photons banked	3449400	average lifetime, shakes		cutoffs	
photon tracks per source particle	7.6555E+00	escape	5.8998E+00	tco	1.0000E+34
photon collisions per source particle	1.2855E+01	capture	5.3923E-01	eco	1.0000E-03
total photon collisions	25709385	capture or escape	5.3999E-01	wc1	-5.0000E-01
		any termination	5.4292E-01	wc2	-2.5000E-01
computer time so far in this run	3706.40 minutes	maximum number ever in bank		10	
computer time in mcrun	3704.38 minutes	bank overflows to backup file		0	
source particles per minute	5.3990E+02	field length		0	
random numbers generated	271013269	most random numbers used was		28850 in history	1522057

range of sampled source weights = 1.0000E+00 to 1.0000E+00

warning. importance function may be poor. see print table 120.

Section II: Cell Activity

1photon **activity in each cell** print table 126

	cell	tracks	population	collisions	collisions * weight (per history)	number weighted energy	flux weighted energy	average track weight (relative)	average track mfp (cm)
1	101	15468	14760	7518	9.3975E-04	5.0208E-02	5.0208E-02	1.0000E+00	1.4532E+01
2	103	11684	11173	6307	7.8837E-04	4.9002E-02	4.9002E-02	1.0000E+00	1.4317E+01
3	105	58087	55643	110807	5.5403E-02	5.0463E-02	5.0463E-02	1.0000E+00	4.4493E+00
4	106	1200	1180	3222	1.6110E-03	5.0729E-02	5.0729E-02	1.0000E+00	4.4686E+00
5	7	1104180	1028390	1965997	9.8300E-01	5.9496E-02	5.9496E-02	1.0000E+00	4.8198E+00
6	8	354220	338942	445444	2.2272E-01	5.3455E-02	5.3455E-02	1.0000E+00	4.5760E+00
7	9	3038556	2198066	87266	4.3633E-02	5.9824E-02	5.9824E-02	1.0000E+00	4.3065E+03

```
-----------------------
lines skipped
-----------------------
   26   30    4386376     4418233    10509861   1.3137E+00  6.8256E-02  6.8256E-02  1.0000E+00  5.8117E-01
   27   40     424572      448773      740929   9.2616E-02  5.5291E-02  5.5291E-02  1.0000E+00  7.7109E-02
   28   50     712568      756907     1253129   1.5664E-01  5.7528E-02  5.7528E-02  1.0000E+00  8.1068E-02

    total    18849050    18089865    25709385   3.3710E+00
```

Section III: Tallies

```
1tally  5       nps =  2000000
+                           (Src axis) Outside -x direction
        tally type 5    particle flux at a point detector.
        tally for  photons

        this tally is modified by a dose function.

 detector located at x,y,z =-3.16480E+02 0.00000E+00 0.00000E+00
     energy
   1.0000E-02  6.58292E-28 0.7926
   1.2000E-02  8.11385E-30 1.0000
   1.4000E-02  3.06456E-49 0.9967
   1.6000E-02  7.57486E-28 1.0000
-----------------------
lines skipped
-----------------------
   1.5600E-01  0.00000E+00 0.0000
   1.5800E-01  0.00000E+00 0.0000
   1.6000E-01  0.00000E+00 0.0000
    total      3.30437E-22 0.1115
```

detector located at x,y,z =-3.16480E+02 0.00000E+00 0.00000E+00
uncollided photon flux

energy		
1.0000E-02	6.58288E-28	0.7926
1.2000E-02	8.11385E-30	1.0000
1.4000E-02	9.45976E-52	1.0000
1.6000E-02	7.57486E-28	1.0000

---

lines skipped

1.5400E-01	0.00000E+00	0.0000
1.5600E-01	0.00000E+00	0.0000
1.5800E-01	0.00000E+00	0.0000
1.6000E-01	0.00000E+00	0.0000
total	9.35894E-26	0.6707

detector score diagnostics

times average score	cumulative fraction of transmissions	tally per transmissions	cumulative fraction of history	tally total tally
0.00000E+00	0	0.00000	0.00000E+00	0.00000
1.00000E+00	7603544	0.98592	6.17125E-14	0.00734
2.00000E+00	34359	0.99038	2.15729E-13	0.03299
5.00000E+00	34485	0.99485	4.68229E-13	0.08867
1.00000E+01	16250	0.99696	4.90606E-13	0.14701
1.00000E+02	19149	0.99944	1.71526E-12	0.35097
1.00000E+03	2826	0.99981	5.70158E-13	0.41876
1.00000E+38	705	0.99990	4.88801E-12	1.00000
1st 200 histories	774	1.00000	1.70713E-17	1.00000

average tally per history = 8.40972E-12 largest score = 3.47464E-07
(largest score)/(average tally) = 4.13170E+04 nps of largest score = 352998

score contributions by cell

	cell	misses	hits	tally per history	weight per hit
1	101	1590	4676	4.28011E-18	1.83067E-15
2	103	1166	4009	4.10776E-17	2.04927E-14
3	105	41909	52056	1.34741E-15	5.17678E-14
4	106	482	2271	2.25682E-17	1.98752E-14
5	7	1061567	686372	1.86963E-24	5.44787E-24
6	8	284455	99737	1.18247E-25	2.37118E-24
7	9	2032978	42959	3.32066E-15	1.54597E-13

---

lines skipped

26	30	2972562	3938154	4.89876E-25	2.48785E-25
27	40	289514	25605	1.81329E-21	1.41636E-19
28	50	475790	68191	2.49245E-21	7.31021E-20
	total	9454341	7712092	8.40972E-12	2.18092E-12

score misses

russian roulette on pd	0
psc=0.	2255233
russian roulette in transmission	0
underflow in transmission	7199108
hit a zero-importance cell	0
energy cutoff	0

1analysis of the results in the tally fluctuation chart bin (tfc) for tally 5 with nps = 2000000 print table 160

normed average tally per history = 3.30437E-22 unnormed average tally per history = 3.30437E-22
estimated tally relative error = 0.1115 estimated variance of the variance = 0.0995
relative error from zero tallies = 0.0006 relative error from nonzero scores = 0.1115

number of nonzero history tallies = 1175207 efficiency for the nonzero tallies = 0.5876
history number of largest tally = 540253 largest unnormalized history tally = 3.86819E-17
(largest tally)/(average tally) = 1.17063E+05 (largest tally)/(avg nonzero tally)= 6.87865E+04

(confidence interval shift)/mean = 0.0146 shifted confidence interval center = 3.35265E-22

if the largest history score sampled so far were to occur on the very next history, the tfc bin quantities would change as follows:

estimated quantities	value at nps	value at nps+1	value(nps+1)/value(nps)-1.
mean	3.30437E-22	3.49778E-22	0.058531
relative error	1.11542E-01	1.19001E-01	0.066871
variance of the variance	9.94772E-02	1.07773E-01	0.083399
shifted center	3.35265E-22	3.36310E-22	0.003119
figure of merit	2.16974E-02	1.90627E-02	-0.121430

the estimated inverse power slope of the 200 largest tallies starting at 4.50882E-19 is 2.5177
the history score probability density function appears to have an unsampled region at the largest history scores: please examine.

==========

results of 10 statistical checks for the estimated answer for the tally fluctuation chart (tfc) bin of tally 5

tfc bin	--mean--	---------relative error---------			----variance of the variance----			--figure of merit--		-pdf-
behavior	behavior	value	decrease	decrease rate	value	decrease	decrease rate	value	behavior	slope
desired	random	<0.05	yes	1/sqrt(nps)	<0.10	yes	1/nps	constant	random	>3.00
observed	random	0.11	yes	yes	0.10	yes	yes	constant	random	2.52
passed?	yes	no	yes	yes	yes	yes	yes	yes	yes	no

==========

warning. the tally in the tally fluctuation chart bin did not pass 2 of the 10 statistical checks.
1unnormed tally density for tally 5 nonzero tally mean(m) = 5.623E-22 nps = 2000000 print table 161

abscissa ordinate log plot of tally probability density function in tally fluctuation chart bin(d=decade,slope= 2.5)
tally number num den log den:d----d-----d-----d-----d-----d-----d-----d-----d-----d-----d-----d-----d-----d----d-----d-----d-----
2.00-30 4904 2.46+27 27.392
**********|**********|**********|**********|**********
3.98-30 5034 1.27+27 27.103
**********|**********|**********|**********|**********

---

lines skipped

2.51-22 1996 7.97+18 18.901 **********|**********|********** | | |
5.01-22 3002 6.00+18 18.778 **********|**********|********** | | |
1.00-21 2332 2.34+18 18.369 mmmmmmmmmmmmmmmmmm|mmmmmmmmmmmmmmmmmm|mmmmmmmmmm |
2.00-21 2157 1.08+18 18.035 **********|**********|******** | | |

---

lines skipped

3.98-17 1 6.11+10 10.786 * s | | | | |
total 122404 6.12-02 d----d-----d-----d-----d-----d-----d-----d-----d-----d-----d-----d-----d-----d----d-----d-----d-----
a total of 1052803 tallies were below the score grid bin boundaries.

---

lines skipped (rest of tallies)

---

tally result of statistical checks for the tfc bin (the first check not passed is listed) and error magnitude check for all bins

5 missed 2 of 10 tfc bin checks: the relative error exceeds the recommended value of 0.05 for point detector tallies
missed all bin error check: 154 tally bins had 66 bins with zeros and 87 bins with relative errors exceeding 0.05

15 missed 3 of 10 tfc bin checks: the relative error exceeds the recommended value of 0.05 for point detector tallies
missed all bin error check: 154 tally bins had 40 bins with zeros and 82 bins with relative errors exceeding 0.05

---

lines skipped

---

165 missed 8 of 10 tfc bin checks: the relative error exceeds the recommended value of 0.05 for point detector tallies
missed all bin error check: 154 tally bins had 68 bins with zeros and 86 bins with relative errors exceeding 0.05

the 10 statistical checks are only for the tally fluctuation chart bin and do not apply to other tally bins.

the tally bins with zeros may or may not be correct: compare the source, cutoffs, multipliers, et cetera with the tally bins.

warning. 10 of the 11 tally fluctuation chart bins did not pass all 10 statistical checks.
warning. 11 of the 11 tallies had bins with relative errors greater than recommended.

Section IV: Tally Fluctuation Charts

1tally fluctuation charts

	tally 5					tally 15					tally 45				
nps	mean	error	vov	slope	fom	mean	error	vov	slope	fom	mean	error	vov	slope	fom
100000	4.3842E-22	0.5393	0.4912	1.6	1.9E-02	1.1336E-21	0.3432	0.2378	1.4	4.6E-02	2.7610E-13	0.0220	0.0006	6.2	11
200000	3.1952E-22	0.3823	0.4323	1.5	1.8E-02	1.7554E-21	0.2469	0.2249	1.5	4.4E-02	2.7254E-13	0.0157	0.0003	10.0	11

---

lines skipped

2000000	3.3044E-22	0.1115	0.0995	2.5	2.2E-02	1.5605E-21	0.1693	0.5238	2.1	9.4E-03	2.7245E-13	0.0049	0.0000	10.0	11

	tally 55					tally 65					tally 105				
nps	mean	error	vov	slope	fom	mean	error	vov	slope	fom	mean	error	vov	slope	fom
100000	8.9305E-22	0.2959	0.2604	1.5	6.1E-02	1.0915E-22	0.1796	0.0750	1.5	1.7E-01	7.6596E-22	0.5404	0.8823	1.5	1.8E-02

---

lines skipped

1900000	1.0469E-21	0.0978	0.0603	2.3	3.0E-02	2.1749E-22	0.1450	0.2716	2.2	1.4E-02	7.9357E-22	0.1284	0.0832	2.0	1.7E-02
2000000	1.0284E-21	0.0950	0.0593	2.3	3.0E-02	2.1476E-22	0.1397	0.2703	2.1	1.4E-02	7.8374E-22	0.1242	0.0815	2.0	1.8E-02

1tally fluctuation charts

	tally 115					tally 125					tally 135				
nps	mean	error	vov	slope	fom	mean	error	vov	slope	fom	mean	error	vov	slope	fom
100000	2.5295E-21	0.2705	0.2637	1.5	7.4E-02	8.7194E-22	0.2698	0.5941	2.0	7.4E-02	5.7701E-21	0.1645	0.1734	2.2	2.0E-01

---

lines skipped

1800000	2.5828E-21	0.0694	0.0490	3.2	6.2E-02	6.9238E-22	0.0689	0.1780	2.4	6.3E-02	5.9492E-21	0.0350	0.0191	4.2	2.4E-01
1900000	2.5599E-21	0.0670	0.0472	3.6	6.3E-02	6.9084E-22	0.0665	0.1672	2.4	6.4E-02	6.0304E-21	0.0362	0.0320	3.5	2.2E-01
2000000	2.6554E-21	0.0663	0.0426	3.6	6.1E-02	6.8833E-22	0.0637	0.1646	2.4	6.7E-02	6.0151E-21	0.0348	0.0307	3.4	2.2E-01

	tally 155					tally 165				
nps	mean	error	vov	slope	fom	mean	error	vov	slope	fom
100000	1.9192E-21	0.3062	0.7236	1.5	5.7E-02	1.1596E-22	0.2158	0.1776	1.7	1.2E-01

---

lines skipped

1900000	2.3276E-21	0.0764	0.0433	2.4	4.9E-02	2.9160E-22	0.1768	0.2904	1.9	9.1E-03
2000000	2.3101E-21	0.0740	0.0415	2.5	4.9E-02	2.8295E-22	0.1731	0.2899	2.0	9.0E-03

Section V: Termination

dump no. 21 on file runt0 nps = 2000000 coll = 25709385 ctm = 3704.38 nrn = 271013269

tally data written to file mct0

255 warning messages so far.

run terminated when 2000000 particle histories were done.

computer time = 3706.47 minutes

mcnp version 4a 10/01/93 09/02/95 10:35:04 probid = 08/28/95 23:44:10

Appendix C: Bone-In vs No-Bone Spectra

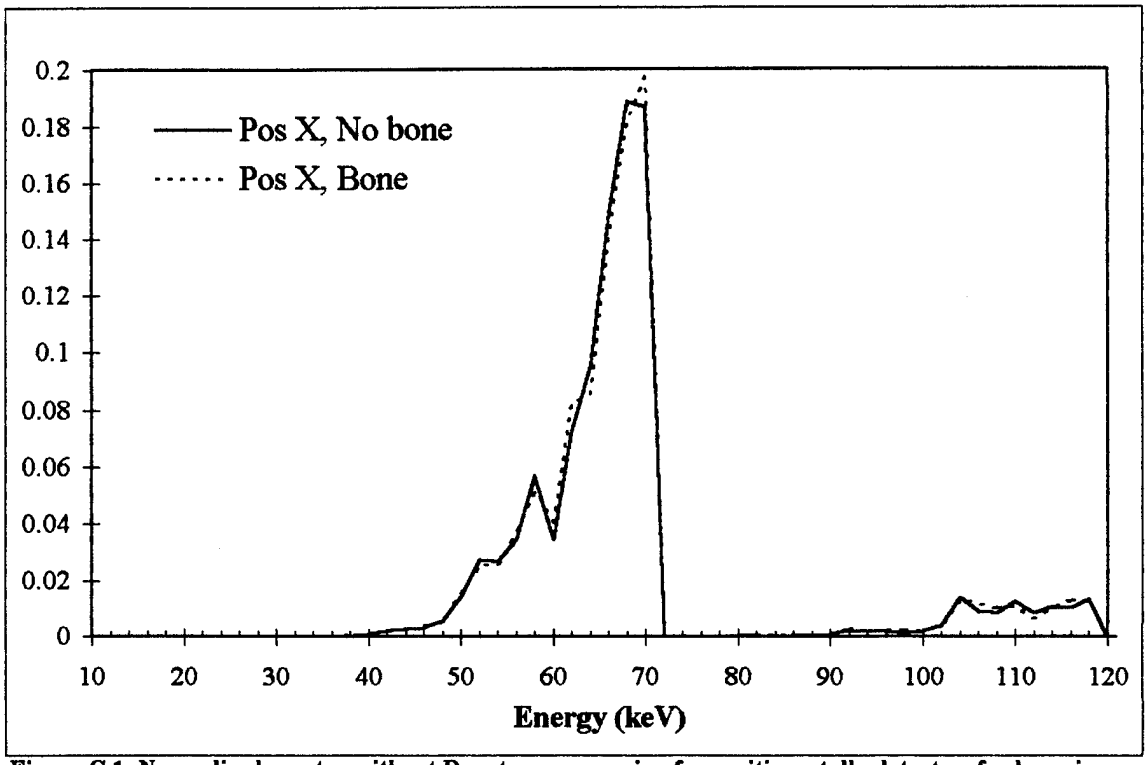

Figure C.1 Normalized spectra without Roentgen conversion for positive x tally detector for bone-in and no-bone comparison.

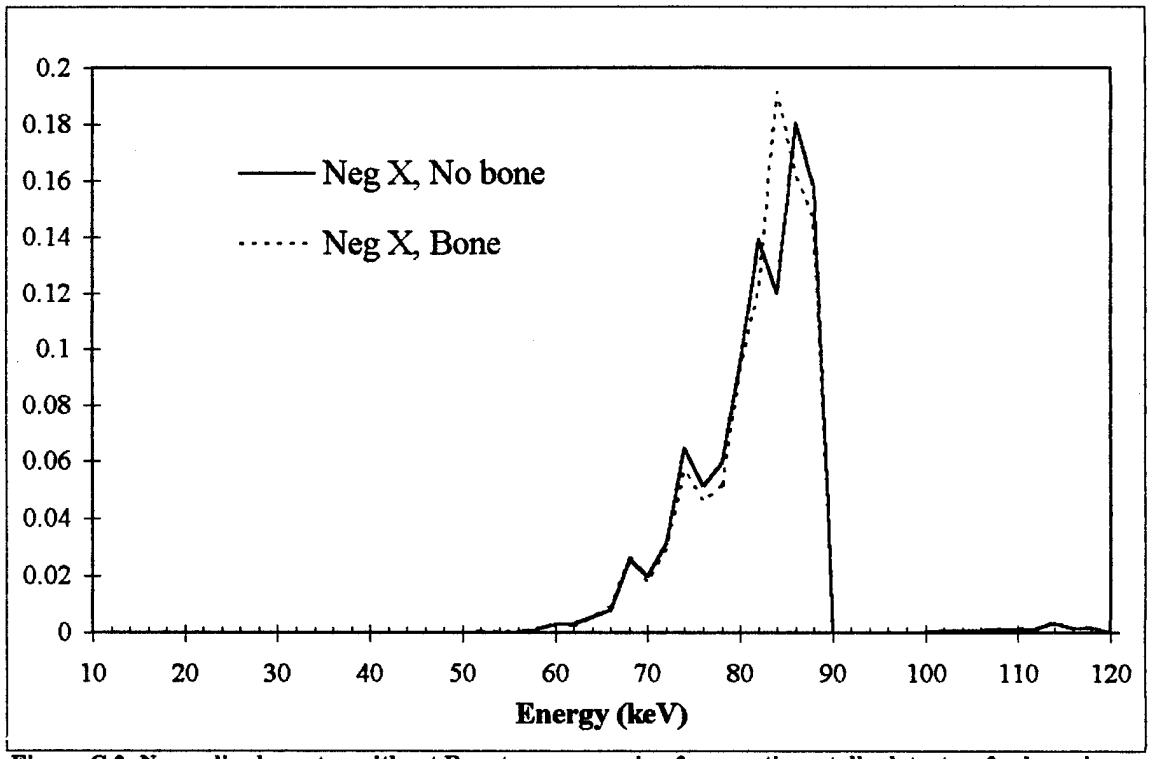

Figure C.2 Normalized spectra without Roentgen conversion for negative x tally detector for bone-in and no-bone comparison.

Appendix C: Bone-In vs No-Bone Spectra

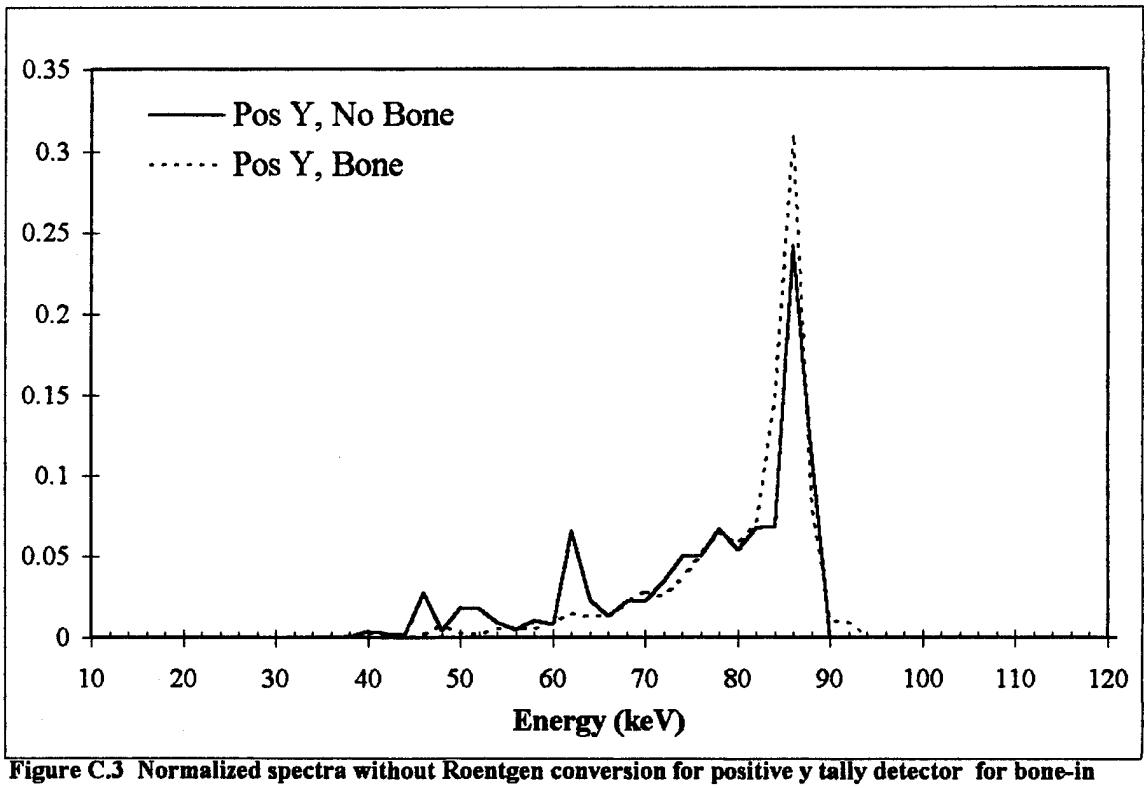

Figure C.3 Normalized spectra without Roentgen conversion for positive y tally detector for bone-in and no-bone comparison.

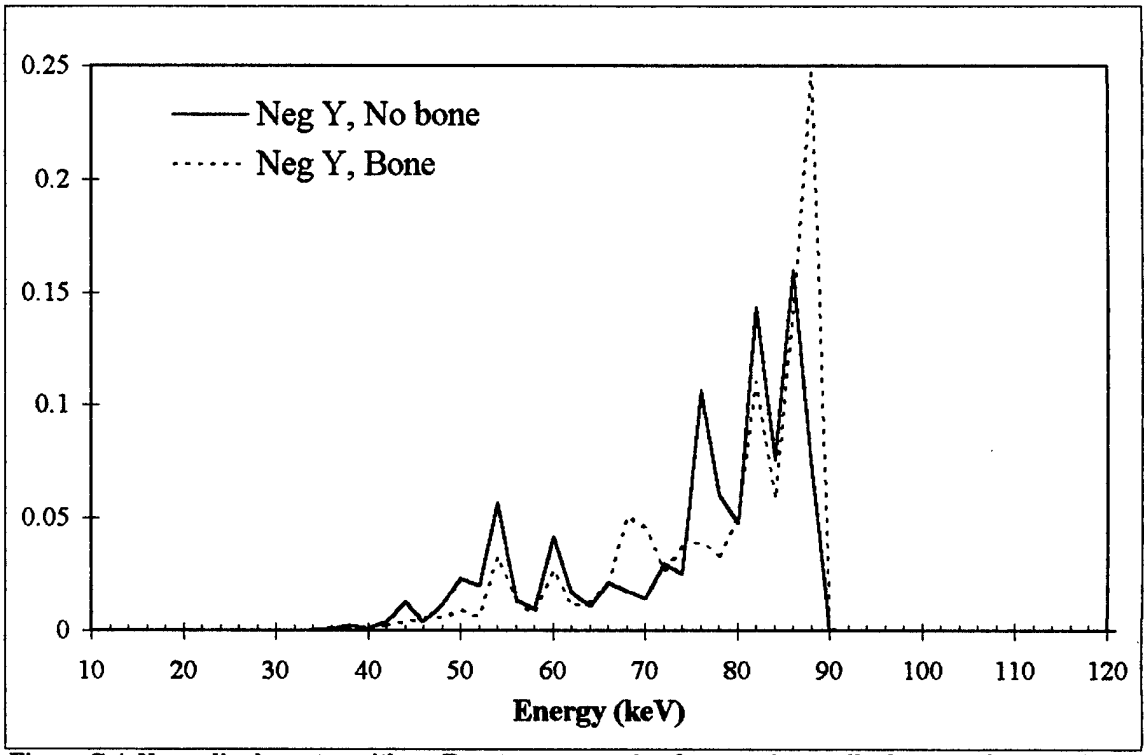

Figure C.4 Normalized spectra without Roentgen conversion for negative y tally detector for bone-in and no-bone comparison.

Appendix C: Bone-In vs No-Bone Spectra

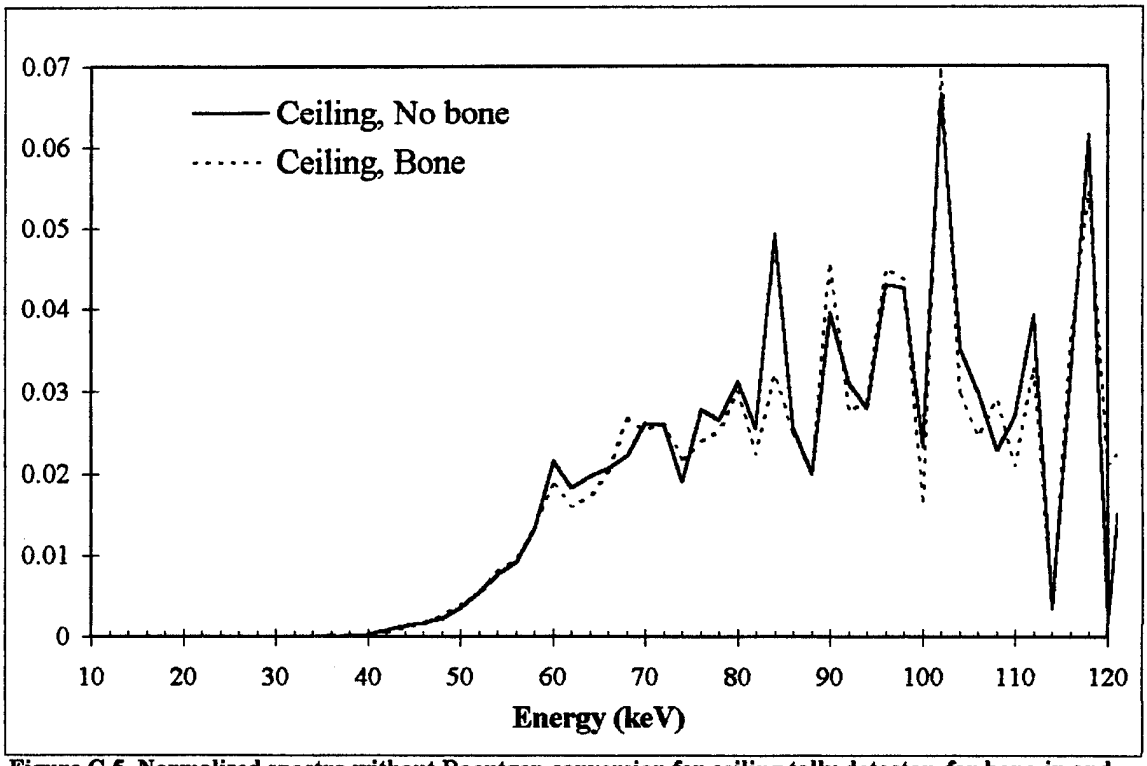

Figure C.5 Normalized spectra without Roentgen conversion for ceiling tally detector for bone-in and no-bone comparison.

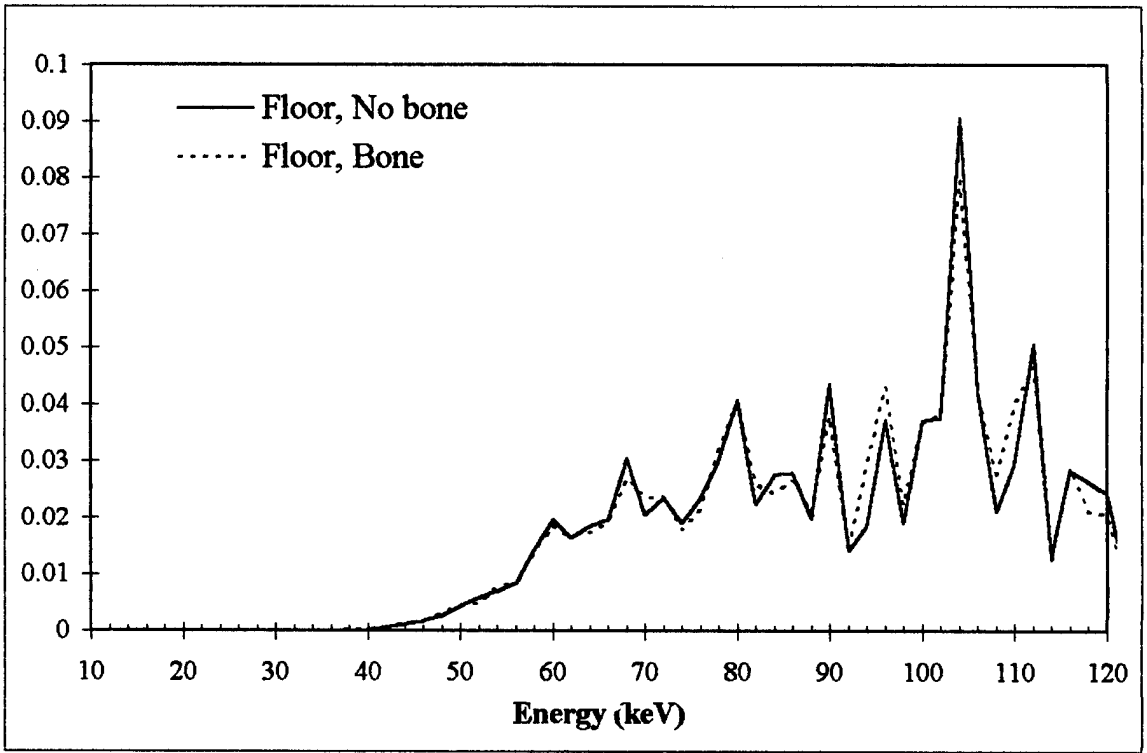

Figure C.6 Normalized spectra without Roentgen conversion for floor tally detector for bone-in and no-bone comparison.

Appendix C: Bone-In vs No-Bone Spectra

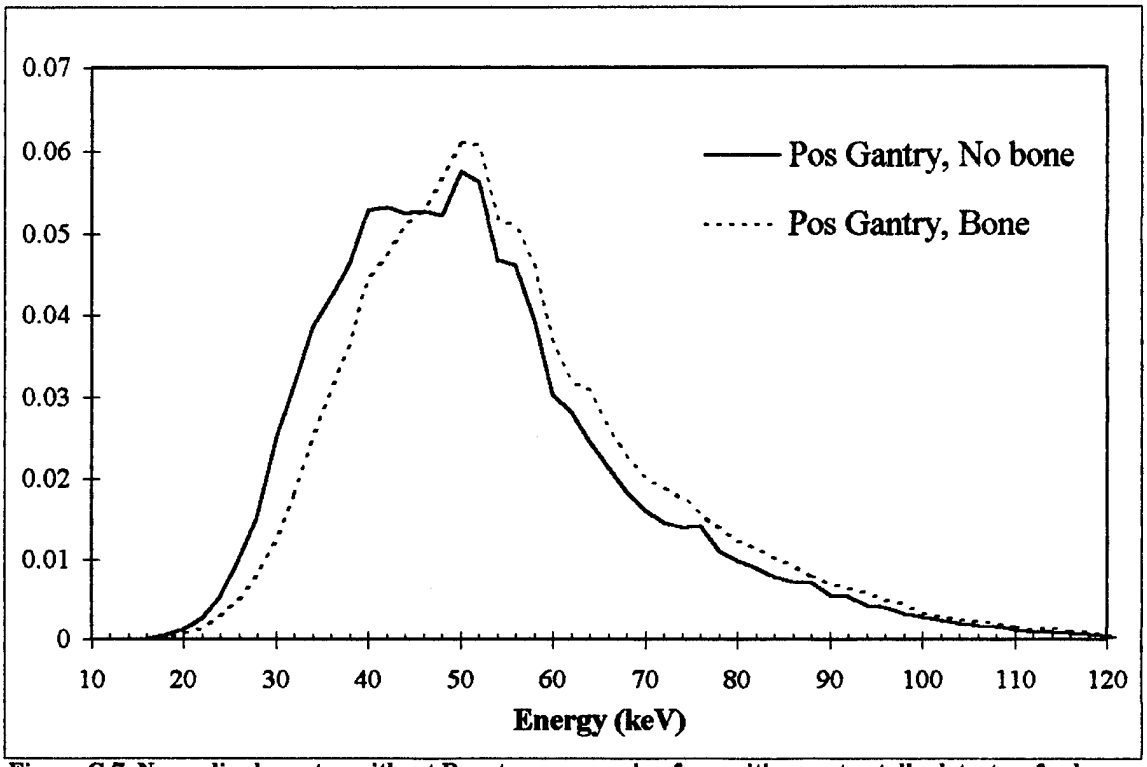

Figure C.7 Normalized spectra without Roentgen conversion for positive gantry tally detector for bone-in and no-bone comparison.

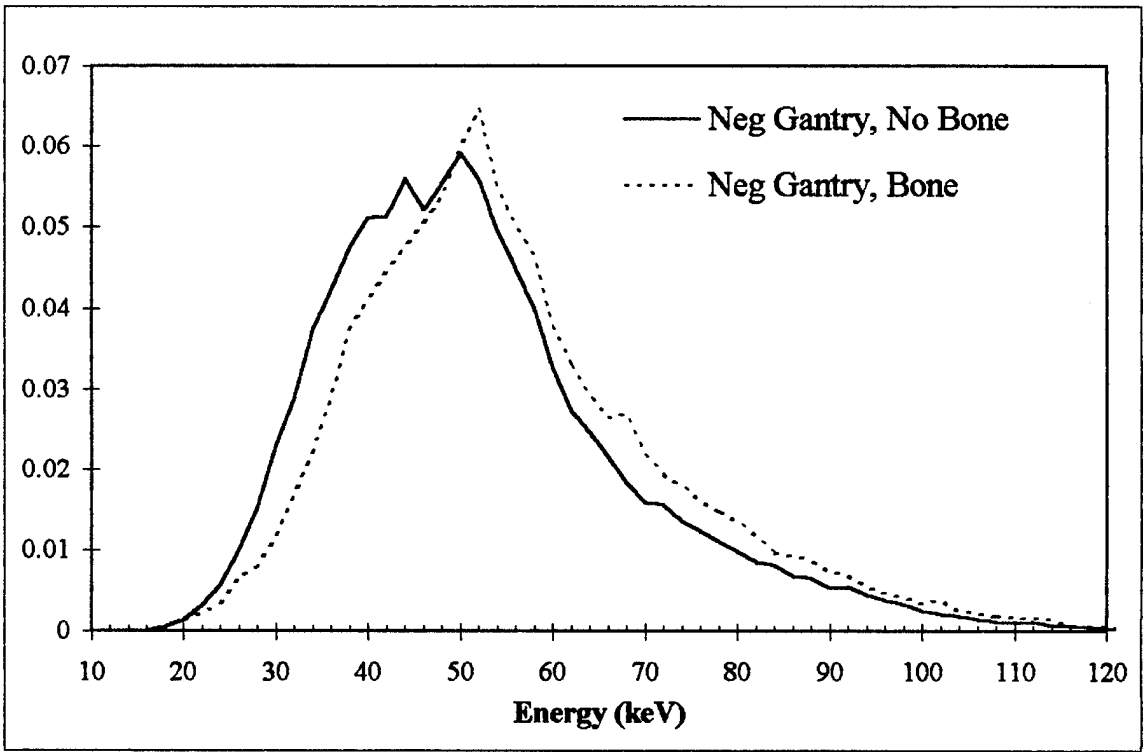

Figure C.8 Normalized spectra without Roentgen conversion for negative gantry tally detector for bone-in and no-bone comparison.

Appendix D: CT in X-Ray Room

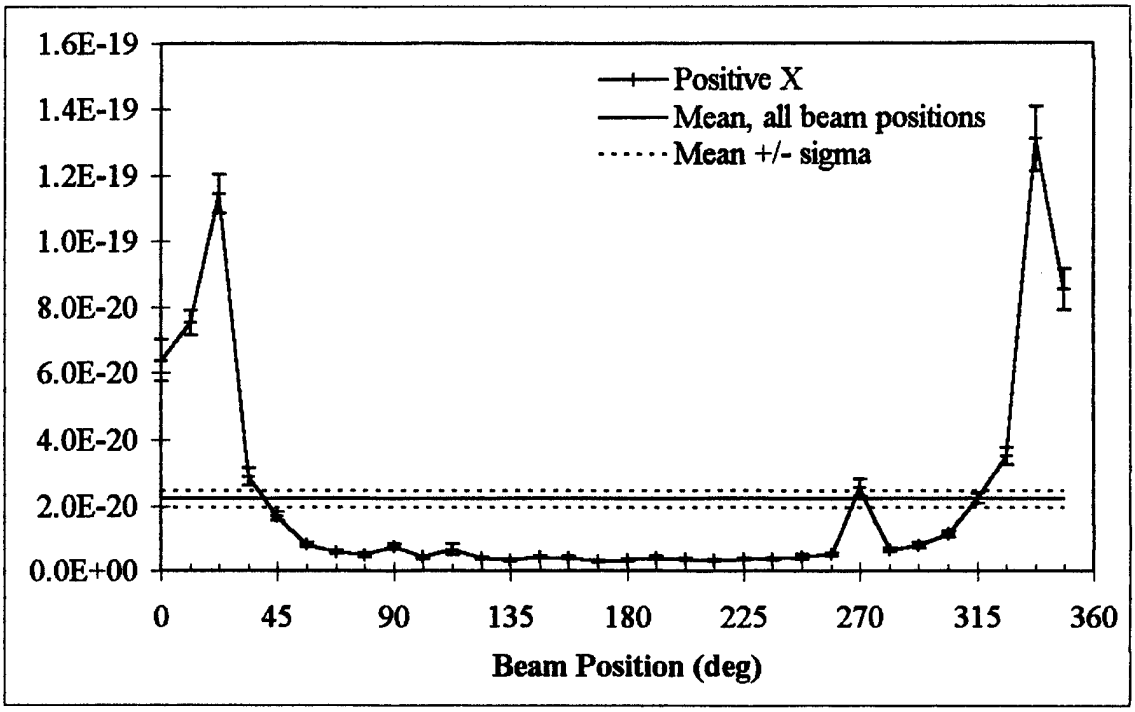

Figure D.1 Positive x exposure (R/s/particle), CT in X-ray room. 0 degree direct beam position.

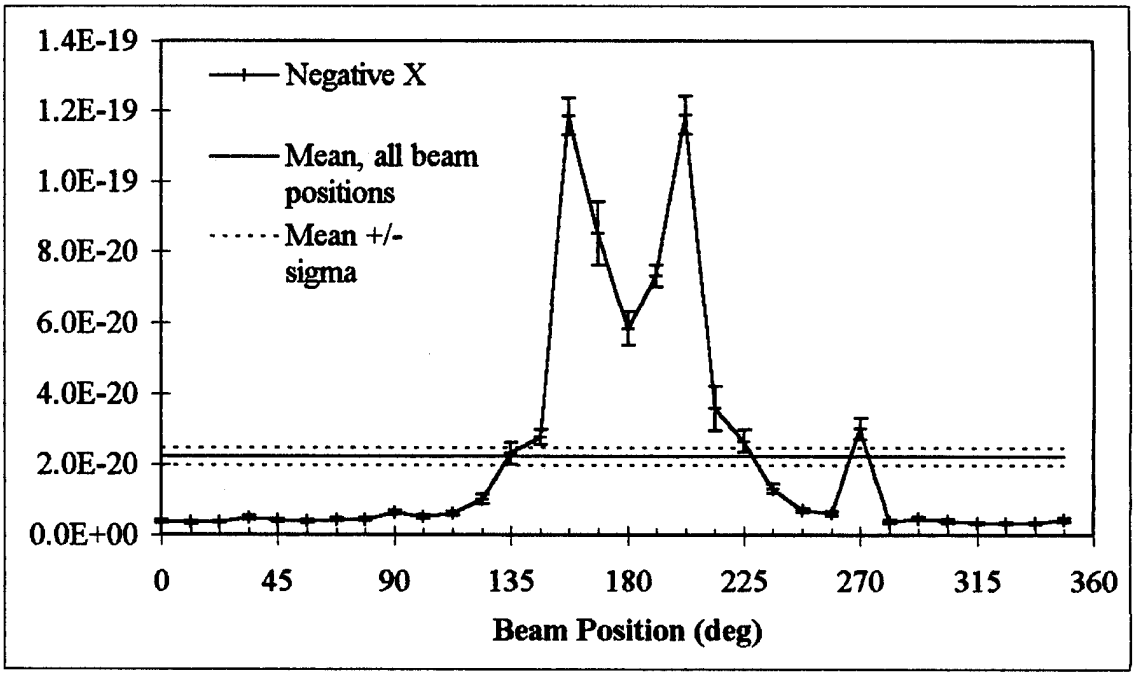

Figure D.2 Negative x exposure (R/s/particle) for CT in X-ray room. 180 degree direct beam position.

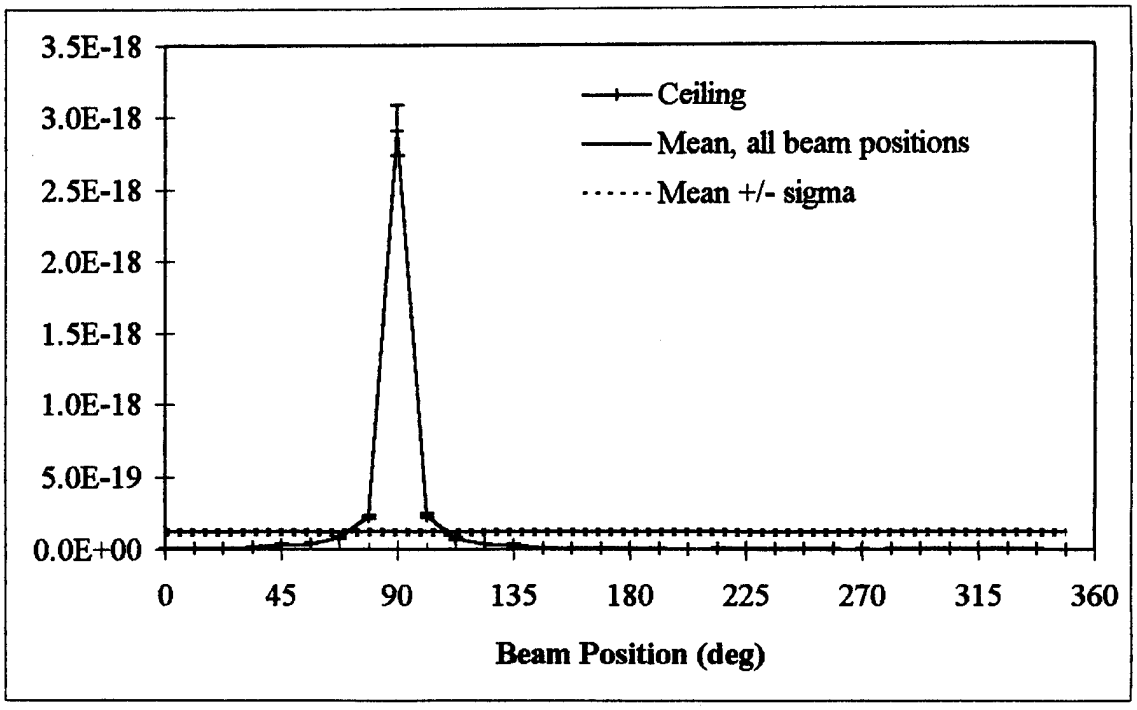

Figure D.3 Ceiling exposure (R/s/particle) for CT in X-ray room. 90 degree direct beam position.

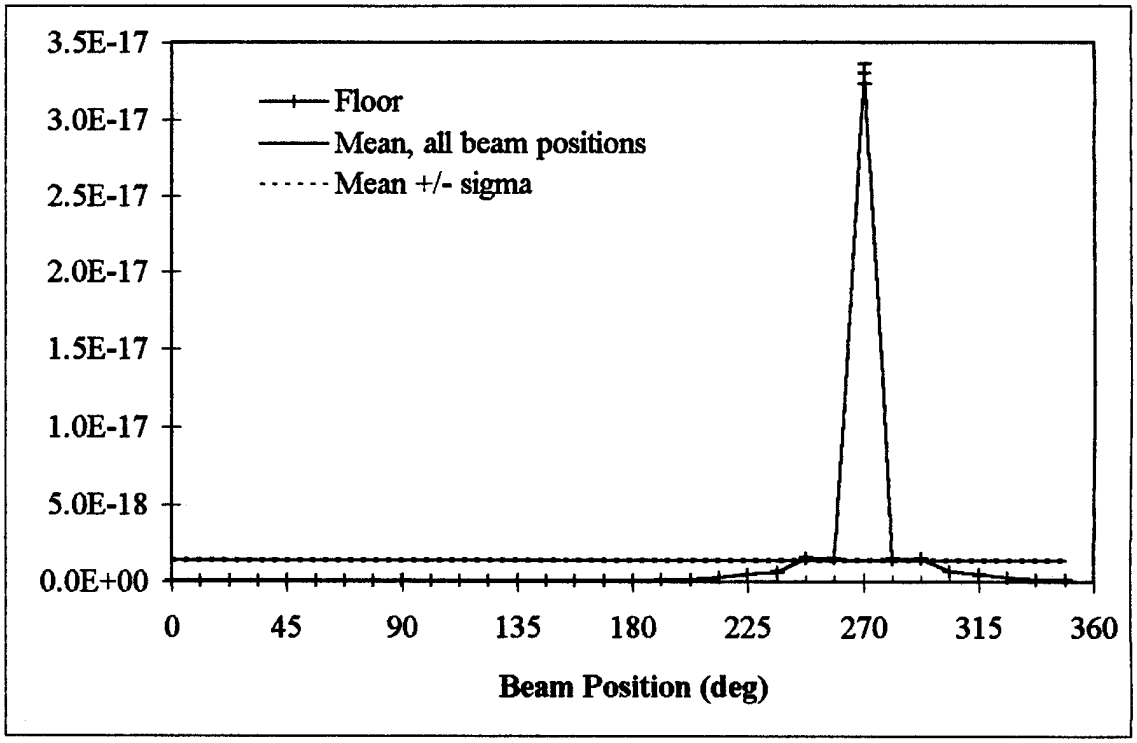

Figure D.4 Floor exposure(R/s/particle) for CT in X-ray room. 270 degree direct beam position.

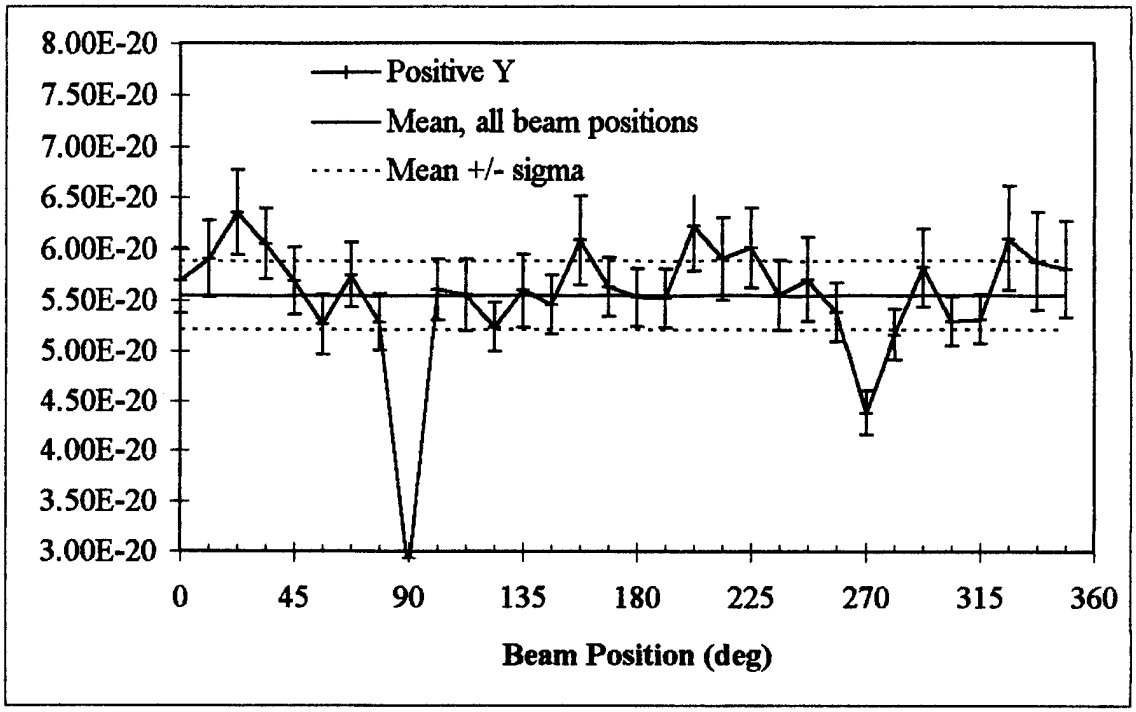

Figure D.5 Positive y exposure(R/s/particle) for CT in X-ray room. No direct beam position.

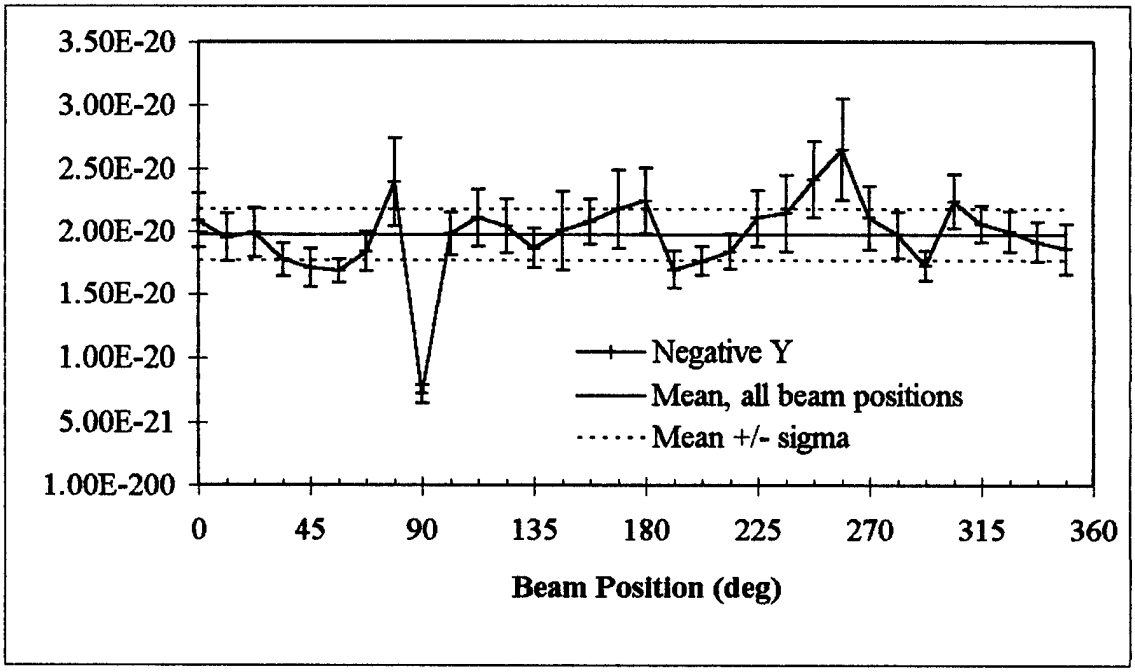

Figure D.6 Negative y exposure (R/s/particle) for CT in X-ray room. No degree direct beam position.

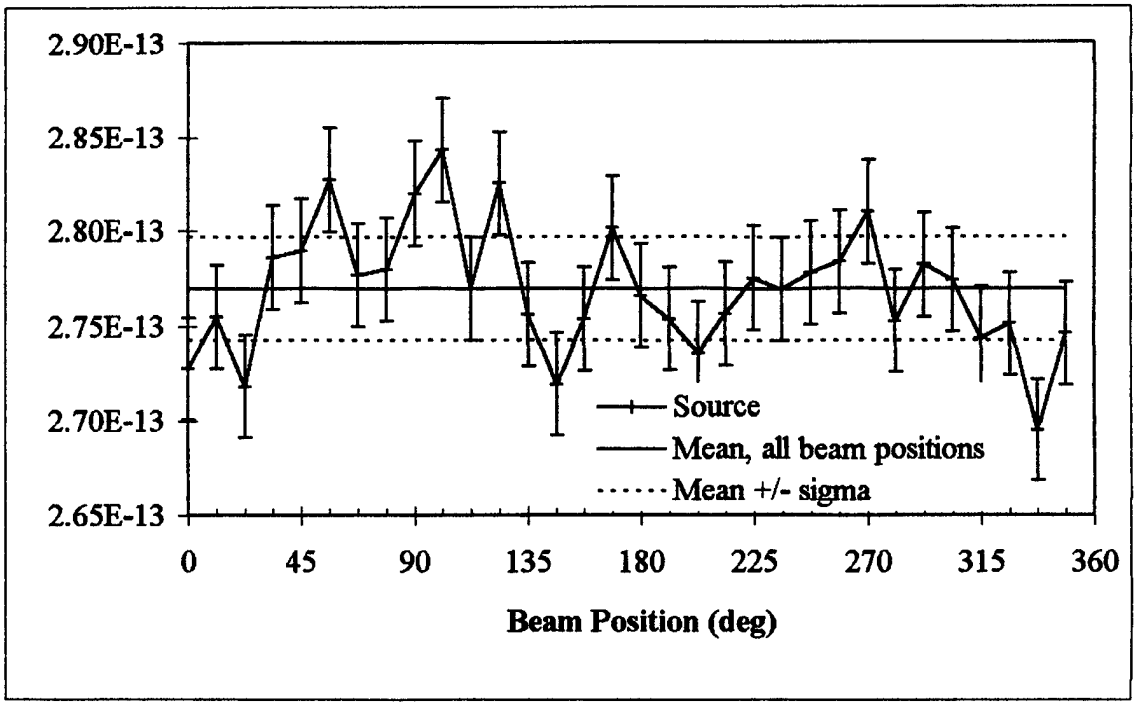

Figure D.7 Source exposure (R/s/particle) for CT in X-ray room. This is representative of source detector tallies for all analyses.

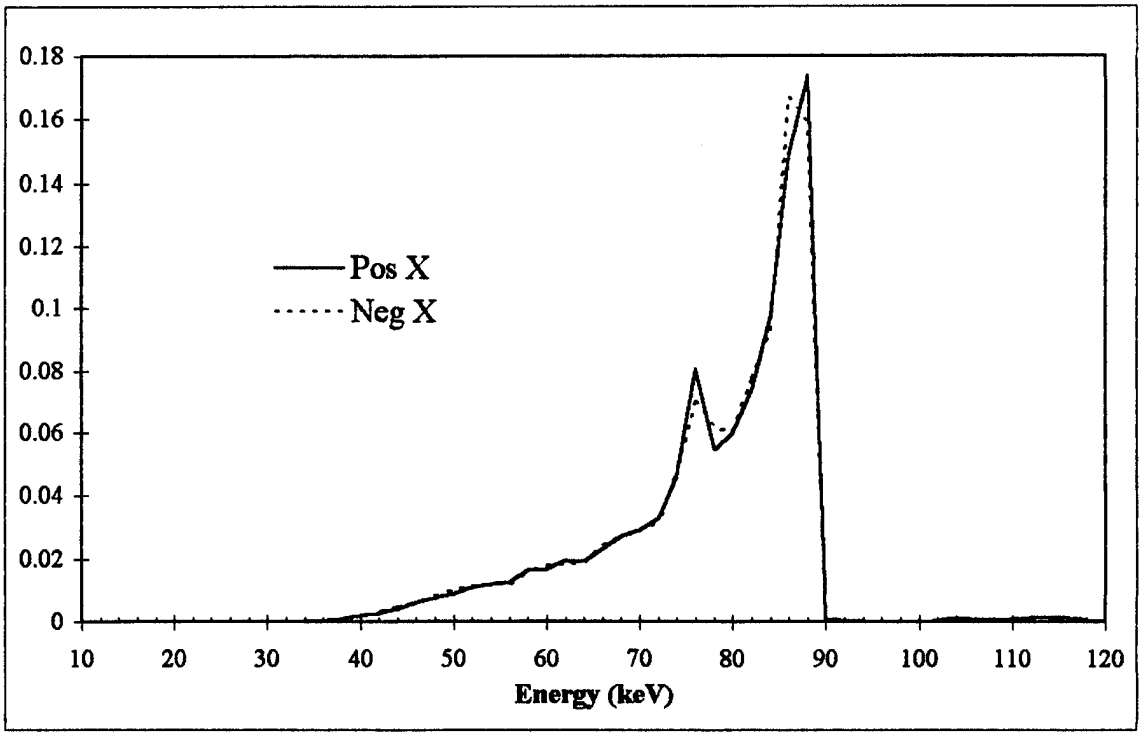

Figure D.8 Positive and negative x detector normalized average spectra without Roentgen conversion for CT in X-ray room.

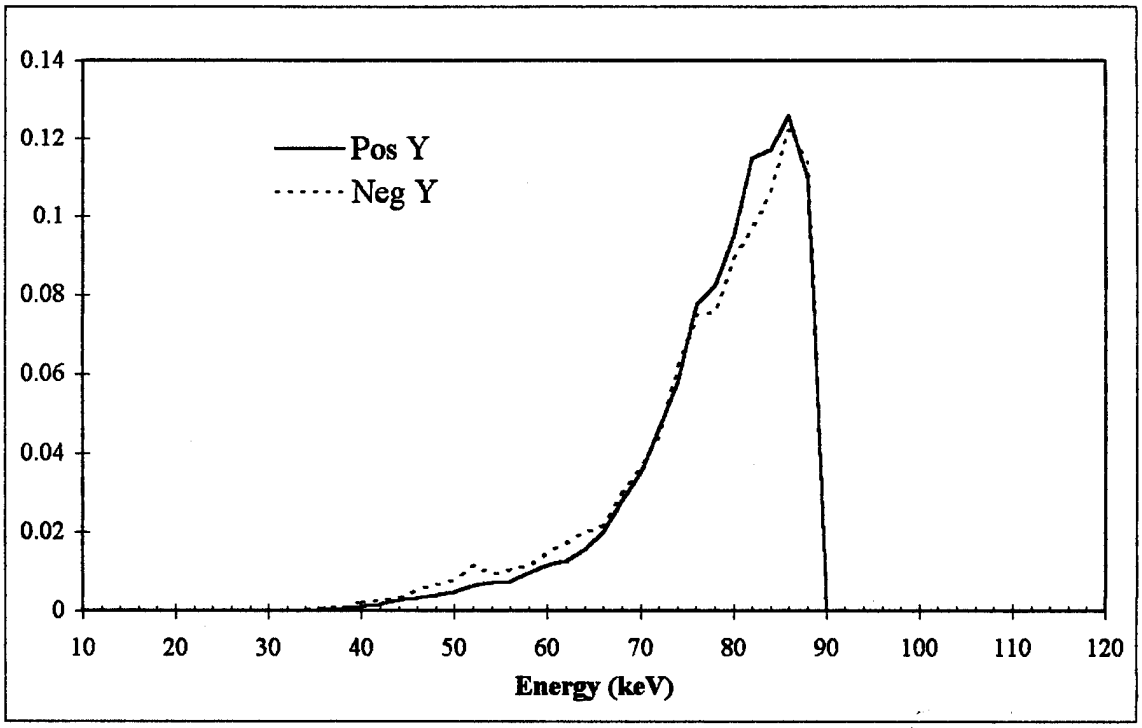

Figure D.9 Positive and negative y detector normalized average spectra without Roentgen conversion for CT in X-ray room.

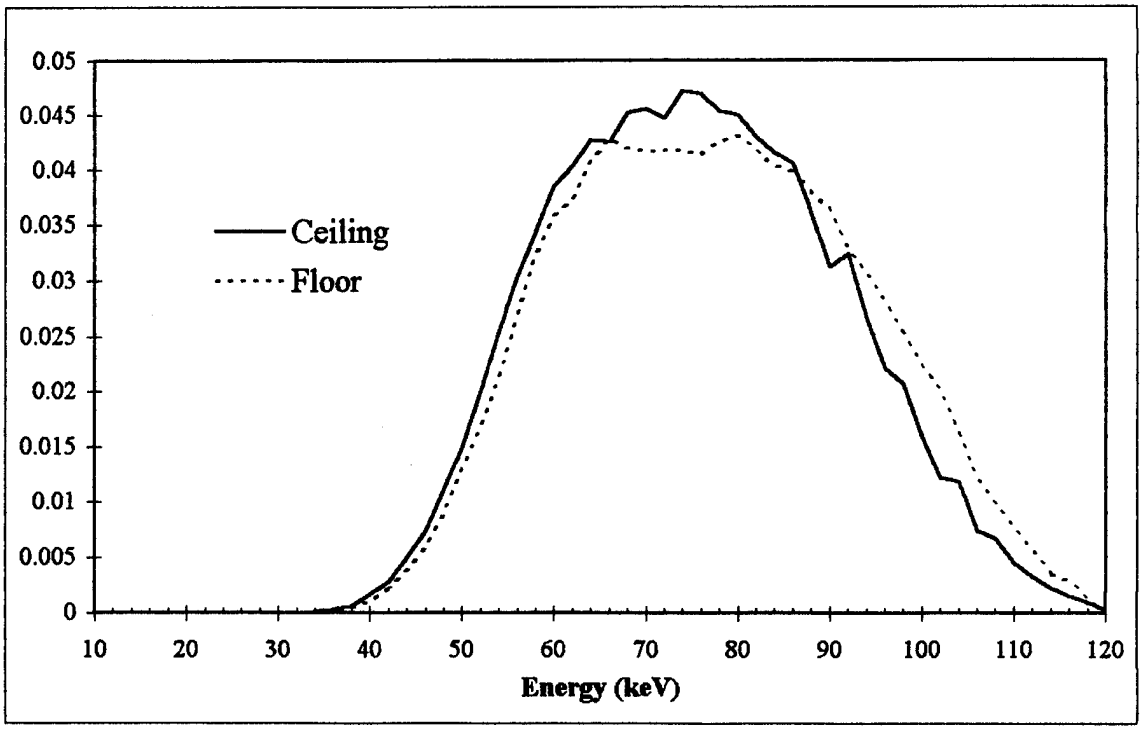

Figure D.10 Ceiling and floor detector normalized average spectra without Roentgen conversion for CT in X-ray room.

Appendix E: CT Inside WPMC, Head Scan

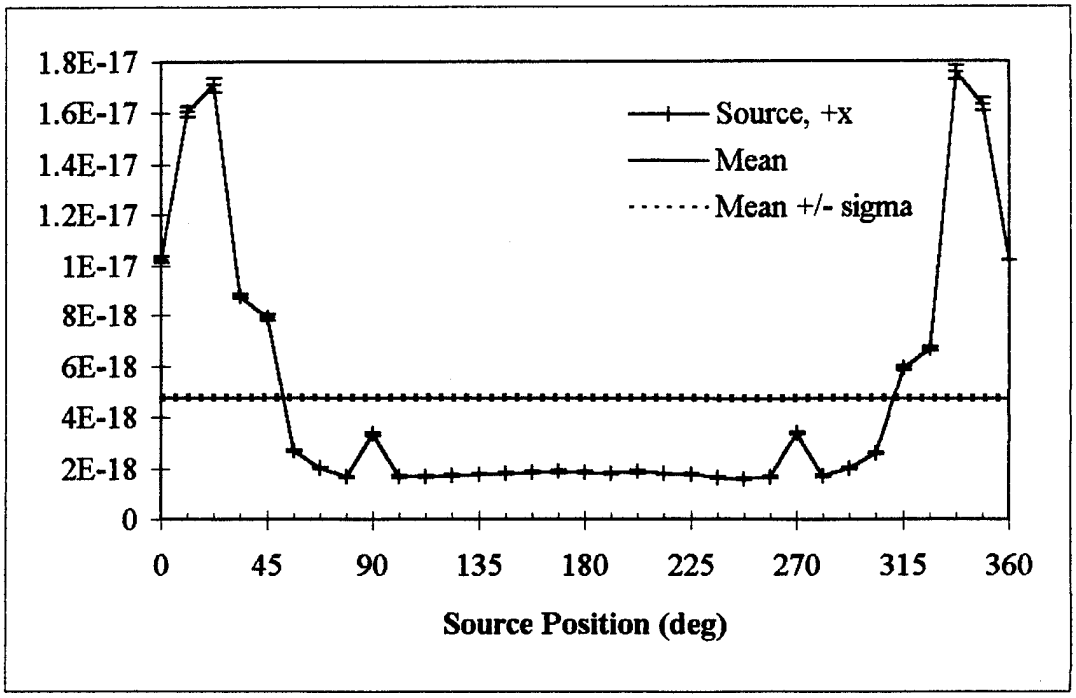

Figure E.1 Exposure (R/s/particle) for positive x source axis detector inside CT suite at WPMC, head scan. 0 degree direct beam.

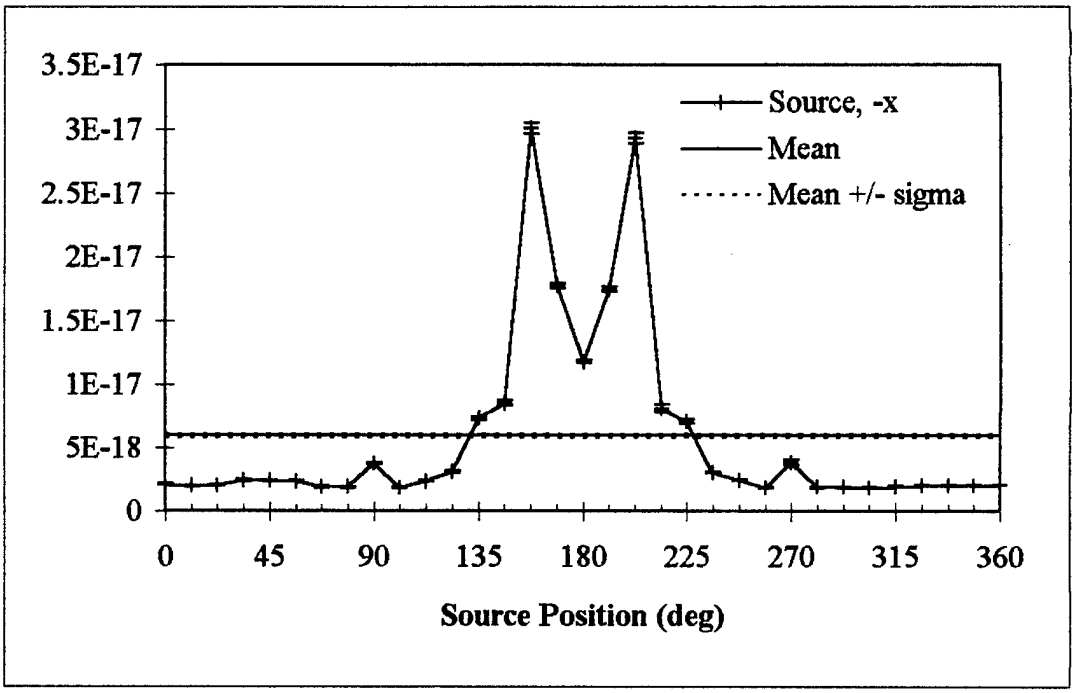

Figure E.2. Exposure (R/s/particle) for negative x source axis detector inside CT suite at WPMC, head scan, direct beam at 180 degrees.

Appendix E: CT Inside WPMC, Head Scan

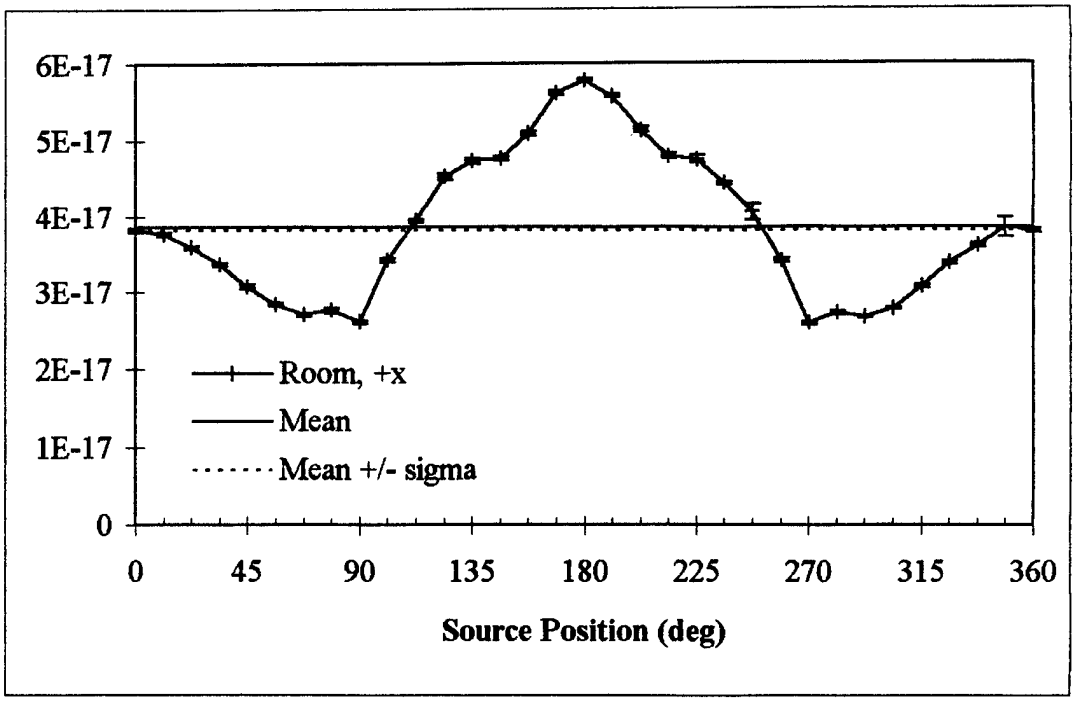

Figure E.3 Exposure (R/s/particle) for positive x room axis detector inside CT suite at WPMC, head scan, no direct beam.

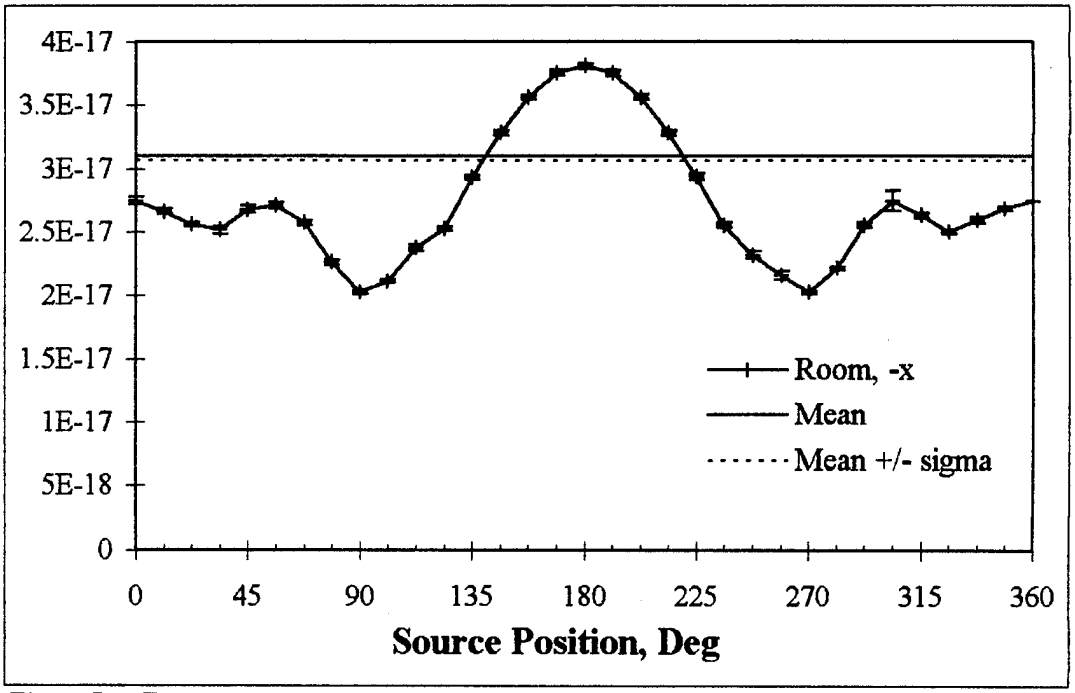

Figure E.4 Exposure (R/s/particle) for negative x room axis detector inside CT suite at WPMC, head scan, no direct beam.

Appendix E: CT Inside WPMC, Head Scan

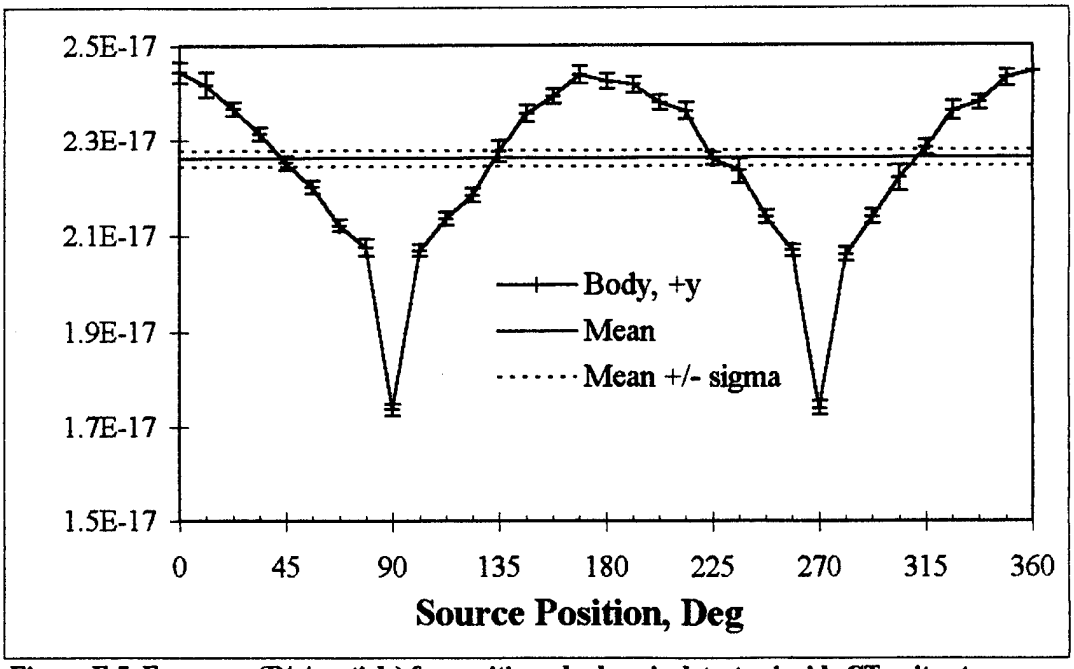

Figure E.5 Exposure (R/s/particle) for positive y body axis detector inside CT suite at WPMC, head scan, no direct beam.

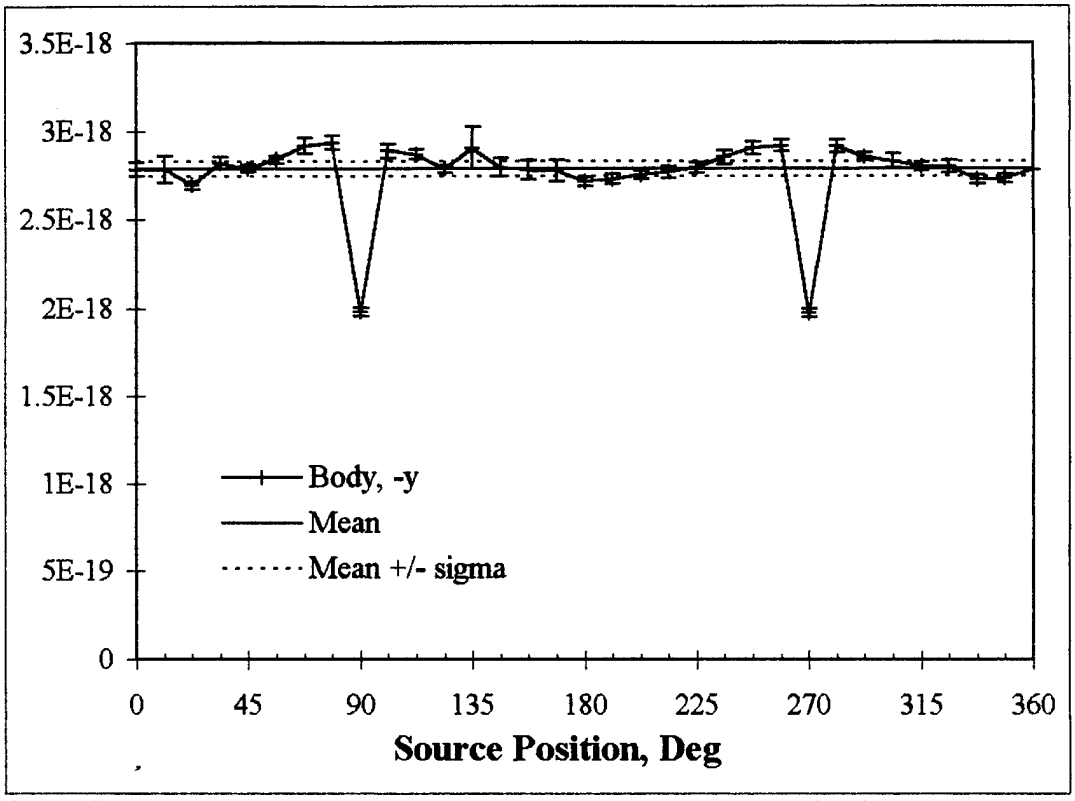

Figure E.6 Exposure (R/s/particle) for negative y body axis detector inside CT suite at WPMC, head scan, no direct beam.

Appendix E: CT Inside WPMC, Head Scan

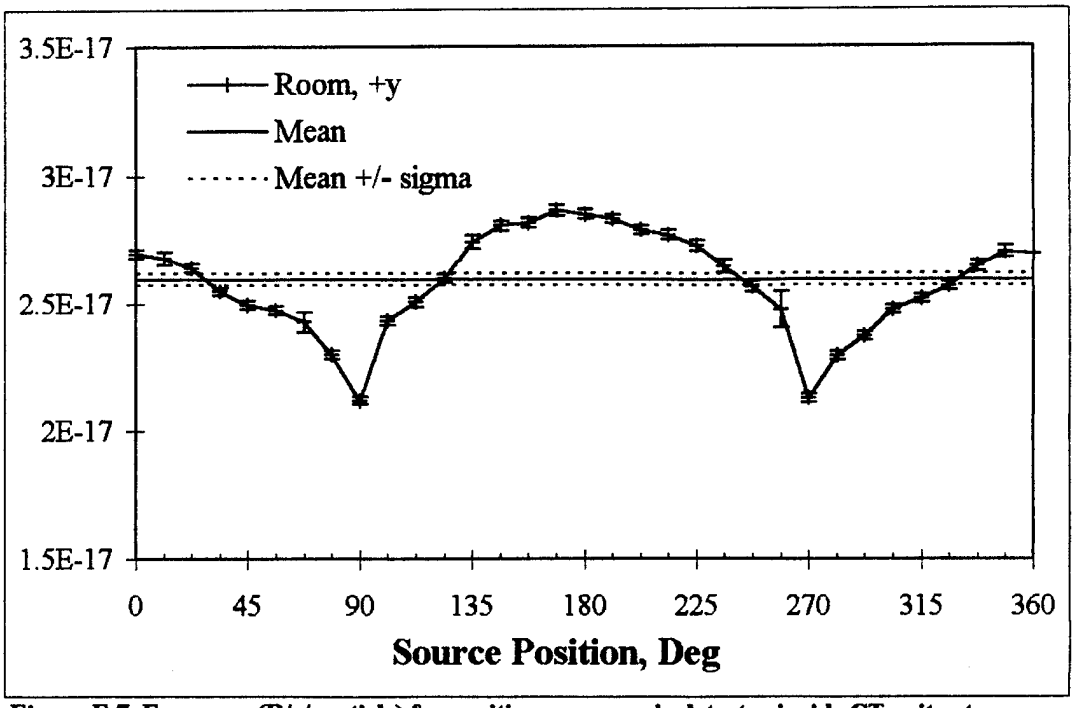

Figure E.7 Exposure (R/s/particle) for positive y room axis detector inside CT suite at WPMC, head scan, no direct beam.

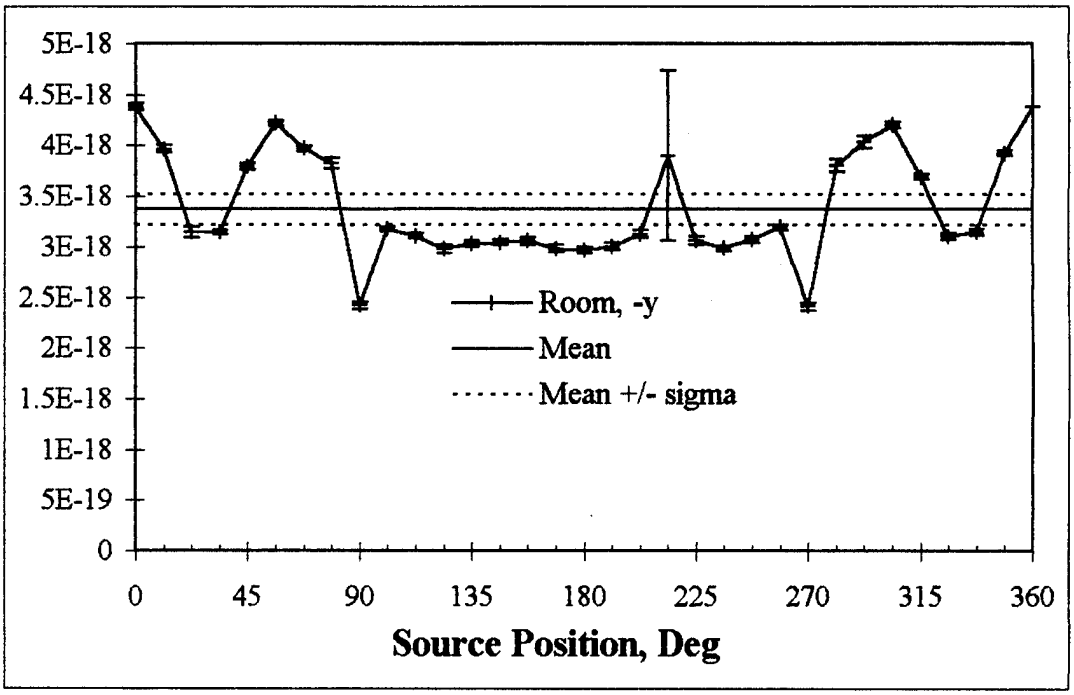

Figure E.8 Exposure (R/s/particle) for negative y room axis detector inside CT suite at WPMC, head scan. No direct beam.

Appendix E: CT Inside WPMC, Head Scan

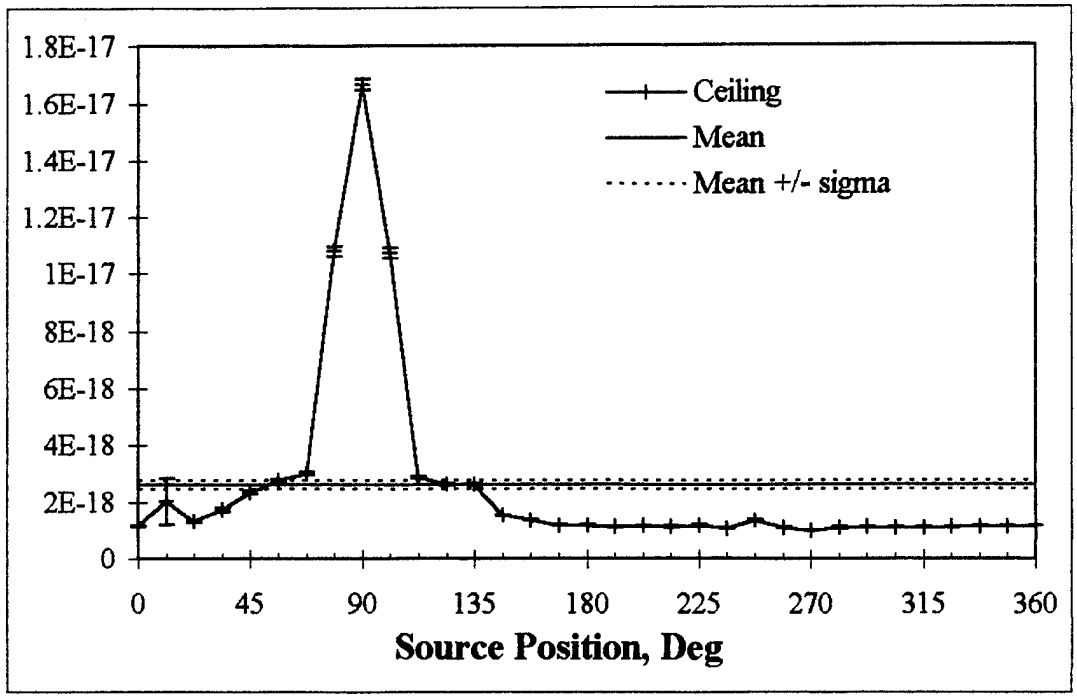

Figure E.9 Exposure (R/s/particle) for ceiling detector inside CT suite at WPMC, head scan. 90 degree direct beam.

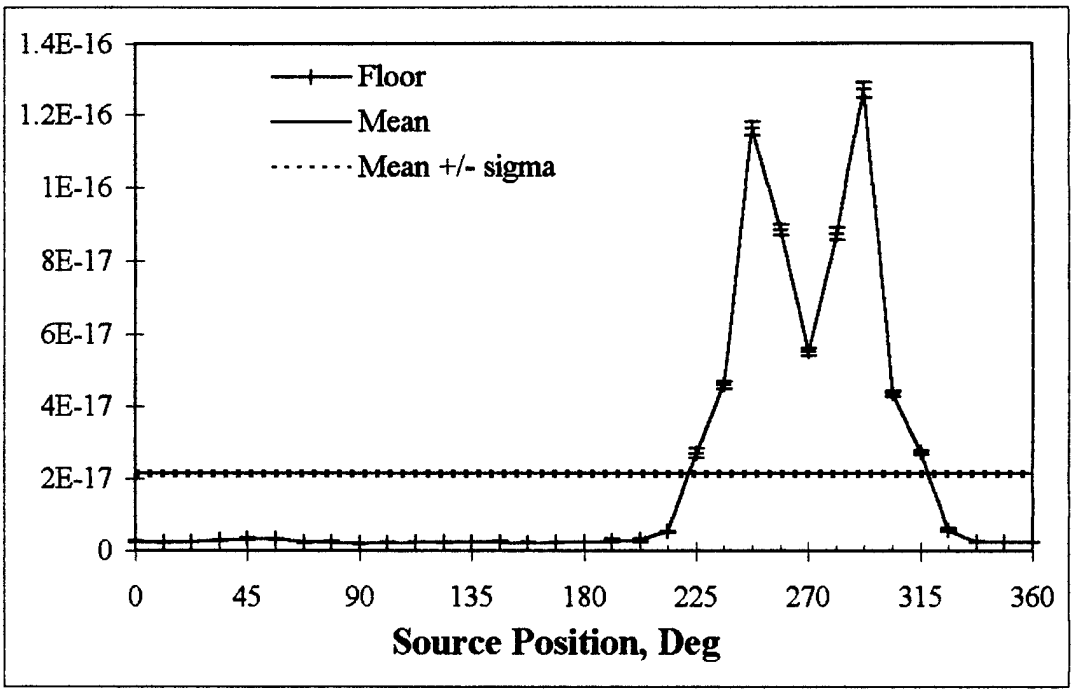

Figure E.10. Exposure (R/s/particle) for floor detector inside CT suite at WPMC, head scan. 270 degree direct beam.

Appendix E: Inside WPMC CT Suite, Head Scan

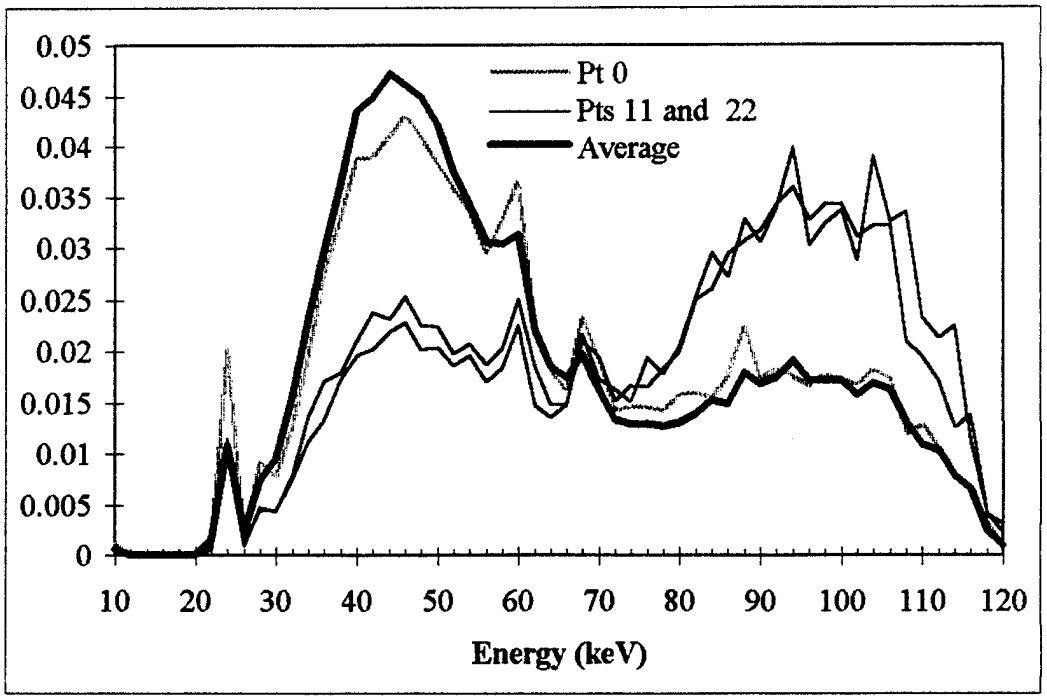

Figure E.11 Average normalized spectrum and spectra for beam positions 0, 11 and 22 for positive x source axis detectors inside WPMC CT suite for head slice

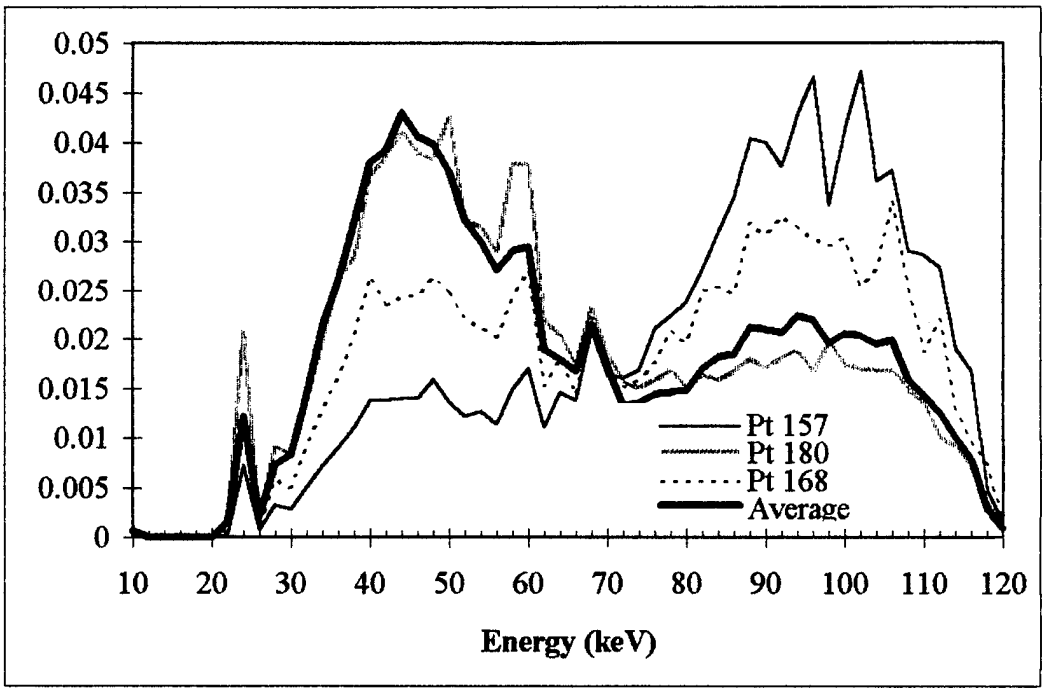

Figure E.12 Average normalized spectrum and spectra for beam positions 157, 168 and 180 for positive x source axis detectors inside WPMC CT suite for head slice

Appendix E: Inside WPMC CT Suite, Head Scan

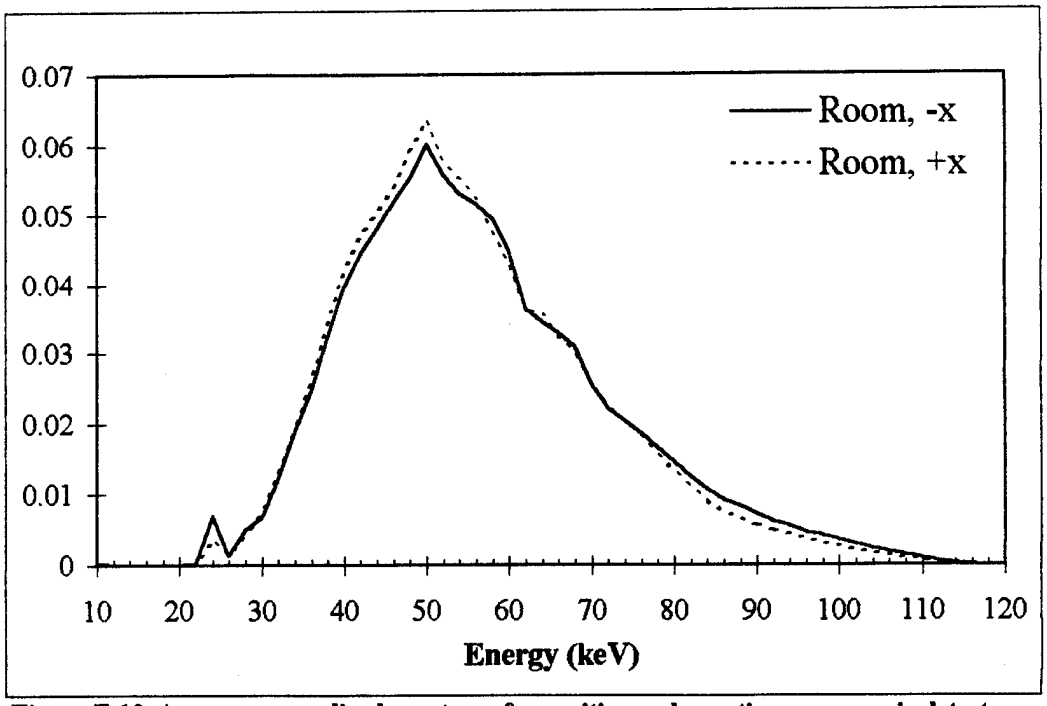

Figure E.13 Average normalized spectrum for positive and negative x room axis detectors inside WPMC CT suite for head slice.

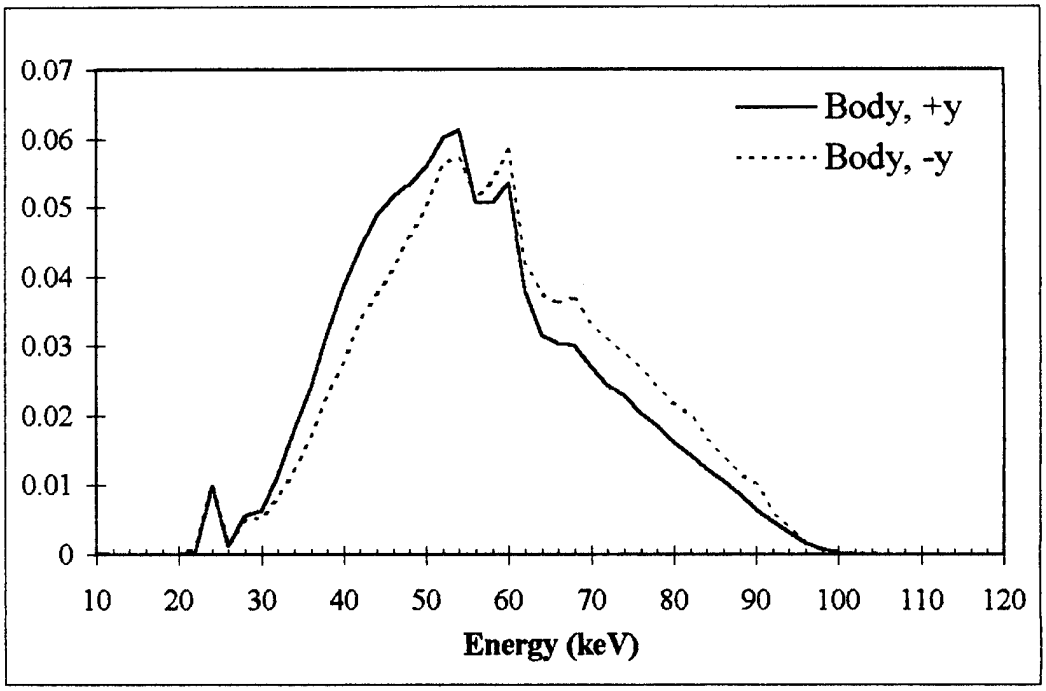

Figure E.14 Average normalized spectrum for positive and negative y body axis detectors inside WPMC CT suite for head slice.

Appendix E: Inside WPMC CT Suite, Head Scan

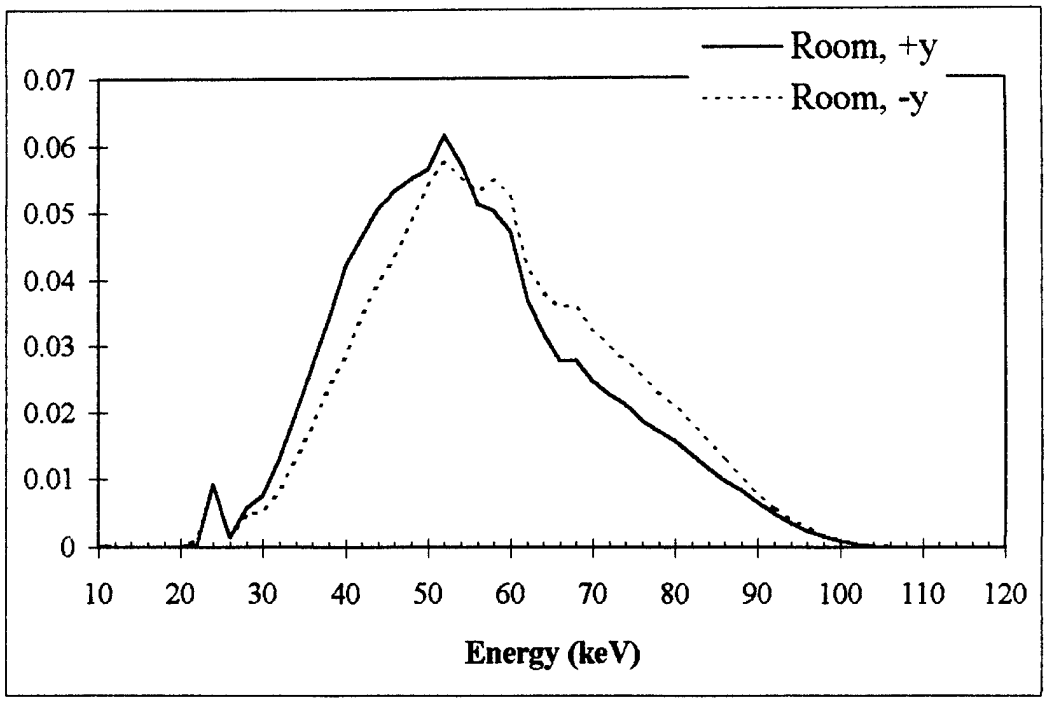

Figure E.15 Average normalized spectrum for positive and negative y room axis detectors inside WPMC CT suite for head slice

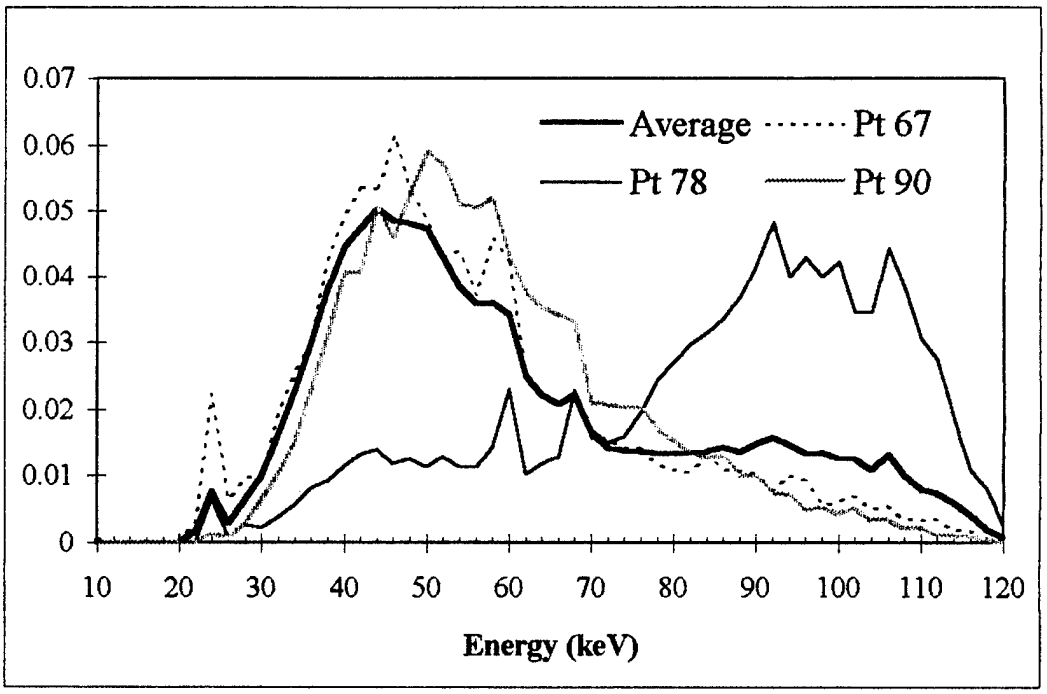

Figure E.16 Average normalized spectrum and individual spectra for beam positions 78, 90 and 101 for ceiling detector inside WPMC CT suite for head slice.

Appendix E: Inside WPMC CT Suite, Head Scan

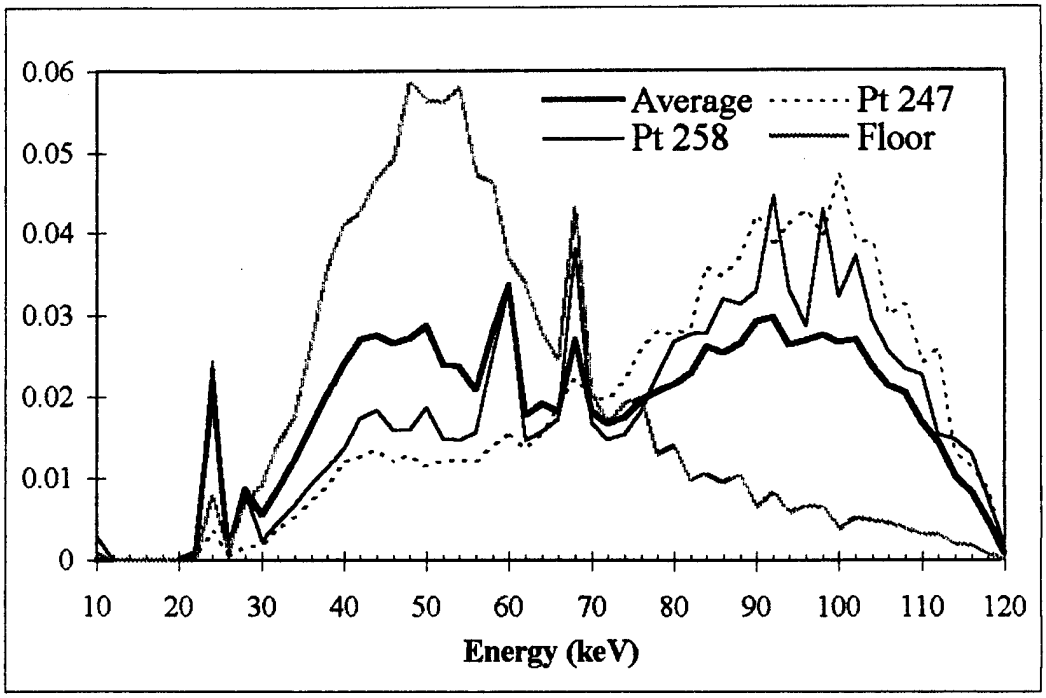

Figure E.17 Average normalized spectrum and individual spectra for beam positions 247 through 292 for floor detector inside WPMC CT suite for head slice.

Appendix F: Inside WPMC CT Suite, Abdomen Scan

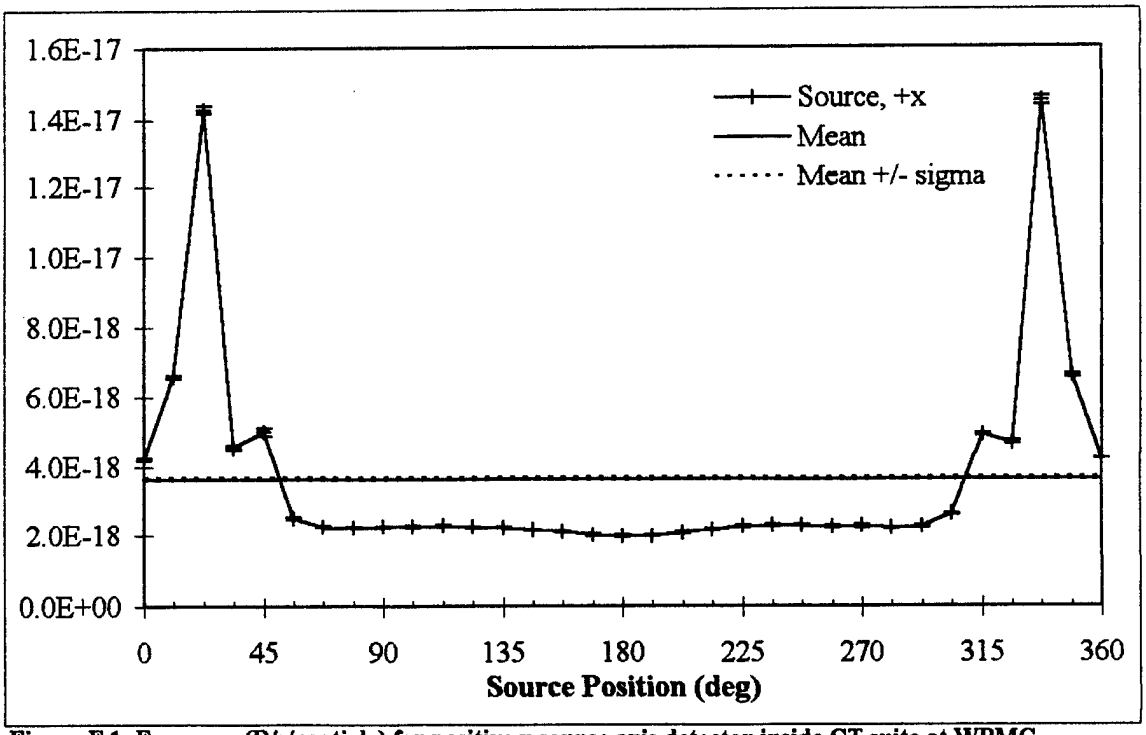

Figure F.1 Exposure (R/s/particle) for positive x source axis detector inside CT suite at WPMC, abdomen scan.

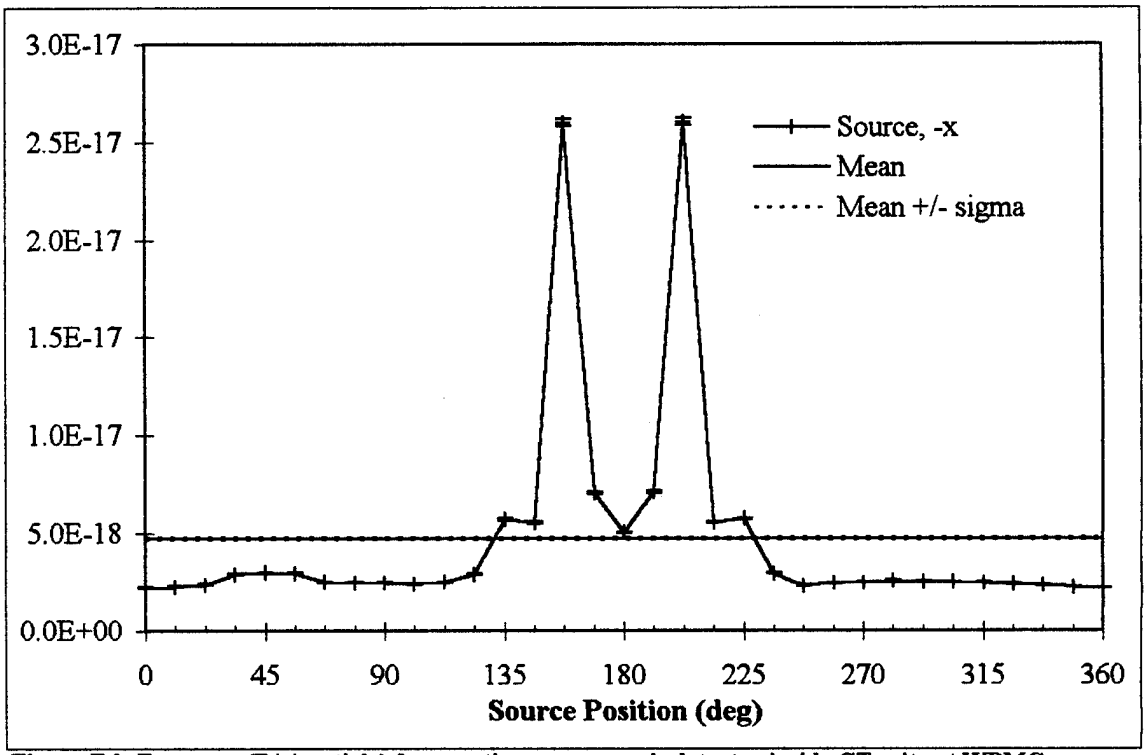

Figure F.2 Exposure (R/s/particle) for negative x source axis detector inside CT suite at WPMC, abdomen scan.

Appendix F: Inside WPMC CT Suite, Abdomen Scan

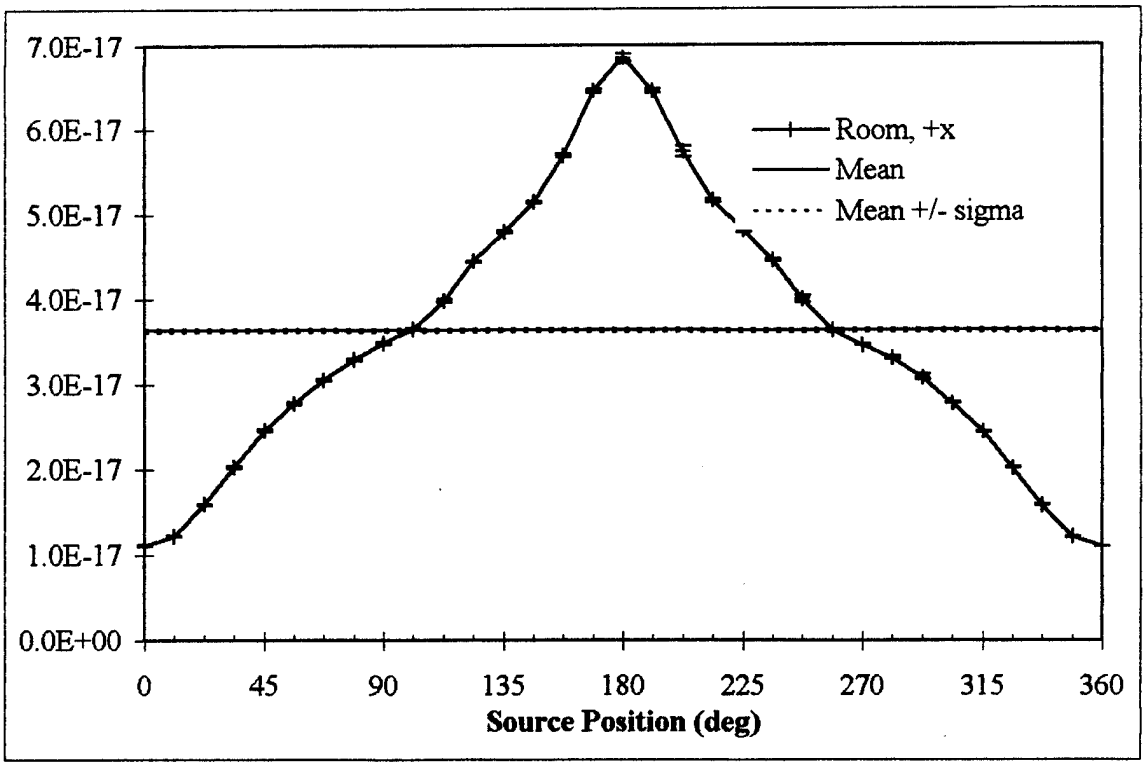

Figure F.3 Exposure (R/s/particle) for positive x room axis detector inside CT suite at WPMC, abdomen scan.

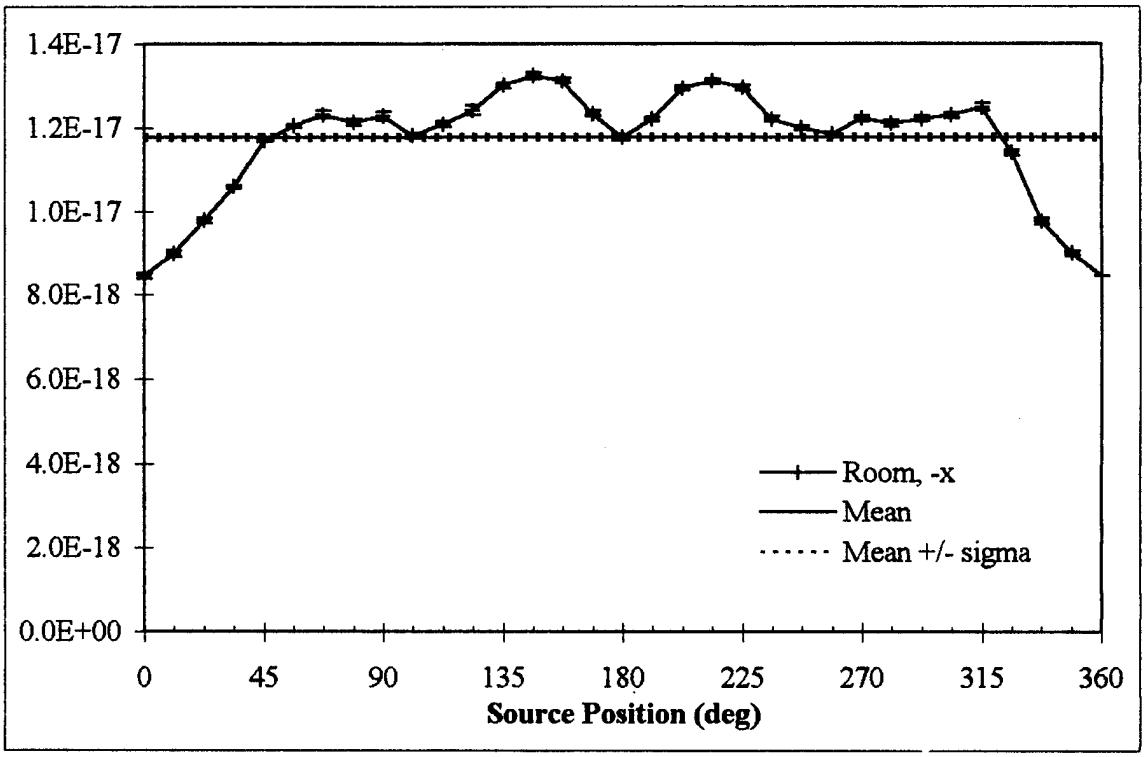

Figure F.4 Exposure (R/s/particle) for negative x room axis detector inside CT suite at WPMC, abdomen scan.

Appendix F: Inside WPMC CT Suite, Abdomen Scan

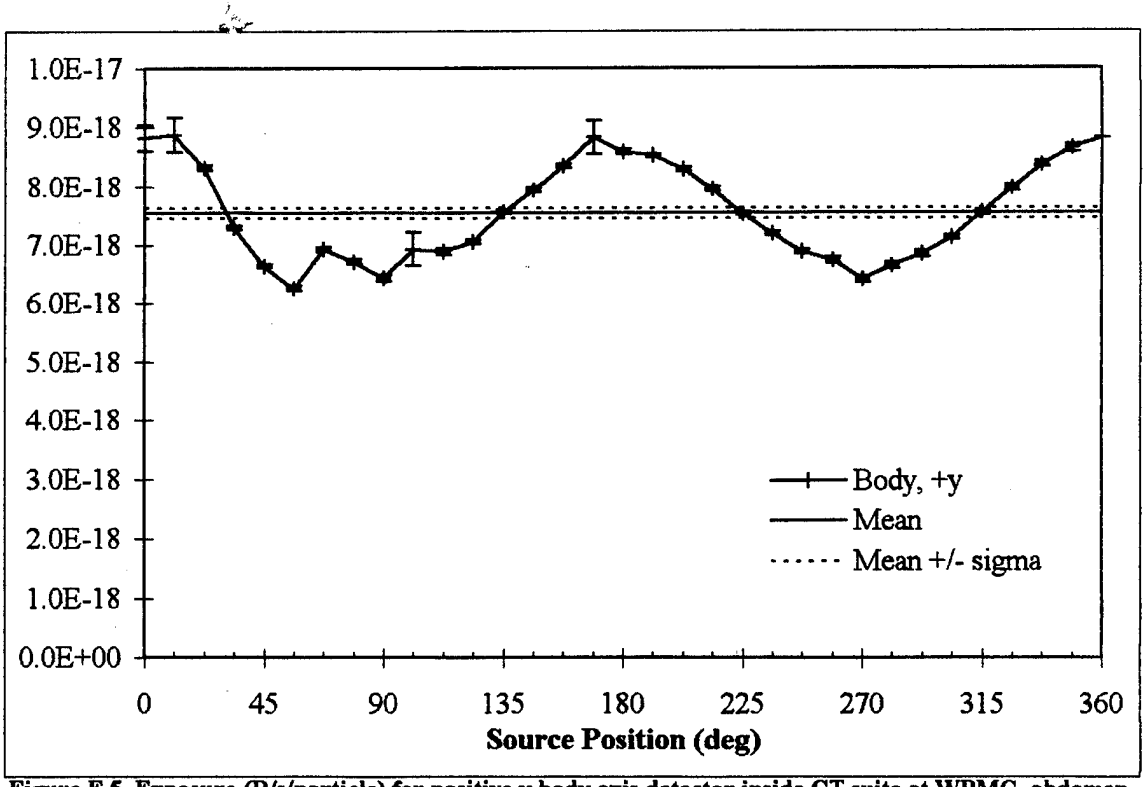

Figure F.5 Exposure (R/s/particle) for positive y body axis detector inside CT suite at WPMC, abdomen scan.

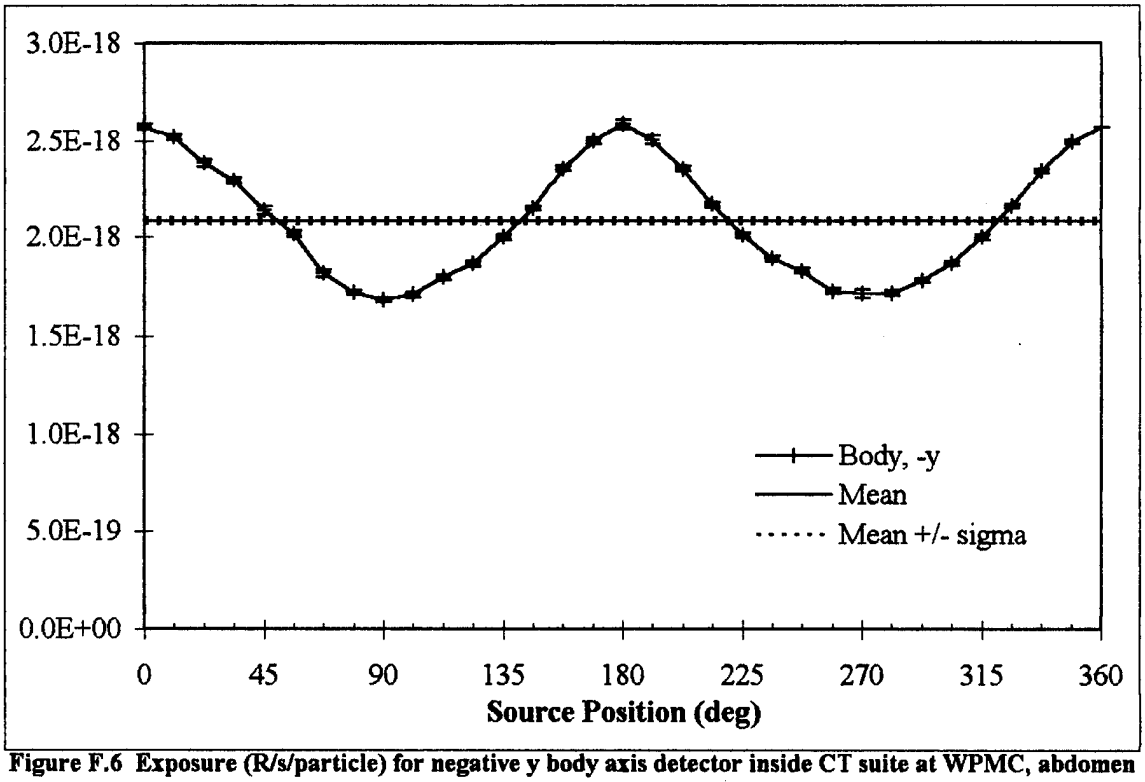

Figure F.6 Exposure (R/s/particle) for negative y body axis detector inside CT suite at WPMC, abdomen scan.

Appendix F: Inside WPMC CT Suite, Abdomen Scan

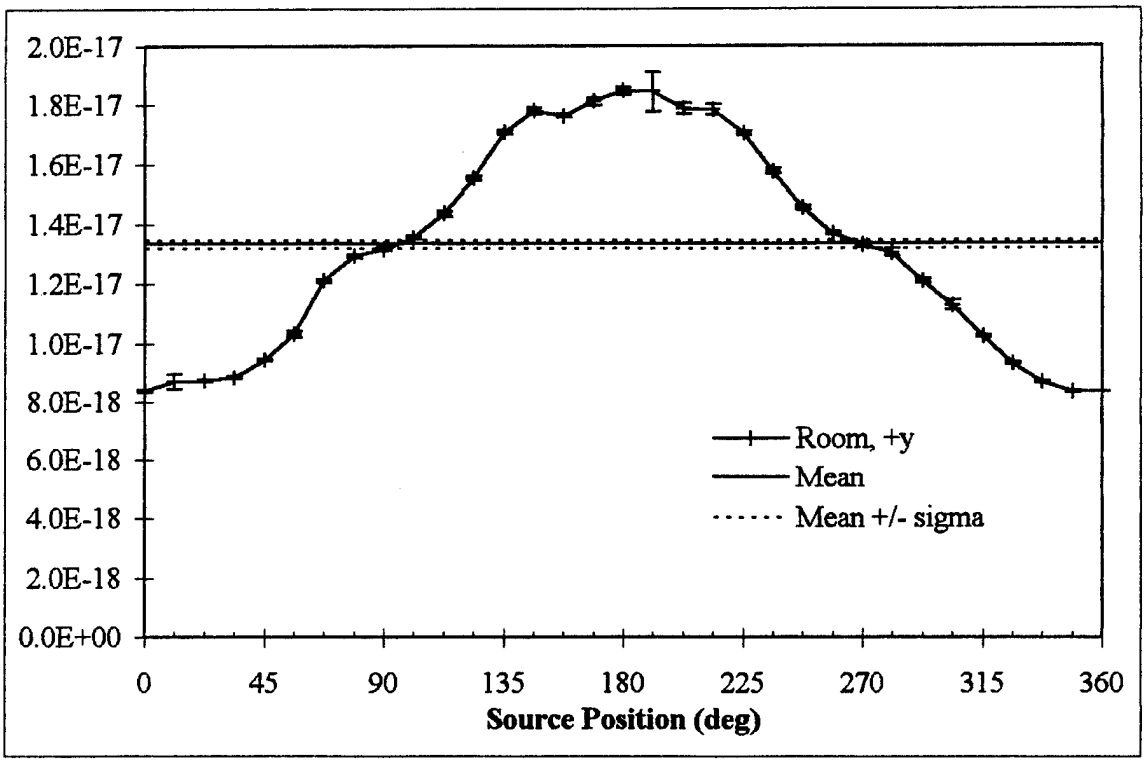

Figure F.7 Exposure (R/s/particle) for positive y room axis detector inside CT suite at WPMC, abdomen scan.

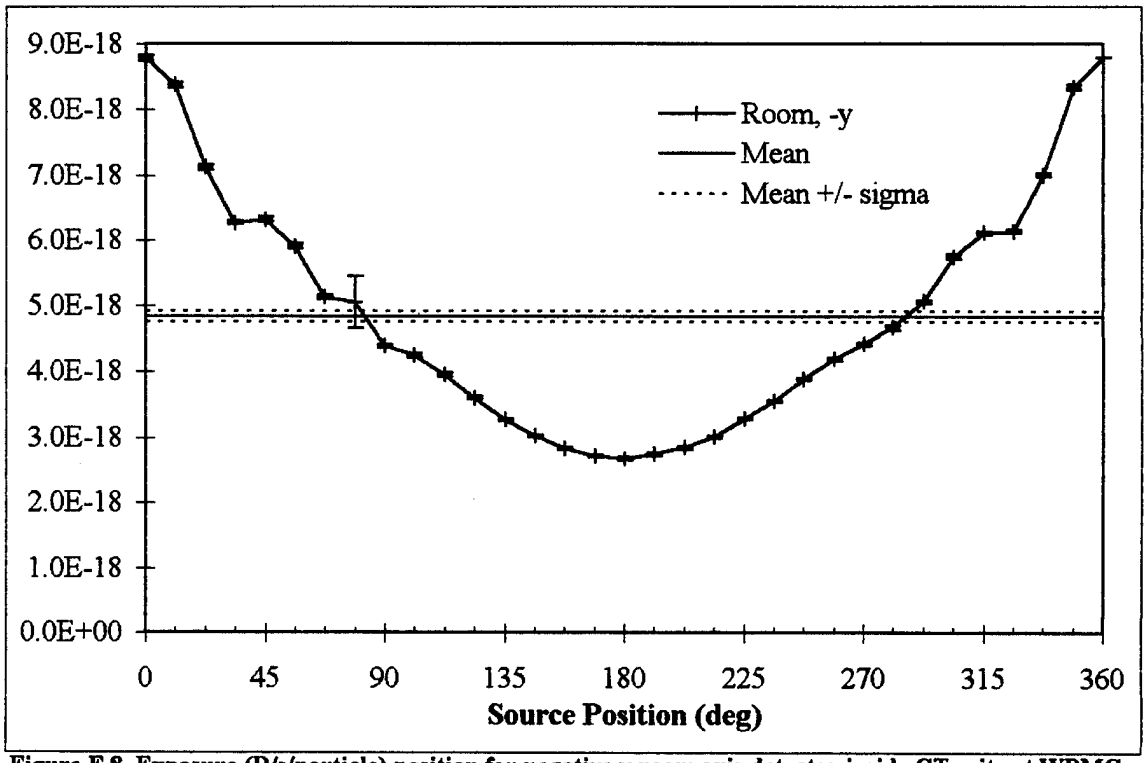

Figure F.8 Exposure (R/s/particle) position for negative y room axis detector inside CT suite at WPMC, abdomen scan.

Appendix F: Inside WPMC CT Suite, Abdomen Scan

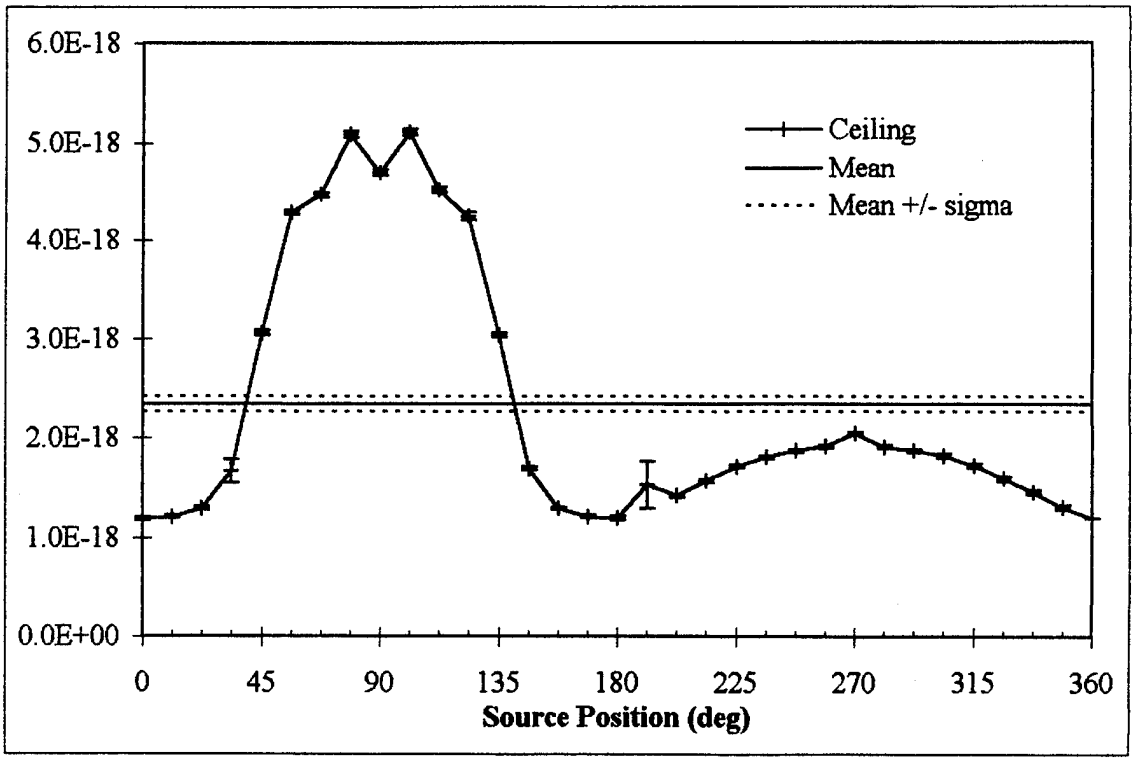

Figure F.9 Exposure (R/s/particle) for ceiling detector inside CT suite at WPMC, abdomen scan.

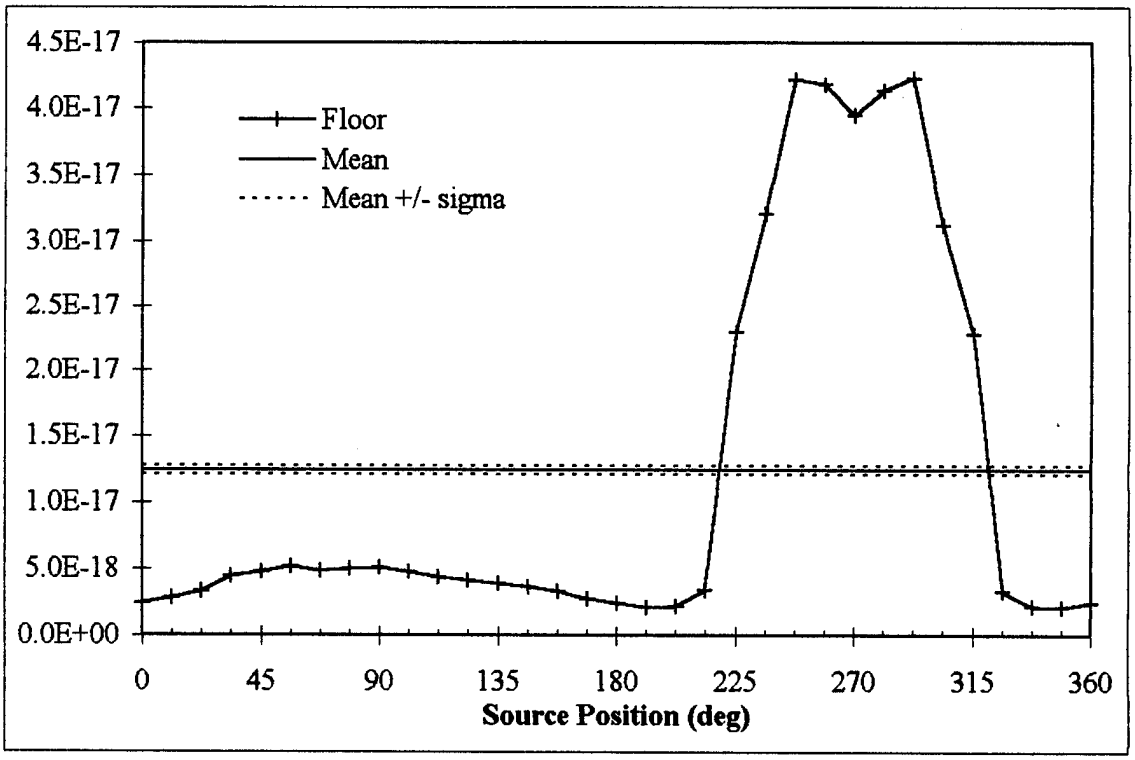

Figure F.10 Exposure (R/s/particle) for floor detector inside CT suite at WPMC, abdomen scan.

Appendix F: Inside WPMC CT Suite, Abdomen Scan

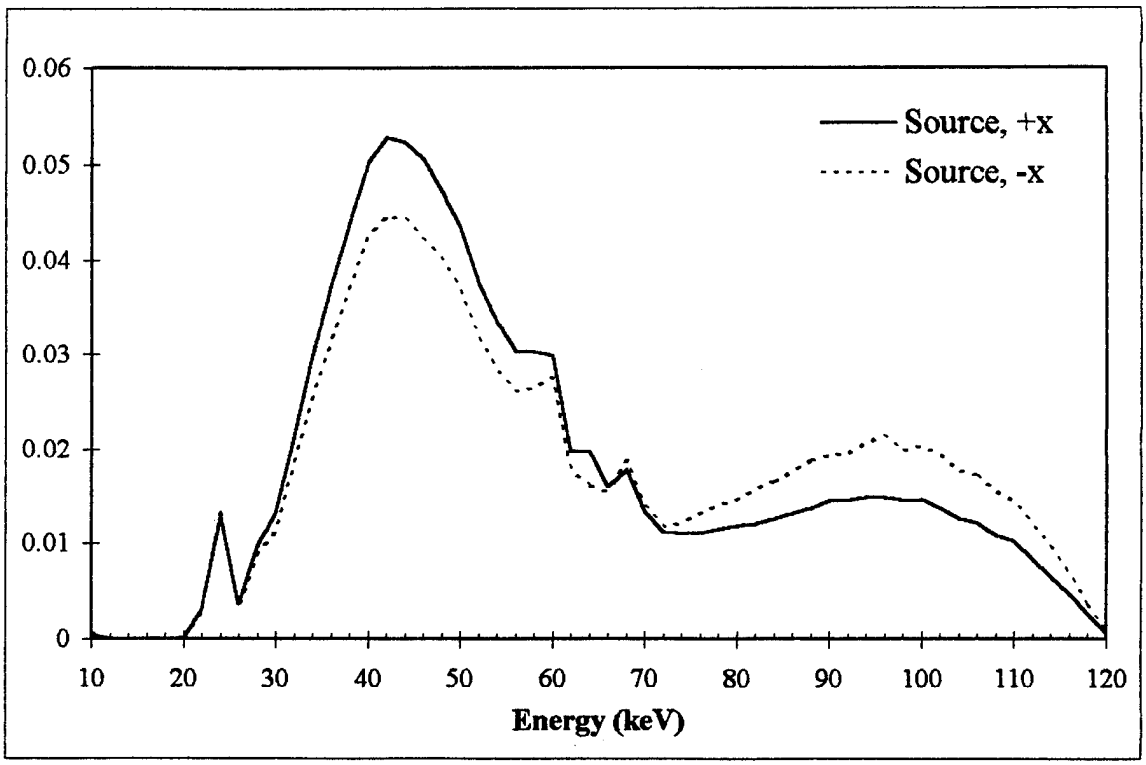

Figure F.11 Normalized average spectrum for positive and negative x source axis detectors inside CT suite at WPMC, abdomen scan.

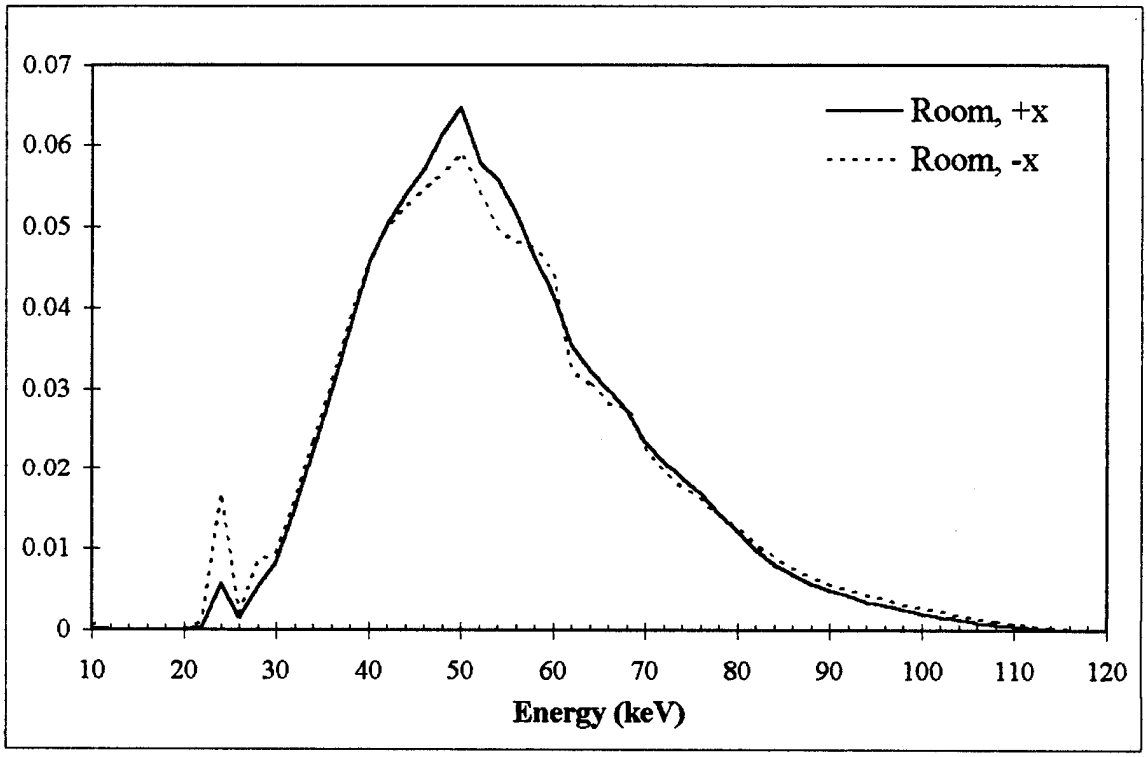

Figure F.12 Normalized average spectrum for positive and negative x room axis detectors inside CT suite at WPMC, abdomen scan.

Appendix F: Inside WPMC CT Suite, Abdomen Scan

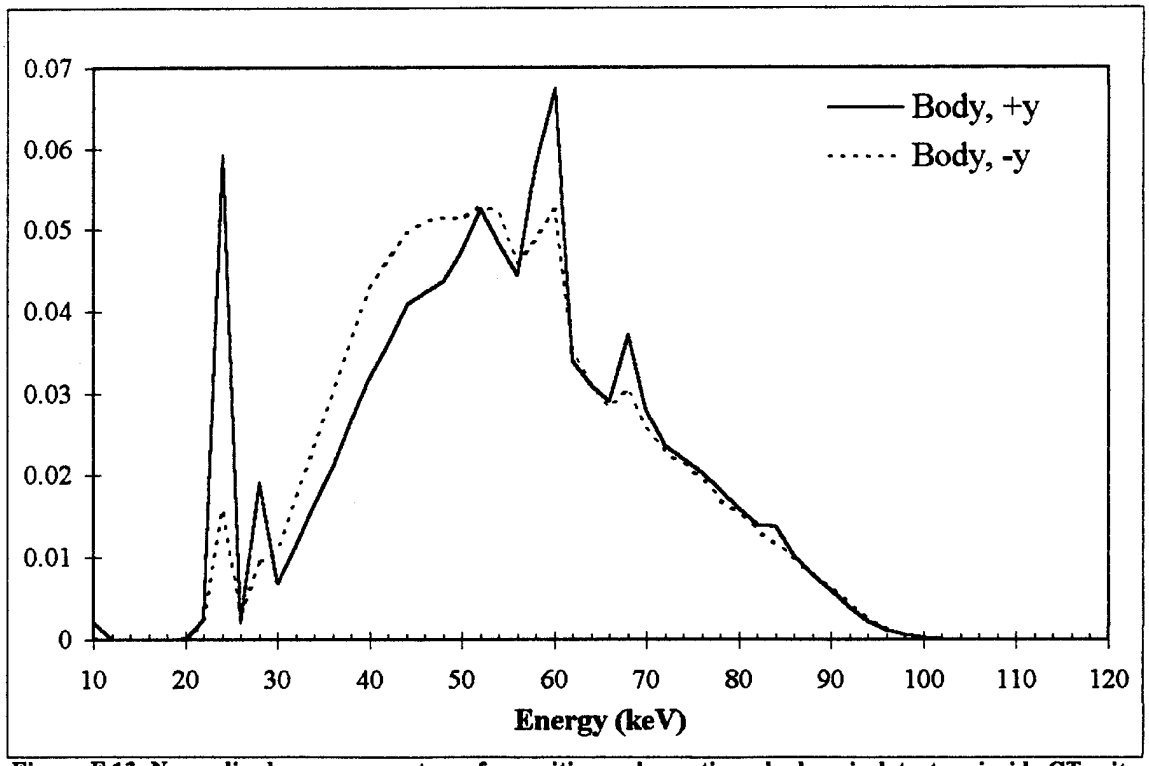

Figure F.13 Normalized average spectrum for positive and negative y body axis detectors inside CT suite at WPMC, abdomen scan.

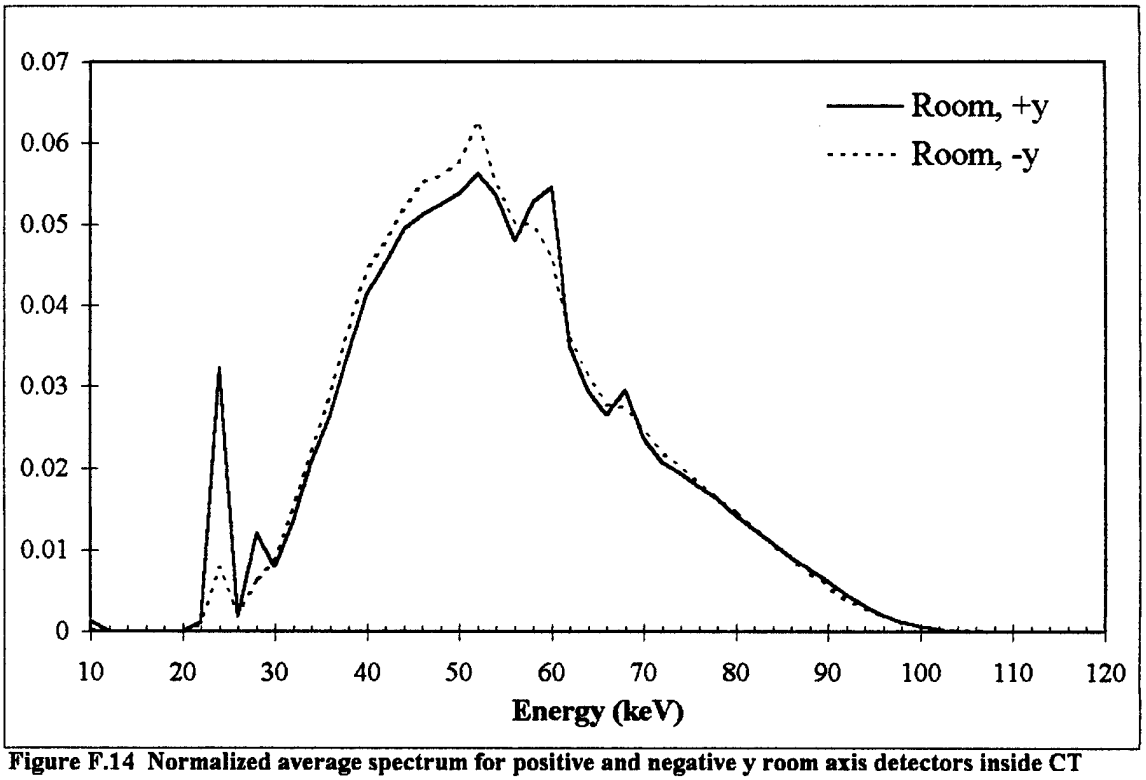

Figure F.14 Normalized average spectrum for positive and negative y room axis detectors inside CT suite at WPMC, abdomen scan.

Appendix F: Inside WPMC CT Suite, Abdomen Scan

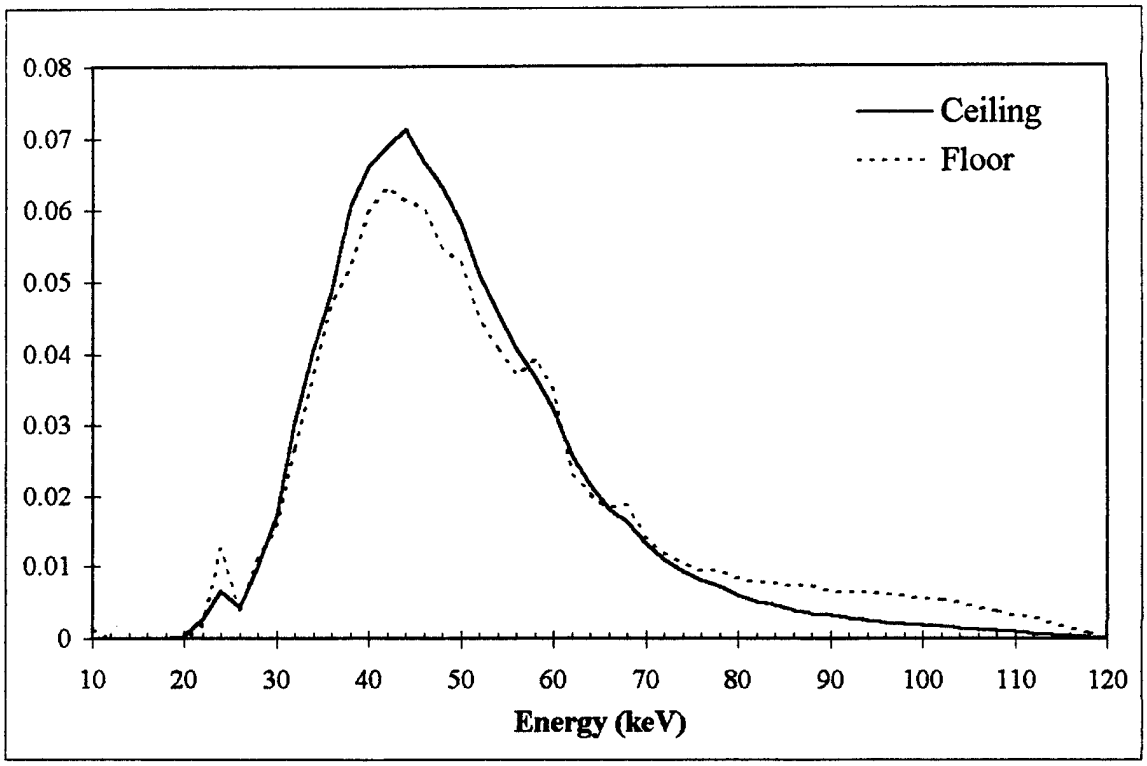

Figure F.15 Normalized average spectrum for ceiling and floor detectors inside CT suite at WPMC, abdomen scan.

Appendix G: WPMC CT Suite. 1/16" Lead Shielding, Head Scan

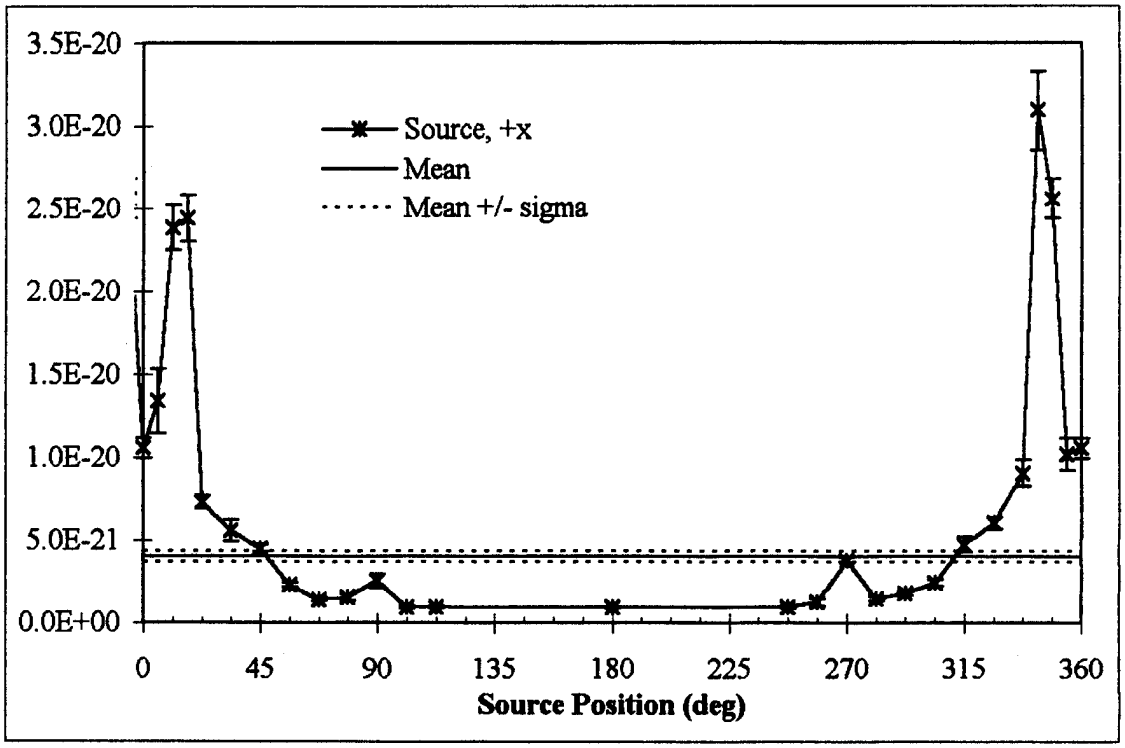

Figure G.1 Exposure (R/s/particle) at each source point for positive x source axis detector with CT in WPMC, 1/16" lead, head scan.

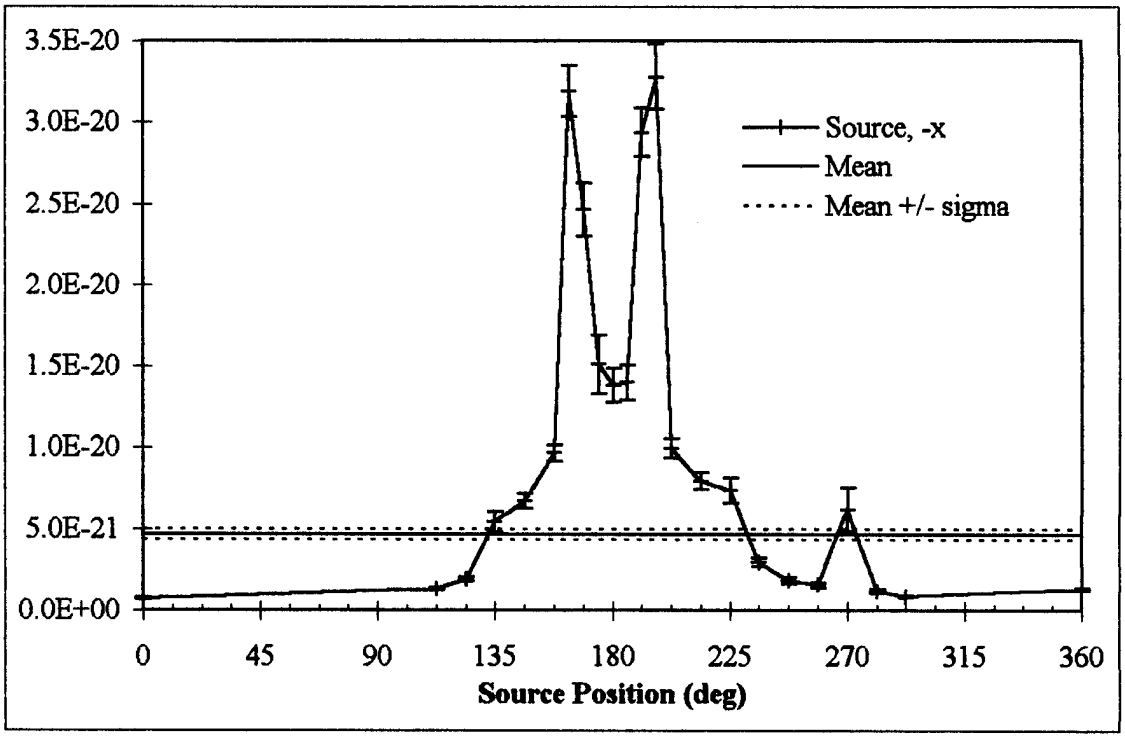

Figure G.2 Exposure (R/s/particle) at each source point for negative x source axis detector with CT in WPMC suite, 1/16" lead shielding, head scan.

Appendix G: WPMC CT Suite. 1/16" Lead Shielding, Head Scan

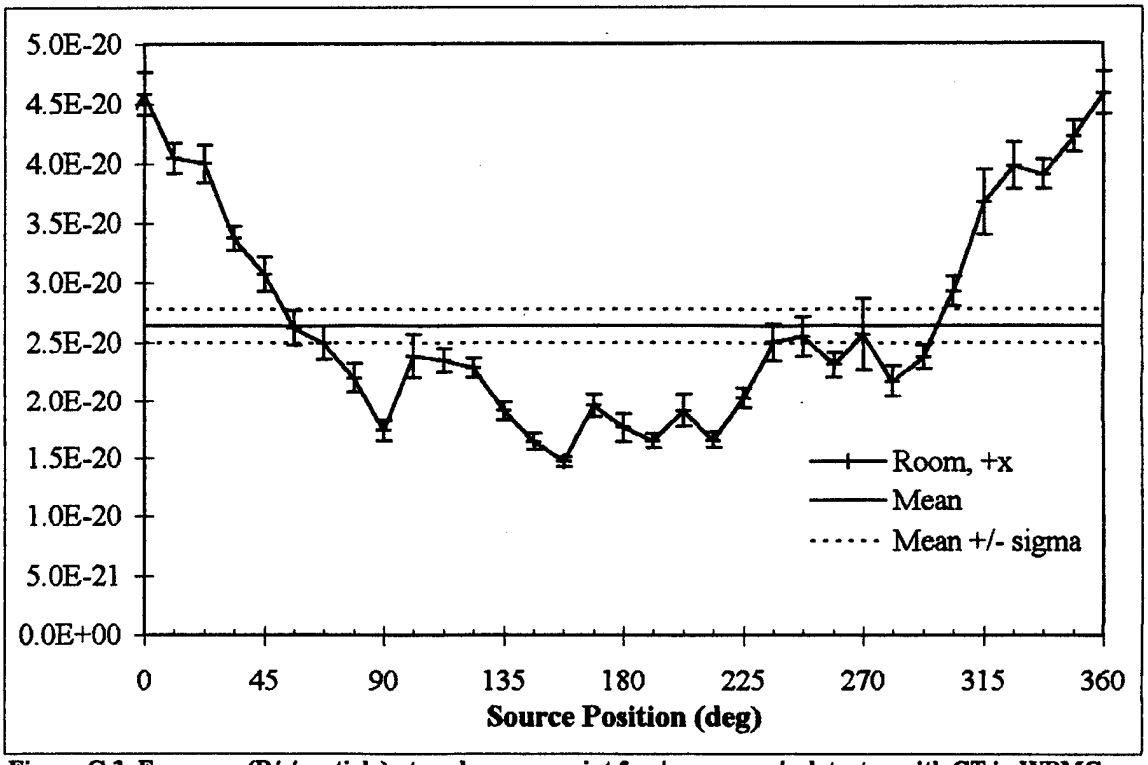

Figure G.3 Exposure (R/s/particle) at each source point for +x room axis detector with CT in WPMC cuite, 1/16" lead, head scan.

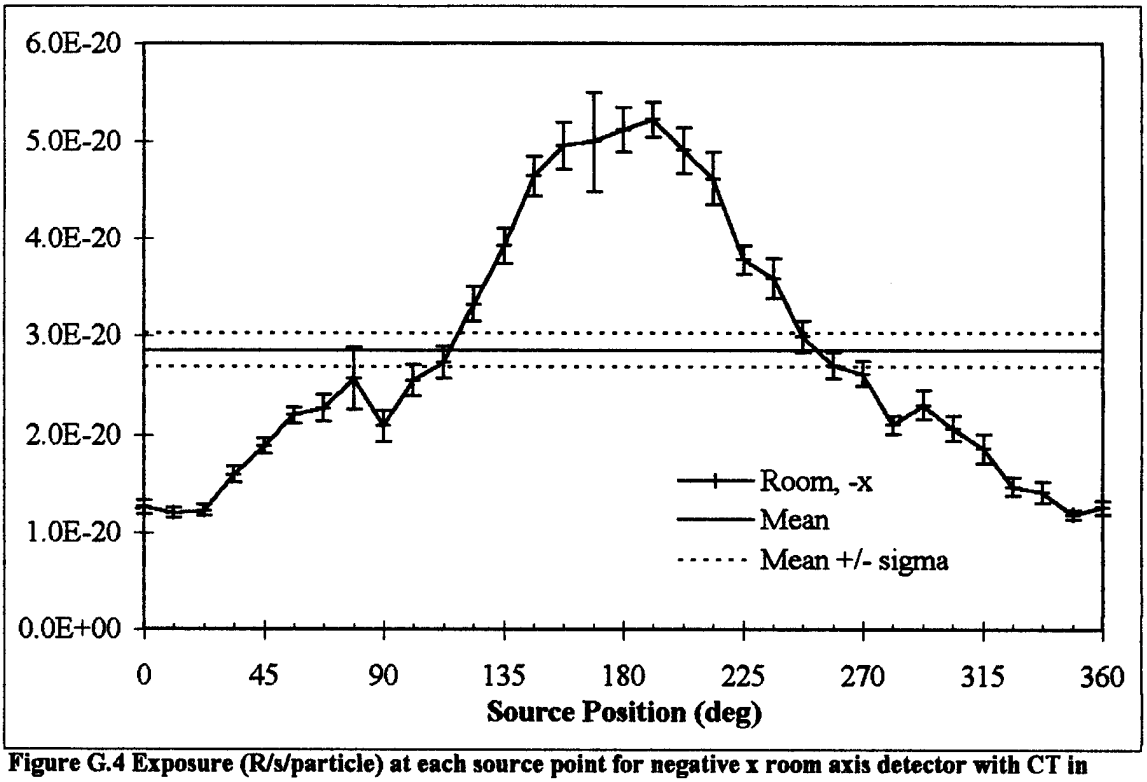

Figure G.4 Exposure (R/s/particle) at each source point for negative x room axis detector with CT in WPMC suite, 1/16" lead shielding, head scan.

Appendix G: WPMC CT Suite. 1/16" Lead Shielding, Head Scan

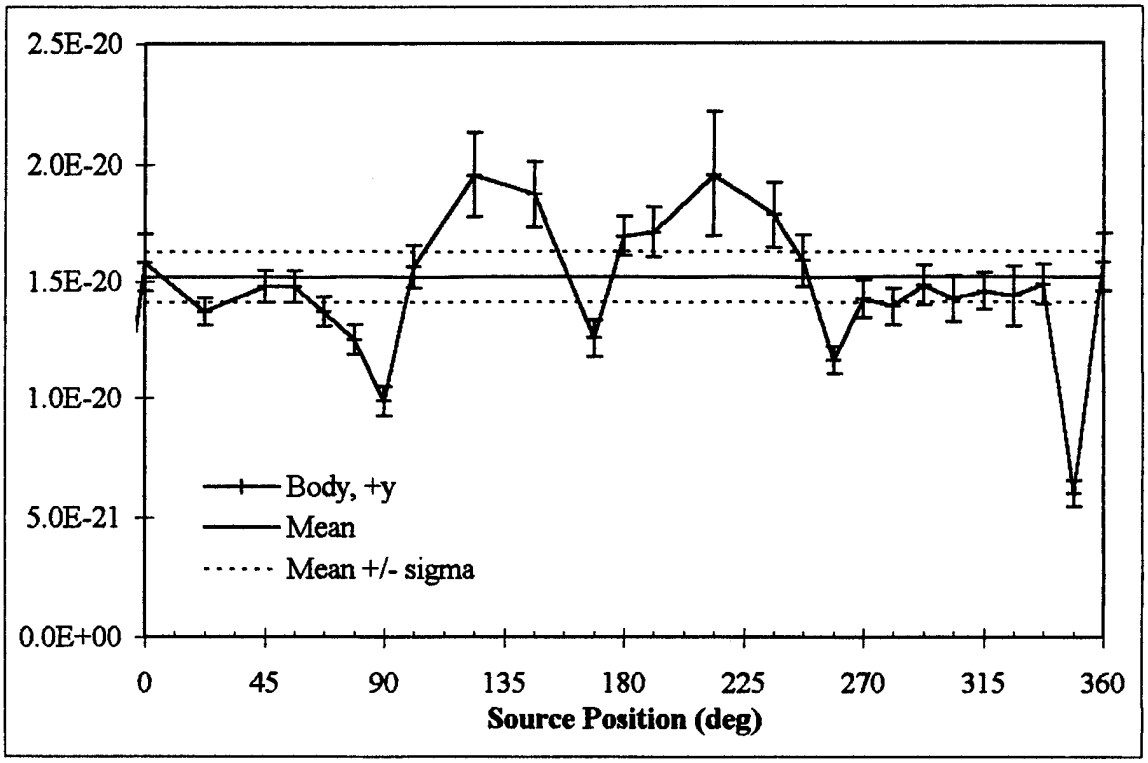

Figure G.5 Exposure (R/s/particle) at each source point for positive y body axis detector with CT in WPMC room, 1/16" lead, head scan.

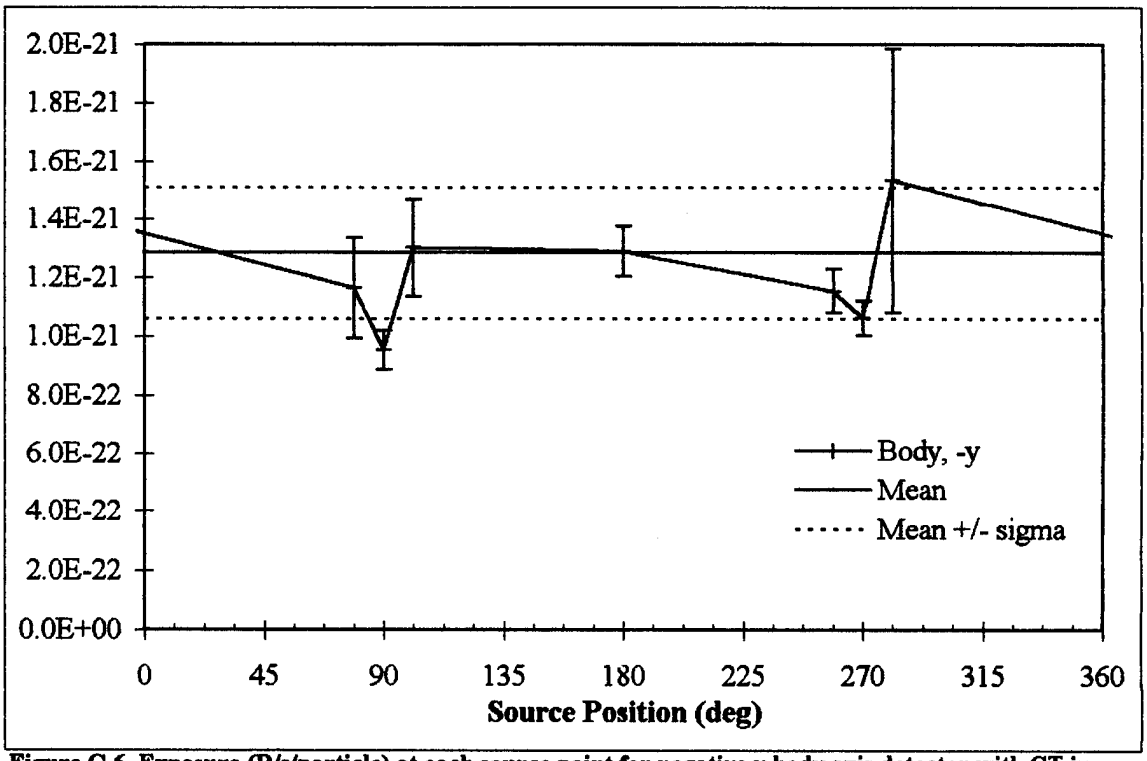

Figure G.6 Exposure (R/s/particle) at each source point for negative y body axis detector with CT in WPMC suite, 1/16" lead shielding, head scan.

Appendix G: WPMC CT Suite. 1/16" Lead Shielding, Head Scan

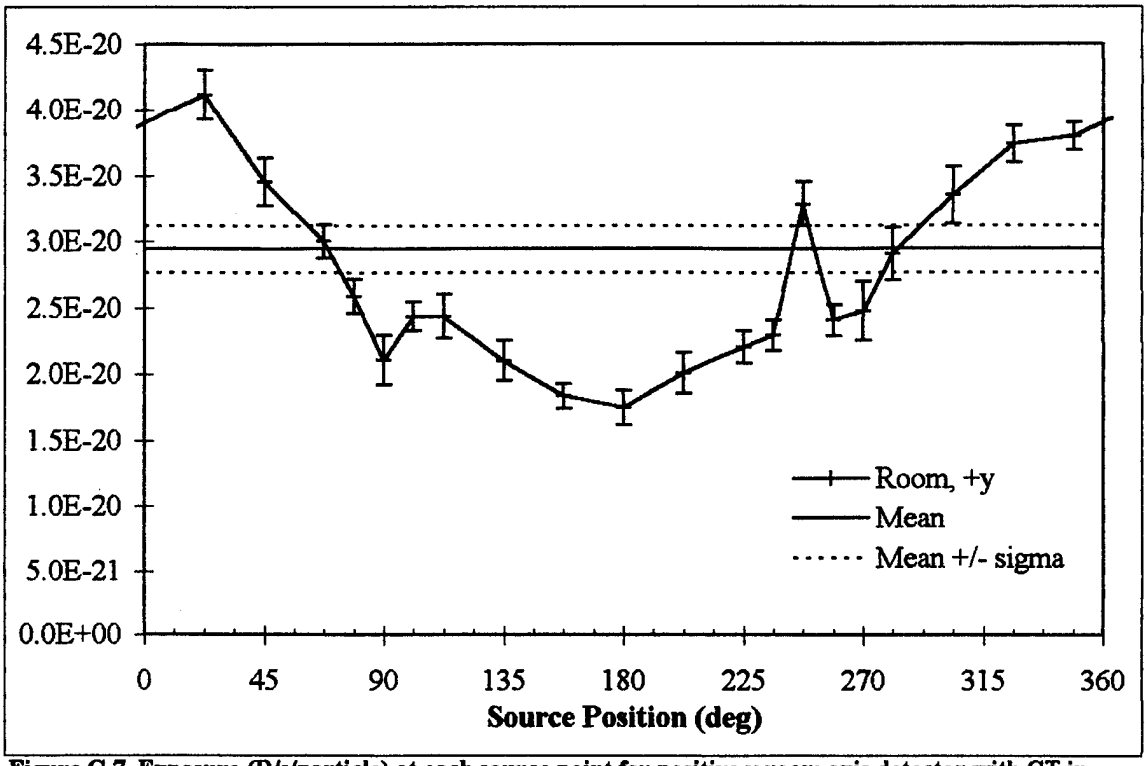

Figure G.7 Exposure (R/s/particle) at each source point for positive y room axis detector with CT in WPMC suite, 1/16" lead, head scan.

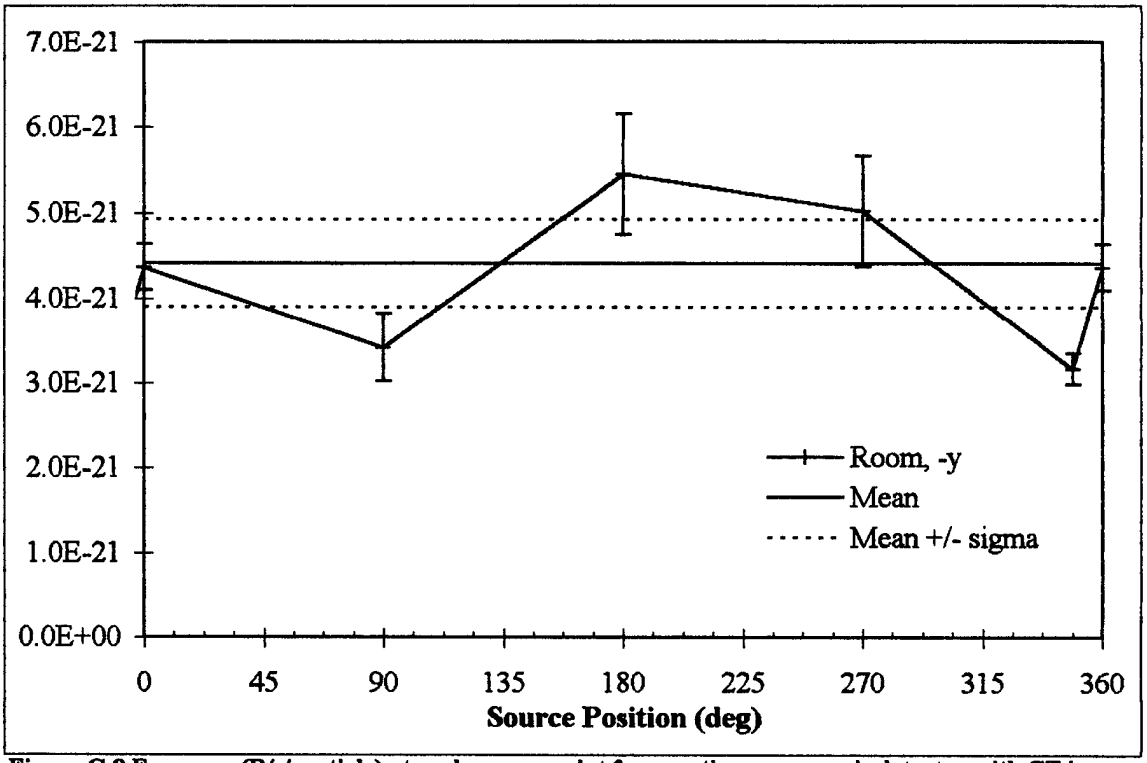

Figure G.8 Exposure (R/s/particle) at each source point for negative y room axis detector with CT in WPMC suite, 1/16" lead shielding, head scan.

Appendix G: WPMC CT Suite, 1/16" Lead Shielding, Head Scan

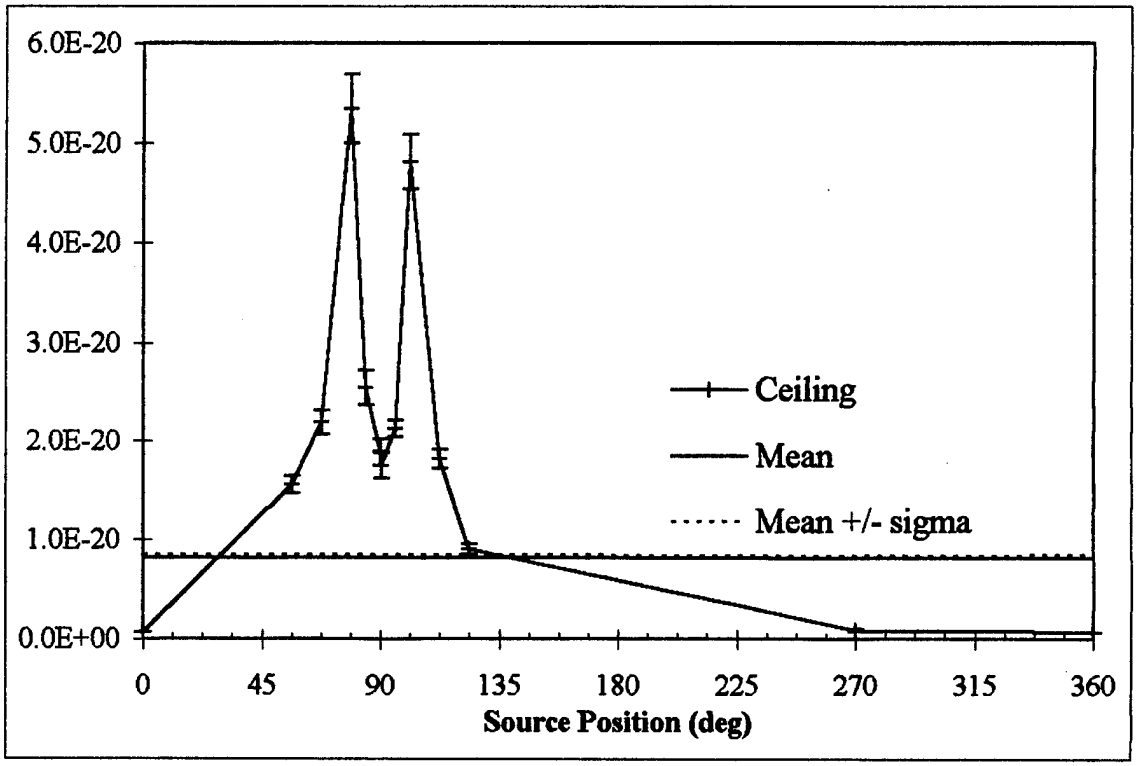

Figure G.9 Exposure (R/s/particle) at each source point for ceiling detector with CT in WPMC, 1/16" lead, head scan.

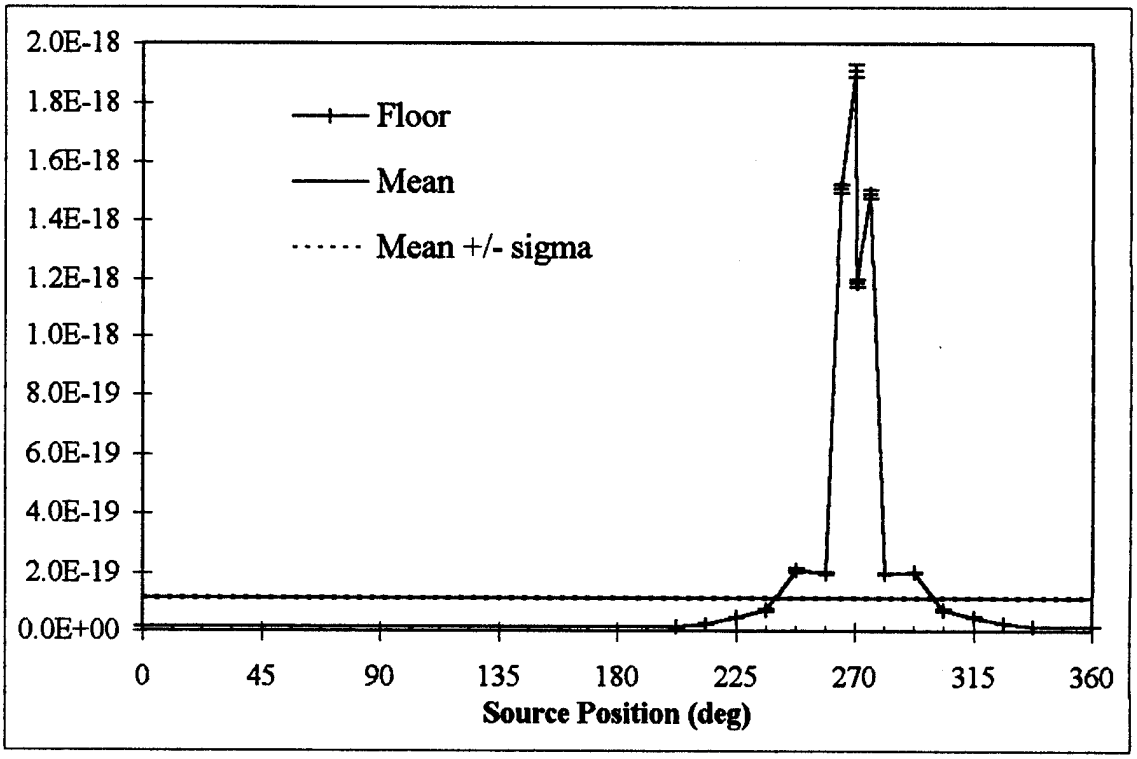

Figure G.10 Exposure (R/s/particle) at each source point for floor detector with CT in WPMC, 1/16" lead shielding, head scan.

Appendix G: WPMC CT Suite. 1/16" Lead Shielding, Head Scan

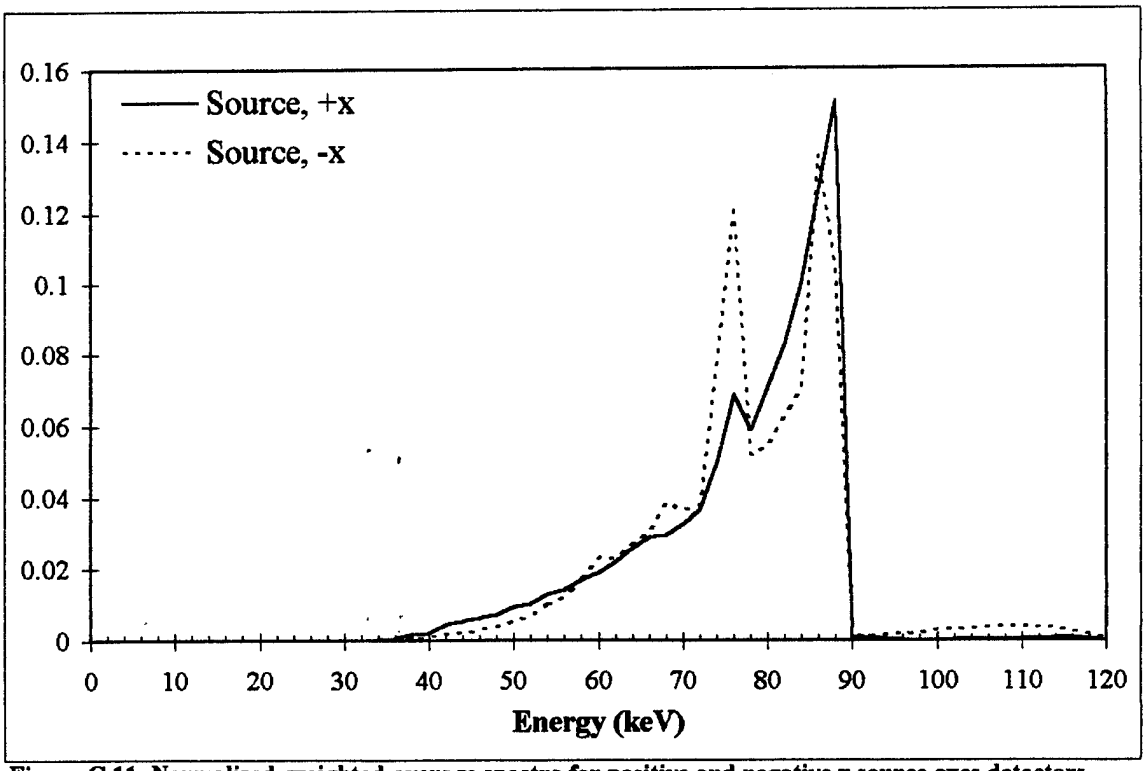

Figure G.11 Normalized, weighted-average spectra for positive and negative x source axes detectors with CT in WPMC, 1/16" lead shielding, head scan.

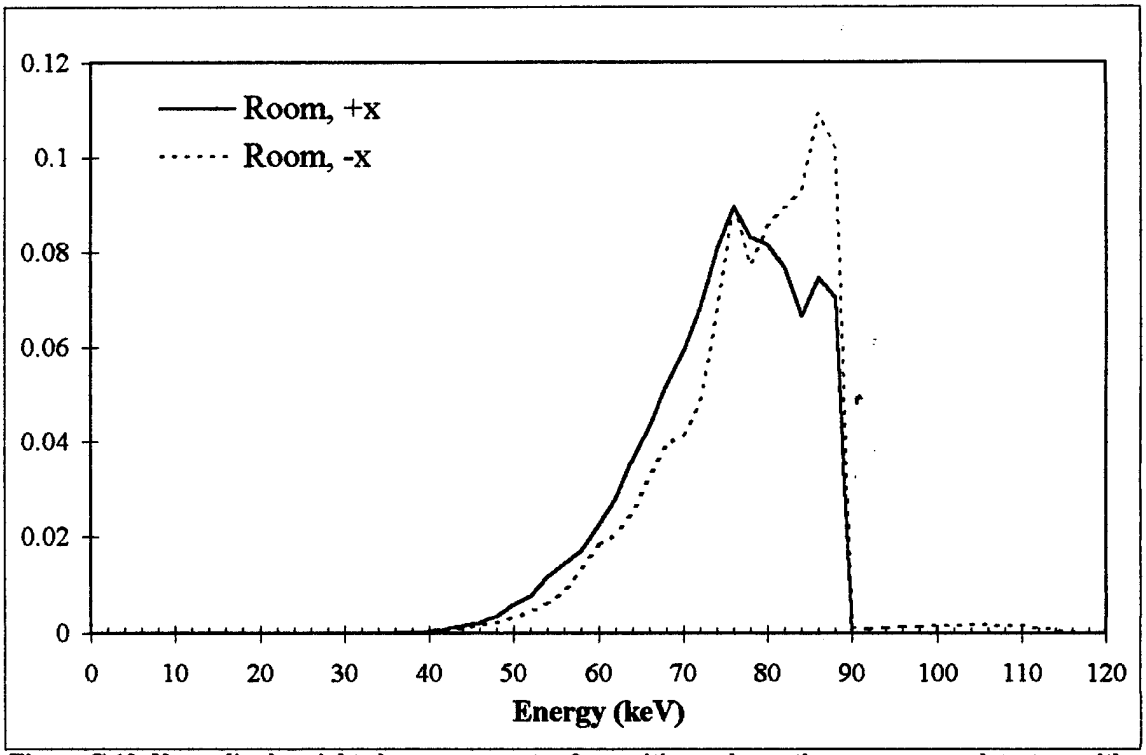

Figure G.12 Normalized, weighted-average spectra for positive and negative x room axes detectors with CT in WPMC, 1/16" lead shielding, head scan.

Appendix G: WPMC CT Suite. 1/16" Lead Shielding, Head Scan

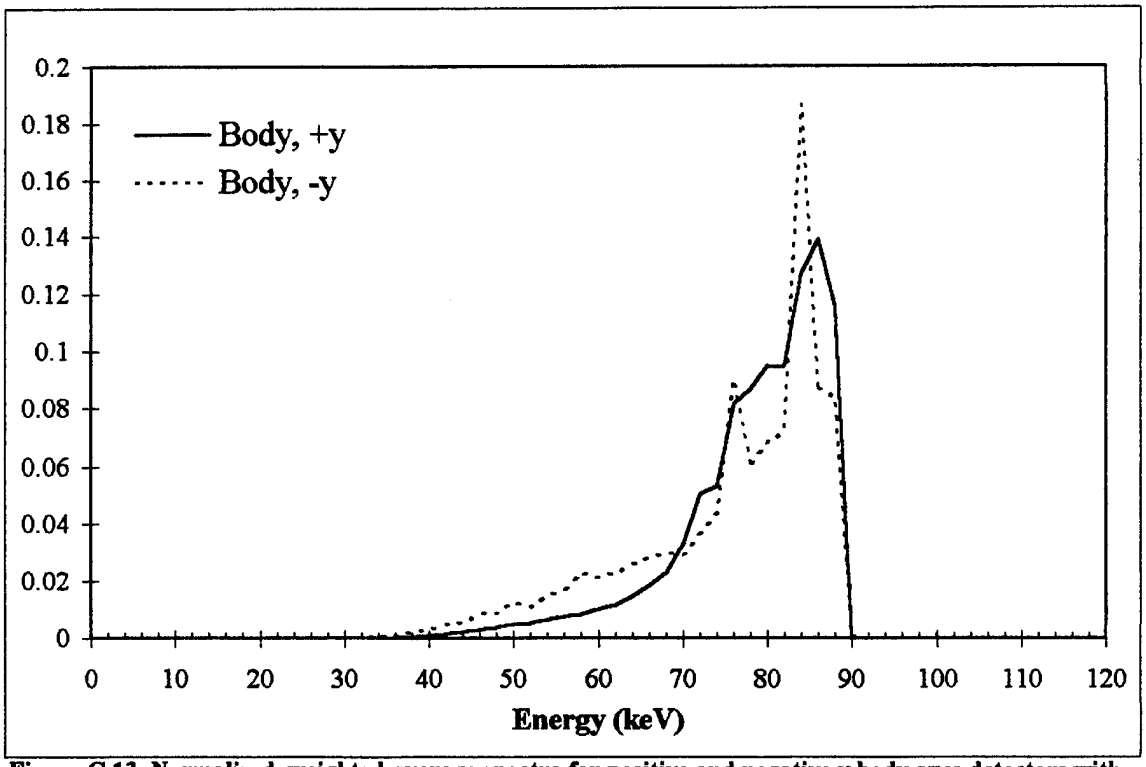

Figure G.13 Normalized, weighted-average spectra for positive and negative y body axes detectors with CT in WPMC, 1/16" lead shielding, head scan.

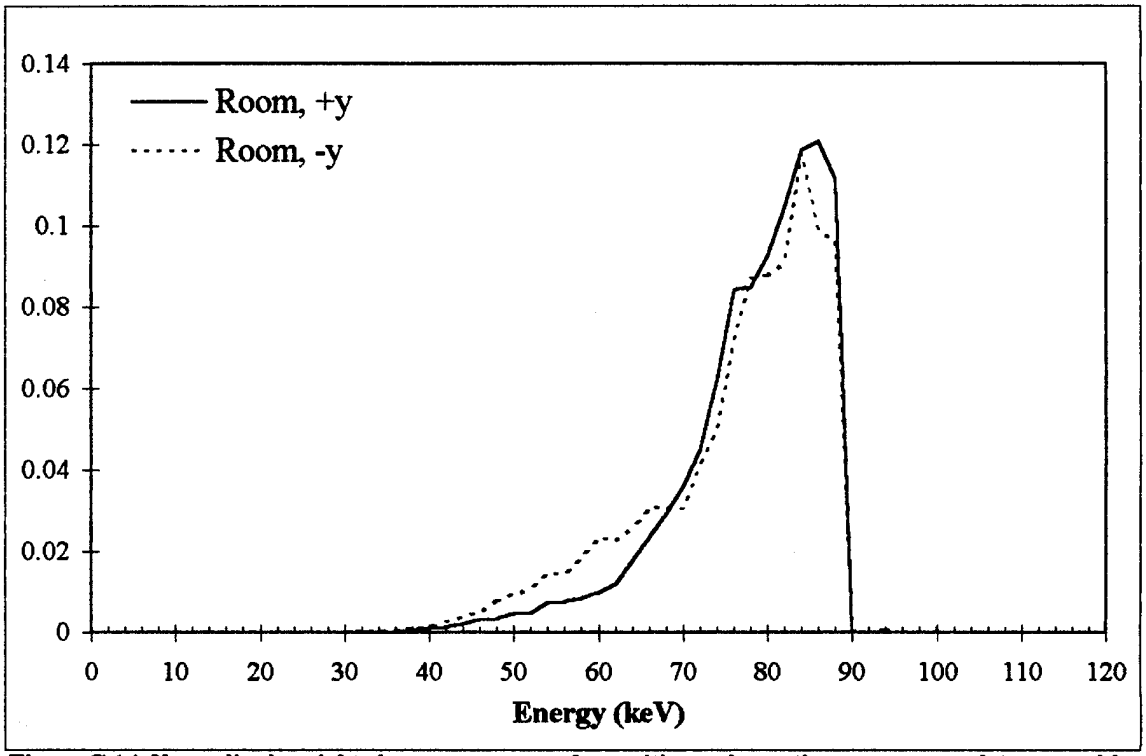

Figure G.14 Normalized, weighted-average spectra for positive and negative y room axes detectors with CT in WPMC, 1/16" lead shielding, head scan.

Appendix G: WPMC CT Suite. 1/16" Lead Shielding, Head Scan

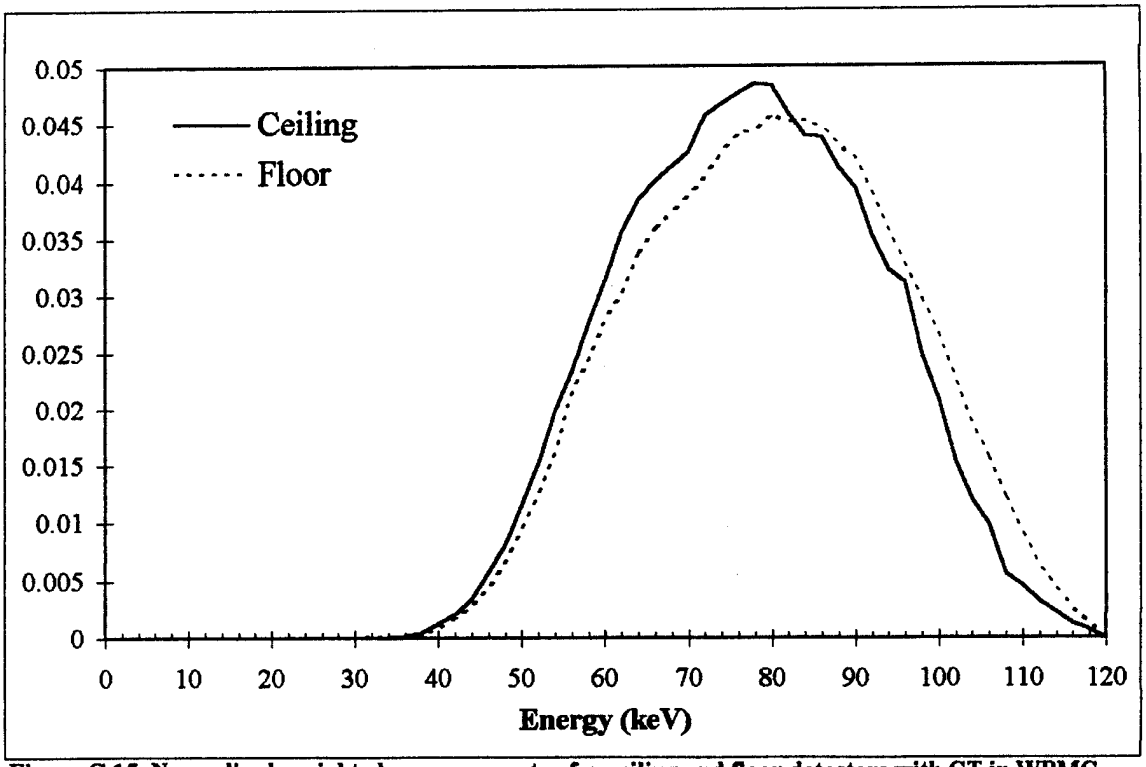

Figure G.15 Normalized, weighted-average spectra for ceiling and floor detectors with CT in WPMC, 1/16" lead shielding, head scan.

Appendix H: WPMC CT Suite, 1/16" Lead Shielding, Abdomen Scan

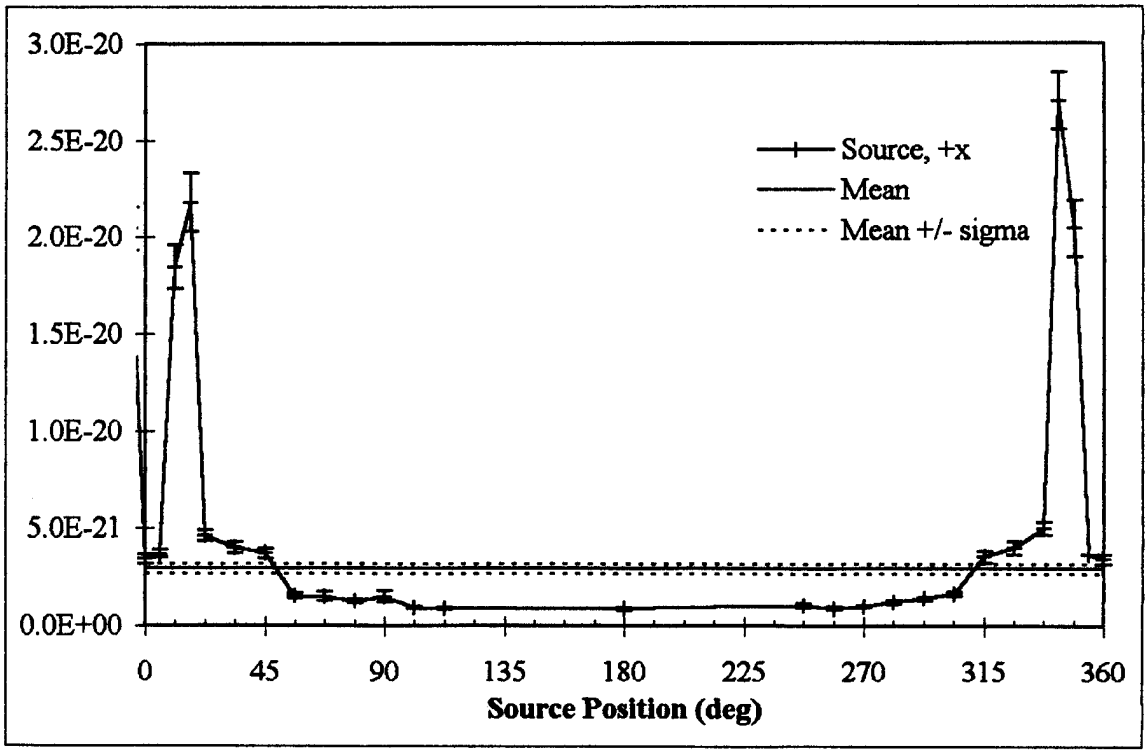

Figure H.1 Exposure (R/s/particle) at each source point for positive x source axis detector with CT in WPMC, 1/16" lead, abdomen scan.

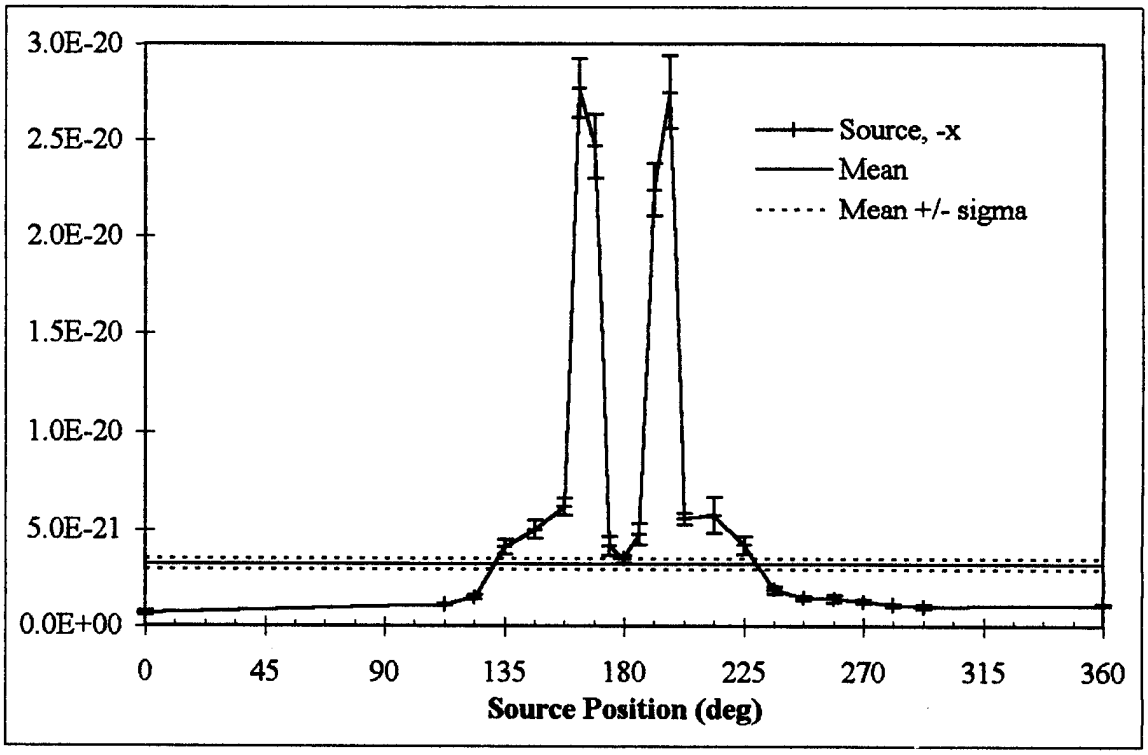

Figure H.2 Exposure (R/s/particle) at each source point for negative x source axis detector with CT in WPMC suite, 1/16" lead shielding, abdomen scan.

Appendix H: WPMC CT Suite, 1/16" Lead Shielding, Abdomen Scan

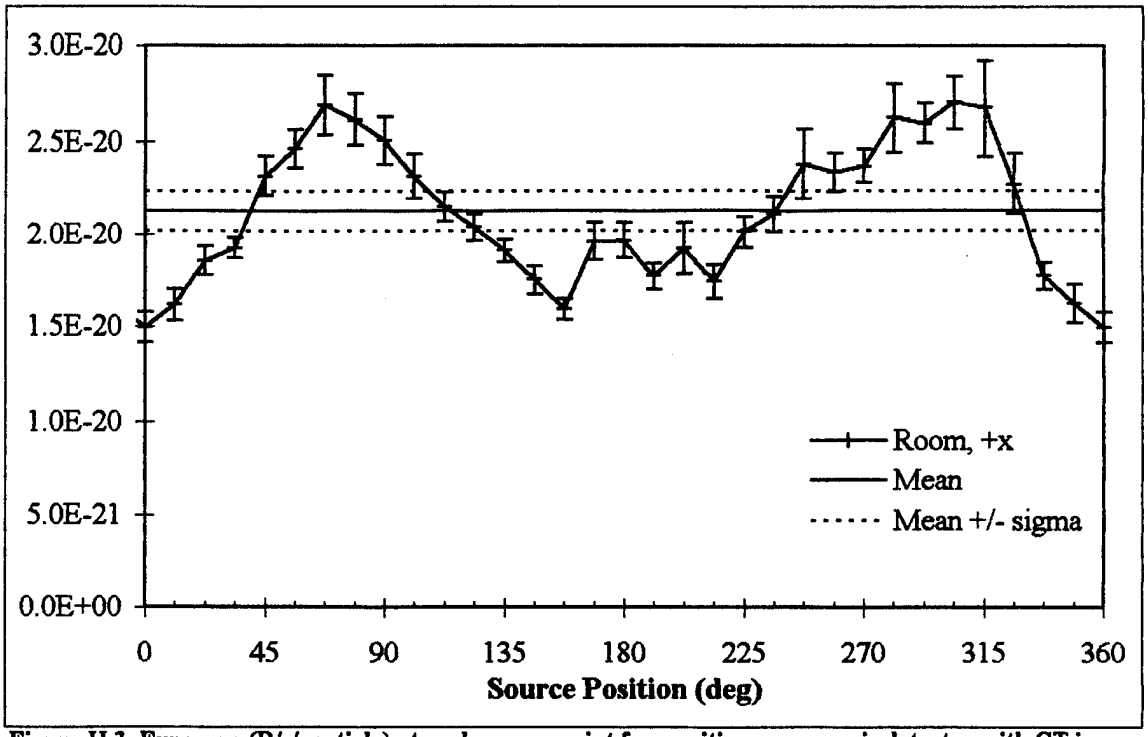

Figure H.3 Exposure (R/s/particle) at each source point for positive x room axis detector with CT in WPMC cuite, 1/16" lead, abdomen scan.

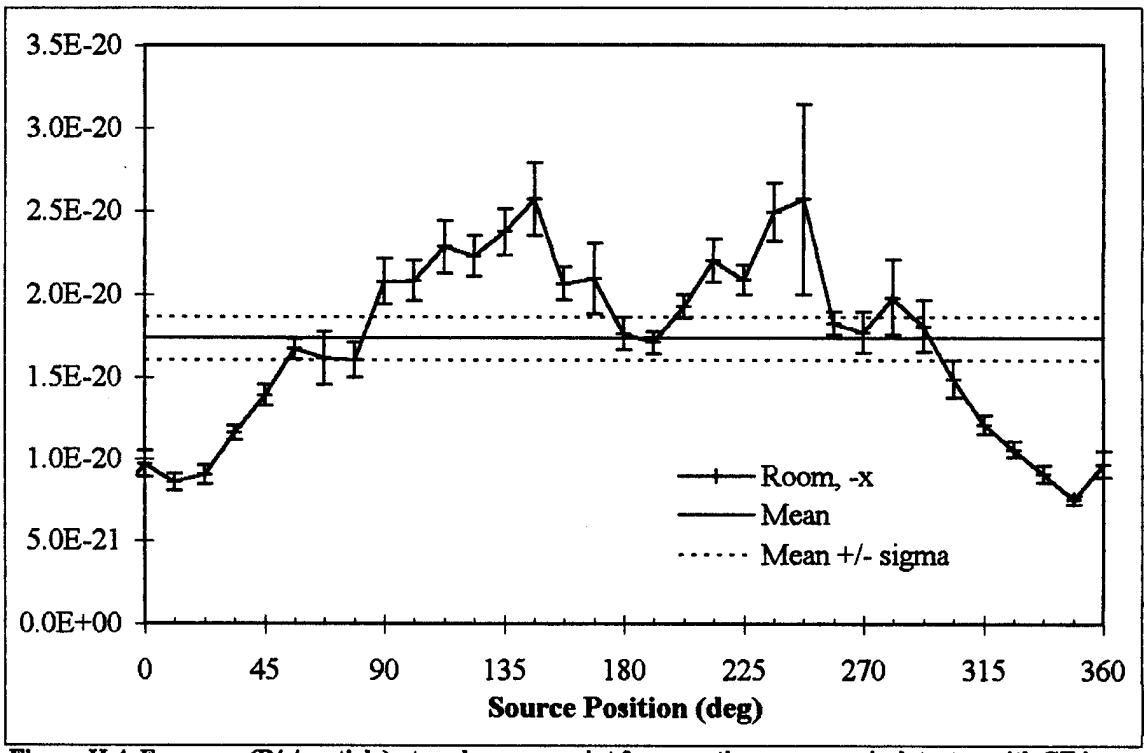

Figure H.4 Exposure (R/s/particle) at each source point for negative x room axis detector with CT in WPMC suite, 1/16" lead shielding, abdomen scan.

Appendix H: WPMC CT Suite, 1/16" Lead Shielding, Abdomen Scan

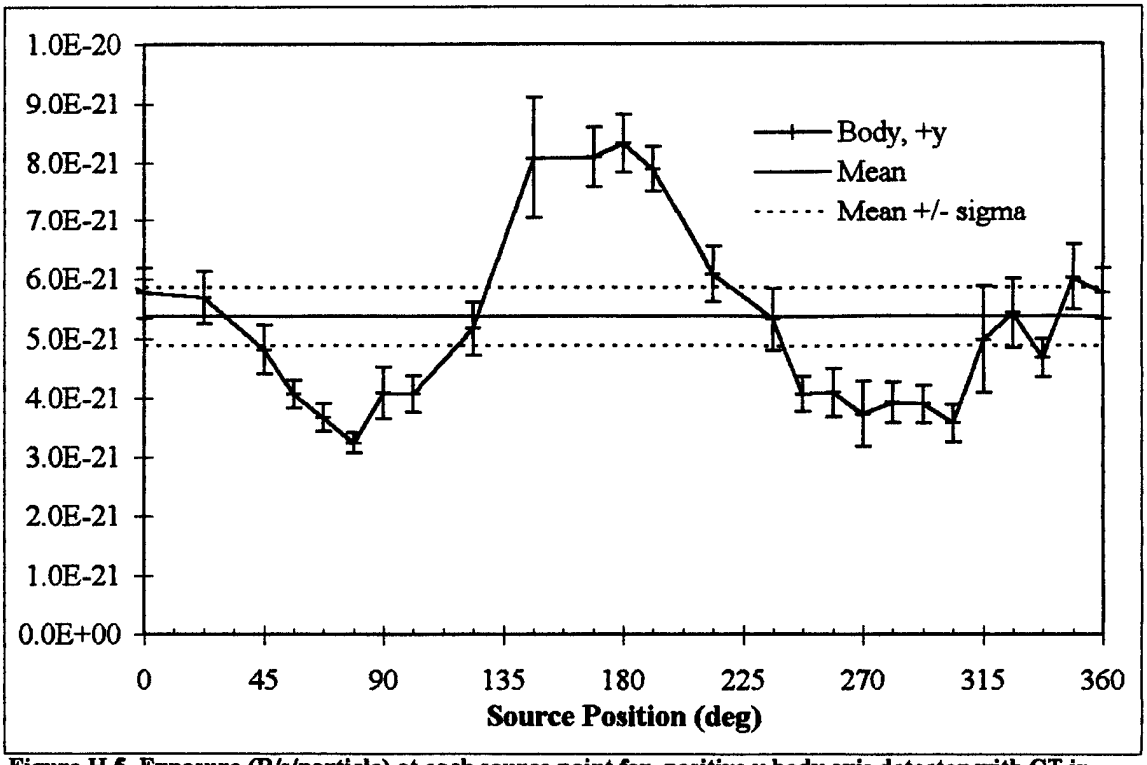

Figure H.5 Exposure (R/s/particle) at each source point for positive y body axis detector with CT in WPMC room, 1/16" lead, abdomen scan.

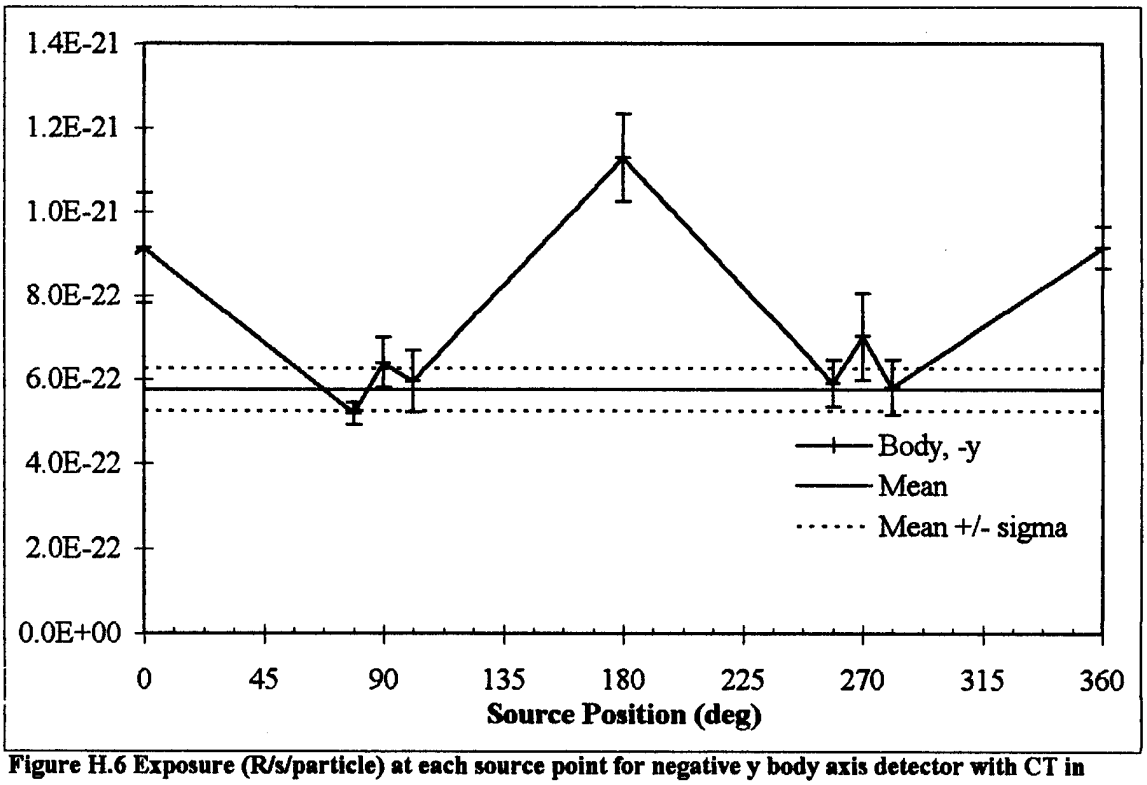

Figure H.6 Exposure (R/s/particle) at each source point for negative y body axis detector with CT in WPMC suite, 1/16" lead shielding, abdomen scan.

Appendix H: WPMC CT Suite, 1/16" Lead Shielding, Abdomen Scan

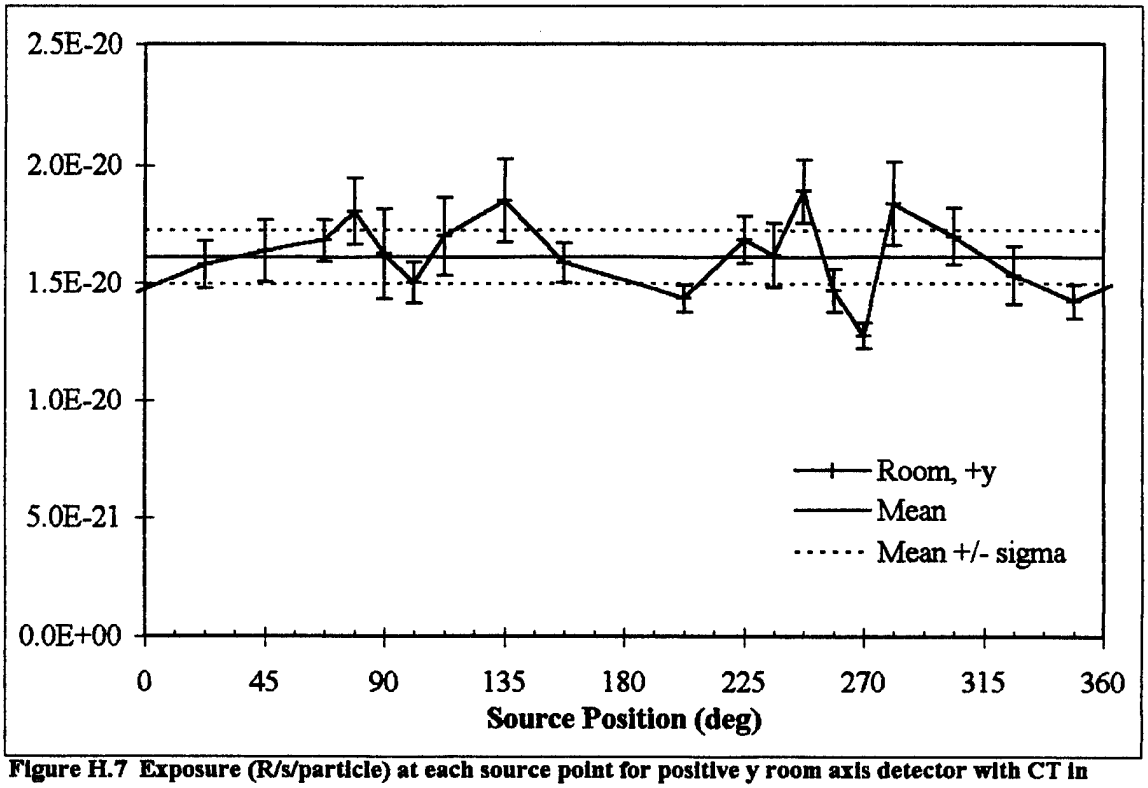

Figure H.7 Exposure (R/s/particle) at each source point for positive y room axis detector with CT in WPMC suite, 1/16" lead, abdomen scan.

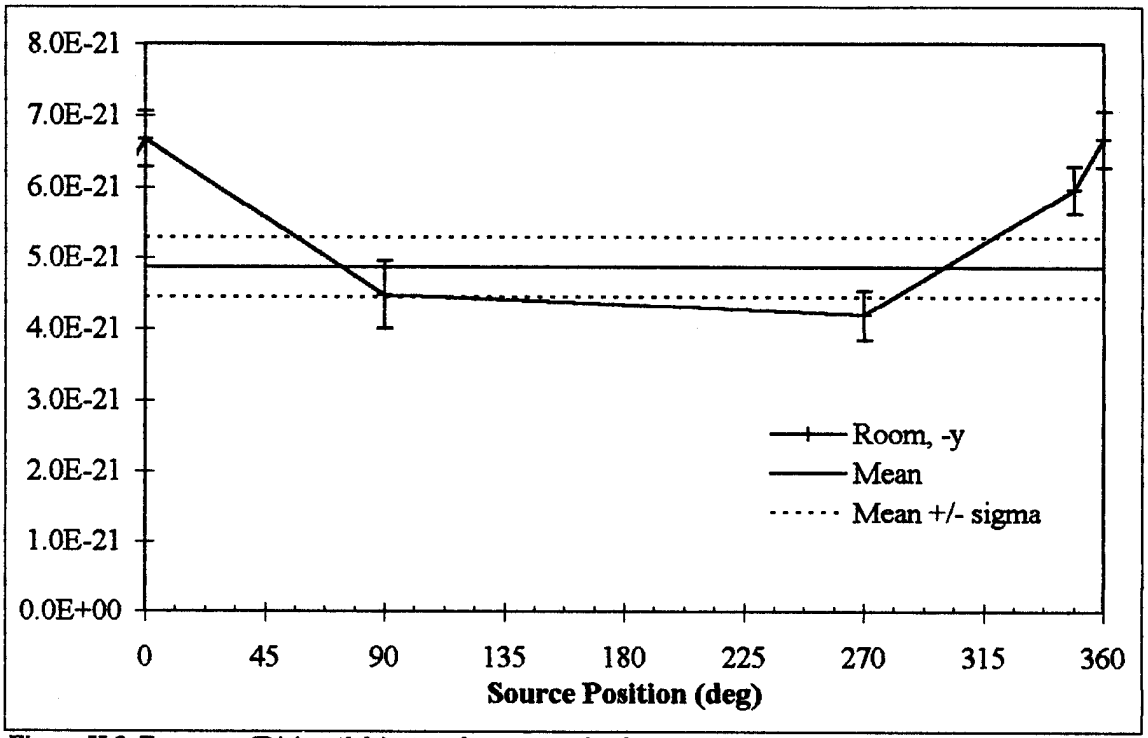

Figure H.8 Exposure (R/s/particle) at each source point for negative y room axis detector with CT in WPMC suite, 1/16" lead shielding, abdomen scan.

Appendix H: WPMC CT Suite, 1/16" Lead Shielding, Abdomen Scan

Figure H.8 Exposure (R/s/particle) at each source point for negative y room axis detector with CT in WPMC suite, 1/16" lead shielding, abdomen scan.

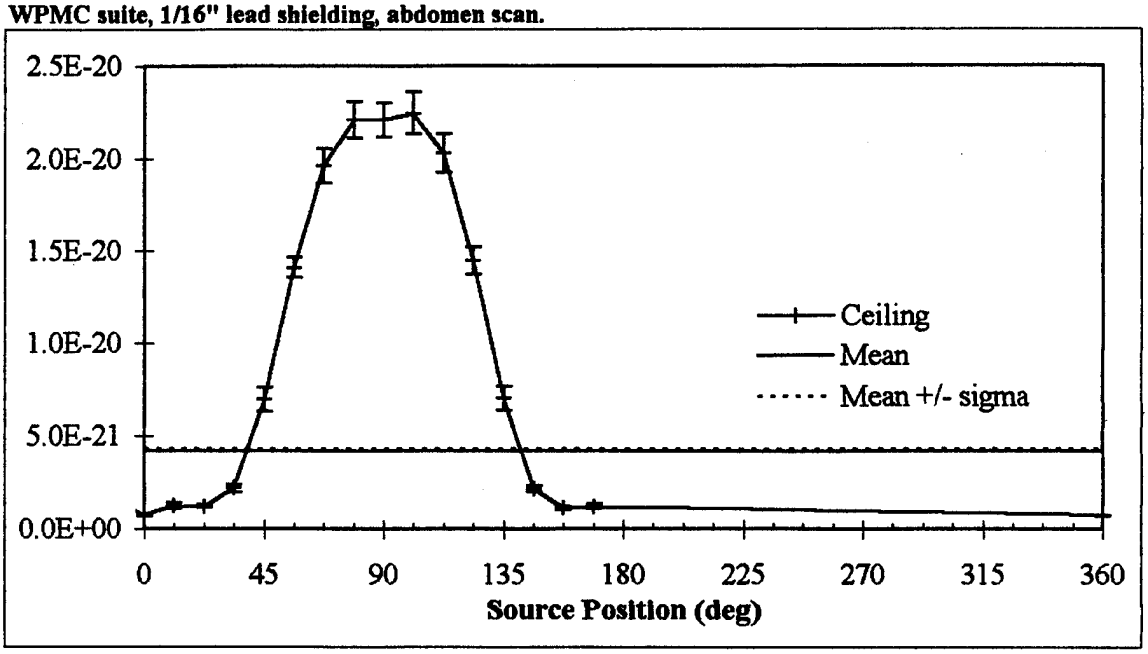

Figure H.9 Exposure (R/s/particle) at each source point for ceiling detector with CT in WPMC, 1/16" lead, abdomen scan.

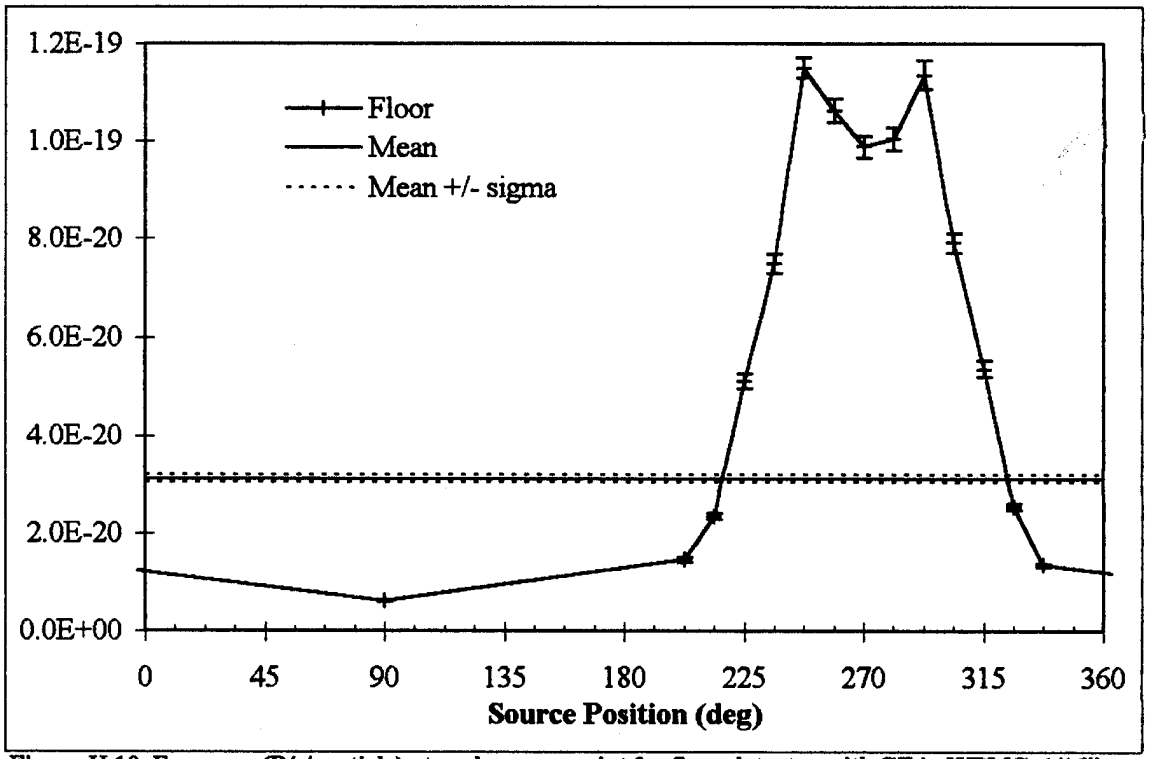

Figure H.10 Exposure (R/s/particle) at each source point for floor detector with CT in WPMC, 1/16" lead shielding, abdomen scan.

Appendix H: WPMC CT Suite, 1/16" Lead Shielding, Abdomen Scan

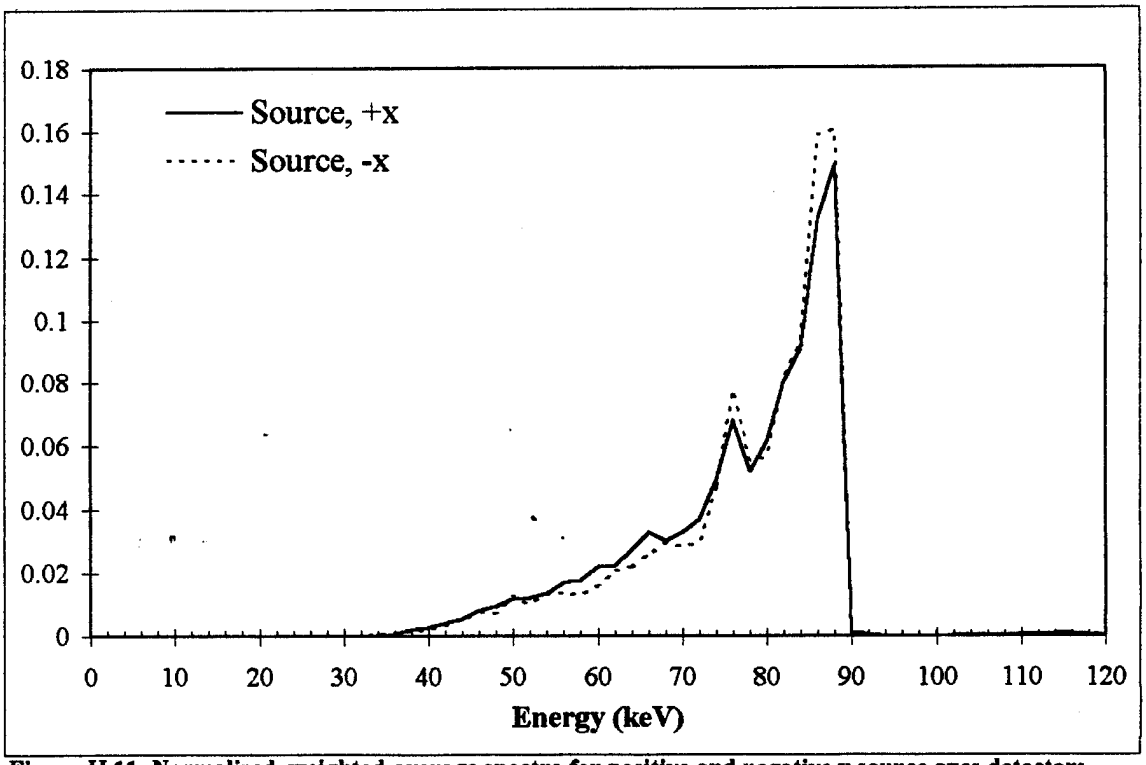

Figure H.11 Normalized, weighted-average spectra for positive and negative x source axes detectors with CT in WPMC, 1/16" lead shielding, abdomen scan.

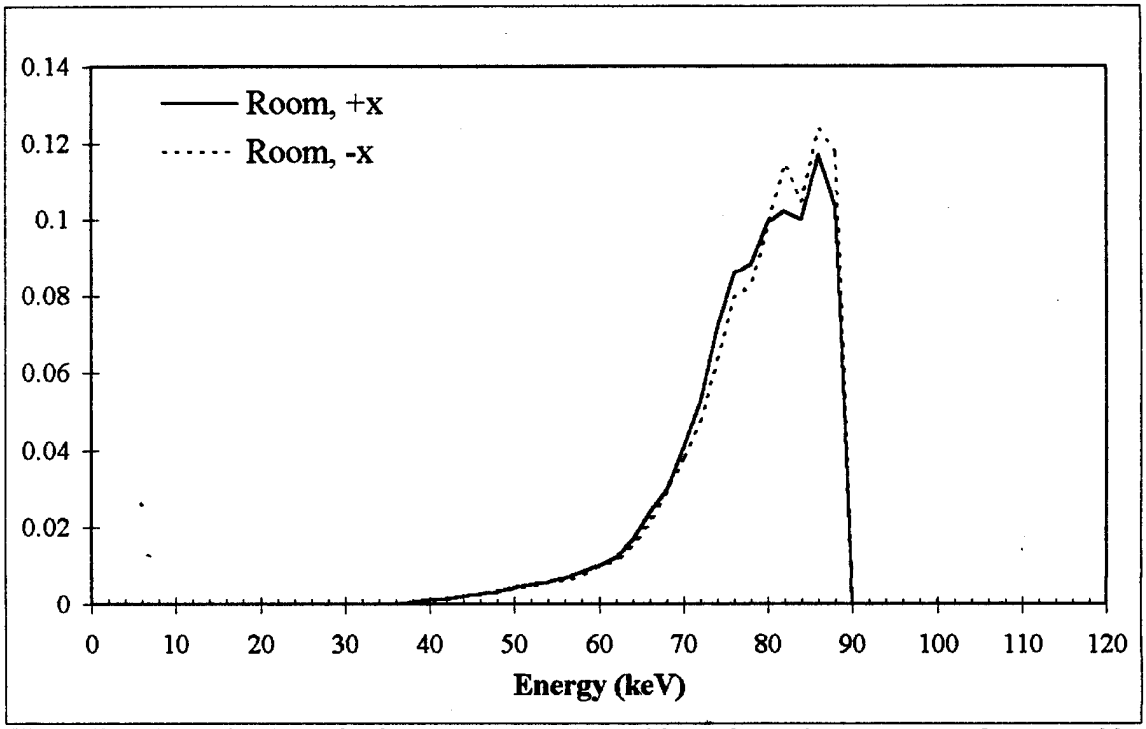

Figure H.12 Normalized, weighted-average spectra for positive and negative x room axes detectors with CT in WPMC, 1/16" lead shielding, abdomen scan.

Appendix H: WPMC CT Suite, 1/16" Lead Shielding, Abdomen Scan

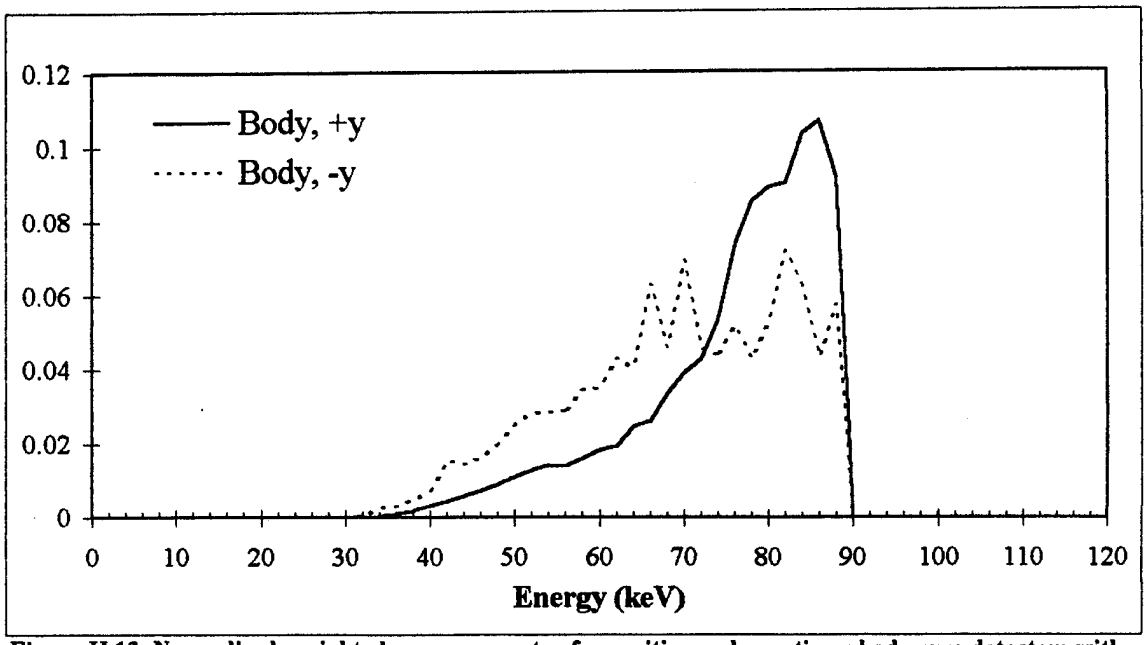

Figure H.13 Normalized, weighted-average spectra for positive and negative y body axes detectors with CT in WPMC, 1/16" lead shielding, abdomen scan.

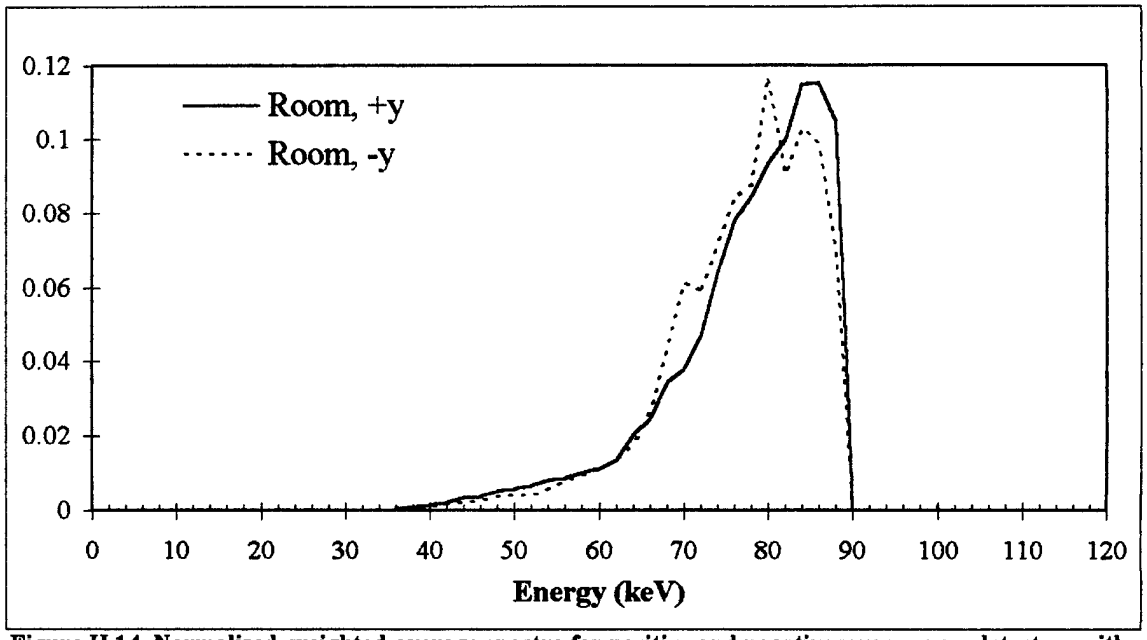

Figure H.14 Normalized, weighted-average spectra for positive and negative y room axes detectors with CT in WPMC, 1/16" lead shielding, abdomen scan.

Appendix H: WPMC CT Suite, 1/16" Lead Shielding, Abdomen Scan

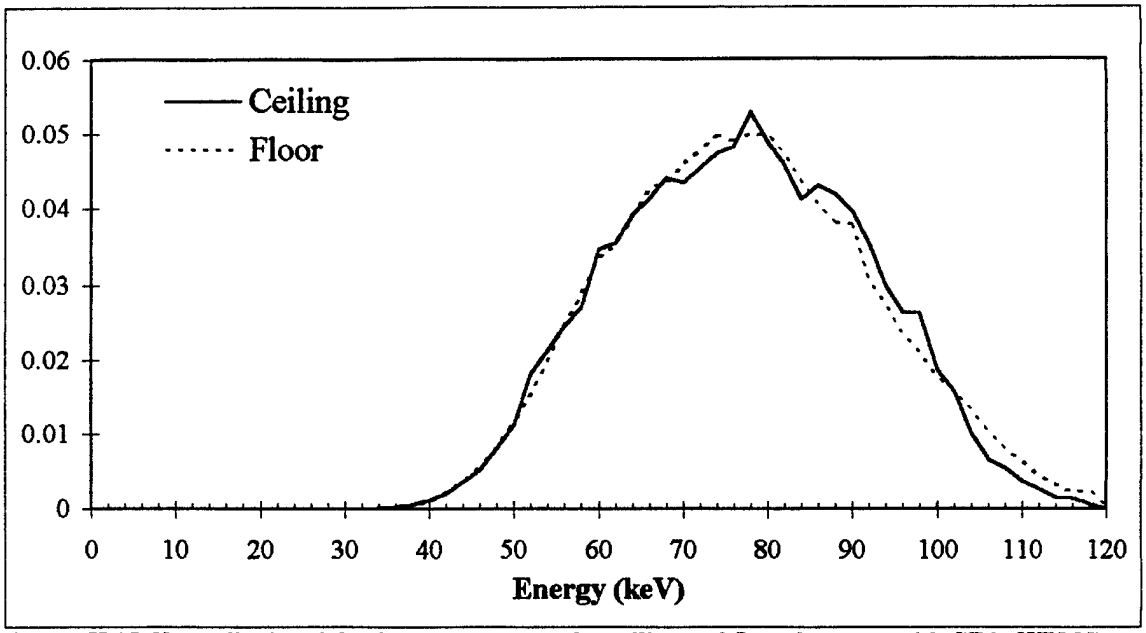

Figure H.15 Normalized, weighted-average spectra for ceiling and floor detectors with CT in WPMC, 1/16" lead shielding, abdomen scan.

Appendix I: WPMC CT Suite, 1/8" Lead, Head Scan

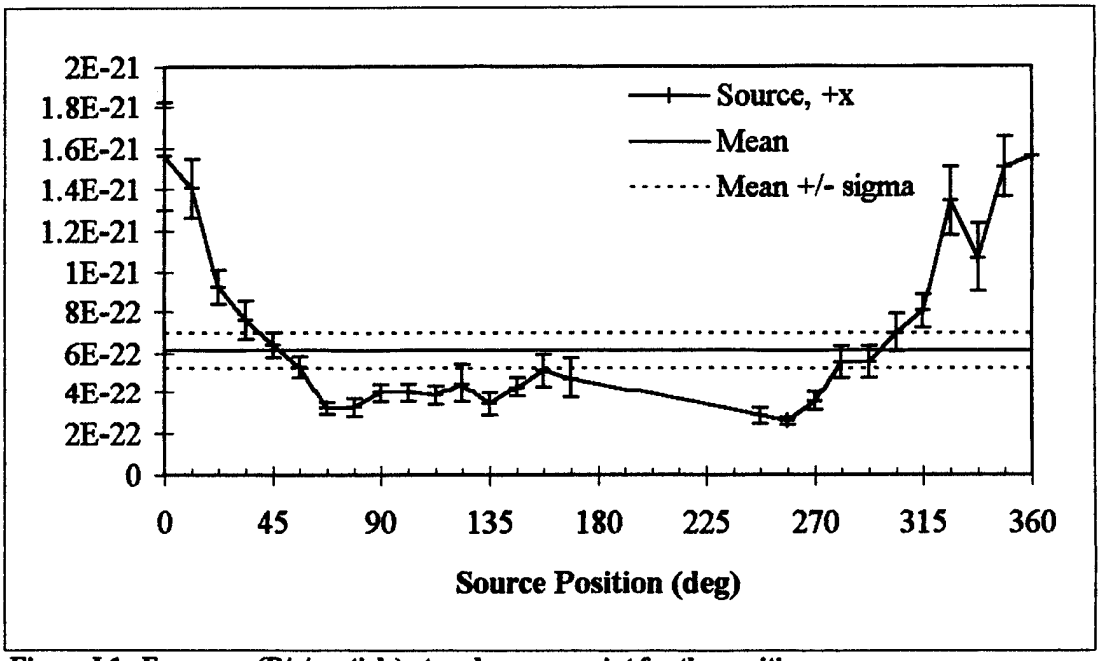

Figure I.1. Exposure (R/s/particle) at each source point for the positive x source axis detector for CT in WPMC with 1/8" lead shielding, head scan.

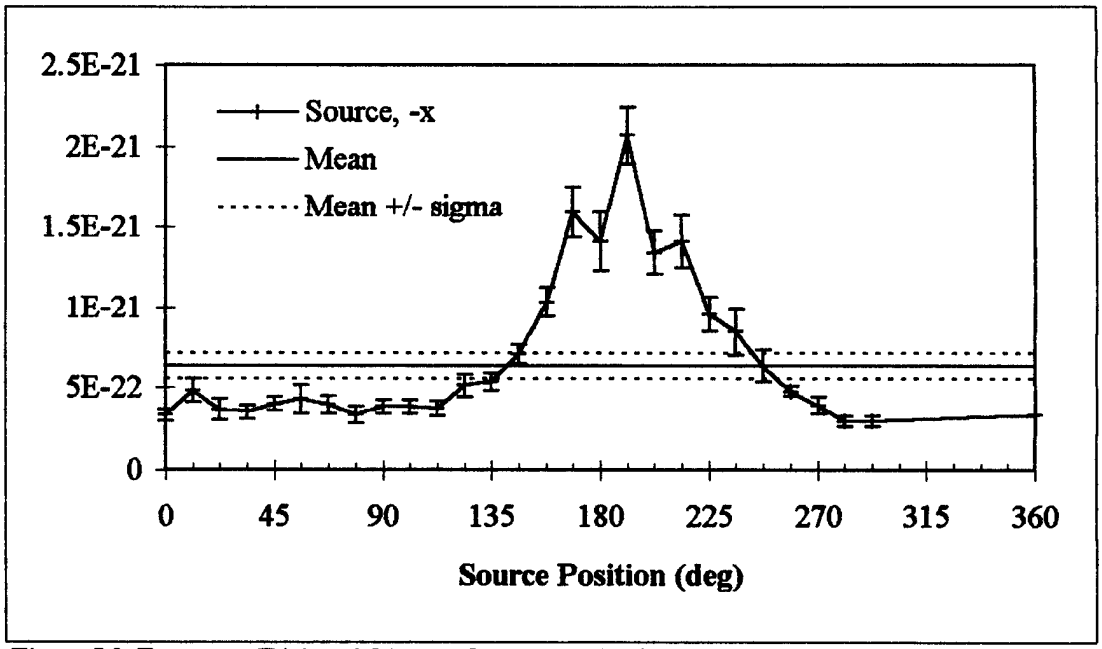

Figure I.2 Exposure (R/s/particle) at each source point for negative x source axis in WPMC with 1/8" lead shielding, head scan.

Appendix I: WPMC CT Suite, 1/8" Lead, Head Scan

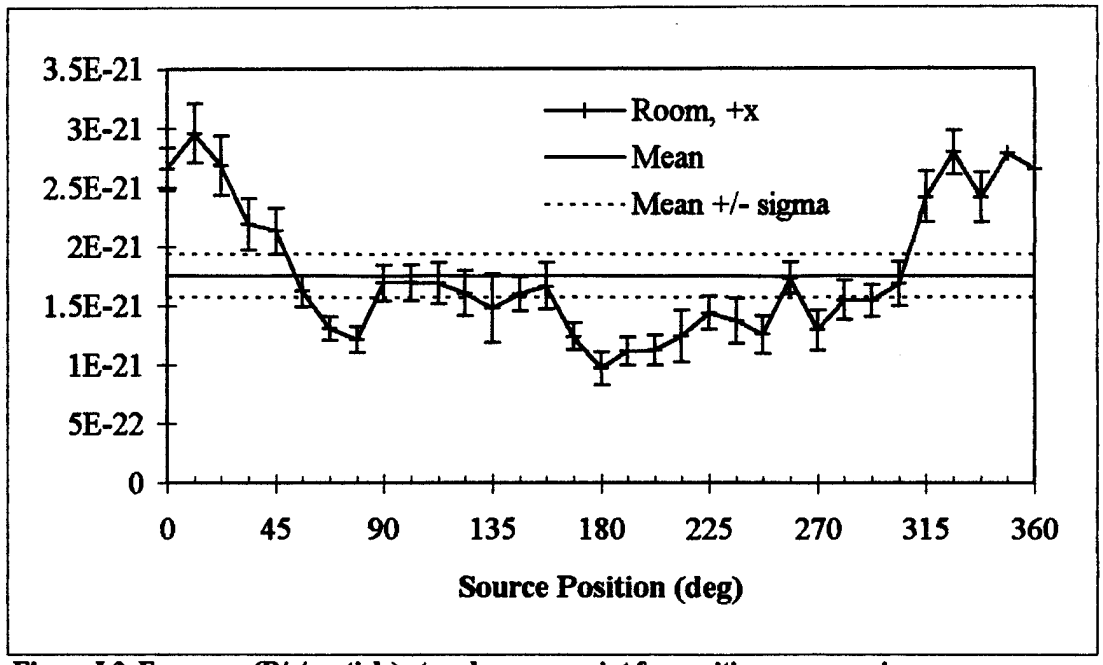

Figure I.3 Exposure (R/s/particle) at each source point for positive x room axis detector for CT detector for CT in WPMC with1/8" lead shielding, head scan.

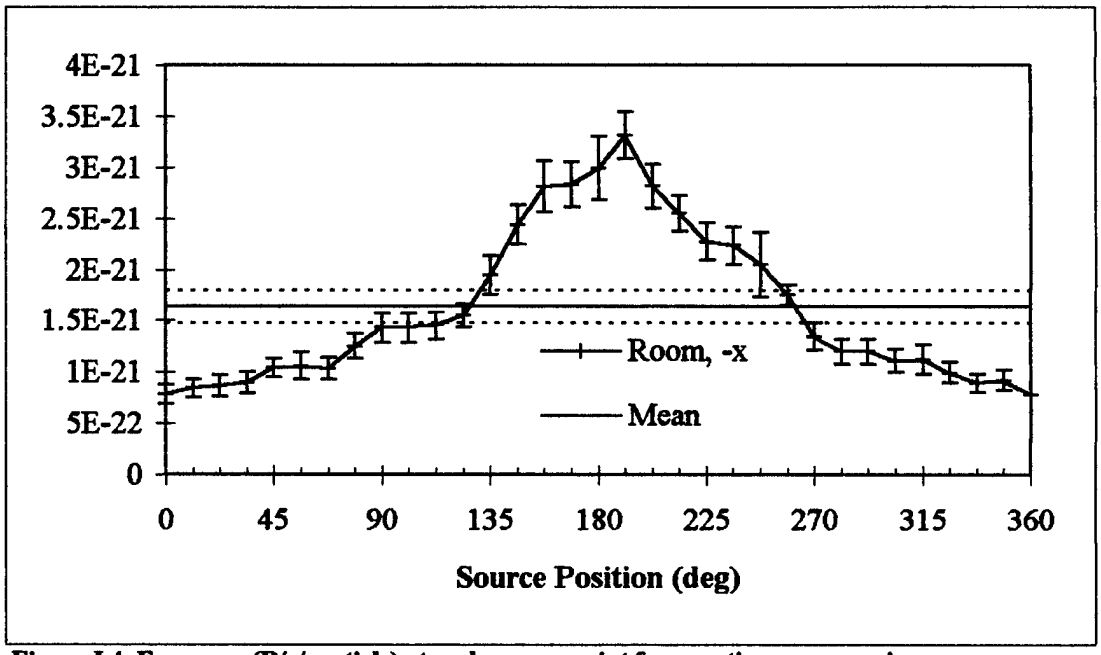

Figure I.4 Exposure (R/s/particle) at each source point for negative x room axis detector for CT in WPMC with 1/8" lead shielding, head scan.

Appendix I: WPMC CT Suite, 1/8" Lead, Head Scan

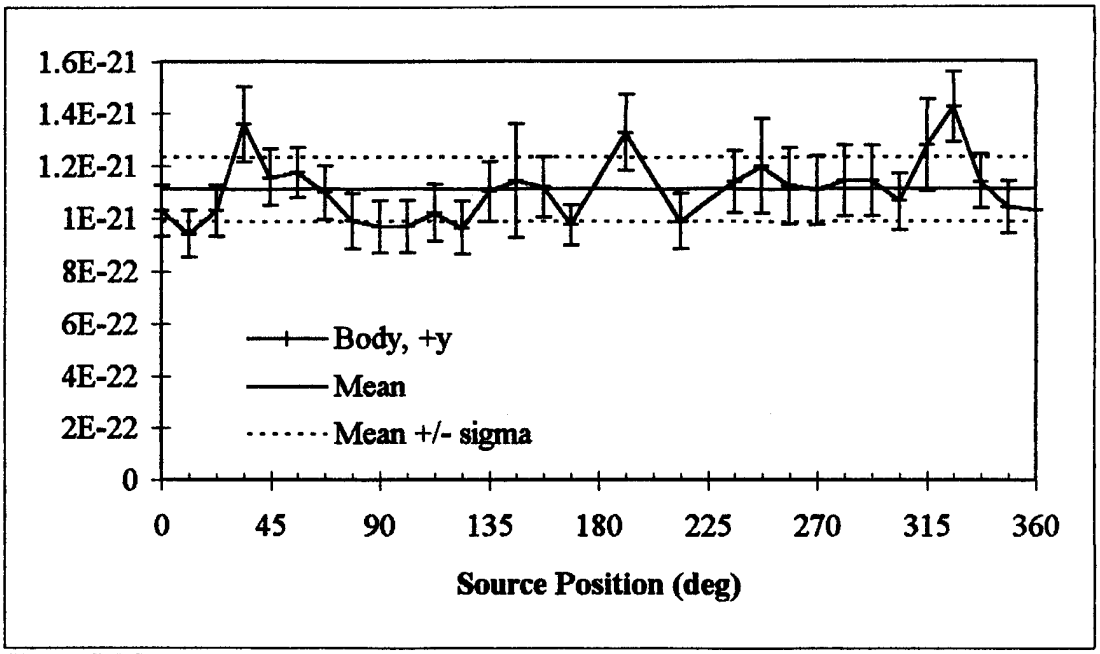

Figure I.5 Exposure (R/s/particle) at each source point for positive y body axis detector for CT in WPMC with 1/8" lead shielding, head scan.

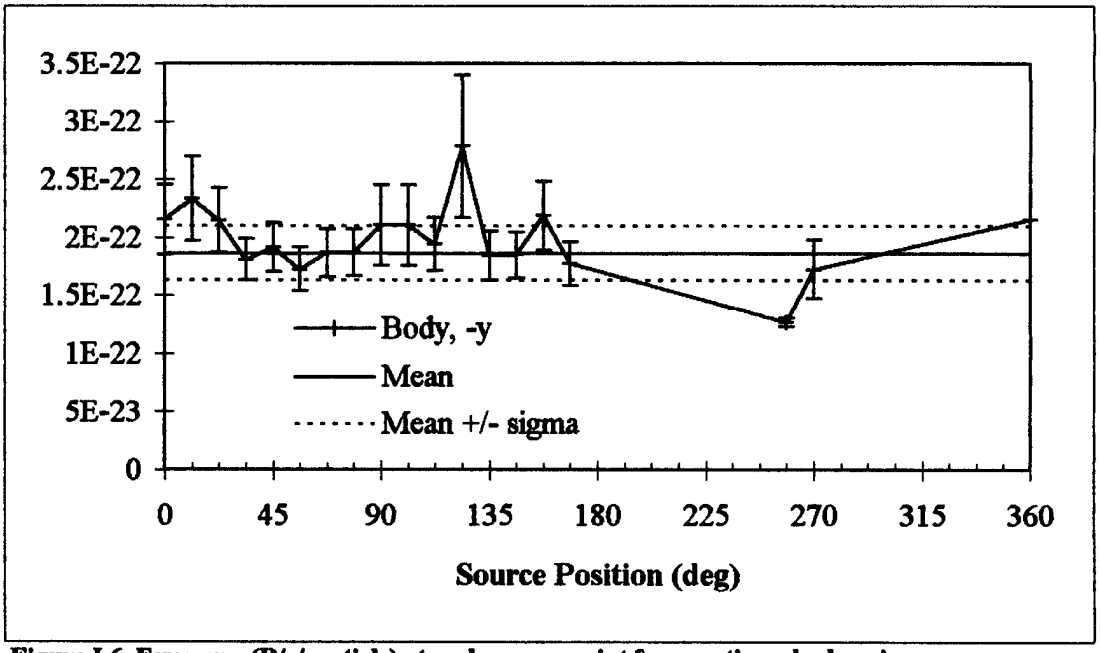

Figure I.6 Exposure (R/s/particle) at each source point for negative y body axis CT in WPMC with 1/8" lead shielding, head scan.

Appendix I: WPMC CT Suite, 1/8" Lead, Head Scan

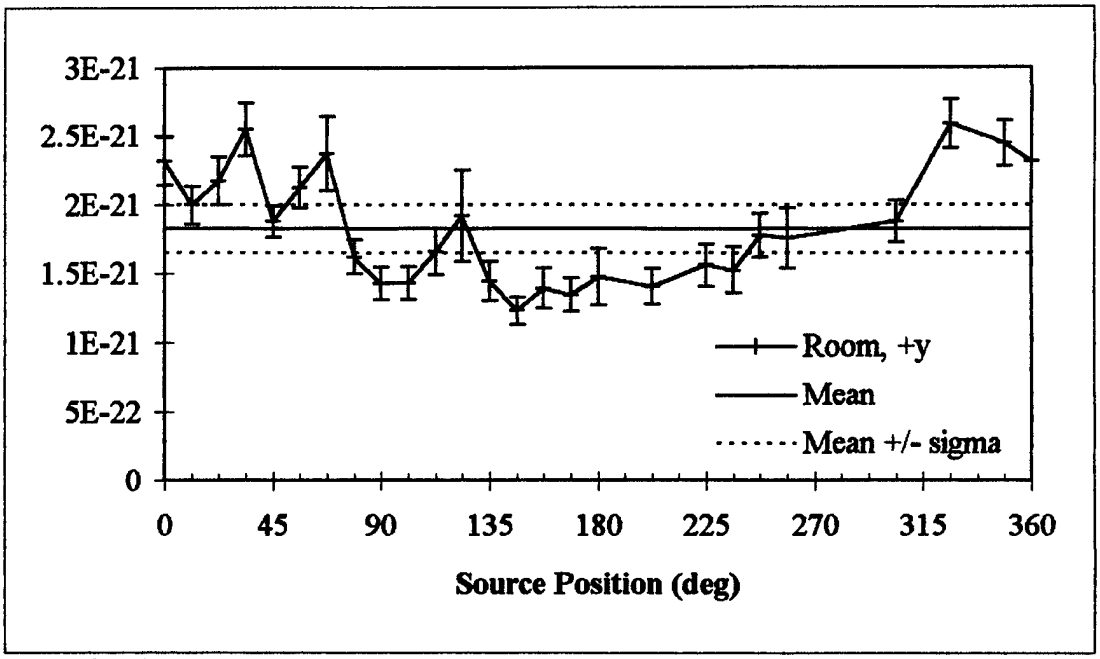

Figure I.7 Exposure (R/s/particle) at each source point for positive y room axis detector for detector for CT in WPMC with 1/8" lead shielding, head scan.

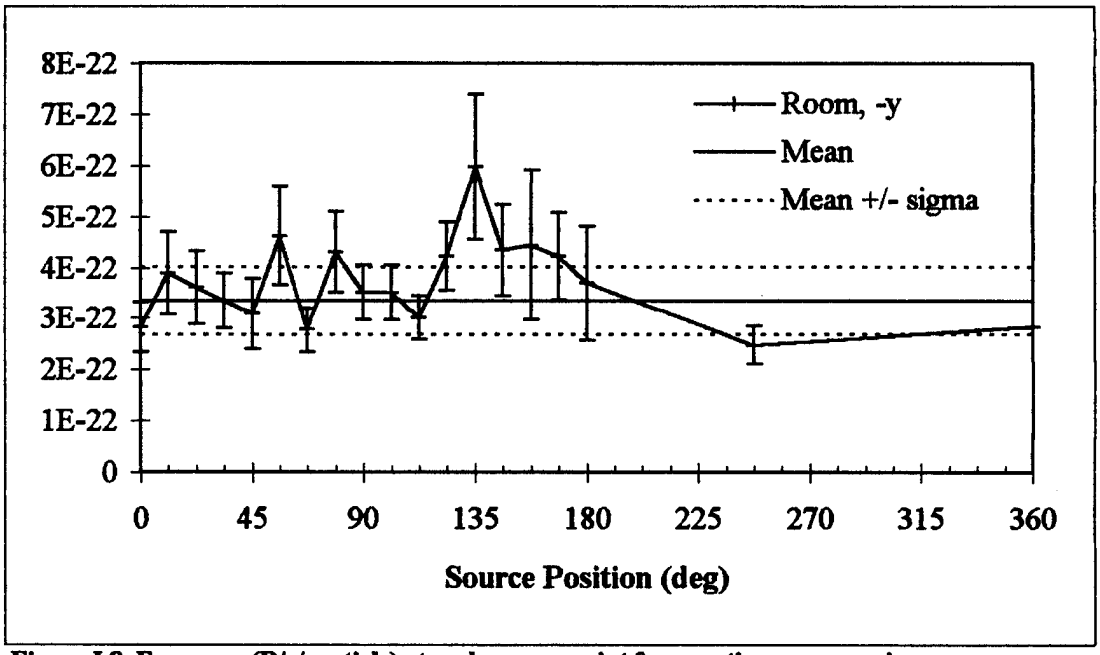

Figure I.8 Exposure (R/s/particle) at each source point for negative x room axis detector for CT in WPMC with 1/8" lead shielding, head scan.

Appendix I: WPMC CT Suite, 1/8" Lead, Head Scan

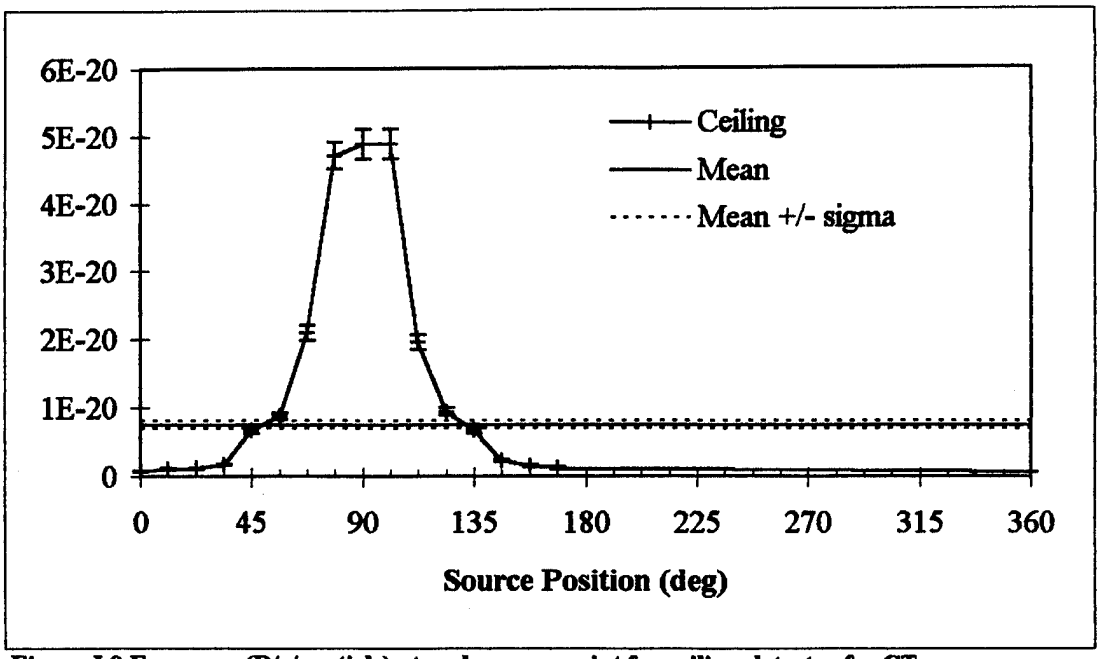

Figure I.9 Exposure (R/s/particle) at each source point for ceiling detector for CT in WPMC with 1/8" lead shielding, head scan.

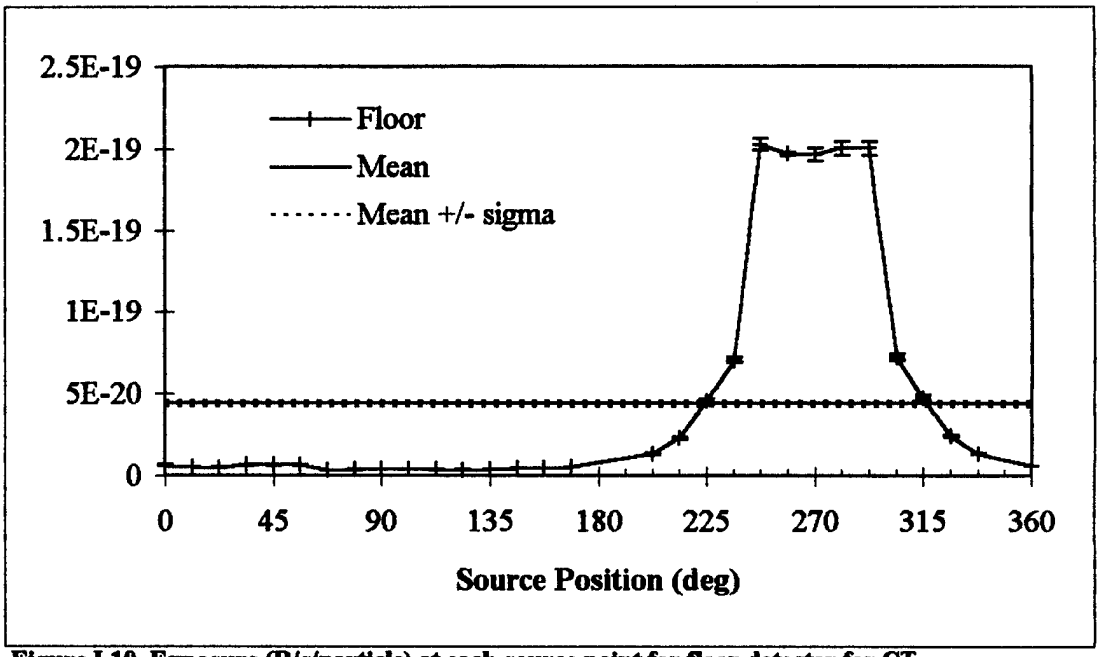

Figure I.10 Exposure (R/s/particle) at each source point for floor detector for CT in WPMC with 1/8" lead shielding, head scan.

Appendix I: WPMC CT Suite, 1/8" Lead Shielding, Head Scan

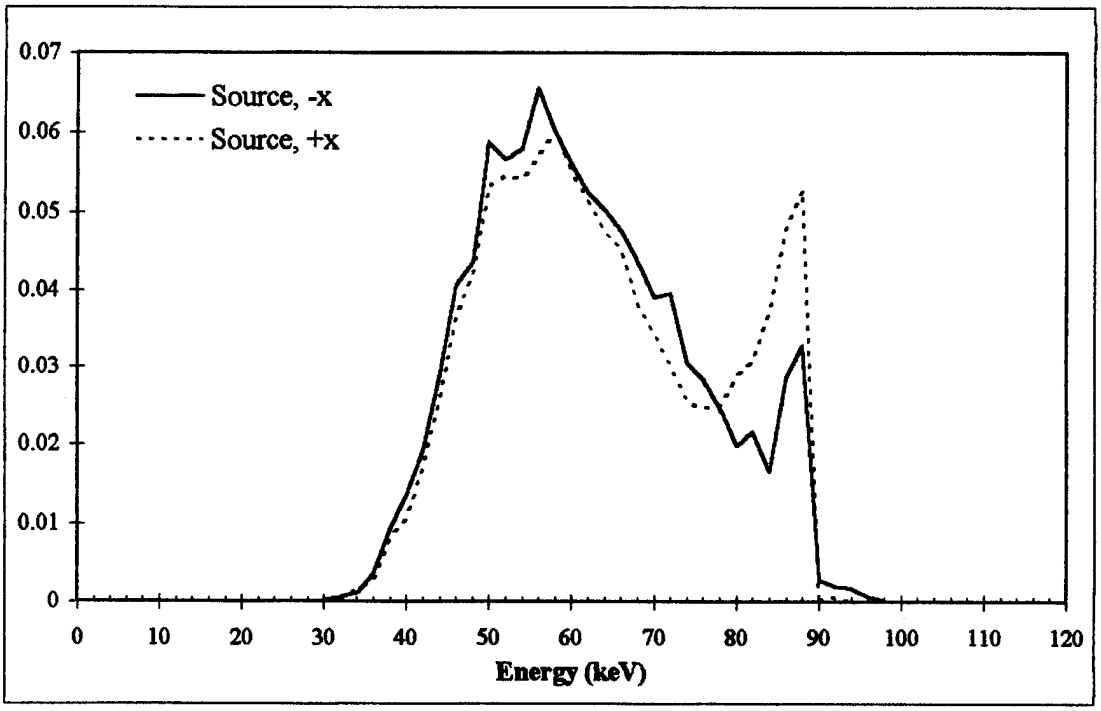

Figure I.11 Spectra for weighted average at the positive and negative x source axes for the CT at WPMC with 1/8" lead shielding, head scan.

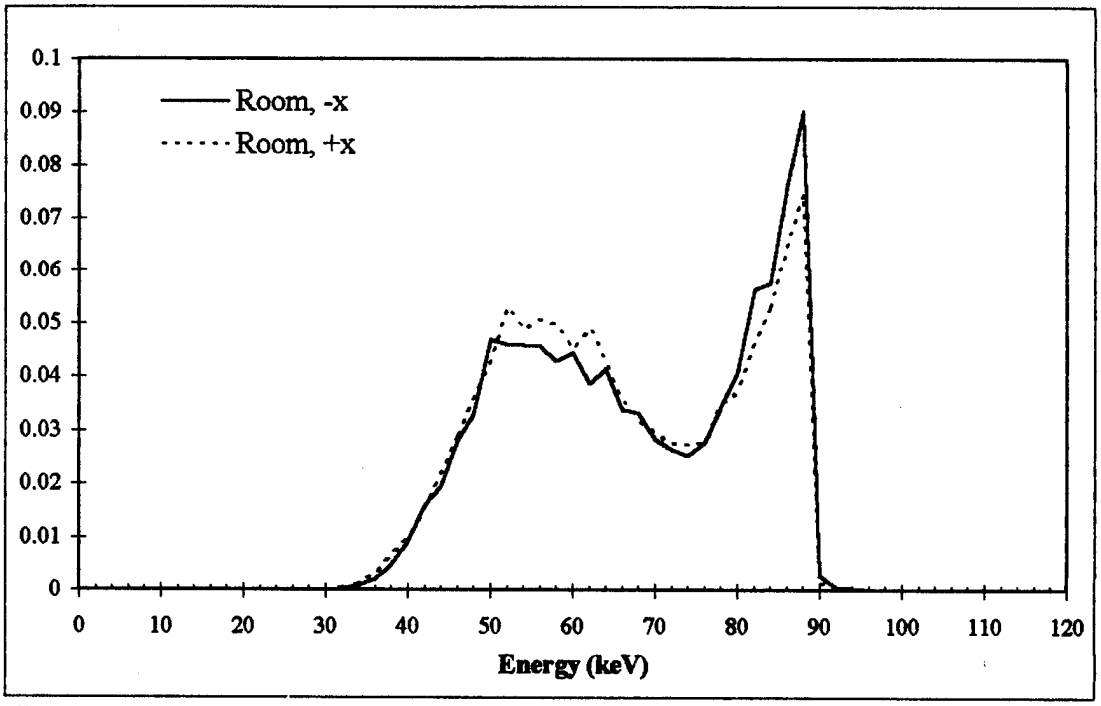

Figure I.12 Spectra for weighted average at the positive and negative x room axes for the CT at WPMC with 1/8" lead shielding, head scan.

Appendix I: WPMC CT Suite, 1/8" Lead Shielding, Head Scan

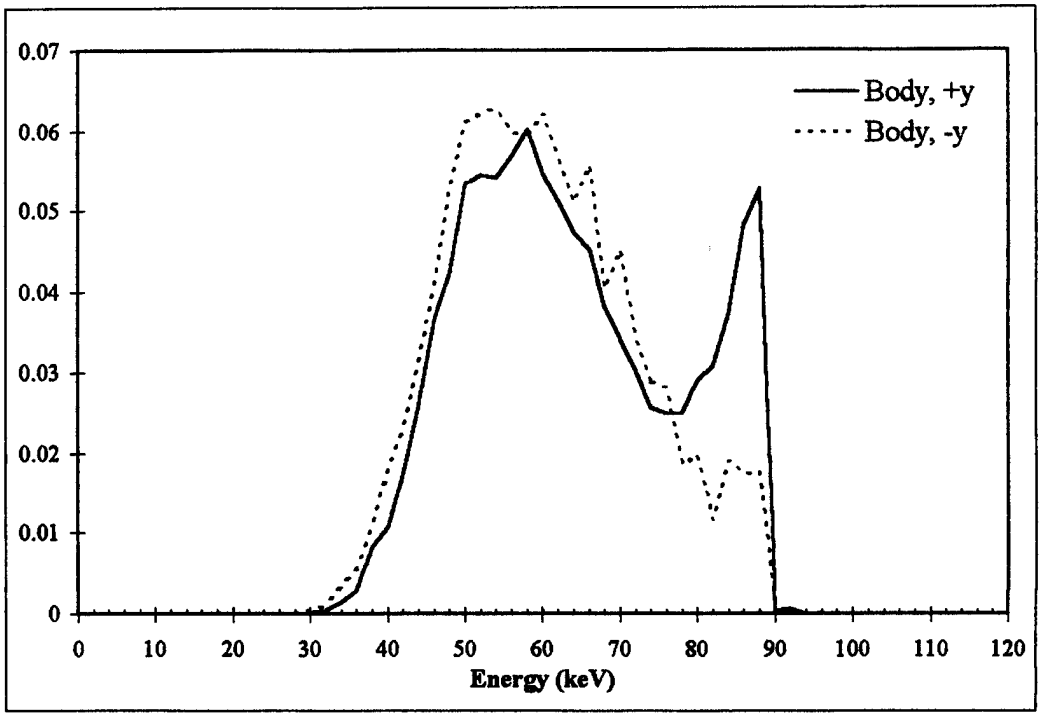

Figure I.13 Spectra for weighted average at the positive and negative y body axes for the CT at WPMC with 1/8" lead shielding, head scan.

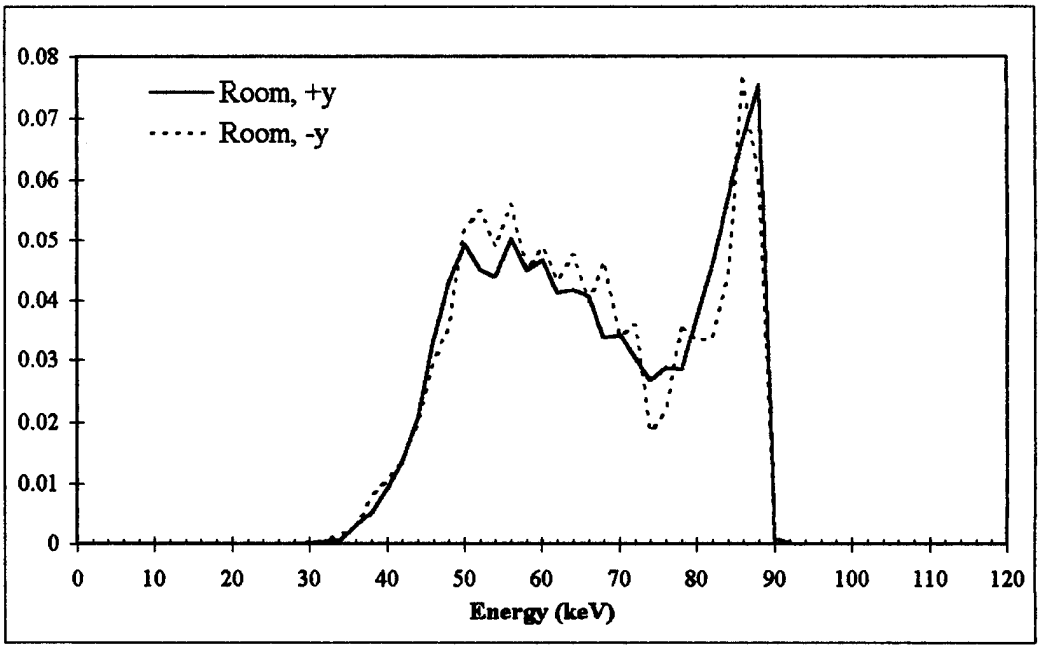

Figure I.14. Spectra for weighted average at the positive and negative y room axes for the CT at WPMC with 1/8" lead shielding, head scan.

Appendix I: WPMC CT Suite, 1/8" Lead Shielding, Head Scan

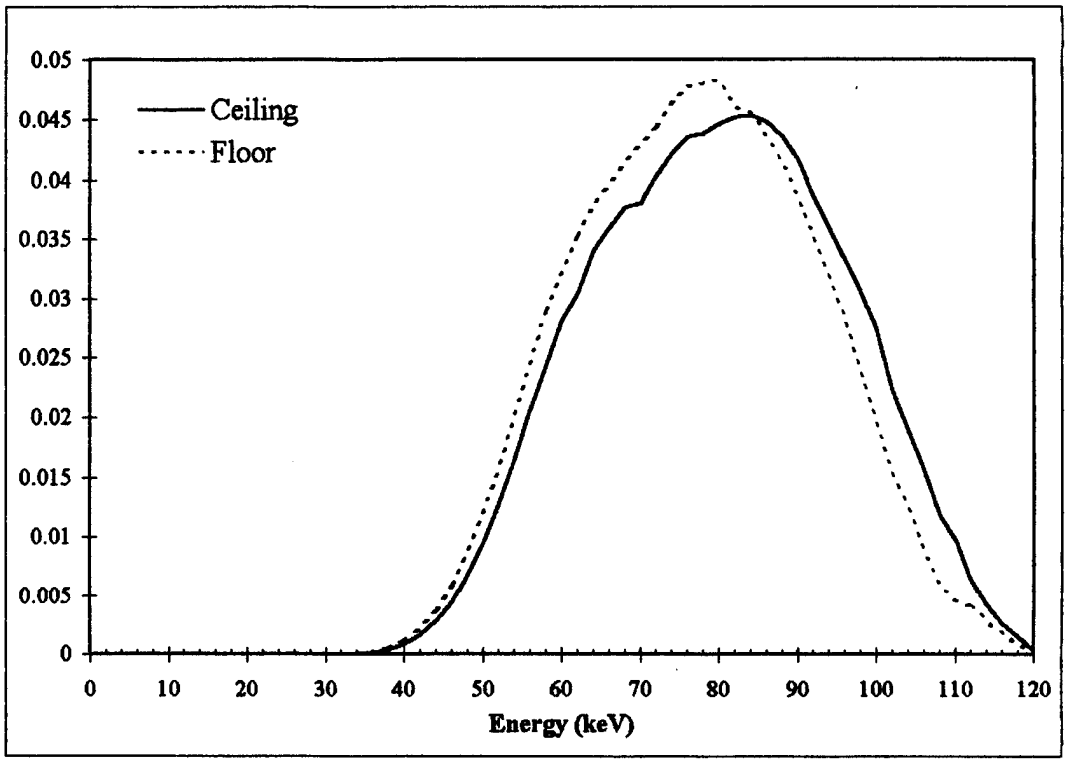

Figure I.15 Spectra for weighted average at the ceiling and floor for the CT at WPMC with 1/8" lead shielding, head scan.

Appendix J: WPMC CT Suite, 1/8" Lead Shielding, Abdomen Scan

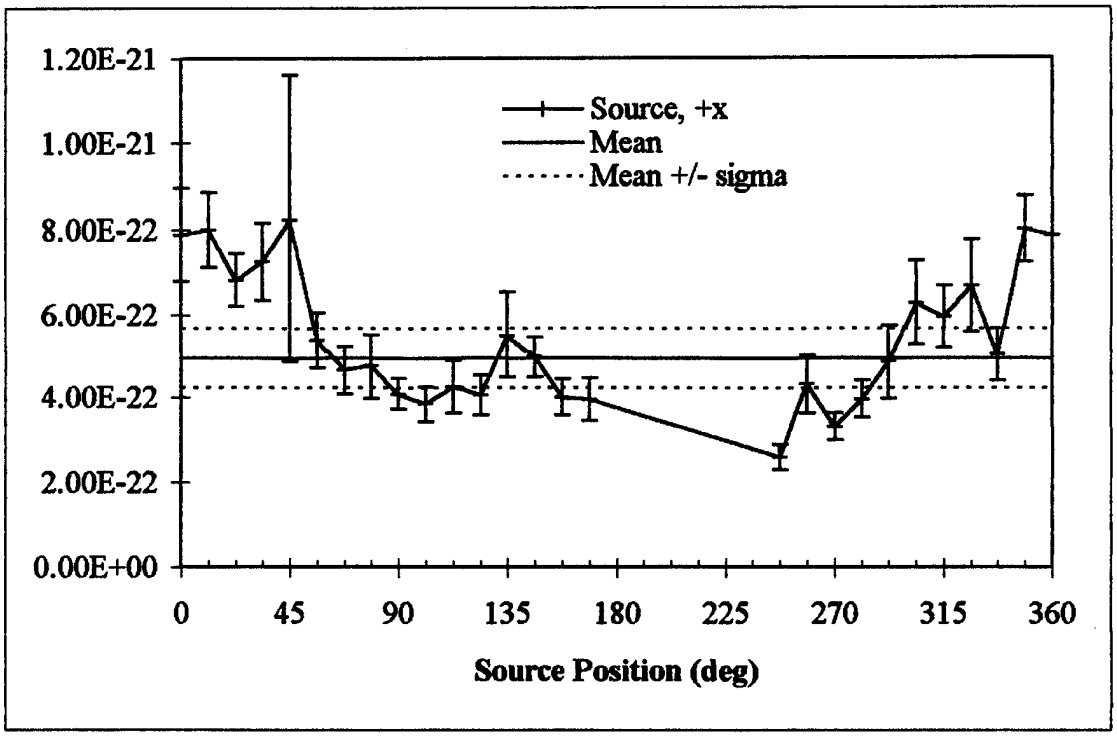

Figure J.1 Exposure (R/s/particle) at each source point for +x source axis detector for CT in WPMC with 1/8" lead shielding, abdomen scan.

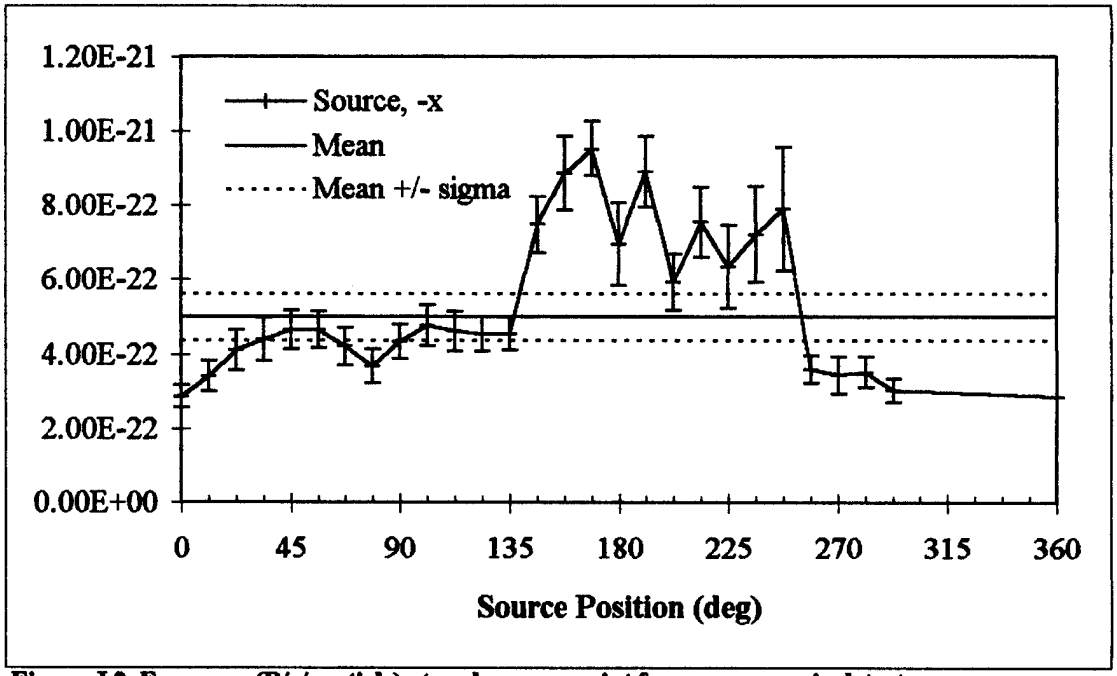

Figure J.2 Exposure (R/s/particle) at each source point for -x source axis detector for CT in WPMC with 1/8" lead shielding, abdomen scan.

Appendix J: WPMC CT Suite, 1/8" Lead Shielding, Abdomen Scan

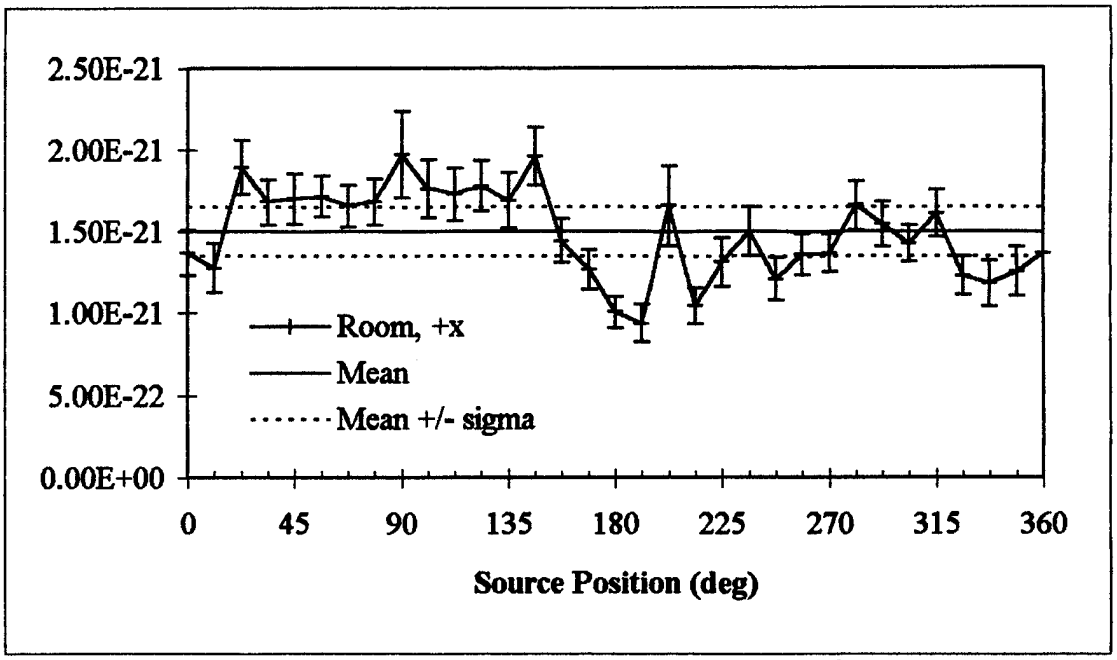

Figure J.3 Exposure (R/s/particle) at each source point for +x room axis detector for CT in WPMC with 1/8" lead shielding, abdomen scan.

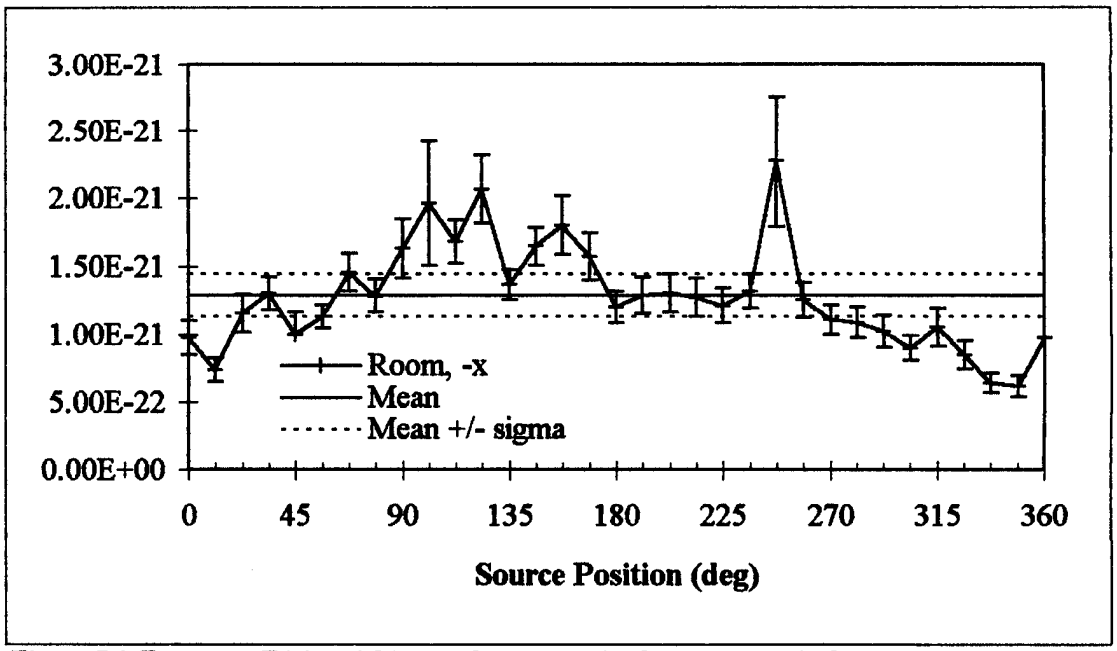

Figure J.4 Exposure (R/s/particle) at each source point for -x room axis detector for CT in WPMC with 1/8" lead shielding, abdomen scan.

Appendix J: WPMC CT Suite, 1/8" Lead Shielding, Abdomen Scan

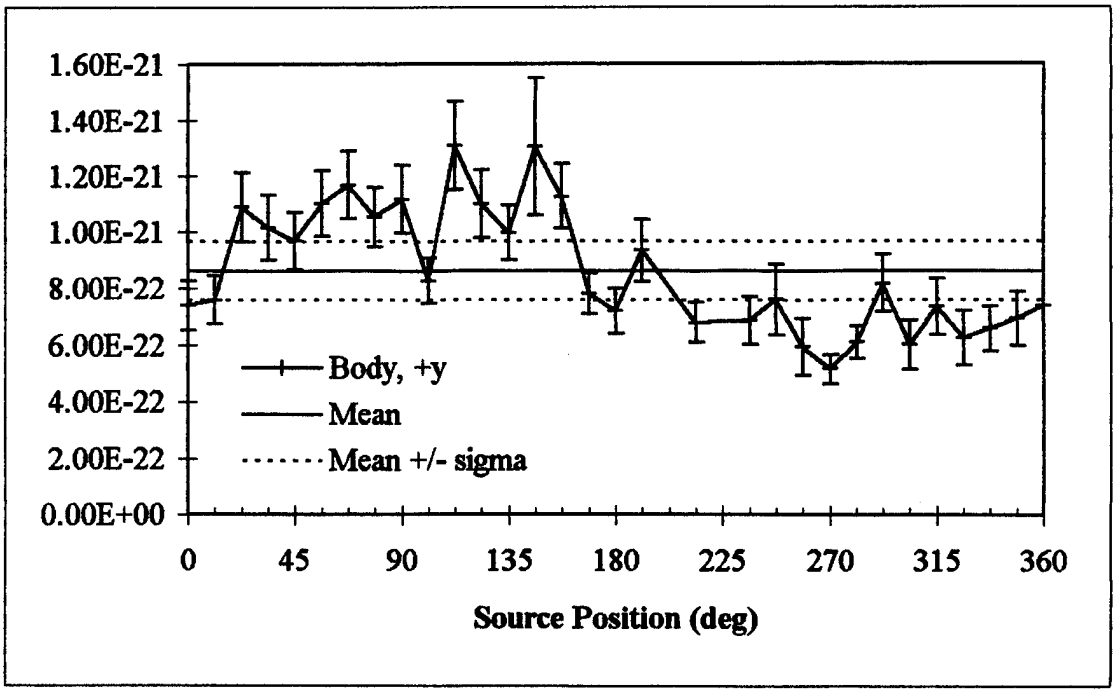

Figure J.5 Exposure (R/s/particle) at each source point for +y source axis detector for CT in WPMC with 1/8" lead shielding, abdomen scan.

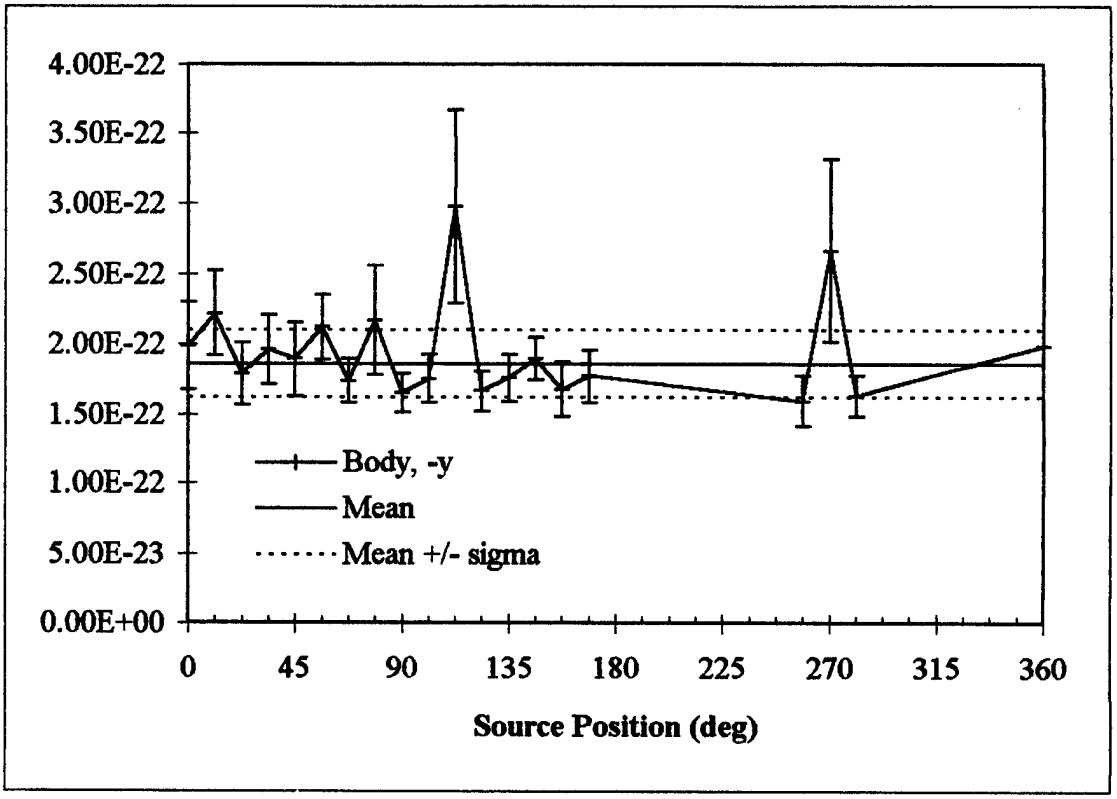

Figure J.6 Exposure (R/s/particle) at each source point for -y body axis detector for CT in WPMC with 1/8" lead shielding, abdomen scan.

Appendix J: WPMC CT Suite, 1/8" Lead Shielding, Abdomen Scan

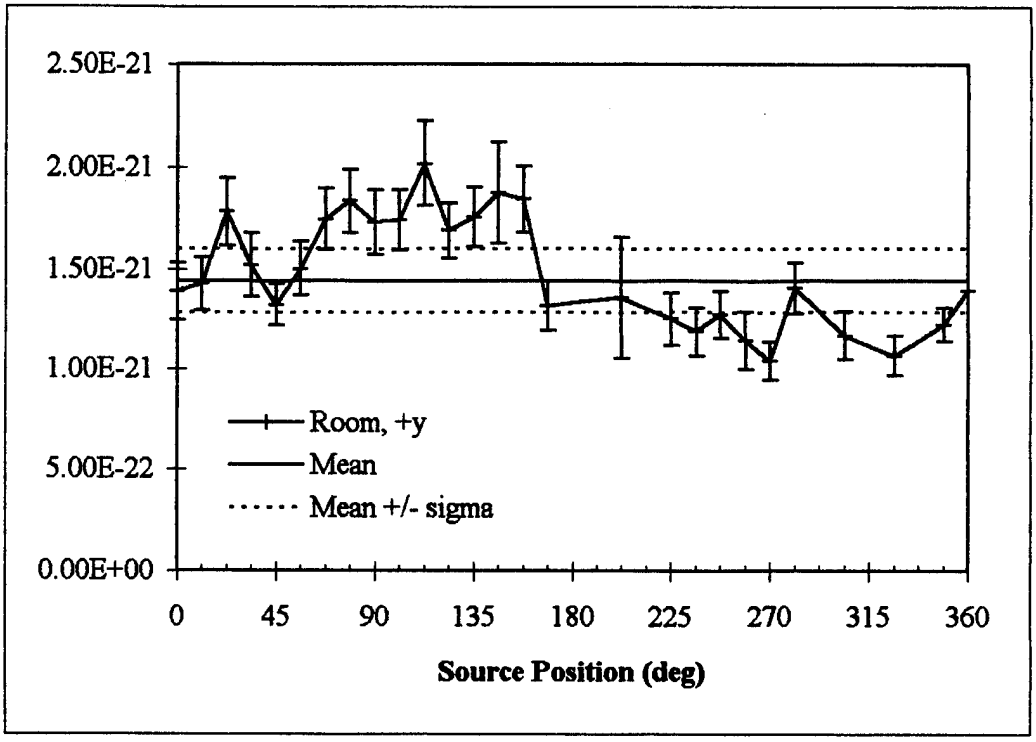

Figure J.7 Exposure (R/s/particle) at each source point for +y room axis detector for CT in WPMC with 1/8" lead shielding, abdomen scan.

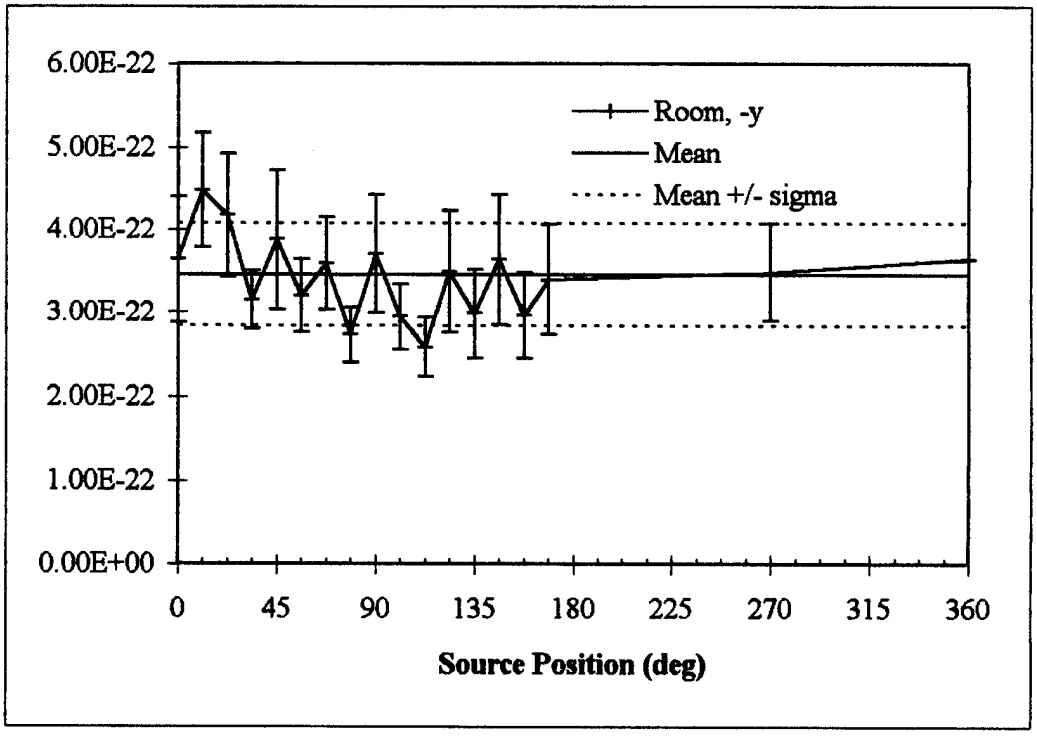

Figure J.8 Exposure (R/s/particle) at each source point for -y room axis detector for CT in WPMC with 1/8" lead shielding, abdomen scan.

Appendix J: WPMC CT Suite, 1/8" Lead Shielding, Abdomen Scan

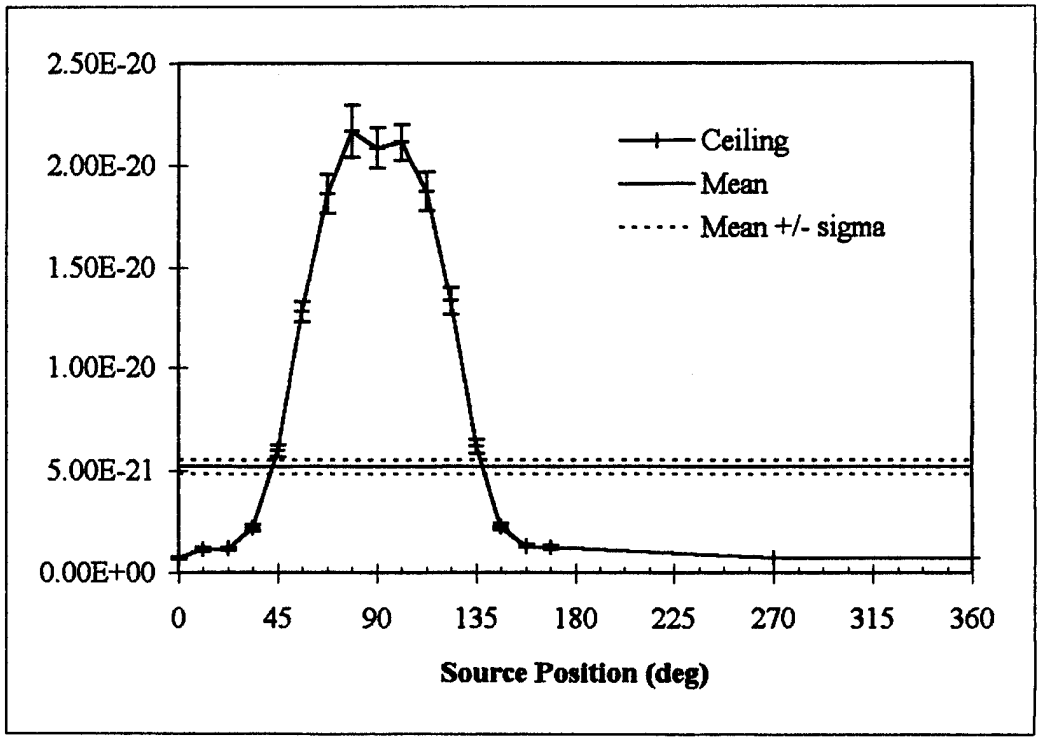

Figure J.9 Exposure (R/s/particle) at each source point for ceiling detector for CT in WPMC with 1/8" lead shielding, abdomen scan.

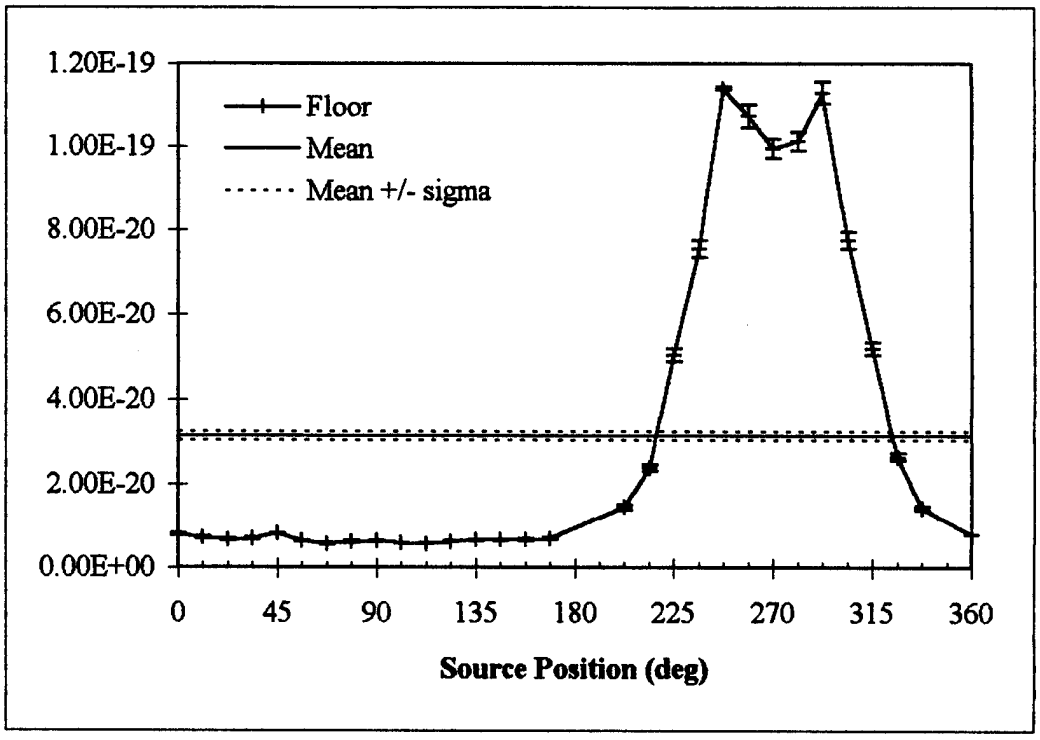

Figure J.10 Exposure (R/s/particle) at each source point for floor detector for CT in WPMC with 1/8" lead shielding, abdomen scan.

Appendix J: WPMC CT Suite, 1/8" Lead Shielding, Abdomen Scan

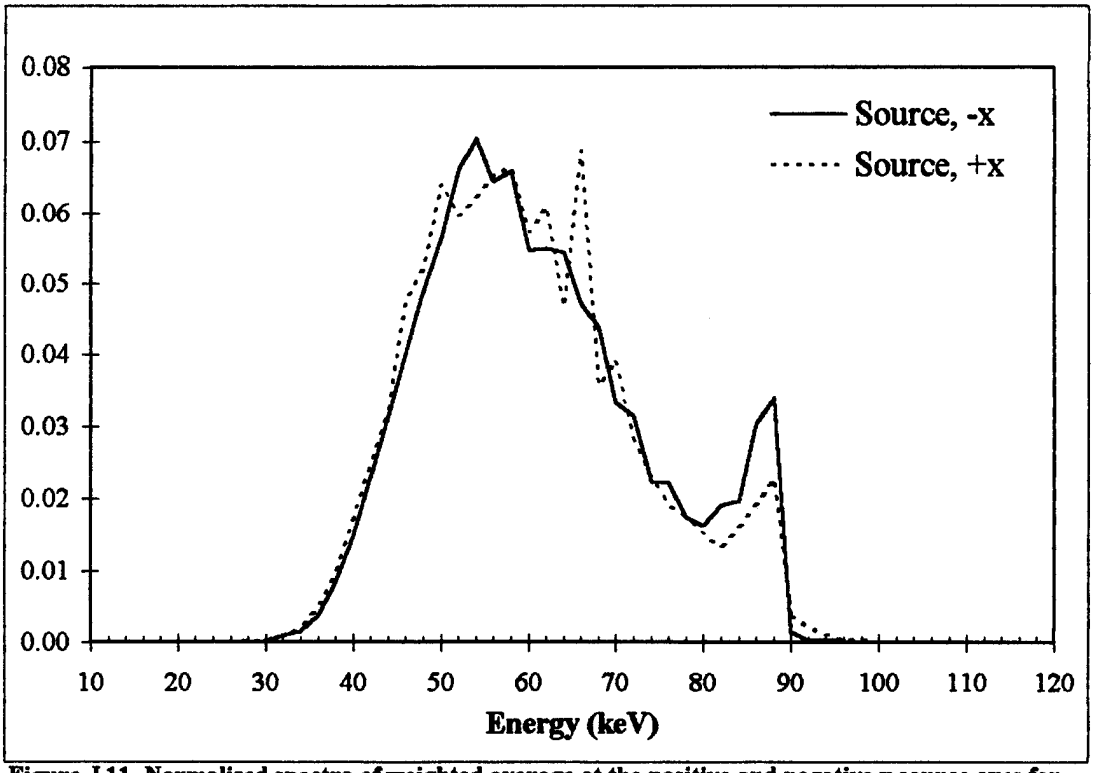

Figure J.11 Normalized spectra of weighted average at the positive and negative x source axes for the CT at WPMC with 1/8" lead shielding, abdomen scan.

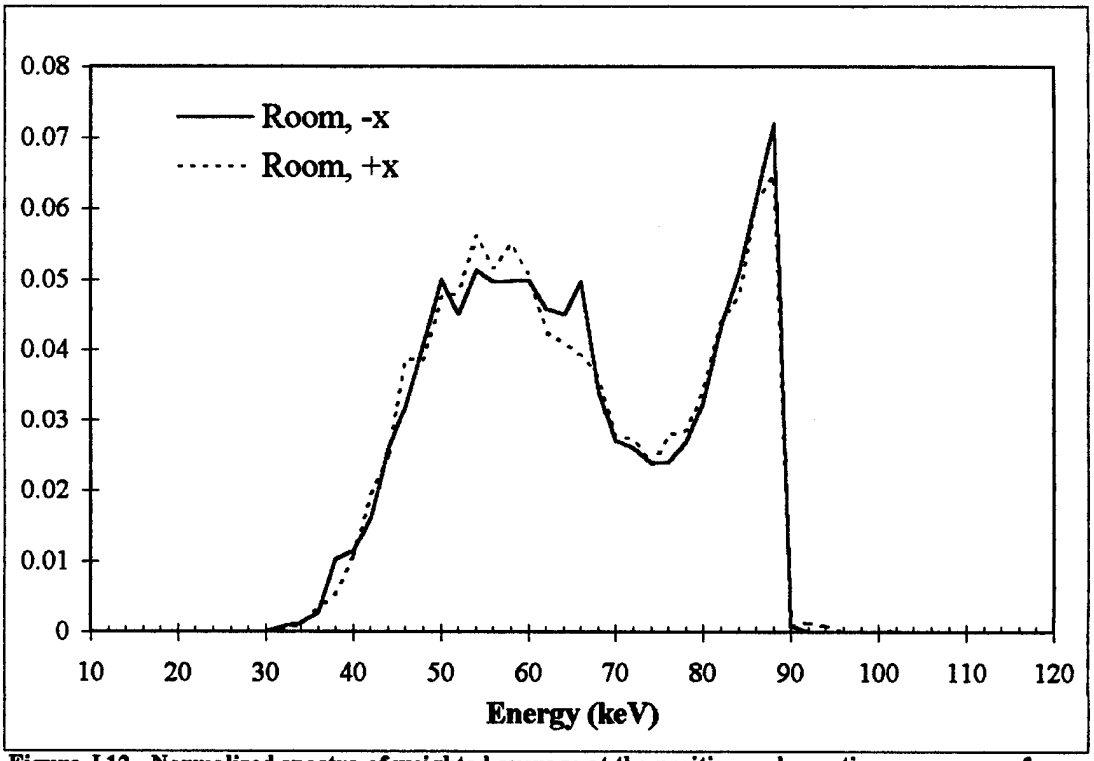

Figure J.12. Normalized spectra of weighted average at the positive and negative x room axes for the CT at WPMC with 1/8" lead shielding, abdomen scan.

Appendix J: WPMC CT Suite, 1/8" Lead Shielding, Abdomen Scan

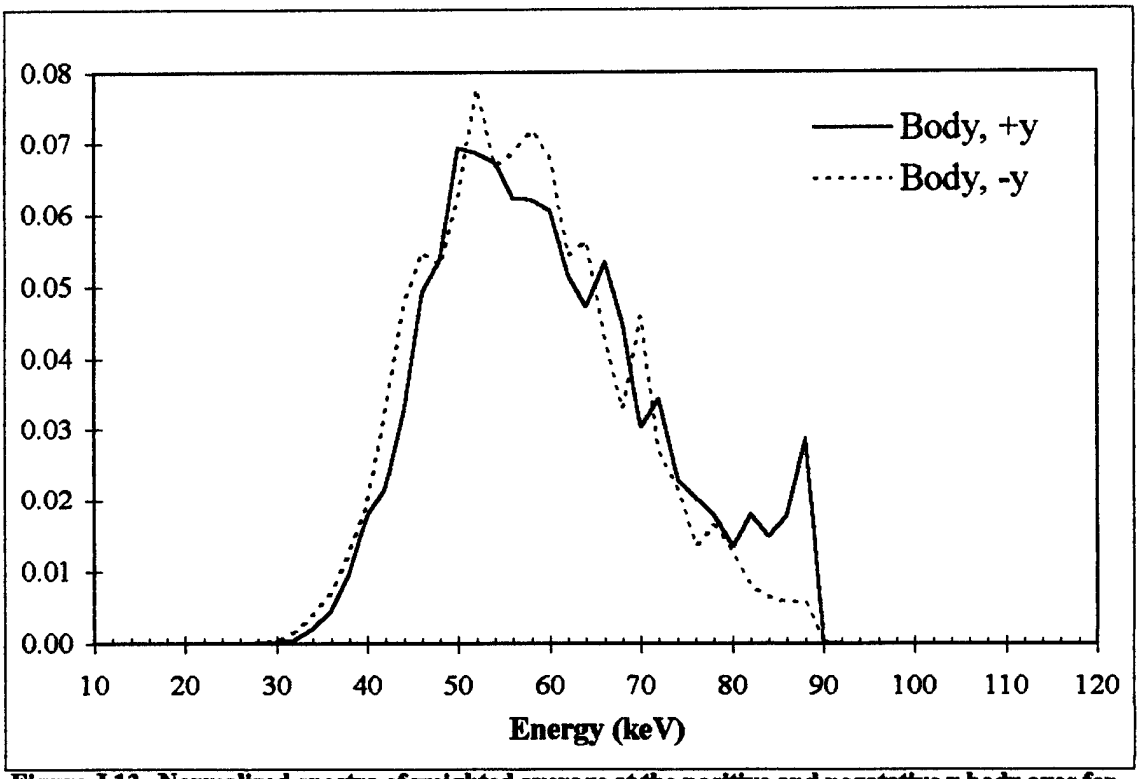

Figure J.13 Normalized spectra of weighted average at the positive and negatative y body axes for the CT at WPMC with 1/8" lead shielding, abdomen scan.

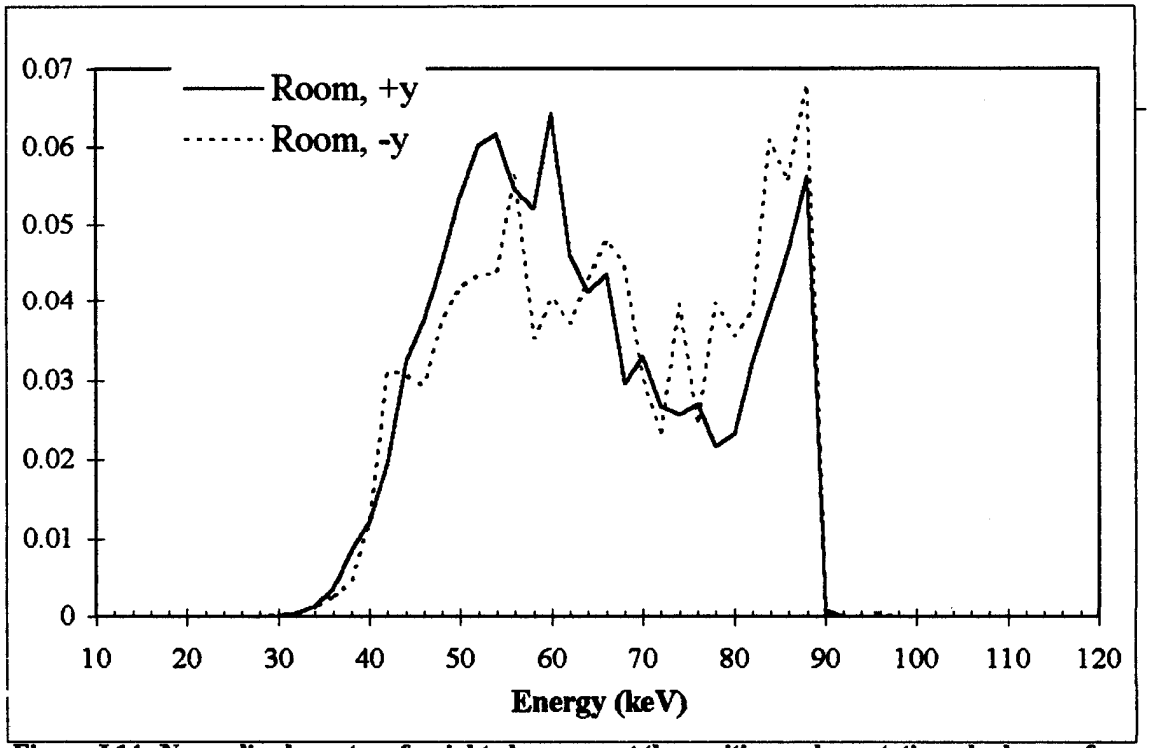

Figure J.14 Normalized spectra of weighted average at the positive and negatative y body axes for the CT at WPMC with 1/8" lead shielding, abdomen scan.

Appendix J: WPMC CT Suite, 1/8" Lead Shielding, Abdomen Scan

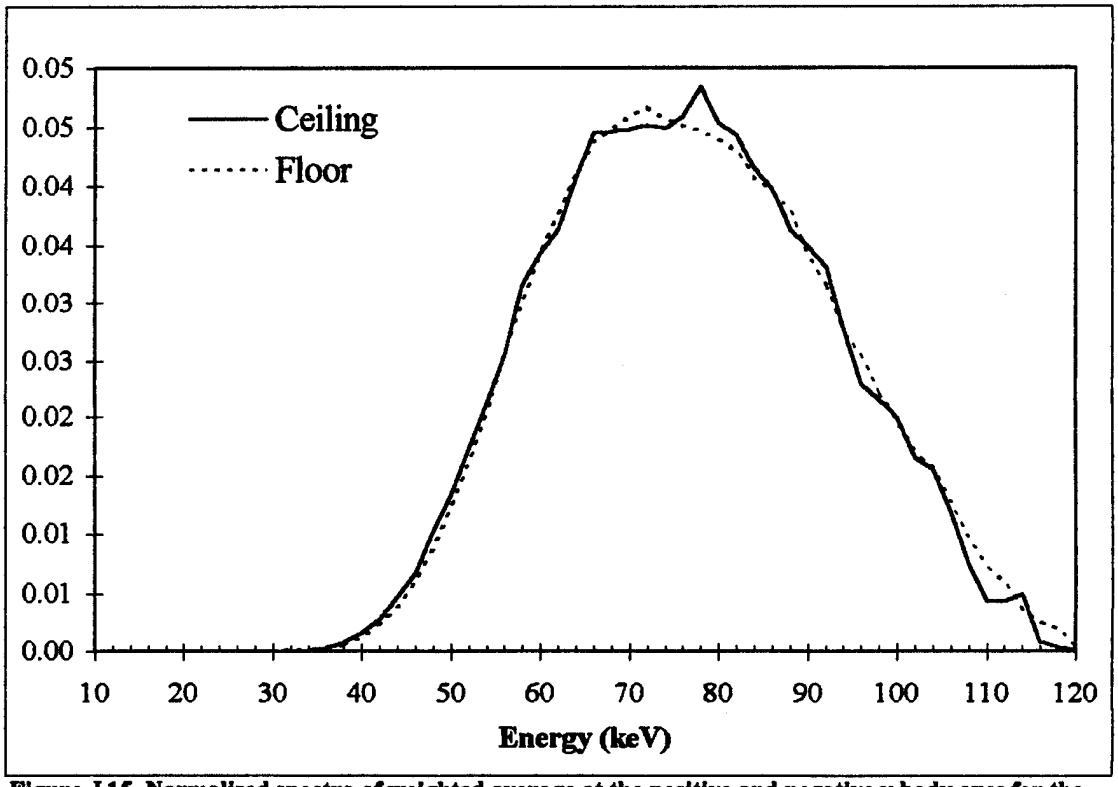

Figure J.15 Normalized spectra of weighted average at the positive and negative y body axes for the CT at WPMC with 1/8" lead shielding, abdomen scan.

Appendix K: GE Minimum Recommended Suite, 1/16" Lead Shielding, Head Scan

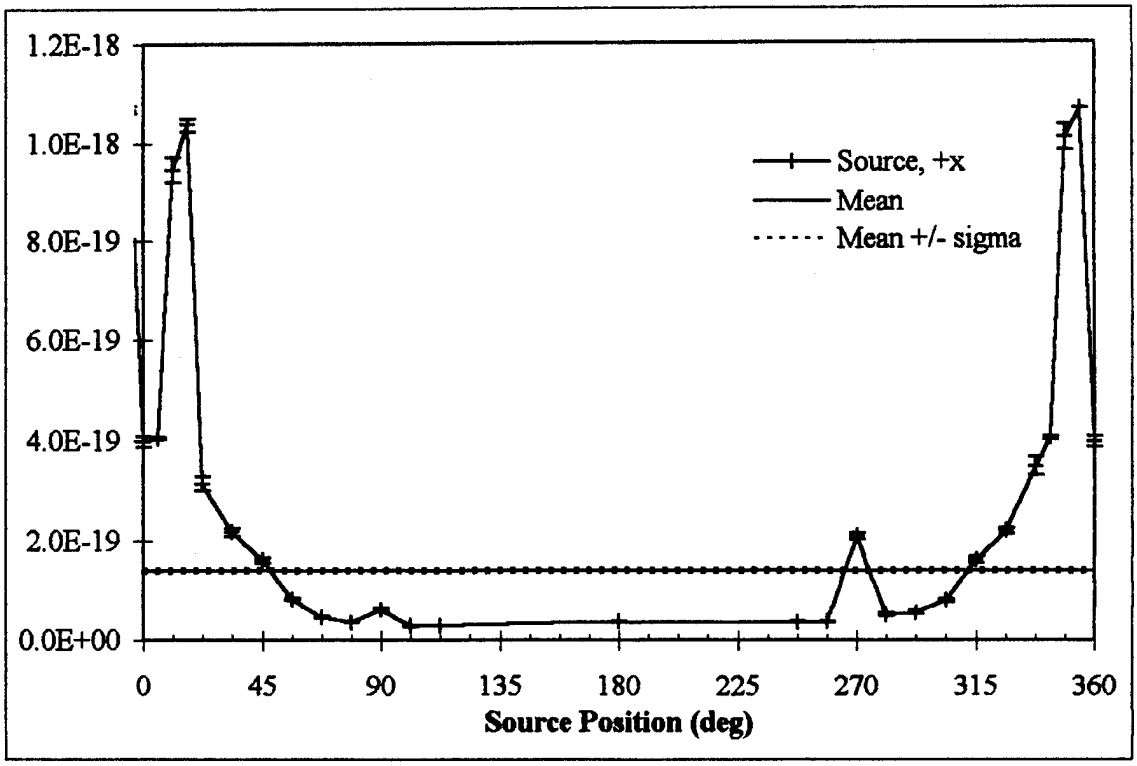

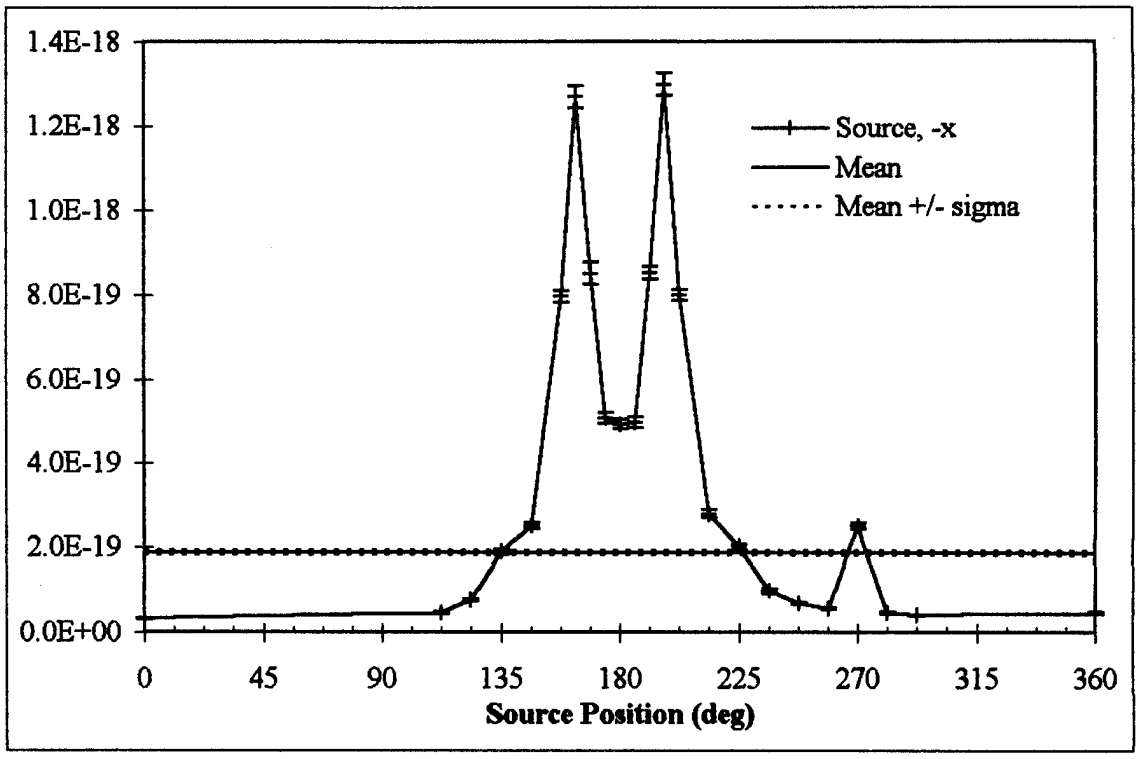

Figure K.2 Exposure (R/s/particle) at each source point for negative x source axis detector with with CT in GE minimum recommended room, 1/16" lead, head scan.

Appendix K: GE Minimum Recommended Suite, 1/16" Lead Shielding, Head Scan

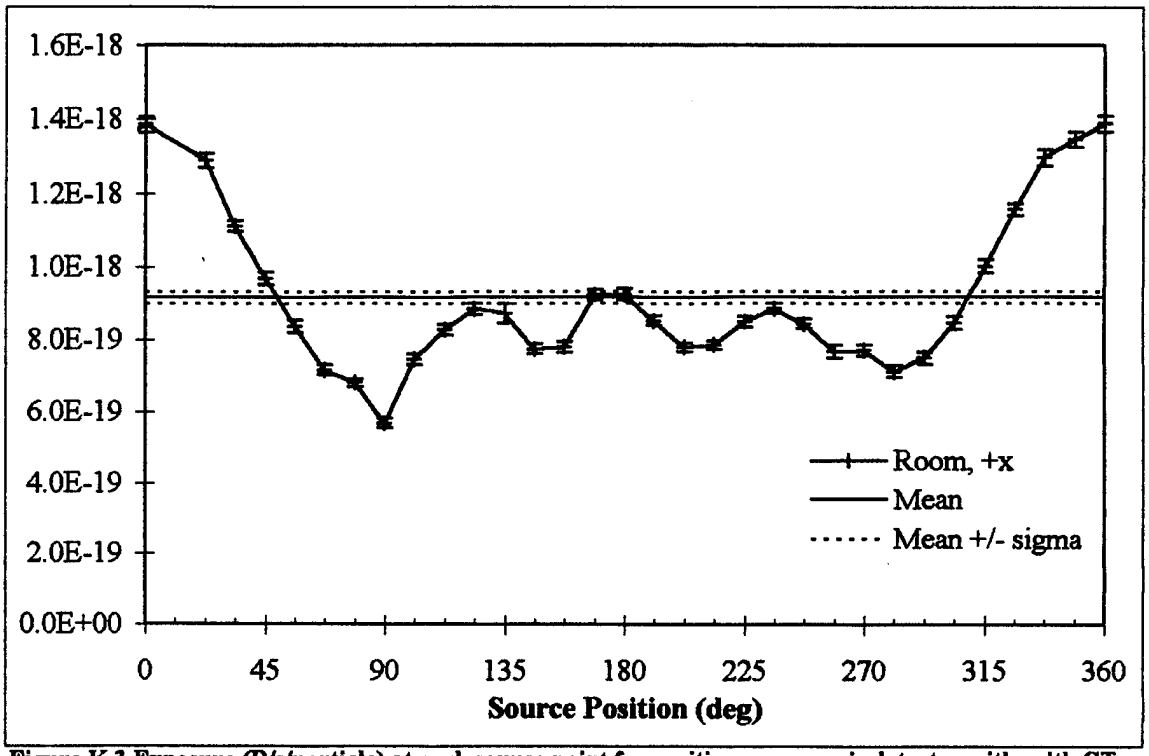

Figure K.3 Exposure (R/s/particle) at each source point for positive x room axis detector with with CT in GE minimum recommended room, 1/16" lead, head scan.

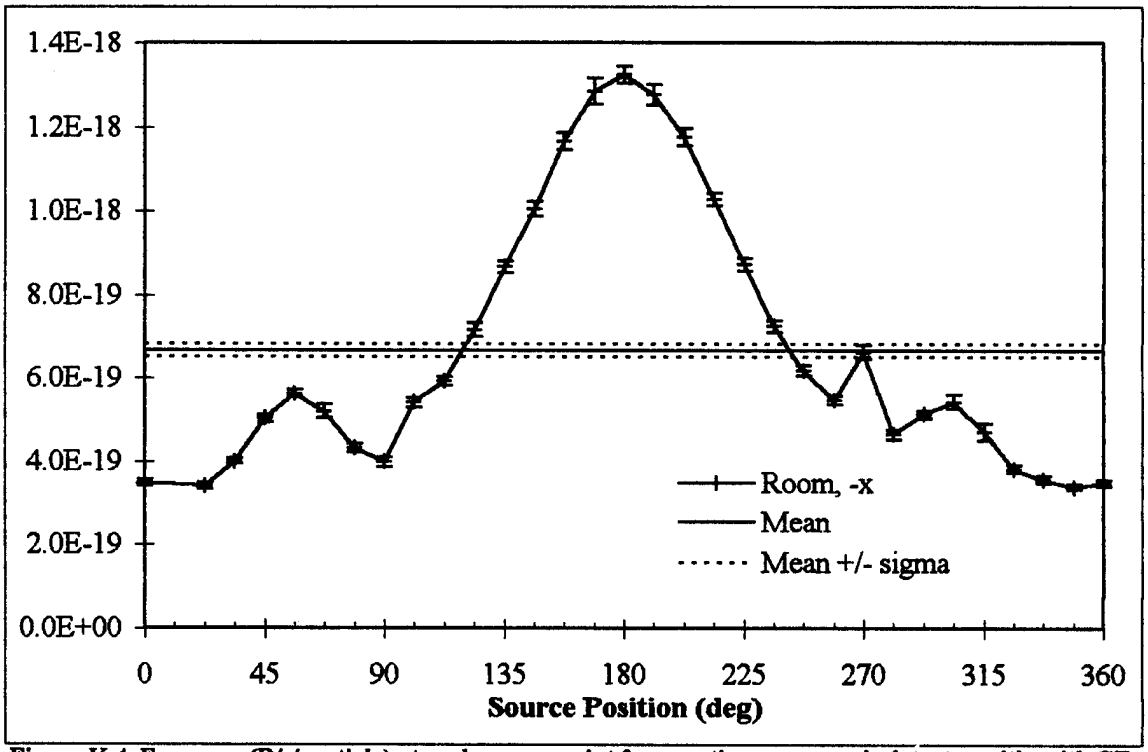

Figure K.4 Exposure (R/s/particle) at each source point for negative x room axis detector with with CT in GE minimum recommended room, 1/16" lead, head scan.

Appendix K: GE Minimum Recommended Suite, 1/16" Lead Shielding, Head Scan

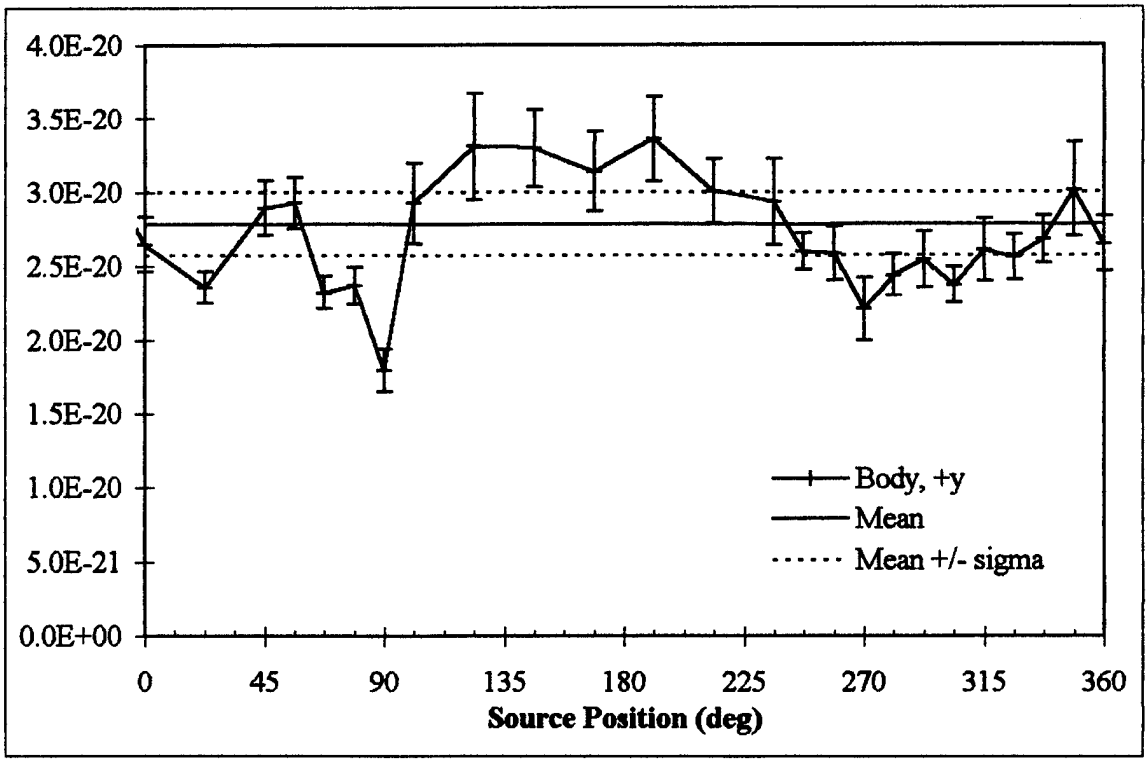

Figure K.5 Exposure (R/s/particle) at each source point for positive y body axis detector with with CT in GE minimum recommended room, 1/16" lead, head scan.

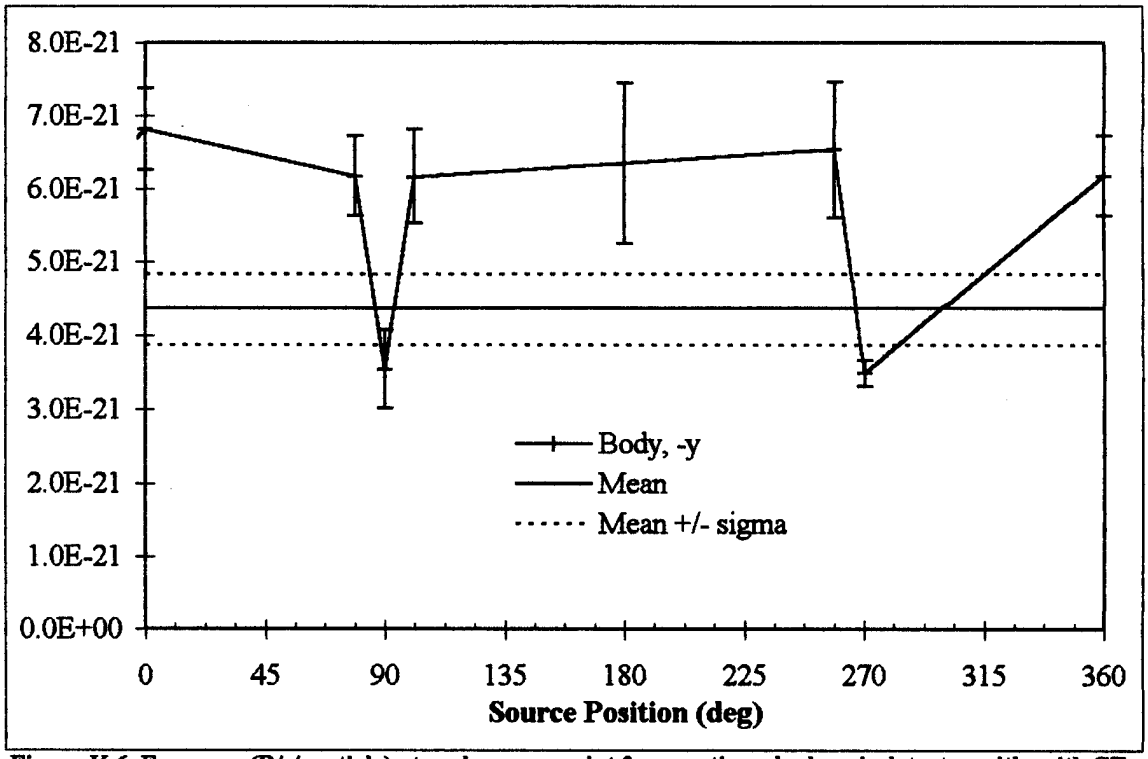

Figure K.6 Exposure (R/s/particle) at each source point for negative y body axis detector with with CT in GE minimum recommended room, 1/16" lead, head scan.

Appendix K: GE Minimum Recommended Suite, 1/16" Lead Shielding, Head Scan

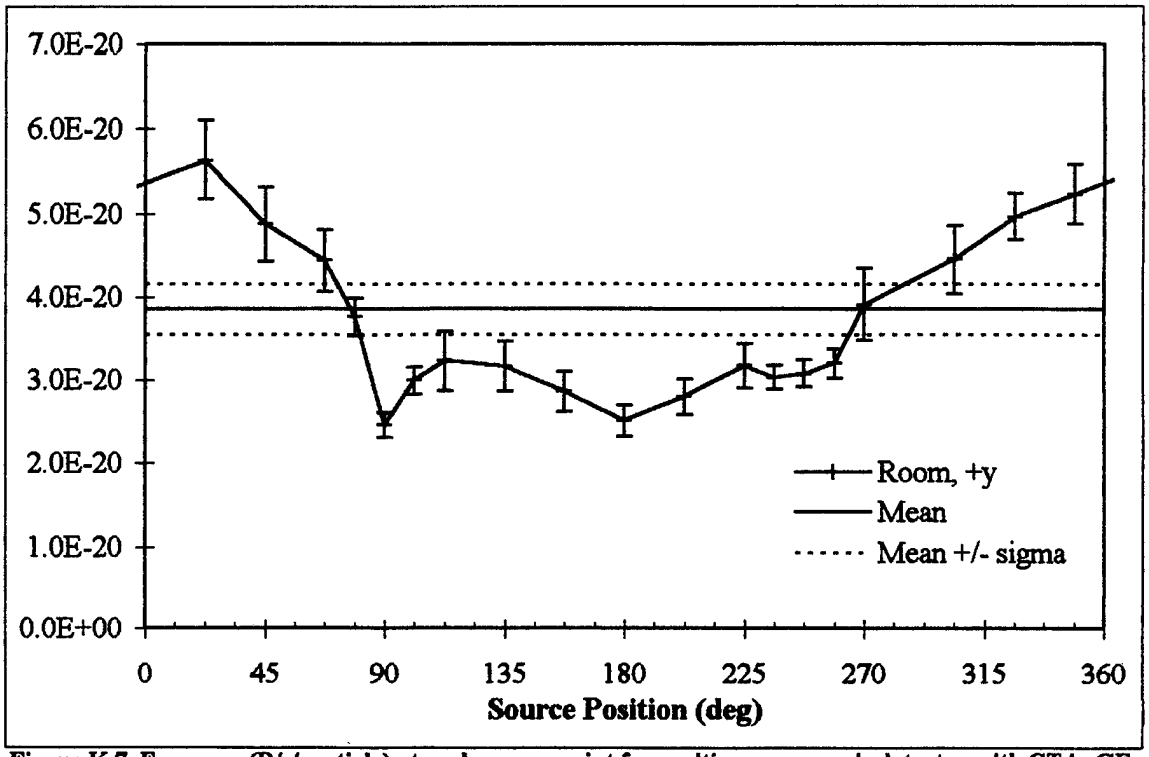

Figure K.7 Exposure (R/s/particle) at each source point for positive y room axis detector with CT in GE minimum recommended room suite, 1/16" lead, head scan.

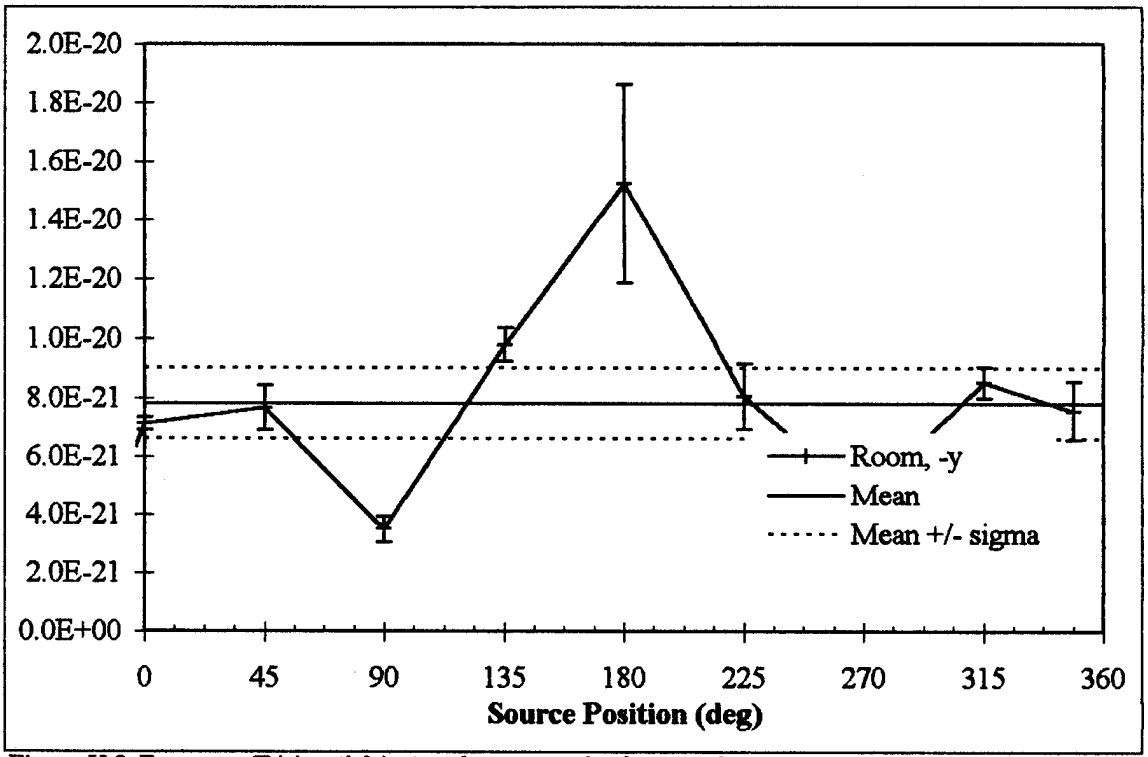

Figure K.8 Exposure (R/s/particle) at each source point for negative y room axis detector with with CT in GE minimum recommended room, 1/16" lead, head scan.

Appendix K: GE Minimum Recommended Suite, 1/16" Lead Shielding, Head Scan

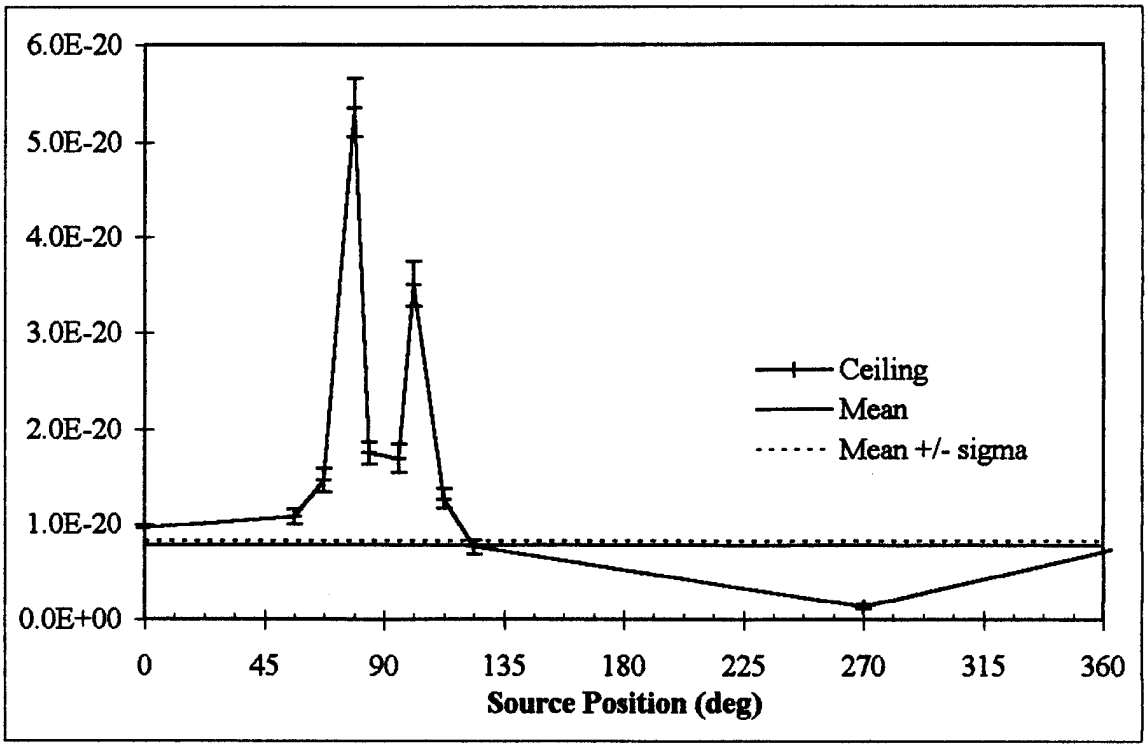

Figure K.9 Exposure (R/s/particle) at each source point for ceiling detector with with CT in GE minimum recommended room, 1/16" lead, head scan.

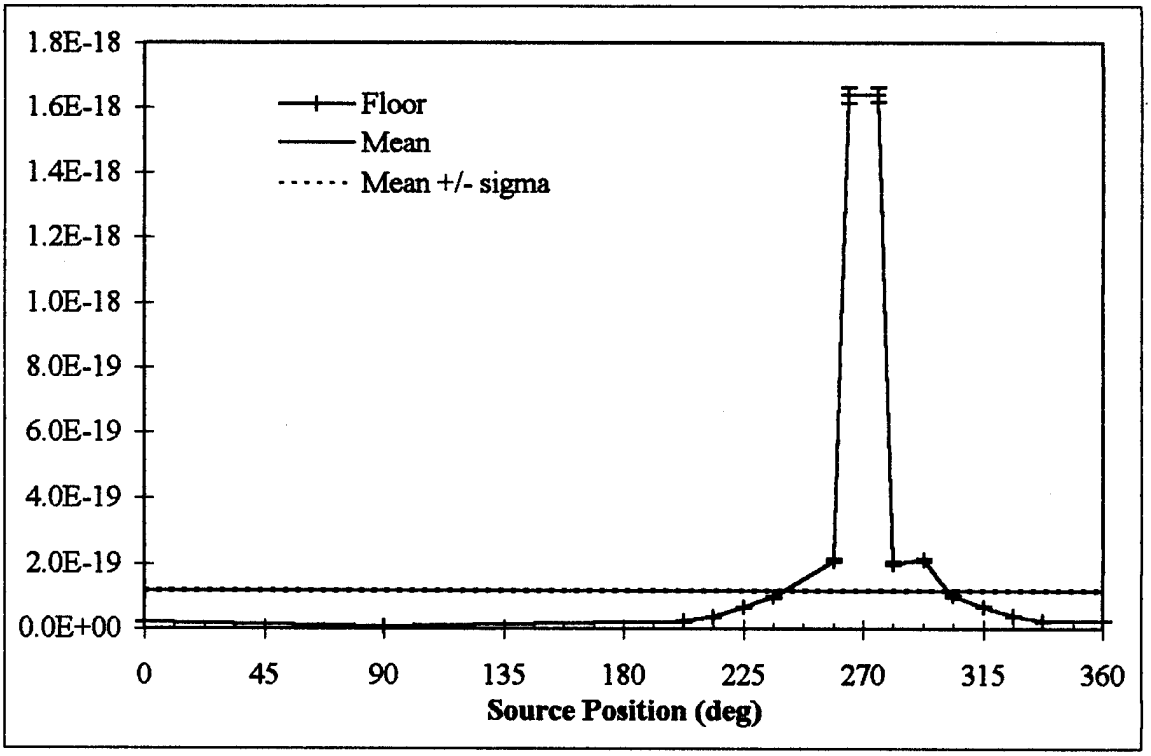

Figure K.10 Exposure (R/s/particle) at each source point for floor detector with CT in GE minimum recommended room, 1/16" lead shielding, head scan.

Appendix K: GE Minimum Recommended Suite, 1/16" Lead Shielding, Head Scan

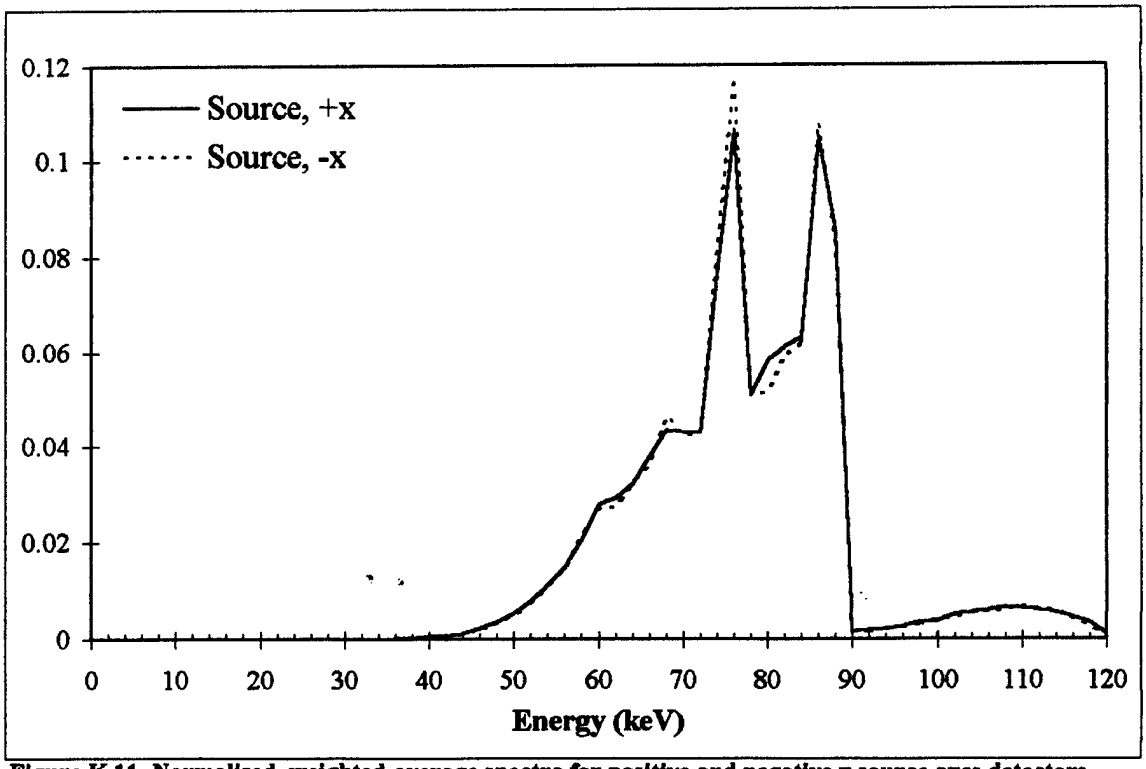

Figure K.11 Normalized, weighted-average spectra for positive and negative x source axes detectors with CT in GE minimum recommended room, 1/16" lead, head scan.

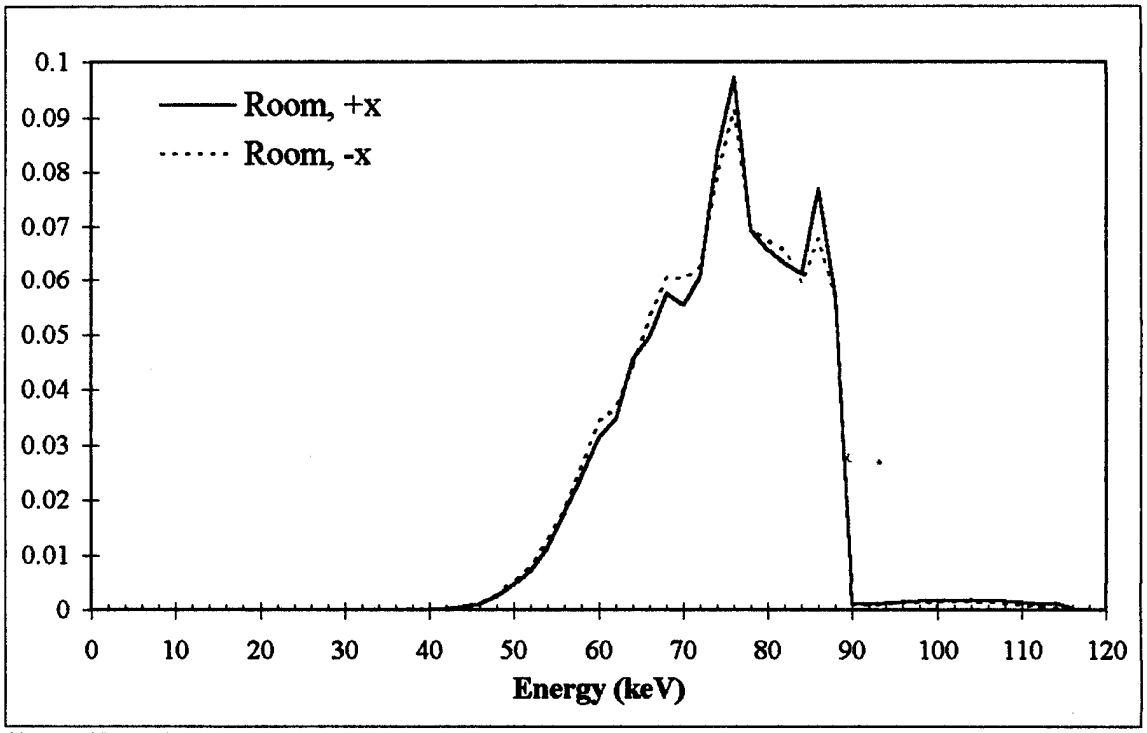

Figure K.12 Normalized, weighted-average spectra for positive and negative x room axes detectors with CT in GE minimum recommended room, 1/16" lead, head scan.

Appendix K: GE Minimum Recommended Suite, 1/16" Lead Shielding, Head Scan

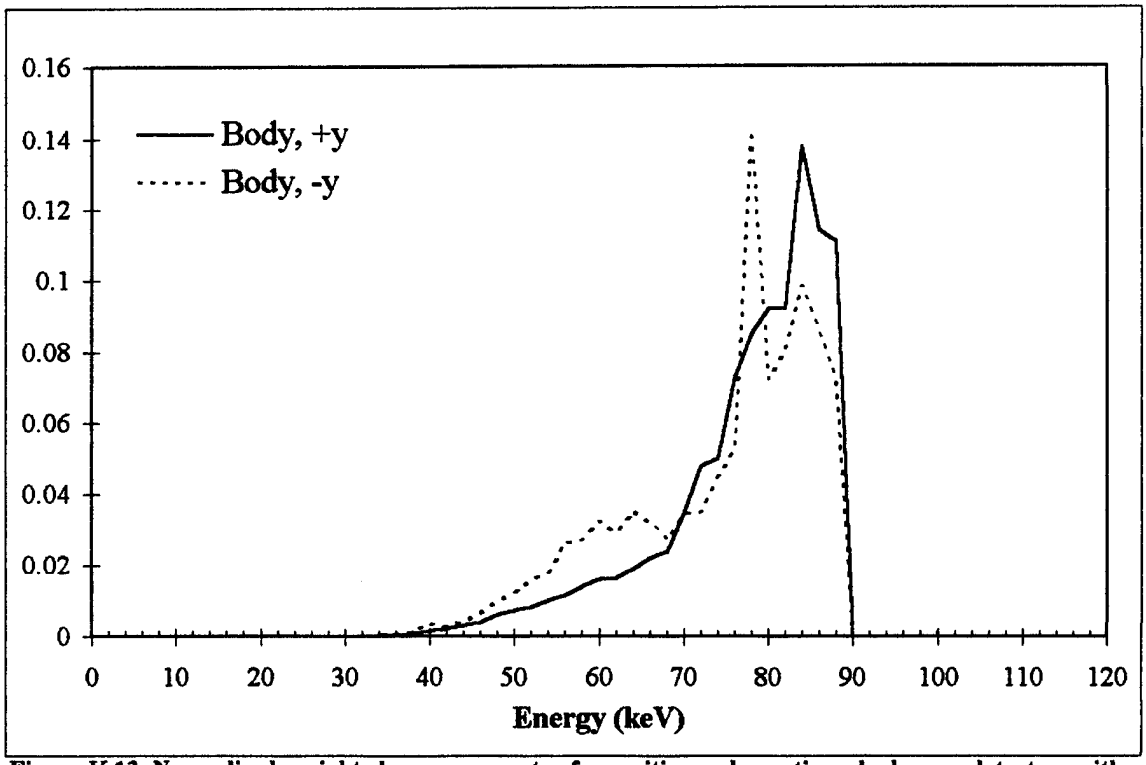

Figure K.13 Normalized, weighted-average spectra for positive and negative y body axes detectors with CT in GE minimum recommended room, 1/16" lead, head scan.

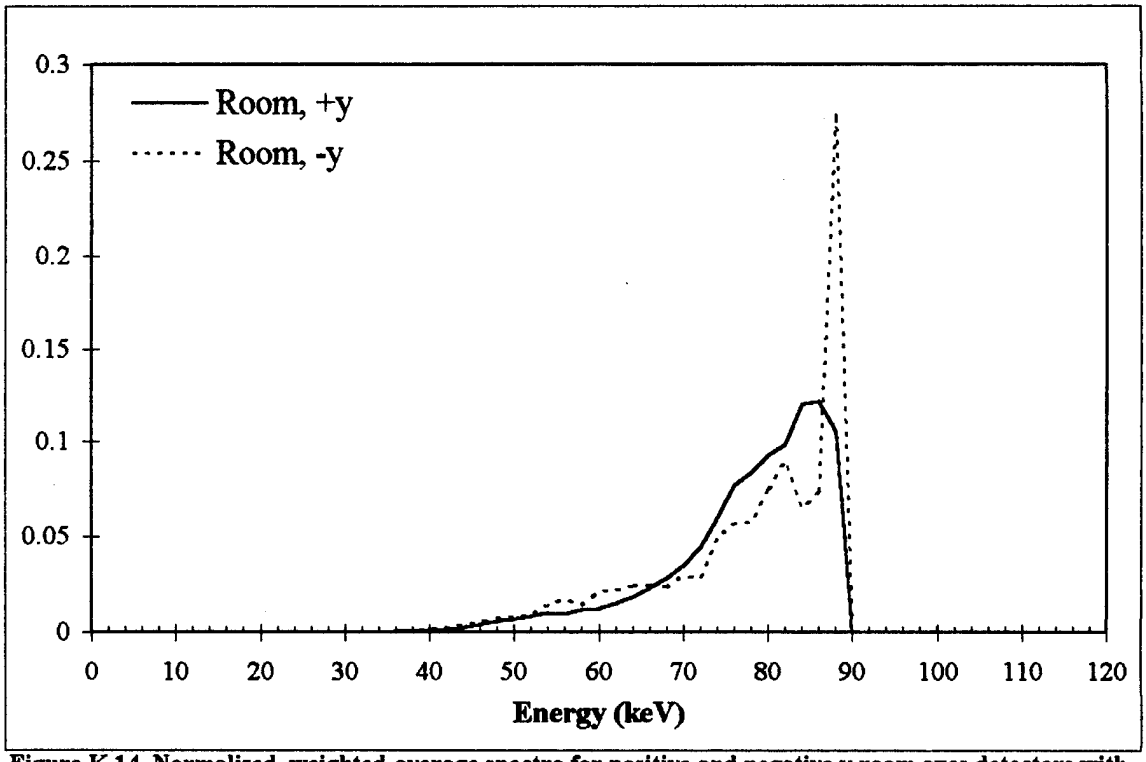

Figure K.14 Normalized, weighted-average spectra for positive and negative y room axes detectors with CT in GE minimum recommended room, 1/16" lead, head scan.

Appendix K: GE Minimum Recommended Suite, 1/16" Lead Shielding, Head Scan

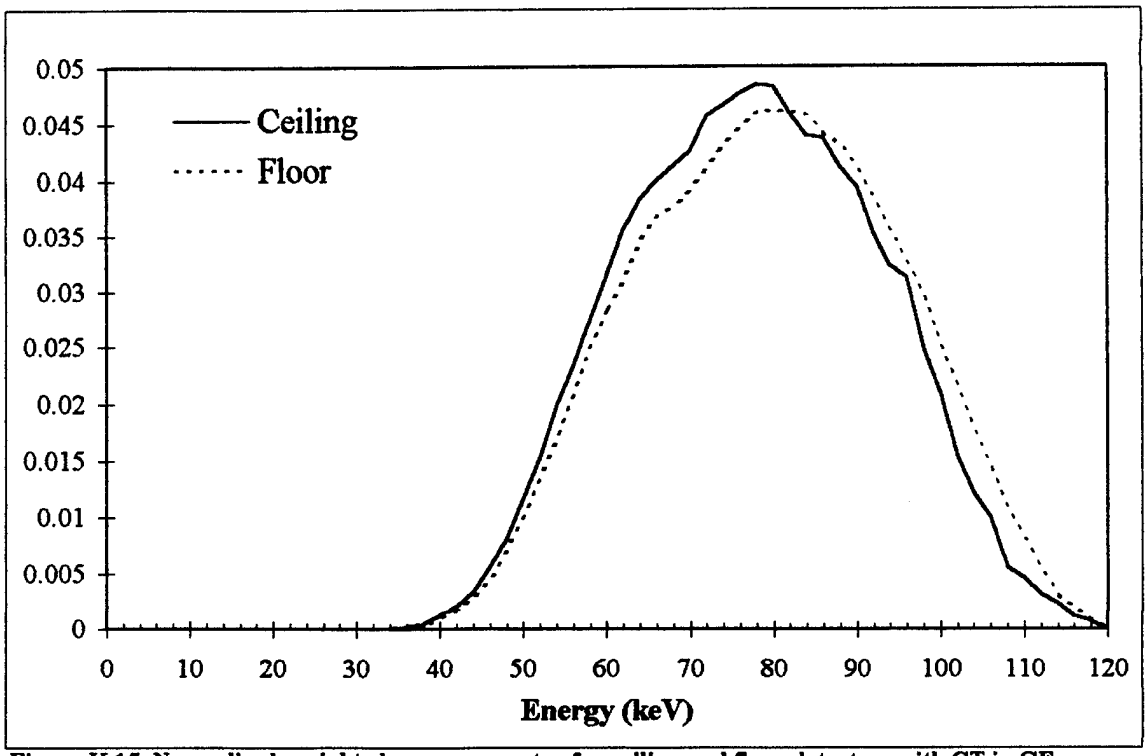

Figure K.15 Normalized, weighted-average spectra for ceiling and floor detectors with CT in GE minimum recommended room, 1/16" lead, head scan.

References

Attix, Frank Herbert. Introduction to Radiological Physics and Radiation Dosimetry. New York: John Wiley & Sons, 1986.

Bevington, Philip R. Data Reduction and Error Analysis for the Physical Sciences. New York: McGraw-Hill Book Company, 1969.

Briesmeister, J. MCNP--A General Monte Carlo Code for Neutron and Photon Transport, Version 3A. Rev. 2, Los Alamos National Laboratory; September 1986. (LA-7396-M).

-----. MCNP-- Monte Carlo N-Particle Transport Code System, Version 4A. Los Alamos National Laboratory, November 1993. (LA-12625-M, UC-705 and UC-700).

Caffey, Jerry. Caffey, Inc., D'Iberville, MS. Fax transmittal to Mike Walling, Wright-Patterson Medical Center. 23 December 1993.

Cashwell, E. D. and others. A Practical Manual on the Monte Carlo Method for Random Walk Problems. Los Alamos: Los Alamos Scientific Laboratory, January 1957. (LA-2120).

Cember, Herman. Introduction to Health Physics. New York: Pergamon Press, 1983.

Chilton, Arthur B. and others. Principles of Radiation Shielding. Englewood Cliffs, NJ: Prentice-Hall, Inc., 1984.

Fewell, T. R.; Shuping, R. E. "The Photon Energy Distribution of Some Typical Diagnostic X-Ray Beams". Medical Physics, Vol. 4, pp. 187-197 (1977).

Fewell, T. R.; Shuping, R. E.; Hawkins, Kermit R., Jr. Handbook of computed Tomography X-ray Spectra. Rockville, MD: U.S. Department of Health and Human Services. (April 1981).

Fox, Stanley. CT Marketing, GE, Milwaukee WI. Telephone interview. 7 July 1995.

-----. CT Marketing, GE, Milwaukee WI. Telephone interview. 22 September 1995.

GE Medical Systems. B7996A, CT HiSpeed Advantage™ Scanner System Product Data. Milwaukee: GE Medical Systems, 1991.

-----. CT HiSpeed Advantage Preinstallation, Direction 46-018301. Milwaukee: GE Medical Systems, March 1995.

-----. CT HiSpeed Advantage Preinstallation, Direction 18001. Milwaukee: GE Medical Systems, March 1995.

Harmon, Charles K. II; Busch, Robert D.; Briemiester, J.; Forster, R. Arthur. Criticality Calculations with MCNP: A Primer. Los Alamos National Laboratory, August 1994. (LA-12827-M, UC-714).

International Commission on Radiation Units and Measurements. Radiation Quantities and Units, ICRU Report 33. Washington: ICRU, April 1980.

-----. Annual Limits on Intake of Radionuclides by Workers Based on the 1990 Recommendations, ICRU Report 61. Washington: ICRU, April 1991.

Kak, Avinash C. and Slaney, Malcolm. Principles of Computerized Tomographic Imaging. New York: The Institute of Electrical and Electronics Engineers, Inc., 1987.

Lederer, C. Michael and others. Table of Isotopes (Seventh Edition). New York: John Wiley & Sons, 1978.

Lewis, E. E. and Miller, W. F. Jr. Computational Methods of Neutron Transport. New York: John Wiley & Sons, 1984.

Livingston, Thomas. Salesman, GE, Dayton OH. Telephone interview. June 1995.

Lynch, Charles T. CRC Handbook of Material Science, Vol II, Metals, Composites and Refractory Materials. Cleveland: CRC Press, Inc., 1975.

Macovski, Albert. Medical Imaging Systems. Englewood Cliffs, NJ: Prentice-Hall, Inc., 1983.

Mathews, Kirk. Informal tutorial notes on Monte Carlo method. Air Force Institute of Technology, Wright-Patterson AFB OH, May 1995.

MCNP. Version 4a, 8mm DAT Tape. Computer software. Radiation Transport Group, Los Alamos National Laboratory NM. (1993).

Metzger, Robert; Richardson, Rebecca; Van Riper, Kenneth A. "A Monte Carlo Model for Retrospective Analysis of Shield Design in Diagnostic X-Ray Room". Health Physics, Vol. 65, No. 2: pp. 164-171 (1993).

Metzger, Robert. Radiation Safety Engineering, Chandler, AZ. Telephone interview. July 1995.

-----. Radiation Safety Engineering, Chandler, AZ. Telephone interview. 21 September 1995.

Michael, Cliff, SSgt, USAF. CT Department, Wright-Patterson Medical Center. Personal interviews. Summer 1995.

National Council on Radiation Protection and Measurements. Structural Shielding Design and Evaluation for Medical Use of X-Rays and Gamma Rays of Energies of Up to 10 MeV, NCRP Report No. 49. Bethesda, MD: NCRP, 1976.

-----. Recommendations on Limits for Exposure to Ionizing Radiation, NCRP Report No. 91. Bethesda, MD: NCRP, 1987.

-----. Medical X-ray, Electron Beam and Gamma-Ray Protection for Energies Up To 50 MeV (Equipment Design, Performance and Use), NCRP Report No. 102. Bethesda, MD: NCRP, 1989.

-----. Conceptual Basis for Calculations of Absorbed Dose Distributions, NCRP Report No. 108. Bethesda, MD: NCRP, 1991.

Nuclear Regulatory Commission. 10CFR Part 20 et al. Standards for Protection Against Radiation. Washington: NRC, 28 April 1995.

Parker, Sybil P., Editor in Chief. Dictionary of Scientific and Technical Terms, Fourth Edition. New York: McGraw-Hill Book Company, 1989.

Poteat, Susan. Radiation Safety Office, Wright-Patterson Medical Center. Personal interviews. Summer 1995.

Profio, A. Edward. Radiation Shielding and Dosimetry. New York: John Wiley & Sons, 1979.

Shleien, Bernard, Editor. The Health Physics and Radiological Health Handbook, Revised Edition. Silver Spring, MD: Scinta, Inc., 1992.

Simpkin, Douglas J. "Radiation Shielding of Multiple X-ray Sources I Diagnostic Radiology", Health Physics, Vol. 50, No. 1: pp. 117-122 (January 1986).

-----. "A General Solution to the Shielding of Medical X and γ Rays by the NCRP Report No. 49 Methods", Health Physics, Vol. 52, No. 4: pp. 431-436 (April 1987).

-----. "Fitting Parameters for Medical Diagnostic X Ray Transmission Data ", Health Physics, Vol. 54, No. 3: pp. 345-347 (March 1988).

-----. "Shielding Requirements for Constant-Potential Diagnostic X-Ray Beams Determined By a Monte Carlo Calculation", Health Physics, Vol. 56, No. 2: pp. 151-164 (February 1989).

-----. "Transmission of Scatter Radiation from Computed Tomography (CT) Scanners Determined by a Monte Carlo Calculation", Health Physics, Note, Vol. 58, No. 3: pp. 363-367 (March 1990).

-----. "Shielding a Spectrum of Workloads in Diagnostic Radiology", Health Physics, Vol. 61, No. 2: pp. 259-261 (1991).

-----. Department of Radiology, St. Luke's Medical Center, Milwaukee WI. Telephone interview. 7 July 1995.

Snyder, W.; Ford, M.; Warner, G. Estimates of Specific Absorbed Fractions for Photon Sources Uniformly Distributed in Various Organs of a Heterogeneous Phantom, MIRD Pamphlet No. 5. New York: Society of Nuclear Medicine; Revised, 1978.

Van Riper, Kenneth A. Los Alamos National Laboratory, Los Alamos NM. Telephone interview. July 1995.

-----. Los Alamos National Laboratory, Los Alamos NM. E-mail. 21 September 1995.

Wildi, Theodore. Units and Conversion Charts, A Handbook for Scientists and Engineers. New York: The Institute of Electrical and Electronics Engineers, 1991.

Wood, James. Computational Methods in Reactor Shielding. Oxford: Pergamon Press, 1982.

Vita

Capt Karyl J. Davis was born on 1 June 1962 in Racine, Wisconsin. She graduated from Northland Pines High School in 1980. In 1981 she enlisted, attending basic training at Lackland AFB, Texas. She attended Air Traffic Control Radar Maintenance technical training at Keesler AFB, MS. Her first assignment in the ATC radar maintenance career field was also at Keesler AFB. While there she attended Jefferson Davis Junior College, where, along with the credits from her technical training, she completed a CCAF Electronics Systems Technology associates degree. In 1986 she was accepted for the Airman's Education Commissioning Program. She completed her undergraduate degree at the University of Maryland, College Park, Maryland. While there, she completed the course work necessary for a CCAF Electronics Engineering associates degree. She graduated cum laude with a bachelor's degree in physics in 1990 with Departmental and General Honors. She received her commission on 1 October 1990 after attending Officer Training School at Lackland AFB. Her first commissioned assignment was at Kelly AFB, TX as an electronic warfare physicist at the then Air Force Electronic Warfare Center (now: AF Information Warfare Center) in the Studies and Analysis directorate. In June 1994, she entered the School of Computers and Engineering at the AF Institute of Technology as a master's candidate in engineering physics. She has been married since 1982 and has one son, born December 1991.

Permanent Address: 1642 Apache Trail
St. Germain, WI 54558

REPORT DOCUMENTATION PAGE

Form Approved
OMB No. 0704-0188

1. AGENCY USE ONLY *(Leave blank)*	2. REPORT DATE	3. REPORT TYPE AND DATES COVERED
	Dec 95	Master's Thesis

4. TITLE AND SUBTITLE

A MONTE CARLO ANALYSIS OF COMPUTERIZED TOMOGRAPHY

5. FUNDING NUMBERS

6. AUTHOR(S)

Karyl J. Davis, Capt, USAF

7. PERFORMING ORGANIZATION NAME(S) AND ADDRESS(ES)

Air Force Institute of Technology
2750 P Street
WPAFB OH 45433-6583

8. PERFORMING ORGANIZATION REPORT NUMBER

AFIT/ENP/GAP/95D-3

9. SPONSORING/MONITORING AGENCY NAME(S) AND ADDRESS(ES)

William Ruck, Capt, USAF
Radiation Safety Officer, WPMC
WPAFB OH 45433

10. SPONSORING/MONITORING AGENCY REPORT NUMBER

11. SUPPLEMENTARY NOTES

12a. DISTRIBUTION/AVAILABILITY STATEMENT

Approved for public release; unlimited distribution

12b. DISTRIBUTION CODE

13. ABSTRACT *(Maximum 200 words)*

This thesis modeled computerized tomography (CT) using Monte Carlo methods to determine the non-occupational dose outside the suite at Wright-Patterson Medical Center and at a generic suite. This was driven by the recent inclusion of the most recent NCRP recommended dose limits into 10CFR20. Modeling was done with MCNP, a general-purpose Monte Carlo N-particle transport model. WPMC average usage was used to establish usage factors and workload. Suite walls were lead shielding between gypsum drywall. Film badges placed in the CT suite at WPMC were compared to MCNP modeling results to validate method and results. They agreed within a factor of two. Outside both the WPMC CT suite and the generic room, the continuous exposure non-occupational dose limit was exceeded below the floor and above the ceiling, the infrequent exposure non-occupational dose limit was exceeded below the floor. The occupational and non-occupational dose limit outside the x walls of the generic room was exceeded. The scattered radiation spectrum is a softened source spectrum.

14. SUBJECT TERMS

Monte Carlo, computerized tomography, radiation protection, scattered radiation

15. NUMBER OF PAGES

220

16. PRICE CODE

17. SECURITY CLASSIFICATION OF REPORT	18. SECURITY CLASSIFICATION OF THIS PAGE	19. SECURITY CLASSIFICATION OF ABSTRACT	20. LIMITATION OF ABSTRACT
Unclassified			UL